Diss. ETH No. 21243

Quantum Magnetism with Ultracold Fermions in an Optical Lattice

A dissertation submitted to the

ETH Zurich

for the degree of
Doctor of Sciences

presented by

Daniel Günther Greif

Master of Arts,
State University of New York at Stony Brook, USA

born 13th January 1984 in Hialeah, Florida, USA
citizen of Germany and USA

accepted on the recommendation of
Prof. Dr. Tilman Esslinger, examiner
Prof. Dr. Manfred Sigrist, co-examiner

2013

To my family and friends

Zusammenfassung

Die vorliegende Arbeit stellt Experimente mit ultrakalten, fermionischen Quantengasen in optischen Gittern zur Untersuchung von Festkörper Modellsystemen für Quantenmagnetismus und Graphen vor. Zentral für die Realisierung der niedrigen Temperaturen, die Detektion der Spin Korrelationen, sowie die Herstellung des hexagonalen Gitters von Graphen ist ein neu entwickeltes optisches Gitter mit variabler Geometrie, welches im Zuge dieser Doktorarbeit entwickelt und gebaut wurde. Dieses Gitter erlaubt ein breites Spektrum an realisierbaren Topologien, welche von dreieckigen und hexagonalen Mustern bis hin zu schachbrettartigen und dimerisierten Strukturen reichen. Zudem erlaubt der Aufbau eine dynamische Veränderung zwischen den verschiedenen Geometrien.

Die für Quantenmagnetismus notwendigen niedrigen Temperaturen werden durch ein lokales Entropieumverteilungsschema erreicht. Im Experiment wird ein repulsives, fermionisches Quantengas bestehend aus zwei Spinkomponenten des Elements ^{40}K in entweder ein dimerisiertes oder anisotropes kubisches Gitter geladen. Die magnetische Ordnung zwischen den zwei Spinkomponenten wird anschliessend beobachtet. Diese wird charakterisiert durch die Messung der Spinkorrelationen auf benachbarten Gitterplätzen, welche anhand von kohärenten Singlet-Triplet Oszillationen und anschliessender Verschmelzung zweier benachbarter Gitterplätze gemessen wird. Ein Vergleich unserer experimentellen Resultate mit theoretischen Berechnungen basierend auf einer Hochtemperatur Entwicklung bis zur zweiten Ordnung ergibt eine sehr gute Übereinstimmung.

Eine weitere, alternative Detektionsmethode zur Messung von Korrelation auf benachbarten Gitterplätzen für wechselwirkenden Fermionen in optischen Gittern wird ausserdem vorgestellt. Die Messgrösse ist sensitiv sowohl auf Dichte- als auch Spinkorrelationen und misst die Wahrscheinlichkeit, zwei Teilchen mit entgegen gesetztem Spin auf benachbarten Gitterplätzen zu finden. Die experimentelle Methode basiert auf periodischer Modulation der Gittertiefe, was zur Erzeugung von zusätzlichen Doppelbesetzungen führt. Für stark repulsive, fermionische Gase in isotropen, einfach kubischen Gittern wird eine starke Abhänigkeit des Messsignales von der Entropie pro Teilchen beobachtet. Die experimentellen Beobachtungen sind in guter Übereinstimmung mit den theoretischen Berechnungen, welche ebenfalls auf einer Hochtemperatur Entwicklung bis zur zweiten Ordnung basieren.

In einer weiteren experimentellen Messreihe wird ein nichtwechselwirkendes fermionisches Gas in ein hexagonales Gitter geladen und die Existenz zweier Dirac Punkte in der Bandstruktur direkt beobachtet. Die Detektionsmethode basiert auf der Identifikation eines Minimums in der Bandlücke, welches durch impulsaufgelöste Interbandübergänge beobachtet wird. Die Flexibilität des Gitteraufbaus erlaubt eine Veränderung der Eigenschaften der Dirac Punkte, so zum Beispiel deren Position im Impulsraum oder die Steigung der linearen Dispersionsrelation. Des Weiteren kann die effektive Masse der Dirac Fermionen kontrolliert werden indem

die Inversionssymmetrie des Gitters gebrochen wird. Für einen kritischen Wert der Gitterparameter wird die Verschmelzung und Vernichtung der beiden Dirac Punkte beobachtet. Dieser topologische Übergang ist in exzellenter Übereinstimmung mit *ab initio* Bandstrukturrechnungen.

Abstract

This thesis reports on experiments with ultracold fermionic quantum gases in an optical lattice for the study of solid state model systems of quantum magentism and graphene. The key for reaching the low-temperature regime of quantum magnetism, detecting the magnetic spin correlations and realizing the honeycomb lattice of graphene is a newly developed tunable-geometry optical lattice, which was designed and built during the course of this thesis. This lattice gives access to a broad variety of geometries ranging from triangular, honeycomb, chequerboard and dimerized lattices, and additionally allows dynamic tuning between the different structures.

The low temperatures necessary for quantum magnetism are achieved via a local entropy redistribution scheme. After loading a repulsive two-component fermionic quantum gas of ^{40}K into either a dimerized cubic lattice or anisotropic simple cubic lattice, magnetic ordering on neighbouring sites is observed. The magnetic ordering is characterized by measuring spin correlations on neighbouring sites, which are obtained from coherent singlet-triplet oscillations and subsequent merging of adjacent lattice sites. When comparing our results to the predictions of a high-temperature series up to second order, we find very good agreement.

An alternative probe of nearest-neighbour correlations for fermions with interactions in an optical lattice is realized. This probe is sensitive to both density and spin correlations and measures the probability of finding two particles with opposite spins on neighbouring sites. The experimental method relies on periodic modulation of the lattice depth, which leads to the creation of additional double occupancies. Applying this method for strongly repulsive fermionic quantum gases in isotropic simple cubic lattices, a strong dependence of the doublon production rate on entropy per particle is found. The observations are in close agreement to theoretical predictions from a high-temperature series up to second order.

When changing the lattice geometry to a honeycomb lattice and loading a non-interacting fermionic gas into the lattice potential, we directly observe Dirac points in the band structure. The detection method is based on identifying a minimum band gap inside the Brillouin zone, which is observed from momentum-resolved interband transitions. The flexibility of the tunable-geometry optical lattice allows adjusting the properties of the Dirac points, for example their position in momentum space and the slope of the linear dispersion at the Dirac points. Additionally, the effective mass of the Dirac fermions can be changed by breaking the inversion symmetry. For a critical value of lattice parameters, the two Dirac points are observed to merge and annihilate each other. This topological transition is found to be in excellent agreement with *ab initio* band structure calculations.

Contents

1 Introduction

The complex interplay between the interactions of electrons and the underlying crystalline structure lies at the heart of solid state research and determines the electronic and magnetic properties in materials. Their physics and open questions provide a key inspiration for the cold atom experiments presented in this thesis, which focus on model systems for quantum magnetism and graphene.

In solid state systems, the combination of large particle numbers and Coulomb interactions often makes a detailed understanding of the underlying many-body physics very difficult. For some materials an effective band theory description of non-interacting particles is possible, which allows the distinction between metallic, semi-conducting and insulating states. Yet, it is precisely in complex materials with strong interactions where novel and surprising effects appear. Examples range from frustrated spin systems [1] to high-temperature superconductivity first observed by K. Müller and J. Bednorz in 1986 [2]. A central difficulty in understanding these phenomena is the associated many-body state emerging at low temperatures, where the strong correlations between the microscopic particles lead to novel quantum phases, instead of merely being single-particle effects.

Apart from interactions, the behaviour of electrons in a solid is determined by the underlying crystalline structure, which can lead to surprising phenomena in complex lattice geometries. A prominent example is the case of Graphene, which is a single two-dimensional layer of carbon atoms arranged in a honeycomb structure [3]. The presence of Dirac points in the Graphene band structure, which are topological defects in the form of touching points of the two lowest bands in the presence of a linear dispersion relation, is the origin for its extraordinary optical, electronic and mechanical properties. These include ultra-high mobilities, very large spin coherence lengths and one of the highest material stiffness values ever measured. Moreover, Graphene is a realization of massless Dirac fermions leading to surprising effects such as Klein tunneling and the anomalous quantum Hall-effect at room temperature. Despite the tremendous progress of Graphene research, open questions remain for the case of strong interactions and very low temperatures, where a spin-liquid sate has been predicted and debated [4, 5].

The magnetism in solids has proven to be a second important key in advancing today's material research and has revolutionized data storage and reading in multiple ways. Particularly promising for next-generation applications are materials in the regime of quantum magnetism, where quantum mechanical spins order spatially in the crystalline structure. The origin of magnetism is a complex interplay between delocalization and interaction effects as well as quantum statistics [6, 7], which gives rise to an exchange energy between spins and leads to a vast number of different magnetic states. In many cases these systems show long-range spin order at low temperatures, with either a spatially alternating or parallel orientation

of the electronic spins (corresponding to antiferromagnetic or ferromagnetic order). Owing to the exponentially growing number of quantum states, a theoretical analysis is already for seemingly simple cases, such as Heisenberg antiferromagnets, exceedingly difficult. The situation becomes even more complex when long-range order is frustrated, for example by changing the doping, geometry or dimensionality [8, 9]. In this case, the state of the system is dominated by the competition of long-range spin order and quantum fluctuations, giving rise to exotic states such as spin-liquids, spin glasses and resonating valence-bond states [6, 10, 11]. While these examples consider short-range magnetic interactions, quite surprising phenomena appear for the case of long-range interactions, where liquid-crystal phases such as nematic, smectic or chiral states are expected [12].

In some cases a detailed understanding of the electronic and magnetic properties of these materials is possible by introducing simplified model systems for the complex many-body problem. For several materials however already the formulation of a simplified model system is difficult owing to non-negligible contributions of the long-range electron-electron interactions, higher lattice orbital effects and coupling between electron and phonon modes in the crystal. In addition, understanding even the simplest fermionic model systems is far from easy, as they have found to be numerically challenging to tackle in the low-temperature regime. Until today, this remains a field of intense study in theoretical solid state research.

One of the simplest models for interacting fermionic particles in a crystal is the Fermi-Hubbard model [13]. It simplifies the crystalline structure by a periodic arrangement of lattice sites, which are filled with fermionic spin 1/2 particles that delocalize via tunnelling to neighbouring sites and share a common interaction energy when occupying the same site. Despite the simplicity of the Fermi-Hubbard model, it is a fertile starting ground for investigating the interplay between charge and spin degrees of freedom, which is considered to be the origin for high-temperature superconductivity in two-dimensional doped systems [14]. For a three-dimensional simple cubic lattice in the lowest band, the Fermi-Hubbard model predicts a cross-over from a metallic to Mott-insulating state at half-filling (one particle per site), whereas at sufficiently low temperatures a phase transition to an antiferromagnetically ordered state appears. Despite intense efforts from the solid state community over the last few decades, many questions remain unanswered for the Fermi-Hubbard model [15] and the exact ground-state of the two-and three-dimensional simple cubic lattice is still not clear. Furthermore, the case of more complex lattice structures, such as dimerized or honeycomb lattices, is equally little understood and even the qualitative nature of the phase diagram remains for some lattice geometries disputed until today [4, 5].

Promising developments towards further understanding of solid state model systems comes from an unexpected direction: ultracold quantum gases in optical lattices. The basic idea is to cool a dilute atomic gas down to quantum degeneracy and expose the gas to an optical lattice, which is formed by a standing wave pattern of intersecting laser beams. Owing to the atom-light interaction [16], the atoms move in a potential landscape that is proportional to the laser intensity distribution. The role of the charge carrying electrons is then taken by the gaseous atoms, whereas the crystalline structure is formed by the optical lattice. This technique of creating and studying *artificial solids* has proven to be a particularly clean and highly flexible route to condensed matter model systems, as on the one hand the underlying microscopic Hamiltonian is very well known and on the other hand all relevant energy scales and parameters – for example the interaction energy, kinetic energy, filling, temperature

and lattice geometry – can be tuned almost freely and at will. The idea of studying a quantum system by choosing a physically different, but fully controllable system with the same properties goes back to R. Feynman, who called this strategy *quantum simulation* [17].

In solids the degeneracy temperature, where quantum effects start to play an important role, is typically on the order of the room temperature. In an optical lattice the situation is different, as the spacing between lattice sites is around $a = 1\,\mu$m, which is a factor of 10^4 larger than in normal solids. As the characteristic energy of the system scales as $1/ma^2$, where m is the mass of the atoms, the temperature requirements for reaching the quantum regime are in the ultralow range of a few nK. While cryogenic techniques are completely hopeless, the key to reaching these temperature scales came with the invention of laser and evaporative cooling [18]. A breakthrough was reported in 1995 with the first realization of Bose-Einstein condensation of ^{87}Rb and ^{23}Na [19, 20]. The realization of the first degenerate Fermi gas, the fermionic counter-part of the Bose-Einstein condensate, was reported only a few years later in 1999 with ^{40}K [21], soon followed by the condensation of Feshbach molecules [22, 23, 24] and Cooper pairs [25]. Detailed overviews of the creation of and experiments with degenerate bosonic and fermionic quantum gases can be found in [26, 27, 28, 29, 30, 31].

After the realization of the conceptual connection between ultracold quantum gases in optical lattices and solid state model systems in 1998 [32], the first experimental demonstration followed soon after in 2001 with the superfluid to Mott-insulator quantum phase transition for bosonic atoms [33]. This experiment impressively demonstrated the capability of ultracold atoms to accurately simulate and study quantum phases within the Bose-Hubbard model and laid the foundation for a series of further experimental studies with interacting bosonic atoms in optical lattices by various groups [34, 35, 36, 37, 38, 39]. Recently, even the Mott-insulating shell structure could be spatially observed on the single-site level using high-resolution microscopes [40, 41].

The first ultracold fermionic quantum gas in a three-dimensional optical lattice was created in 2005 with ^{40}K [42], two years after the realization in a one-dimensional configuration [43]. First experiments with ultracold fermions in three-dimensional lattices focussed on the non-interacting and two-particle interaction regime, with the investigation of s- and p-wave Feshbach resonances in various dimensions [44, 45, 46, 47] and the observation of fermion antibunching [48]. Other experiments studied the physics of higher bands [49] and the influence of fermionic atoms on the superfluid to Mott-insulator transition in Bose-Fermi mixtures [50, 51, 52]. This was later extended to a detailed analysis of the collapse and revival dynamcics of a Bose-Fermi mixture in a simple cubic lattice [53]. The unique control over particle interactions provided by Feshbach resonances also allowed the study of strongly interacting fermionic gases in optical lattices. This lead to the observation of interaction-controlled transport [54] and the realization of a Mott-insulating state for repulsive interactions [55, 56], whereas for attractive interactions the thermodynamic properties were studied [57].

Experiments with ultracold fermions in optical lattices have so far focussed on the charge degree of freedom in simple cubic lattice geometries, whereas the spin-ordered regime of quantum magnetism could not be reached so far. This is mainly due to the low temperatures required, where the relevant energy scale is given by the exchange energy. This scale is usually much lower than the already very small tunnelling and interaction energy in cold atom systems and therefore leads to ultra-low temperature requirements in the lattice of on the order of 1 nK. Although achieving these temperatures in cold atom laboratories is far from

easy, reaching the regime of quantum magnetism in experiments has been declared a major goal in the cold atoms community. Promising developments have already been reported with bosonic atoms in the last years [58, 59, 60, 61, 62].

Complex lattice geometries for ultracold atoms have so far only been realized with bosonic atoms. The realization of a Bose-Einstein condensate in a two-dimensional double-well lattice [63] was soon followed by its one-dimensional variant [64]. Only very recently, triangular, hexagonal, Kagome and bipartite square lattice structures became experimentally accessible [65, 66, 67, 68]. Using a one-dimensional bichromatic lattice the linear crossing of two high-energy bands was investigated and Klein-tunnelling could be observed [69, 70]. A clear observation of Dirac points in the hexagonal lattice structure or direct evidence for flat bands in the Kagome lattice could however not be achieved.

In this thesis the first experimental realization of quantum magnetism with repulsively interacting ultracold fermions in an optical lattice is demonstrated [71]. The key for both reaching the low-temperature regime and detecting the magnetic ordering is a newly developed tunable-geometry optical lattice, which was designed and built during the course of this thesis. This lattice gives access to a broad variety of geometries ranging from triangular, honeycomb, chequerboard and dimerized lattices, and, at the same time, allows dynamic tuning between the different structures. The tunable-geometry optical lattice is created by interfering laser beams intersecting under 90°, where the corresponding interference phase is actively stabilized using a technique similar to the phase locking of long-distance fibers commonly employed in the synchronization of optical clocks [72].

The low temperatures necessary for quantum magnetism are achieved via a local entropy redistribution scheme, which is implemented by adjusting the lattice geometry to either a dimerized cubic lattice or anisotropic simple cubic lattice. Already previously entropy redistribution schemes between different regions of the trap have been proposed, but an experimental implementation was so far not reported [73, 74, 75]. In the experiment, the magnetic ordering is characterized by probing the spin correlations on neighboring sites, which are obtained by merging adjacent sites together. The detection method is an extension of a previously developed technique for bosonic atoms [76]. When comparing our results to the predictions of a high-temperature series up to second order, we find very good agreement. In the dimerized lattice configuration the corresponding temperatures in the lattice are found to be below half the magnetic exchange energy.

We furthermore implement and study an alternative probe of nearest-neighbour correlations for interacting fermions in an optical lattice [77]. The probe is sensitive to both density and spin correlations and measures the probability of finding two particles with opposite spins on neighbouring sites. The experimental method relies on periodic modulation of the lattice depth, where the associated kinetic energy perturbation causes tunnelling of particles to adjacent sites [78]. This leads to a constant energy absorption in the system, which is observed as a production rate of additional double occupancies. For large interactions, the value of the doublon production rate is then directly given by the nearest-neighbour correlator [79, 80, 81, 82]. This technique is applied to an isotropic simple cubic lattice and a strong dependence on entropy per particle is found, in close agreement with theoretical predictions from a high-temperature series up to second order. The method can be used for a reliable determination of the temperature in the lattice, which was later applied to other fermionic

elements with a large number of spin components by a different experimental group [83]. For the case of a weakly or non-interacting gas, lattice modulation was found to be a reliable probe for the underlying band structure [84].

When changing the lattice geometry to a honeycomb lattice and loading a non-interacting fermionic gas of ^{40}K into the lattice potential, we directly observe Dirac points in the band structure [85, 86]. The detection method is based on identifying a minimum band gap inside the Brillouin zone, which is observed from momentum-resolved interband transitions. The employed technique is closely related to a method recently used with bosonic atoms to characterize the linear crossing of two high-energy bands [69] – with the extension of providing additional momentum resolution. The unique tunability of the tunable-geometry optical lattice allows adjusting the properties of the Dirac points. The effective mass of the Dirac fermions can be changed by breaking the inversion symmetry. Additionally, a change in the lattice anisotropy leads to a shift of the position of the Dirac points inside the Brillouin zone. When increasing the anisotropy beyond a critical limit, the two Dirac points are observed to merge and annihilate each other – a situation that has recently attracted considerable theoretical interest [87, 88, 89, 90, 91], but seems extremely challenging to observe in solids [92]. This topological transition in lattice parameter space is mapped out and is found to be in excellent agreement with *ab initio* calculations. In a second set of investigations the experimental results were compared to simple theoretical models for Landau-Zener transfers between the two lowest bands [86, 93, 94]. This will however not be covered in this thesis and will be subject of future work.

During the course of this thesis and before the construction of the tunable-geometry optical lattice further experiments were done. The metal to Mott-insulator transition for repulsively interacting fermions in a simple cubic lattice geometry was studied on a quantitative level including a detailed analysis of systematic and statistic uncertainties [95]. The dependence of the experimental equilibrium double occupancy over a broad range of interaction energies and fillings was compared to theoretical predictions. The measurements allowed a reliable determination of the entropy per particle in the lattice and benchmarked the functionality of the cold atoms *quantum simulator* with *ab initio* theoretical calculations. A similar detailed quantitative comparison was performed with bosonic atoms [35], which was later followed by the observation of Mott insulating states for different atomic species [96, 83]. In a second series of experiments the equilibrium regime was left behind and the decay of high-energy excitations in form of additional double occupancies was studied [97, 98]. The additional doublons were found to decay exponentially in time via a high-order scattering process involving several neighbouring particles. As predicted from perturbation theory, the corresponding decay time scales exponentially with the ratio of interaction to kinetic energy. Owing to the ultra-low energy scales characteristic for cold atoms systems, the decay of doublons could be directly observed in time. This study was followed by further experiments done in other groups, which investigate the expansion dynamics and higher band effects of ultracold fermions in optical lattices [99, 100]. Since both the experiments on the quantitative study of the Mott-insulating state and the elastic decay of doublons have been described in full detail in previous work [101, 102], they will not be presented in this thesis.

The work during the course of this thesis has been carried out together with Niels Strohmaier, Henning Moritz, Robert Jördens, Leticia Tarruell, Thomas Uehlinger, Gregor Jotzu and Tilman Esslinger.

Outline of this thesis

- Chapter 2 is devoted to the experimental setup of the tunable-geometry optical lattice. The setup of the intersecting laser beams and the accessible geometries are explained. Additonally, the technique for stabilizing the interference and symmetry phase, which determine the lattice potential, is presented. The chapter concludes with a brief analysis of the different realized band stuctures and tight-binding models for the optical lattice.

- Chapter 3 begins with a brief introduction to scattering theory, Feshbach resonances and a scetch of the Fermi-Hubbard model construction with cold atoms in optical lattices. This is followed by a detailed explanation of the high-temperature series expansion technique in simple cubic and dimerized lattices, which is used throughout this thesis for a reliable comparison between experiment and theory.

- A very brief overview of the experimental apparatus, the preparation technique of an ultracold atomic gas and the most relevant detection methods is given in Chapter 4. Further details can be found in previous work [103, 104].

- The technique for probing nearest-neighbor correlations via lattice modulation is presented in Chapter 5, along with the dependence of the doublon production rate on entropy per particle.

- Chapter 6 and 7 are devoted to the measurement of spin correlations in the low-temperature regime of quantum magnetism. The first chapter gives a detailed explanation of the detection technique, starting from singlet-triplet oscillation on isolated double-wells and extending the method to thermalized many body systems, while considering technical details such as the detection lattice ramp, removal of double occupancies and contrast of the singlet-triplet oscillation signal. The second chapter presents, after a brief introduction to quantum magnetism in the solid state context, the measured spin correlations on neighbouring sites for a repulsive fermionic gas either in a dimerized or anisotropic simple cubic lattice.

- The observation and manipulation of Dirac points in the tunable honeycomb lattice is presented in Chapter 8. The results on changing the effective mass of the Dirac fermions and controlling the linear dispersion slope at the Dirac points are presented and discussed. Furthermore, the control over the position of the two Dirac points in reciprocal space and their subsequent merging and annihilation for a critical value of lattice parameters is demonstrated.

2 The Tunable-Geometry Optical Lattice

During the course of this thesis a novel optical lattice setup was developed with a two-fold motivation:

- access to a broad range of different lattice topologies
- dynamic tunability of the lattice structure for probing correlations on neighbouring lattice sites

The standard optical lattice configuration successfully used in many ultracold atoms experiments is an arrangement of counter-propagating laser beams with perpendicular intersections. The laser beams are far detuned from the atomic resonance and are additionally detuned with respect to each other by several MHz. This detuning causes a rapid oscillation of the time-phase dependent interference term between perpendicular laser beams, which is much faster than the motional timescale of the atoms given by the on-site lattice frequency [105]. The resulting time-averaged potential is then insensitive to the rapidly varying time-phase, which improves the heating rates in the lattice [106].

While this approach gives access to a simple cubic configuration, more complex lattice topologies require different techniques. One possibility are interfering laser beams in a monochromatic optical lattice, where by correct choice of the beam angles and polarizations a whole range of geometries can be accessed [107]. First pioneering experiments were done in two-dimensional [108] and three-dimensional configurations [109, 110], which were all susceptible to phase fluctuations between the interfering beams. Later a double-well lattice in two dimensions with passive phase stability was implemented using electro-optical modulators [63], followed by a one-dimensional variant using a bichromatic lattice setup [64]. Recently, triangular, hexagonal and Kagome structures could be created using interfering beams intersecting under 120° in combination with an active phase stabilization [65, 66, 68]. Using a beam configuration similar to a Michelson interferometer a bipartite square lattice could also be realized [67].

2.1. Introduction

2.1.1. Overview

The tunable-geometry lattice setup consists of an interference pattern in two dimensions with an additional normal standing wave along the third direction. All beams are red-detuned with respect to the atomic resonance and operate at $\lambda = 1064\,\mathrm{nm}$. The beam arrangement for the lattice setup is shown in Fig. 2.1a, including two incoming spatially overlapped beams at frequencies ν and $\nu + \Delta$ along the x-direction and one perpendicular beam along the y-axis at

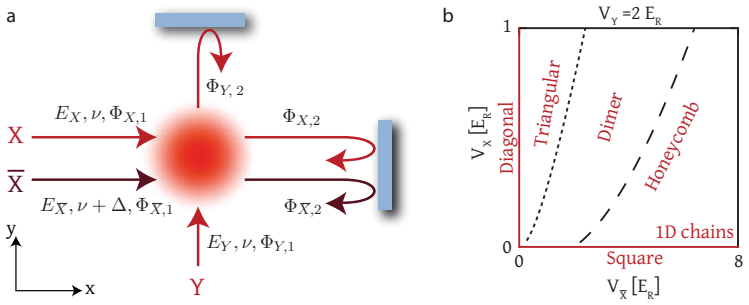

FIGURE 2.1.: **Laser beams forming the tunable-geometry optical lattice.** (a) Two laser beams along the x axis and one beam along the y axis are directed to the atoms and intersect under 90°. All beams are retro-reflected from a 0° mirror. The beams X and $\overline{X}$ are exactly overlapped, as they originate from the same optical fiber. The corresponding electric fields, laser frequencies and light-phases are denoted for each beam. (b) Overview of accessible lattice topologies with the setup. A broad range of structures can be accessed by varying the laser beam intensities.

frequency ν. Along the vertical z-axis a third beam is present at a different frequency $\nu+\Delta_z$. After passing through the atomic cloud all laser beams are retro-reflected from a 0° mirror. All beams in the x-y plane are linearly polarized along the z-axis, such that the interference term becomes relevant, whereas the vertical z-beam is polarized along the y-axis[1]. Neglecting for the moment the spatial laser beam profiles, the electric field distribution for the atoms then reads [111]

$$\begin{aligned}
\vec{E} &= \vec{E}_{\bar{X}} + \vec{E}_X + \vec{E}_Y + \vec{E}_Z \\
\vec{E}_{\bar{X}} &= E_{\bar{X}}\vec{e}_z \left(e^{i(k'x+\phi_{\bar{X},1})} + e^{i(-k'x+\phi_{\bar{X},1}+\phi_{\bar{X},2})}\right) e^{i2\pi\Delta t} \\
\vec{E}_X &= E_X\vec{e}_z \left(e^{i(kx+\phi_{X,1})} + e^{i(-kx+\phi_{X,1}+\phi_{X,2})}\right) \\
\vec{E}_Y &= E_Y\vec{e}_z \left(e^{i(ky+\phi_{Y,1})} + e^{i(-ky+\phi_{Y,1}+\phi_{Y,2})}\right) \\
\vec{E}_Z &= E_Z\vec{e}_y \left(e^{i(k''z+\phi_{Z,1})} + e^{i(-k''y+\phi_{Z,1}+\phi_{Z,2})}\right) e^{i2\pi\Delta_z t}.
\end{aligned} \tag{2.1}$$

Here we omitted the time-dependence $e^{i2\pi\nu t}$ for all terms, where $\nu = c/\lambda$ is the lattice laser frequency. The detunings between the different beams are chosen to be $\Delta = -384.8$ MHz and $\Delta_z = -70.1$ MHz respectively. Since the atomic motional timescale is much slower, the interference between detuned laser beams oscillates rapidly and averages to a constant potential for the atoms. We then find for the atomic potential

$$V_{\mathrm{at}}(x,y,z) \propto |\vec{E}_{\bar{X}}|^2 + |\vec{E}_X + \vec{E}_Y|^2 + |\vec{E}_Z|^2 \tag{2.2}$$

The chosen detunings correspond to a fractional wavelength change on the order of 10^{-6}, such that all wavevectors $k = 2\pi/\lambda$, $k' = 2\pi/\lambda'$ and $k'' = 2\pi/\lambda''$ can safely be set equal when calculating the expressions for the atomic potential. For the case of a red-detuned optical

[1]Note that the y and z-axes used in this thesis are interchanged as compared to the laboratory coordinates.

lattice one finds for the atomic potential

$$\begin{aligned} V_{at}(x,y,z) = &- V_{\bar{X}}\cos^2(kx+\theta/2) - V_X\cos^2(kx) \\ &- V_Y\cos^2(ky) - 2\sqrt{V_X V_Y}\cos(kx)\cos(ky)\cos(\phi) \\ &- V_Z\cos^2(kz). \end{aligned} \tag{2.3}$$

Here $V_{\bar{X}}$, V_X, V_Y and V_Z denote the single beam lattice depths. Apart from a displacement of the lattice structure, the potential in the x-y plane only depends on two phases as compared to the initial six in Eq. 2.1

$$\text{interference phase} \quad \phi = \phi_{Y,1} - \phi_{X,1} + \frac{\phi_{Y,2} - \phi_{X,2}}{2} \tag{2.4}$$

$$\text{symmetry phase} \quad \theta = \phi_{X,2} - \phi_{\bar{X},2}. \tag{2.5}$$

As will be explained in the following sections, all lattice depths and phases in the atomic potential in Eq. 2.3 can be independently controlled and tuned. This gives access to several different lattice geometries in the x-y plane in the experiment. An overview is shown in Fig. 2.1b, where by adjusting the lattice depths V_X and $V_{\bar{X}}$ a square, triangular, dimerized, honeycomb and chequerboard lattice can be created, as well as asymmetrically coupled one-dimensional chains. Tuning the lattice depth V_Z along the third axis gives control over the dimensionality of the system, either three-dimensional or two-dimensional. A detailed discussion of the band structure for the different geometries can be found in section 2.3.

2.1.2. The lattice potential

To gain a better understanding of the accessible two-dimensional topologies with this setup, we rewrite the expression for the atomic potential $V_{at}(x,y)$ from Eq. 2.3 into a different form

$$\begin{aligned} V_{at}(x,y) = &\underbrace{-\widetilde{V_X}\cos^2(kx+\beta/2) - V_Y\cos^2(ky)}_{\text{square}} \\ &\underbrace{-2\sqrt{V_X V_Y}\cos(kx)\cos(ky)\cos(\phi)}_{\text{chequerboard}} \end{aligned} \tag{2.6}$$

The atomic potential in the x-y plane is hence the sum of a square and chequerboard lattice with independently controllable parameters. Here we introduced the new lattice depth $\widetilde{V_X}$ and the position phase β, where

$$\begin{aligned} \widetilde{V_X} &= \pm\sqrt{V_{\bar{X}}^2 + 2V_{\bar{X}}V_X\cos(\theta) + V_X^2}, \quad \text{" } \pm \text{ " for } V_{\bar{X}}\cos\theta + V_X \gtrless 0 \\ \tan(\beta) &= \frac{\sin(\theta)}{\cos(\theta) + V_X/V_{\bar{X}}}. \end{aligned} \tag{2.7}$$

Fig. 2.2 shows the potential for the chequerboard lattice, where the sites are located on a diagonal pattern with a spacing increased by a factor of $\sqrt{2}$ as compared to the normal square lattice. Its depth and strength are determined by the lattice depths V_X and V_Y and additionally by the interference phase ϕ. This phase also determines the location of the potential minima, depending on the sign of the term $\cos(\phi)$. For $\phi = \pi/2 + n\pi, n \in \mathbb{Z}$ only a spatially constant potential instead of a chequerboard pattern is present.

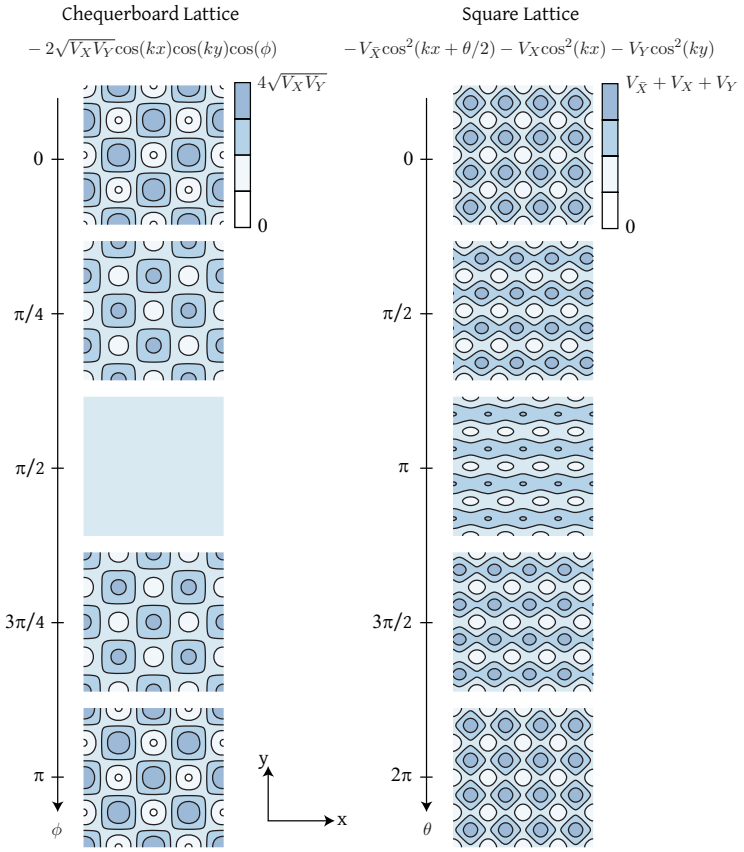

FIGURE 2.2.: **Lattice potential for the atoms.** The lattice potential for the chequerboard pattern is shown as a function of the interference phase ϕ on the left. This phase determines the depth of the pattern and additionally the position of the maxima and minima. Potential minima for the atoms correspond to the white regions. On the right the dependence of the square lattice potential is investigated as a function of the symmetry phase θ. As θ is increased from 0 to 2π, the square lattice shifts in position horizontally by one lattice site, while the depth changes slightly. In this example $V_{\overline{X},X,Y} = [10, 5, 15]E_{\mathrm{R}}$. The total potential seen by the atoms is the sum of the chequerboard and square lattice.

The origin of the chequerboard term from the interfering beams can be understood by noting the equality

$$\begin{aligned} -4\cos(kx)\cos(ky)\cos(\phi) = \quad & \cos\left(k(x-y)-\phi\right) + \cos\left(k(x+y)-\phi\right) \\ + \quad & \cos\left(k(x-y)+\phi\right) + \cos\left(k(x+y)+\phi\right). \end{aligned}$$

The chequerboard pattern is hence created by the four possible interference contributions of two perpendicularly intersecting laser beams at the same frequency ν propagating along the x and y axis, see Fig. 2.1a. This gives rise to four diagonal standing wave patterns, the sum of which creates the chequerboard pattern.

The interfering contributions from the counter-propagating laser beams along the x and y direction – together with the additional standing-wave created by the $\bar{X}$ beam – gives rise to the square potential in Eq. 2.6. Its strength is determined by all three lattice depths $V_{\bar{X}}$,

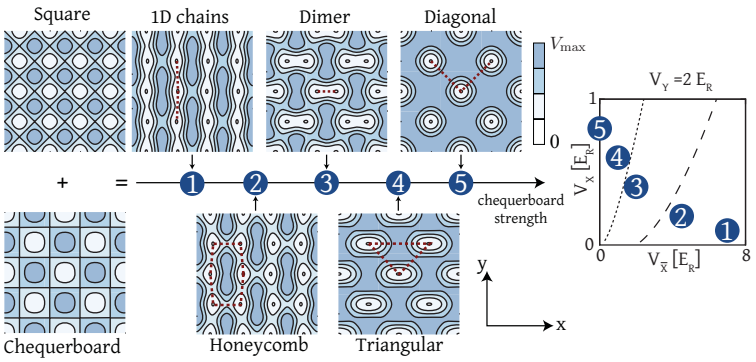

FIGURE 2.3.: **Lattice topologies.** Overview of accessible lattice structures of the tunable-geometry optical lattice. The total lattice potential seen by the atoms is the sum of a square and chequerboard pattern, where their relative strengths can be tuned by changing the lattice depths. As the chequerboard strength is increased (larger V_X), the lattice continuously changes from asymmetrically coupled one-dimensional chains, to honeycomb and dimerized lattices and finally to triangular and diagonal structures. Tunnelling between neighbouring sites is indicated by dashed red lines.

V_X and V_Y. The relative positioning of the square and chequerboard lattice is given by the position phase β, which is essentially determined by the symmetry phase θ. As can be seen in Fig. 2.2, continuous tuning of θ allows to smoothly vary the horizontal relative position along the x-axis of the two lattice potentials. The vertical position however cannot be changed in the current setup and is fixed, such that the sites of the two structures are aligned with respect to each other along the y direction. For $\theta = 0 + n\pi, n \in \mathbb{Z}$ the positioning is independent of the lattice depths $V_{\bar{X}}$ and V_X and the chequerboard sites are located precisely in between neighbouring sites of the square lattice.

A simple picture for the accessible two-dimensional topologies with this setup is given in Fig. 2.3. Starting from a square lattice and a small chequerboard strength (small V_X) at $\phi = 0$ and $\theta = \pi$ essentially changes the tunnelling links along the x-direction on a chequerboard pattern by reducing the corresponding potential barriers for the atoms. This allows the realization of asymmetrically coupled one-dimensional chains. Further increase of the chequerboard strength (i.e. larger V_X) leads to a honeycomb lattice with comparable tunnelling strengths along the honeycomb bonds, and finally to a dimerized cubic lattice, where no Dirac points are present in the band structure. The transition line between the honeycomb and dimerized lattice can be found by calculating the entire two-dimensional band structure and checking for the presence of Dirac points, see section 2.3. In this way the dashed transition line in Fig. 2.3 is numerically calculated. For a very large chequerboard strength the chequerboard pattern becomes dominant and two neighbouring sites of the square lattice merge to a single site. The corresponding transition line is located at

$$V_X = V_{\bar{X}} + \frac{V_Y}{2} - \sqrt{V_Y \left(V_{\bar{X}} + \frac{V_Y}{4} \right)}. \tag{2.8}$$

Due to the presence of the residual small square lattice in this regime, the sites have an anisotropic shape, which leads to a significant next-nearest neighbour coupling along the x-direction as compared to the y-direction. This gives rise to a triangular lattice with tunable

tunnelling strengths. For a vanishing lattice depth $V_{\bar{X}}$ a diagonal pattern remains.

2.2. Experimental implementation

2.2.1. Optical setup

The following section is devoted to the beam setup of the tunable-geometry optical lattice. The setup is summarized in Fig. 2.4 and consists of two main parts, the beam preparation section and the experiment section for the x-y plane and the z axis. The laser light is derived from a high-power 1064 nm Nd:YAG laser (Innolight Mephisto MOPA 36W NE) with a maximum output power of 40W and a specified linewidth of 1 kHz at 100 ms integration time. The laser contains an Innolight Mephisto master laser with about 2W of output power, followed by three MOPA amplification stages, which are each optically pumped with about 45W laser light generated by diode lasers. Due to thermal lensing in the MOPA stages the beam diameter reduces by more than a factor of three when increasing the output power and reaches a $1/e^2$ radius of about 600 μm at full output[2]. The wavelength is red-detuned with respect to the atomic D-1 and D-2 transition lines of the two alkaline species ^{87}Rb and ^{40}K used in the experiments. The specified relative intensity noise in free running mode is below -130 dB/Hz at frequencies above 10 kHz. For more details concerning the intensity noise and stabilization see section 2.2.5. The cooling of the amplification crystals in the MOPA stages is provided by a 700W water-air chiller (Termotek P307-16707-AW-S).

After passing through a high-power optical isolator (QiOptiq) and Brewster plate for cleaning the polarization (Precision Photonics) the laser power is divided into the different lattice beam arms using thin-film polarizing beam splitters and polarization plates. On each arm an acousto-optical modulator (IntraAction ATM2001A2 and ATM1351A2 with TeO_2 crystal) is used to control the intensity of the laser beams and shift their frequency. The beams are then directed into 11 m long optical fibers (Schäfter-Kirchhoff 6.4 μm MFD with about 75% coupling efficiency) and guided to the experiment table. The $\bar{X}$ and X beams are recombined on the laser table using a 50/50 plate and guided into the same optical fiber with matched linear polarizations of both beams. An additional reference arm is included with an acousto-optical modulator in double-pass configuration. As explained later in section 2.2.2, an additional photodiode is used for the detection and stabilization of the interference phase.

The optical setup on the experiment side is also shown in Fig. 2.4. On each axis a fiber coupler (Schäfter-Kirchhoff, 60SMS-1-4-A8-07 or 60SMS-1-4-A11-02) collimates the laser beam exiting the optical fiber. Polarization optics are then used to clean and control the polarization, which is chosen to be linear on all axes (for the beams in the x-y plane the polarization is along the z axis, whereas for the beam from the z direction the polarization is along y). To monitor and actively feedback the beam intensities, approximately 1% of the total power is split off and directed onto photodiodes (bandwidth DC $-$ 10 MHz), either using an anti-reflection coated plate or the transmission of a highly-reflective mirror. On all axes the lattice beams are focussed down to $1/e^2$ radii of about 170 μm using f = 400 mm achromats (Melles-Griot), are then mixed with several other beams via bichromatic mirrors (not shown

[2] When imaging the output beam in the focus of a lense, a donut profile was observed, whereas the collimated beam profile shows a clear Gaussian TEM-00 mode. Nevertheless, a fiber coupling efficiency of above 70% could be achieved when operating the laser at full power and reducing the fiber input intensity by a Brewster plate

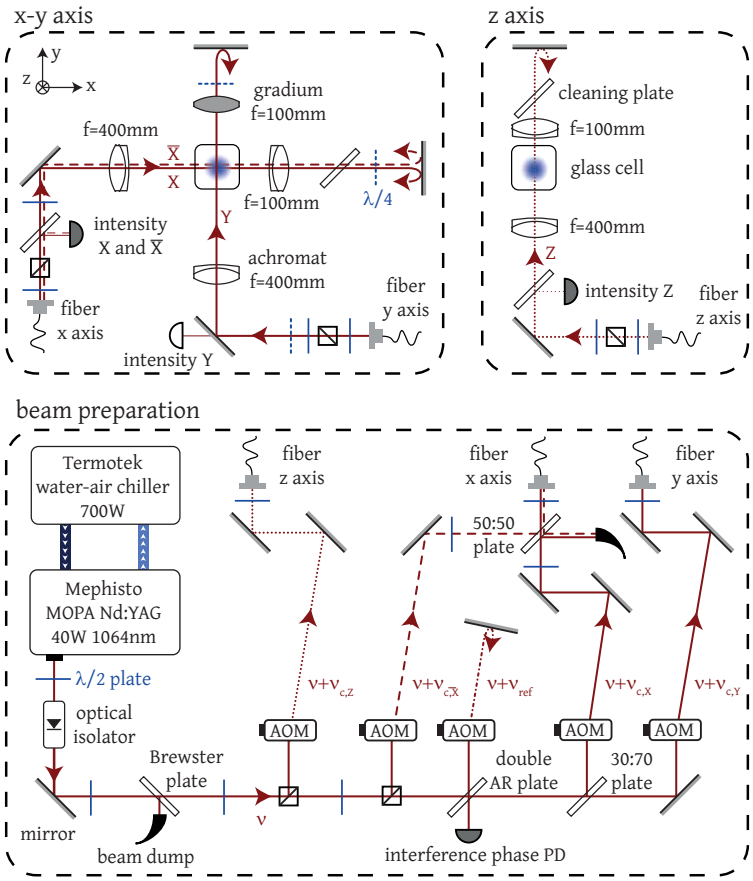

FIGURE 2.4.: **Beam setup of the tunable-geometry optical lattice.** The beam preparation on the laser table (bottom) and the setup on the experiment table for the different axes (top) is shown. The laser beam is marked as a red line, where frequency shifts are indicated by dashed, dotted and dashed-dotted lines. For simplicity the paths of the retro-reflected beams are not shown. Essentially all beams are directed back through the fibers and the AOMs and are finally dumped at the optical isolator on the laser table. On the x-axis of the experiment table the $\bar{X}$ and X beams are exactly overlapped and have the same polarization (solid and dashed line), as they are directed into the same optical fiber on the laser table. For the chosen values of the AOM frequencies see Tab. 2.1.

in Fig. 2.4) and finally directed towards the atoms in the glass cell. After the cell the beams are recollimated by a f = 100 mm achromat or gradium lens depending on the axis and retro-reflected by a 0° mirror. For the x and z axes, where multiple trapping/anti-trapping beams are present, a specially coated plate (LaserOptik Garbsen) is inserted after the second lens, which reflects off the trapping and transmits the lattice beams. An additional $\lambda/4$ wave plate in front of the retro-reflecting mirrors gives access to the linear polarization axis of the retro-reflected beams, which is important for the interfering beams on the x- and y-axes of the setup.

The typical maximum beam power per axis is 2 W, corresponding to roughly $40\,E_R$ depending on the exact beam waists. Care has to be taken for larger intensities, as the entire beam power is retro-reflected back into the optical fibers, which is necessary for the interference phase stabilization (as discussed in the following section)[3]. At too high powers this can lead to significant intensity noise, probably caused by Brillouin backscattering of the retro-reflected beam in the optical fiber, which is then redirected to the photodiode and the atoms. This limits the maximum laser powers on all axes in the experiment.

2.2.2. Interference phase stabilization

As evident from the expression for the atomic lattice potential in Eq. 2.3, there are two phases influencing the lattice structure. In this section the stabilization of the interference phase ϕ is discussed. The phase ϕ is the light phase difference picked up between the splitting point of the X and Y beams and the respective retro-reflecting mirror on the experiment table, see Fig. 2.4. This phase fluctuates in time due to several reasons:

- Both beams traverse through separate fibers, each of which creates independent phase noise. This is mainly caused by vibrational coupling to cooling fans of the electronic equipment.
- Separate optical paths for both beams. Fluctuations in the air pressure, room temperature and humidity lead to a change of the refractive index of air and thus a difference in phase [112, 113, 114].
- Vibration of optical components (e.g. mirrors, plates)

All these effects cause a phase change of 2π on a timescale of a 10 kHz or slower. By guiding the optical fibers through separate tubes, which are mechanically decoupled from the electronic equipment in the lab, this timescale could be reduced to about 1 kHz. The remaining phase fluctuations are actively stabilized. Note that to attribute a sensible phase difference between the two beams, both need to be derived from the same laser and the coherence length ($\gg 1$ km) has to be much larger than the length of the beam path[4]

Basic principle

The interference phase ϕ is actively stabilized in the experiment using a heterodyne interferometer and a phase-locked loop. The technique is related to the standard phase stabilization

[3] Eventually the power is reflected back to the optical isolator in front of the laser, where it is then finally dumped.

[4] While this is the case here, this poses a significant challenge in the synchronization of distant clocks[72].

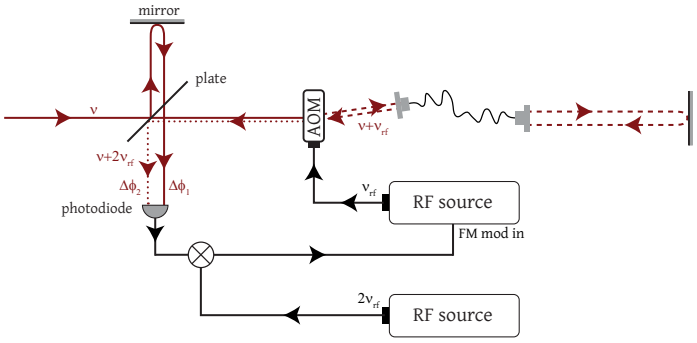

FIGURE 2.5.: **Basic phase stabilization scheme.** A Michelson-type of interferometer is shown, where the beams from the two arms are directed to a common photodiode. A heterodyne phase-detection is employed with a beat signal operating at twice the RF frequency ν_{rf}. After mixing with a reference oscillator operating at the same frequency, the DC feedback signal is sent to the frequency modulation (FM) input of the RF source, which is then applied to the laser beam via the acousto-optical modulator (AOM). The technique is similar to a phase-locked loop (PLL) commonly used in electronic circuits.

of optical fibers used in atomic clock experiments and cold atoms laboratories [115]. The idea is to map the phase noise into an RF signal, compare this to a stable oscillator at the same frequency and feedback the error signal onto the laser beam using frequency modulation of an AOM. Before discussing the full setup, the basic principle is illustrated in a simplified scheme shown in Fig. 2.5: an incoming laser beam at frequency ν hits a two-arm Michelson-type interferometer with a 45° splitting plate. The first arm is directly retro-reflected and hits a photodiode with a total light-phase pickup of $\Delta\phi_1$. The second arm includes an AOM with a frequency shift of ν_{rf} generated by an RF source and an optical fiber. After being retro-reflected the beam passes back through the fiber, is diffracted again by the AOM and finally hits the photodiode with a total light phase pickup of $\Delta\phi_2$ and a frequency of $\nu + 2\nu_{\mathrm{rf}}$. The photodiode signal V_{PD} is proportional to the total beam intensity

$$\begin{aligned} V_{\mathrm{PD}} &\propto \left|\sqrt{I_1}\exp\left(i(-2\pi\nu t + \Delta\phi_1)\right) + \sqrt{I_2}\exp\left(i(-2\pi(\nu+\nu_{\mathrm{rf}})t + \Delta\phi_2)\right)\right|^2 \\ &\propto I_1 + I_2 + 2\sqrt{I_1 I_2}\cos\left(4\pi\nu_{\mathrm{rf}}t + \Delta\phi_1 - \Delta\phi_2\right). \end{aligned}$$

Here I_1 and I_2 denote the single beam intensities and we neglected the k and k' dependence of the plane wave. The photodiode signal is then mixed down with an oscillator operating at frequency $2\nu_{\mathrm{rf}}$ and amplitude A_{osc}, which after low-passing gives a phase-dependent DC signal V_{mix}

$$V_{\mathrm{mix}} \propto \sqrt{I_1 I_2} A_{\mathrm{osc}} \cos\left(\Delta\phi_1 - \Delta\phi_2 - \Delta\phi_{\mathrm{el}}\right).$$

The mixed signal hence has a sinusoidal dependence on the light phase difference, where all additional phase contributions due to the electronics and cable lengths are summarized by $\Delta\phi_{\mathrm{el}}$. These contributions are constant at typical RF operating frequencies of $1 - 100\,\mathrm{MHz}$.

The phase is locked to the zero-crossing of the DC signal. This point has the advantage of being insensitive to the laser intensities and electronic amplitudes and merely depends on the light phase difference $\Delta\phi_1 - \Delta\phi_2$. The regulation loop is closed by direct feedback of V_{mix} to the FM input of the RF source connected to the AOM, analogous to a phase-locked loop (PLL) [116]. The feedback only has an integral part and locks to a positive slope.

The bandwidth of this scheme is usually limited by the FM input of the RF source. Other limitations apply to setups with very long cable-lengths, which cause a delay in the electronic feedback response – another critical aspect for the synchronization of long-distance clocks [72].

Actual setup

The actual phase-lock setup in the experiment is more complicated due to several design constraints:

- large signal-to-noise ratio of error signal
- stable phase-lock with rms phase noise below 10° [117]
- phase-lock stabilization independent of lattice intensity
- computer control of interference phase ϕ
- intensity regulation of all beams
- independent intensity control of the overlapped beams X and $\bar{X}$ obtained from the same fiber on the experiment table

The stabilization consists of two phase-locked loops, each of which stabilizes the light phase difference between a reference beam and the X and Y beam path, respectively. As compared to direct stabilization between the two beams, this approach offers an improved signal-to-noise ratio, as the local oscillator (reference beam) can be made very strong in intensity without perturbation of the atoms in the glass cell. This leads to a large amplitude phase-signal after mixing, see Eq. 2.9. As in the simplified example discussed above, the retro-reflected light traversing back through the optical fiber and AOM on the X and Y beam paths is used to construct the heterodyne interferometer, see Fig. 2.4. The three beams with frequencies ν_{X}, ν_{Y} and ν_{ref} are then directed to the phase-detection photodiode, which gives rise to three different beat frequencies $\nu_{\mathrm{X}} - \nu_{\mathrm{ref}}$, $\nu_{\mathrm{Y}} - \nu_{\mathrm{ref}}$ and $\nu_{\mathrm{X}} - \nu_{\mathrm{Y}}$. Proper filtering and mixing then allows to separate the beats with the reference beam for separate stabilization of the X and Y beam. As shown in Fig. 2.6, the error signal is then sent to the FM input of the corresponding RF sources. As both beams are stabilized to the same reference, this also stabilizes the light phase difference between the X and Y beam from the splitting point to the retro-mirrors and back, i.e. (twice) the interference phase ϕ.

If the same beam that creates the optical lattice would be used for the phase-lock stabilization, the lock signal would scale with the employed lattice beam intensity in the experiment, which would lead to a disturbance of the lock quality. To avoid this, separate beams are used for the phase-lock, which are fixed in intensity and do not change with the actual lattice beam intensity. This is achieved by sending the appropriate frequencies to the AOM, see Fig. 2.6: the optical lattice is created by a carrier RF frequency ν_c, which is variable in power depending on the desired lattice depth. The phase stabilization beam is an additional independent lattice created by two RF frequencies $\nu_c \pm \nu_p$, which are both fixed in power and added to the carrier signal before being sent to the AOM. This decouples the phase-lock signal from the carrier lattice depth. As the lattice beams for each axis are created by a single-pass through the same AOM and – at the same time – need to be guided into the same

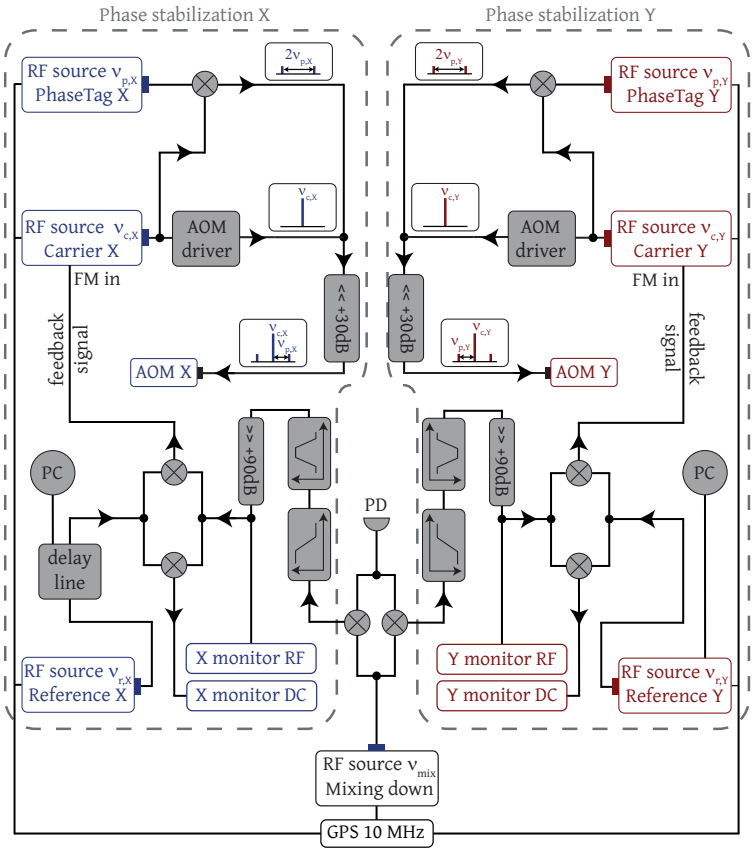

FIGURE 2.6.: **Electronic setup for intereference phase stabilization.** Two separate phase stabilizations are present in the experiment: the stabilization of the X and Y beam with respect to the common reference beam. After mixing, filtering and amplifying the beat signal detected by the photodiode (PD), the respective signals are mixed with a reference oscillator ν_r operating at the same frequency, and the resulting DC error signal is sent to the FM input of the RF source ν_c. To decouple the actual lattice depth seen by the atoms from the phase-lock signal, the phase-lock beat is created by an additional phase tag frequency ν_p.

optical fiber, the phase tag frequency ν_p is limited to a few MHz. The exact frequency and power settings for the RF sources are given in Tab. 2.1.

The decoupling technique leads to multiple frequencies seen by the interference phase photodiode: already the three different RF frequencies being sent to the AOM per axis, ν_c, $\nu_c - \nu_p$ and $\nu_c + \nu_p$, lead to five separate beams with different optical frequencies, as the laser beam passes the AOM twice before reaching the photodiode. This gives rise to numerous beat frequencies, as shown in the overview of laser frequencies and beats in Fig. 2.7, out of which only two are used for the stabilization of the X and Y beam[5]. The separation of the

[5] At full intensity of the X and Y lattice, the undesired beat signals can be up to 60 dB higher than the phase-lock beat. This leads to a non-linear response of the on-board amplifiers behind the photodiode, which results in a fluctuating small signal gain. This can be partially avoided by careful alignment/overlap of the reference beam with the retro-reflected X and Y beams.

RF source	label	frequency (MHz)	power (dBm)
Carrier X	$\nu_{\mathrm{c,X}}$	195.1	12.0
Carrier Y	$\nu_{\mathrm{c,c}}$	195.1	0.0
Carrier $\bar{X}$	$\nu_{\mathrm{c},\bar{\mathrm{X}}}$	−189.7	0.0
Carrier Z (int)	$\nu_{\mathrm{c,Z}}$	125.0	0.0
PhaseTag X	$\nu_{\mathrm{p,X}}$	0.875	−6.0
PhaseTag Y	$\nu_{\mathrm{p,Y}}$	1.35	−8.0
IntensityTag X	$\nu_{\mathrm{i,X}}$	2.27	25.0
IntensityTag $\bar{X}$	$\nu_{\mathrm{i},\bar{\mathrm{X}}}$	3.10	24.0
Reference X	$\nu_{\mathrm{r,X}}$	1.65	+9.0
Reference Y	$\nu_{\mathrm{r,Y}}$	0.7	+9.0
Reference beam	ν_{ref}	138.4	0.0
Mixing Down	ν_{mix}	110.0	+6.0

TABLE 2.1.: Frequencies and powers of the RF sources in the tunable-geometry optical lattice setup used for generating the beams and stabilizing the interference phase and lattice intensities, see Figs. 2.4 and 2.6. The sign of the frequency denotes the diffraction order of the AOM.

relevant beat for the phase-lock is done by down-conversion to the low MHz frequency range with a suitable mixing frequency ν_{mix}, which allows the use of custom-made band-passes, notch filters and low-passes.

The power of the phase tag beams is chosen to be about 5 mW on the experiment table, corresponding to roughly $0.1E_{\mathrm{R}}$, whereas the reference beam is approximately 20 times stronger. This leads to a phase beat signal strength of around $10-20$ dB above the noise floor of the detection photodiode. After frequency down-conversion, filtering and amplification, the signal is mixed with a reference oscillator operating at the same frequency, which results in a DC phase signal similar to that described in Eq. 2.9. This error signal is then sent to the FM input of the carrier frequency. At the same time the RF signal before mixing with the reference oscillator and the DC signal can be monitored – the typical scale for the DC signal amplitude is around $0.1-1$ V. Fig. 2.8 shows a comparison of the locked and unlocked RF beat signal. The residual rms phase noise when locked is below 3°.

For a stable interference phase ϕ all RF sources involved in the phase-lock chain have to be synchronized with each other. This is done by linking all synthesizers to a common 10 MHz clock signal, obtained from a GPS receiver. If all synthesizers are kept continuously on, the lock chain will stabilize to the same interference phase modulo 2π when activated. The phase can be changed by computer control of the output phase of one of the reference oscillators, which can be done once every experimental cycle. To additionally change the phase during one experimental cycle, a delay line setup is included at the output of a reference oscillator. This allows shifting the interference phase by either 0, $\pi/2$ or π, which can be exploited for example to load atoms into a dimerized lattice and detect spin correlations along the weak links, see chapter 7.

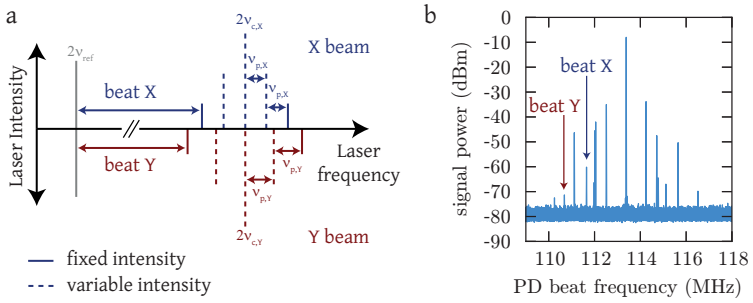

FIGURE 2.7.: **Beat frequencies of interference phase stabilization.** (a) Overview of the different laser beam frequencies seen by the interference phase detection photodiode. The frequencies originating from the intensity stabilization are not shown, see section 2.2.5. The large number of frequencies creates several different beat signals. (b) Frequency spectrum seen by the photodiode in the experiment. Only two of the numerous signals are used for the phase stabilization of the respective axes - all other disturbing signals, which can be up six orders of magnitude higher in power than the phase-lock signals, need to be filtered away.

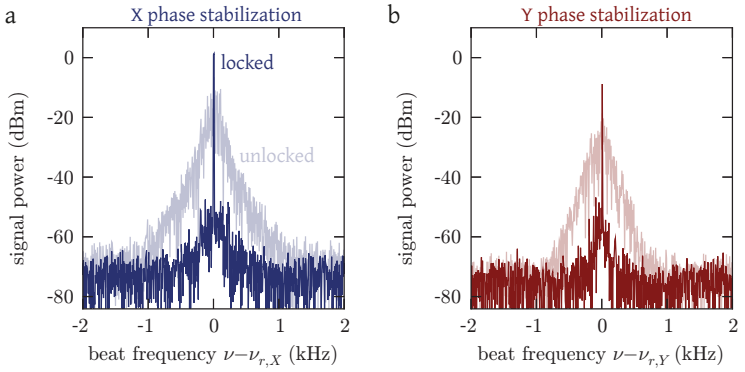

FIGURE 2.8.: **Interference phase stabilization.** Comparison of the frequency spectrum of the heterodyne beat signal seen by the interference phase detection photodiode in the locked and unlocked state for the X and Y beam.

2.2.3. Characterization of interference phase stability

The stability of the interference phase ϕ can be determined experimentally by subjecting a Bose-Einstein condensate abruptly and for a very brief time to the optical lattice potential created by $V_{\overline{X}}$, V_X and V_Y (Raman-Nath diffraction). After free expansion this results in a two-dimensional diffraction pattern, where the atomic momentum peaks are located at momenta corresponding to reciprocal lattice vectors. Fig. 2.9 shows two exemplary cases after pulsing a lattice with different interference phases ϕ. For $\phi = \pi/2$ the lattice potential corresponds to a square lattice, as the interference cancels with $\cos(\phi) = 0$. The diffraction pattern then only contains momenta corresponding to multiples of $2\hbar k$, where $k = 2\pi/\lambda$ is the lattice wave vector. If $\phi \neq \pi/2$ modulo π, additional peaks appear at $(\pm\hbar k, \pm\hbar k)$ and higher multiples, which originate from the interference term $\cos(kx)\cos(ky)$ in the lattice potential, see Eq. 2.3.

The diffraction pattern can be theoretically modelled by performing a time-evolution of

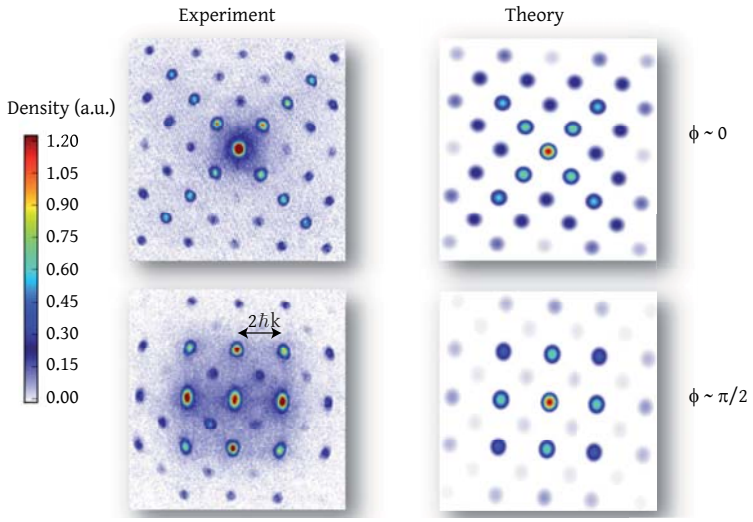

FIGURE 2.9.: **Raman-Nath diffraction.** Two exemplary diffraction patterns are shown after abruptly exposing a Bose-Einstein condensate for a few μs to the optical lattice potential. The pattern depends on the interference phase ϕ. Using an exact time-evolution of the lattice Hamiltonian, see Eq. 2.9, the pattern can be calculated, which is to fit the phase ϕ. On the right panel the corresponding fit functions are shown. The slight tilt originates from the fact that the camera CCD chip is not perfectly aligned with lattice axis.

the two-dimensional lattice Hamiltonian

$$\hat{H}_{\mathrm{lat}} = -\frac{\hbar^2}{2m}\nabla^2 + V_{at}(x,y), \tag{2.9}$$

where $V_{at}(x,y)$ is the two-dimensional lattice potential created by the tunable-geometry optical lattice, see Eq. 2.3. With the initial condition that all atoms are in the $k = 0$ momentum mode, the time evolution leads to a population of higher momentum modes $(i2\hbar k, j2\hbar k)$ and $(\hbar k + i2\hbar k, \hbar k + j2\hbar k)$, where $i, j \in \mathbb{Z}$. The population distribution depends on the lattice depths, the lattice pulse-time and the interference phase ϕ. Using the calculated time-evolution and leaving these parameters free then allows fitting the measured atomic peak distribution to extract ϕ. From this the rms noise of the interference phase stabilization is found to be around 5°. Exemplary fitted momentum distributions are shown in Fig. 2.9.

Owing to an imperfect overlap between all intersecting lattice beams forming the lattice potential, a finite visibility α of the interference term in the lattice potential needs to be taken into account. The entire potential then reads

$$\begin{aligned} V_{at}(x,y,z) = \; & - \; V_{\bar{X}}\cos^2(kx + \theta/2) - V_X\cos^2(kx) - V_Y\cos^2(ky) \\ & - \; 2\alpha\sqrt{V_X V_Y}\cos(kx)\cos(ky)\cos(\phi). \end{aligned} \tag{2.10}$$

The visibility can be measured by varying the set interference phase ϕ_{set} close to $\pi/2$ and extracting the fitted interference phase ϕ_{fit}. The slope of $\cos(\phi_{\mathrm{fit}})$ versus ϕ_{set} then gives the visibility, which is found to be $\alpha = 0.90(5)$, see Fig. 2.10.

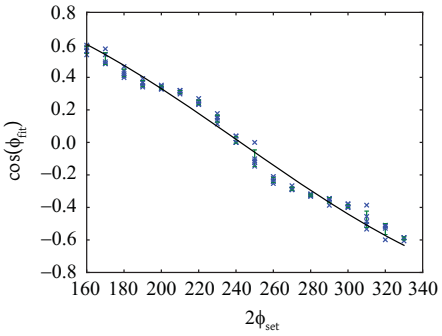

FIGURE 2.10.: **Visibility calibration.** The fitted interference phase ϕ_{fit} using fits similar to those shown in Fig. 2.9 is shown for various different interference phases set by the computer ϕ_{set}. The solid line is a linear fit, which yields a slope of 0.9 corresponding to the value for the visibility α.

2.2.4. Symmetry phase

The symmetry phase θ denotes the light-phase difference between the X and $\bar{X}$ beam starting from the atoms' position to the retro-reflecting mirror and back. The phase pickup between the two beams is different, as both are detuned with respect to each other by $\Delta\nu = \nu_{\mathrm{c,\bar{X}}} - \nu_{\mathrm{c,X}} = 384.8\,\mathrm{MHz}$. The detuning is chosen such that the symmetry phase is close to π for a distance between atoms and mirror of about $\mathrm{L} = 20\,\mathrm{cm}$ in the experiment

$$\theta = \frac{4\pi L}{c}\Delta\nu \tag{2.11}$$

Unlike the interference phase, the symmetry phase does not require active stabilization and is already passively stable. Possible changes and drifts arise from mirror fluctuations, which are expected to lead to a relative phase change of below 10^{-4}. Although differences in room temperature and air pressure alter the refractive index of air, only a dispersive shift can change the difference between the two phases. As the beams are very close in optical frequency, this effect is negligible [114, 113]. A change in temperature can, nevertheless, alter the exact mirror position by thermal expansion, which is estimated to be below a factor of 10^{-4} for a temperature change of 1°C. The finite extent of the atomic cloud along the x axis leads to a spatially varying symmetry phase over the cloud size of approximately a factor of 10^{-4}. The difference in wave vectors of the X and $\bar{X}$ beams leads to a symmetry phase change on a similar level, see Eq. 2.1. The symmetry phase θ can be changed by adjusting the carrier frequency $\nu_{\mathrm{c,\bar{X}}}$ of the $\bar{X}$ beam, which is derived from a computer controllable direct digital synthesizer (DDS) [118]. As the AOM is traversed in a single-pass configuration, changing the frequency requires realignment into the optical fiber.

Calibration of the symmetry phase can be done by Raman-Nath diffraction [119, 120, 121, 122] of a BEC from a one-dimensional lattice created by the X and $\bar{X}$ beams. Both beams are briefly pulsed for $\Delta t_{\mathrm{pulse}} = 20\,\mu\mathrm{s}$, which leads to a population of the higher momentum modes $\pm 2\hbar k$. For $\theta = \pi$ and matched intensities $V_X = V_{\bar{X}}$ the total potential sums to a constant value and no atoms are transferred to higher momenta. A mismatch in symmetry phase $\theta = \pi + \Delta_\theta$ or intensity $\gamma = (V_X - V_{\bar{X}})/V_X$ leads to an approximate weak lattice depth of $\widetilde{V_X} = V_X\sqrt{\gamma^2 + \Delta_\theta^2}$, see Eq. 2.6. The fraction of atoms in higher momentum modes η_{p} is

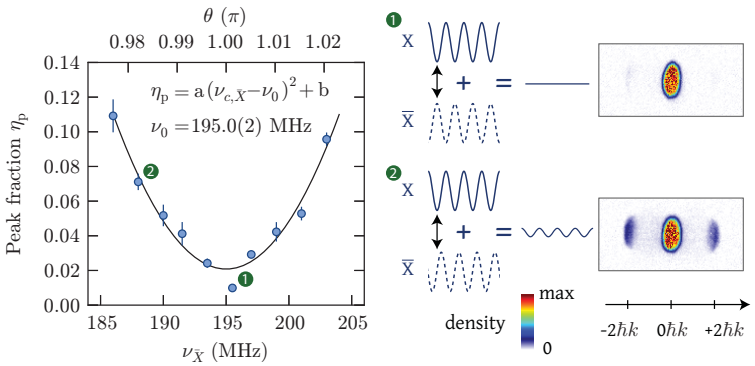

FIGURE 2.11.: **Calibration of symmetry phase θ.** The higher-momentum fraction η_p after Raman-Nath diffraction of a BEC on a one-dimensional lattice created by the $\overline{X}$ and X beam is shown as a function of laser frequency shift $\nu_{\overline{X}}$. If the $\overline{X}$ and X lattice are shifted by exactly half a lattice site and at the same depth, no net lattice remains, whereas a small residual lattice remains otherwise. Two exemplary absorption images obtained after Raman-Nath diffraction and time-of-flight are shown on the right. The peak fraction η_p is obtained by Gaussian fits to the three density profiles.

then given by [121].

$$\eta_{\mathrm{p}} = V_X^2 \left(\frac{\Delta t_{\mathrm{pulse}}}{8\hbar} \right)^2 \left(\gamma^2 + \Delta_\theta^2 \right). \tag{2.12}$$

For fixed pulse times and lattice depths but variable frequency $\nu_{\mathrm{c,\bar{X}}}$ a parabolic dependence of the higher momentum fraction on $\nu_{\mathrm{c,\bar{X}}} - \nu_0$ is expected, where ν_0 denotes the carrier frequency for which $\theta = \pi$. Fig. 2.11 shows the results of such a measurement[6]. From a parabolic fit with three free fit parameters (including an offset) we obtain a central frequency of $\nu_0 = 195.0(2)\,\mathrm{MHz}$.

2.2.5. Intensity tagging and stabilization

The lattice intensities on the y and z axis are stabilized with a standard technique [103, 104]: the beam power is monitored by a photodiode, which is then sent to a PID controller and compared to a computer controllable setpoint. The error signal is then fed back to the amplitude modulation (AM) input of an AOM controller, which changes the RF level sent to the AOM and hence the power in the laser beam. For the x axis the situation is more complicated, as the two beams X and $\bar{X}$ are exactly overlapped, have the same polarization and only differ in frequency by 384.8 MHz. For an independent intensity stabilization a new intensity tagging technique was developed, which essentially encodes each beam power into a specific beat frequency. Filters and band-passes are then used to separate these frequencies for independent stabilization of X and $\bar{X}$.

A schematic overview of the intensity tagging and stabilization for the X beam is shown in Fig. 2.12 (the setup for $\bar{X}$ is analogous). The variable amplitude RF signal $\nu_{\mathrm{c,X}}$ from the AOM driver is mixed with both a constant DC and intensity tag signal $\nu_{\mathrm{i,X}}$ using a

[6] When taking the data an oscillation of the higher momentum fraction η_{p} was observed on a timescale of about 20 min. This may be correlated to the climate control system, which showed a temperature oscillation with a similar period, thus leading to a small oscillation in the symmetry phase θ.

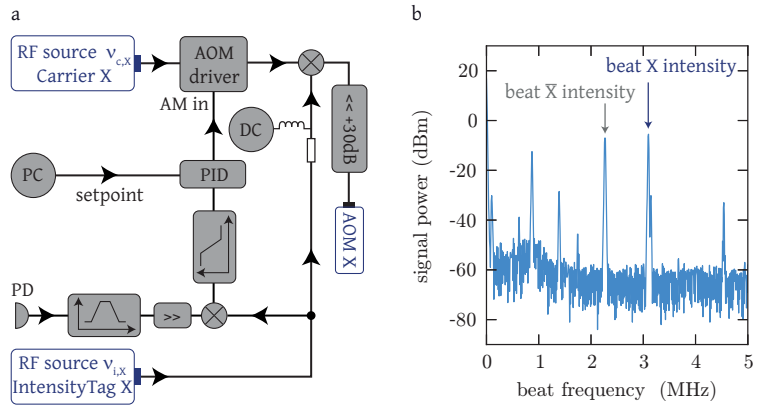

FIGURE 2.12.: **Intensity tagging and stabilization.** (a) The intensity of the X and $\overline{X}$ beams are stabilized using a frequency tagging technique. A tag frequency ν_i is mixed to the main signal ν_c creating the lattice. The intensity regulation photodiode on the experiment table then detects beats, where the relevant intensity beat is obtained after filtering and amplification. This signal is then mixed again with the intensity tag frequency ν_i, which gives a DC signal that is proportional to the lattice beam intensity. This signal is then used in a PID loop to regulate the intensity via amplitude modulation (AM) of the main signal ν_c.

bias-tee. This adds a small amplitude modulation to the main signal, which corresponds to two additional side-peaks to the carrier with a suppression of about 30 dB. The intensity tag frequency is in the low MHz range, such that all laser beams that are diffracted by the AOM can be guided into the optical fiber. The intensity photodiode on the experiment table, see Fig. 2.4, then detects a beat signal at $\nu_{\mathrm{i,X}}$. As the laser power of the carrier beam and the intensity tag beam are proportional to the lattice depth V_X, we find for the photo diode signal V_{PD}

$$V_{\mathrm{PD}} \propto V_X \cos(2\pi\nu_{\mathrm{i,X}} t). \tag{2.13}$$

In principle the amplitude also depends on the light phase difference picked up between the carrier and intensity tag beam. This can be safely considered as constant, as a path length change of about 20 m would be necessary for a phase change of π. As the photodiode observes multiple beat signals originating from the $\bar{X}$ intensity tagging and the interference phase stabilization signals, the relevant beat frequency first needs to be filtered. After amplification this signal is mixed again with the intensity tag. The resulting DC signal V_{mix} is proportional to the lattice depth V_X

$$V_{\mathrm{mix}} \propto V_X \cos(\Delta\phi_{\mathrm{el}}). \tag{2.14}$$

Here all phase shifts (cable lengths, electronic components etc.) are included into $\Delta\phi_{\mathrm{el}}$. The tag frequencies of both beams X and $\bar{X}$ are optimized for a phase factor $\cos(\Delta\phi_{\mathrm{el}})$ close to 1, see Tab. 2.1. The remaining part of the lock chain (PID and feedback to AOM driver) is then analogous to the setup for the y and z axis.

A measurement of the relative intensity noise (RIN) spectrum of the intensity locked and free running X and Y lattice beam is shown in Fig. 2.13a. The bandwidth of the PID loop is around a few kHz, which is probably limited by the PID controller. While the regulation adds noise at higher frequencies, the integrated relative intensity noise remains below 10^{-2}.

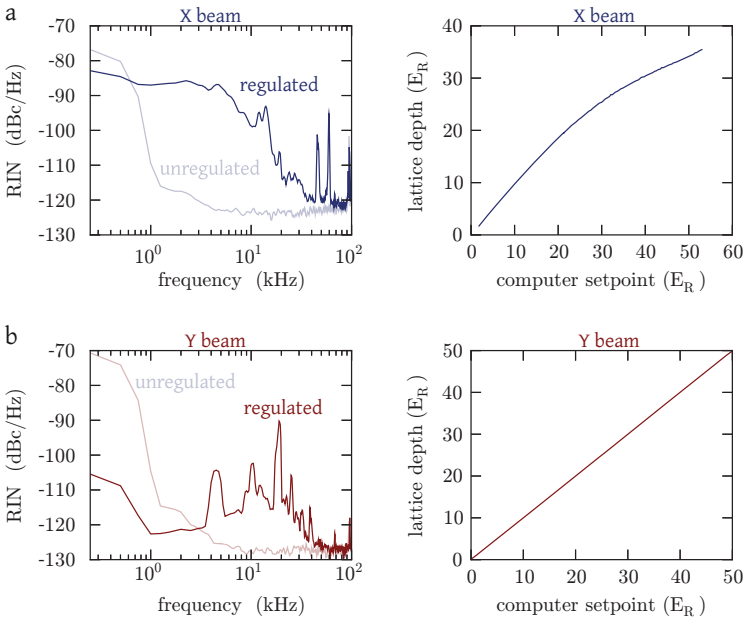

FIGURE 2.13.: **Performance of the intensity stabilization.** The relative intensity noise (RIN) is shown for the regulated and unregulated case of the X and Y beam intensity (a+b). While the performance of the intensity tagging technique of the X and $\overline{X}$ beams is worse than the standard method used for Y, the relative integrated frequency noise up to 100 kHz still remains below 10^{-2} in the regulated state. On the right the calibration of the lattice depth versus the electronic computer setpoint is shown. The intensity tagging leads to a bending-off at high powers due to the reduced diffraction efficiency of the acousto-optical modulator.

For the other lattice beams similar noise behaviour is observed.

So far an AOM diffraction efficiency proportional to the RF power sent to the AOM was assumed in Eq. 2.14. For large RF powers corrections start to play a role, which lead to a non-linear relation of the actual lattice depth and the computer setpoint, see Fig. 2.13b. This effect is taken into account in the experiment by including a non-linear calibration into the computer setpoint. This is only necessary for the lattice beams X and $\bar{X}$, which are stabilized by the intensity tagging technique. The conversion from photodiode voltage to lattice depth in units of E_R is done for all beams by Raman-Nath diffraction of a BEC from a one-dimensional lattice, as explained in [102].

2.3. Band structure and tight-binding model

In this section the band structure for non-interacting particles in the tunable-geometry optical lattice is calculated. As the x-y and z direction decouple, we will restrict the analysis to the x-y plane, where the potential for the atoms reads (see Eq. 2.3)

$$\begin{aligned} V(x,y) = & - V_{\bar{X}}\cos^2(kx+\theta/2) - V_X\cos^2(kx) - V_Y\cos^2(ky) \\ & - 2\sqrt{V_X V_Y}\cos(kx)\cos(ky)\cos(\phi). \end{aligned} \tag{2.15}$$

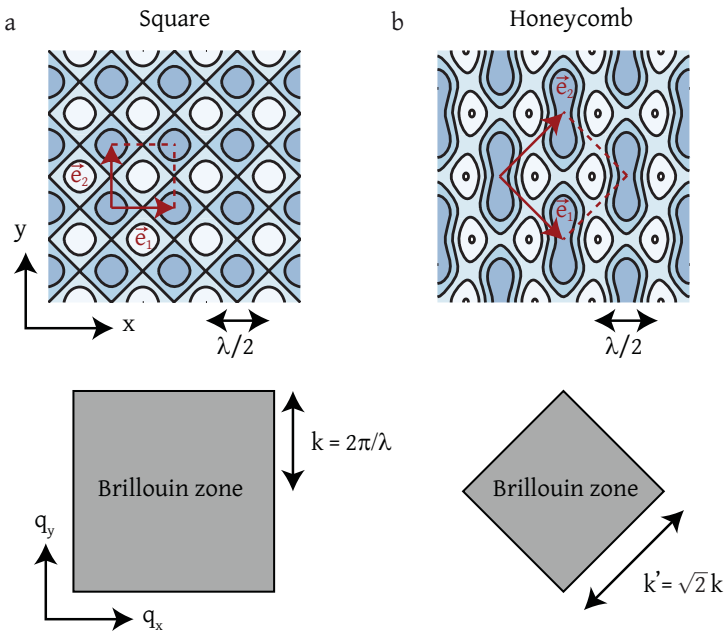

FIGURE 2.14.: **Real and reciprocal space.** (a) The real space potential for a square lattice ($V_X = 0$) is shown with the primitive unit cell vectors $\mathbf{e}_1$ and $\mathbf{e}_2$, which span the unit cell marked in red. Below the Brillouin zone in reciprocal space is shown, which is a square of length $2k$, where $k = 2\pi/\lambda$. (b) The lattice potential for a finite value of $V_X = 0.1E_\mathrm{R}$ ($V_{\overline{X},Y} = [7, 2]E_\mathrm{R}$) in the honeycomb lattice. The real space unit cell is now an enlarged square rotated by 45°, where the length of the primitive vectors is increased by $\sqrt{2}$. The Brillouin zone is correspondingly smaller and also a square rotated by 45°, where the sidelength is reduced by $1/\sqrt{2}$.

Here we denoted the lattice momentum with $k = 2\pi/\lambda$. For $V_X = 0$ the potential is a square lattice and the unit cell in real space contains one site and has a square shape of length $\lambda/2$, see Fig. 2.14a. The corresponding Brillouin zone in momentum space also has a square shape with a length of $2k$. The situation changes for any finite value of $V_X \neq 0$. Owing to the interference between perpendicular beams, the unit cell in real doubles in size and now contains two lattice sites, see Fig. 2.14b. The shape of the real space unit cell is a square rotated by 45° with a length of $\lambda/\sqrt{2}$. In momentum space the Brillouin zone is smaller by a factor of two and also has a square shape rotated by 45° with a length of $k' = \sqrt{2}k$. As will be seen in the following, the fact that already for vanishingly small values of V_X the unit cell contains two sites causes the appearance of two mini-bands in the band structure. These two bands are energetically very close and well separated from the higher bands. Additionally, when deriving a tight-binding model, the two lowest bands have to be taken into account in order to construct localized Wannier functions on every site in the lattice (see below).

Bloch's theorem

The starting point for the generic band structure calculation in two dimensions is the single-particle Hamiltonian

$$\hat{H} = -\frac{\hbar^2}{2m}\nabla^2 + V(x,y). \tag{2.16}$$

The goal is the calculation of the Bloch eigenstates $\Psi_{n,\mathbf{q}}(x,y)$ and energies $E_{n,\mathbf{q}}$ of the eigenvalue problem

$$\hat{H}\Psi_{n,\mathbf{q}}(x,y) = E_{n,\mathbf{q}}\Psi_{n,\mathbf{q}}(x,y), \tag{2.17}$$

where n denotes the band index and $\mathbf{q}$ any quasi-momentum within the Brillouin zone. Using Bloch's theorem the Bloch eigenstates can be written as a product of a plane wave state with any quasi-momentum $\mathbf{q}$ within the Brillouin zone and a function $u_{n,\mathbf{q}}(x,y)$, which has the same periodicity as the lattice potential

$$\Psi_{n,\mathbf{q}}(x,y) = e^{i\mathbf{q}\cdot\mathbf{r}}u_{n,\mathbf{q}}(x,y). \tag{2.18}$$

Here we abbreviated $\mathbf{r} = (x,y)$. The resulting Bloch equation then reads

$$\left(\frac{(\hat{\mathbf{p}} + \hbar\mathbf{q})^2}{2m} + V(x,y)\right) u_{n,\mathbf{q}}(x,y) = E_{n,\mathbf{q}}u_{n,\mathbf{q}}(x,y). \tag{2.19}$$

Since both the atomic potential $V(x,y)$ and $u_{n,\mathbf{q}}(x,y)$ are periodic functions in space, the Bloch equation is most easily solved in momentum space with the Fourier transforms

$$V(\mathbf{r}) = \sum_{\mathbf{G}} V_{\mathbf{G}}e^{i\mathbf{G}\cdot\mathbf{r}} \qquad \text{and} \qquad u_{n,\mathbf{q}}(\mathbf{r}) = \sum_{\mathbf{G}} c_{n,\mathbf{q},\mathbf{G}}e^{i\mathbf{G}\cdot\mathbf{r}}. \tag{2.20}$$

The sum in both expressions is taken over all reciprocal lattice vectors $\mathbf{G}$. The final equation for the plane wave coefficients $c_{n,\mathbf{q},\mathbf{G}}$ then reads

$$\left(\frac{\hbar^2}{2m}(\mathbf{G}+\mathbf{q})^2 - E_{n,\mathbf{q}}\right) c_{n,\mathbf{q},\mathbf{G}} + \sum_{\mathbf{G}'} V_{\mathbf{G}-\mathbf{G}'}c_{n,\mathbf{q},\mathbf{G}'} = 0. \tag{2.21}$$

The initial eigenvalue problem from Eq. 2.16 has thus simplified to an equation in momentum space, where only momenta $\mathbf{k}$ separated by reciprocal lattice vectors are coupled, i.e. $\mathbf{k} = \mathbf{q} + \mathbf{G}$. The total Hamiltonian is therefore Block-diagonal, which simplifies the calculation considerably.

Calculation for tunable-geometry lattice

In the following we use the formalism developed in the previous section to calculate the band structure in the tunable-geometry lattice. The Fourier transform $V_{\mathbf{G}}$ of the lattice potential is most easily obtained by rotating the basis by 45° to the spatial coordinates x' and y' corresponding to the real space unit cell of the lattice potential, see Fig. 2.14b. The transformation is given by

$$x' = \frac{x+y}{\sqrt{2}} \qquad \text{and} \qquad y' = \frac{y-x}{\sqrt{2}}. \tag{2.22}$$

After rotation and omitting constant energy offsets, the lattice potential from Eq. 2.15 is ($k' = \sqrt{2}k$)

$$\begin{aligned} V(x,y) = & - \frac{V_{\bar{X}}}{2}\cos(k'x' - k'y' + \theta) \\ & - \frac{V_X}{2}\cos(k'x' - k'y') - \frac{V_Y}{2}\cos(k'x' + k'y') \\ & - \sqrt{V_X V_Y}\cos(\phi)\left(\cos(k'x') + \cos(k'y')\right). \end{aligned} \tag{2.23}$$

The basis rotation also leads to a rotation in momentum space, which allows a convenient representation of the reciprocal lattice vectors $\mathbf{G}$ and quasi-momenta $\mathbf{q}$

$$\mathbf{G} = k' \begin{pmatrix} m \\ n \end{pmatrix}, \qquad m, n \in \mathbb{Z} \tag{2.24}$$

$$\mathbf{q} = k' \begin{pmatrix} m_q \\ n_q \end{pmatrix}, \qquad m_q, n_q \in [-\frac{1}{2}, \frac{1}{2}]. \tag{2.25}$$

From Eq. 2.21 and setting all energies in units of the recoil energy $E_\mathrm{R} = \hbar^2 k^2/2m$, the final equation for the plane wave coefficients $c_{m,n}$ is immediately obtained (omitting for the moment the indices n and $\mathbf{q}$ for readability)

$$\begin{aligned} \left(\frac{E}{E_\mathrm{R}}\right) c_{m,n} = & \; c_{m,n}\left(2(m+m_q)^2 + 2(n+n_q)^2\right) + c_{m\pm1,n\pm1}\left(-\frac{V_Y}{4E_\mathrm{R}}\right) \\ & + \; c_{m\pm1,n\mp1}\left(-\frac{V_X}{4E_\mathrm{R}} - \frac{V_{\overline{X}}}{4E_\mathrm{R}}e^{\pm i\theta}\right) \\ & + \; (c_{m\pm1,n} + c_{m,n\pm1})\left(-\frac{\sqrt{V_X V_Y}}{2E_\mathrm{R}}\cos(\phi)\right) \end{aligned} \tag{2.26}$$

This tensor equation is solved numerically by limiting the number of higher momenta m, n to typically ± 16.

Figures 2.15 and 2.16 shows the two-dimensional band structure $E(\mathbf{q})$ for different lattice parameters and increasing values of V_X. For $V_X = 0$, two inter-penetrating mini-bands are clearly visible, which touch energetically on a one-dimensional line in $\mathbf{q}$-space. The appearance of the two mini-bands can in this case be reproduced by folding back the square lattice band structure defined on the large square-shaped Brillouin zone to the smaller rotated diamond-shaped Brillouin zone. For $V_{\overline{X}} > V_Y$ (Fig. 2.15) the two one-dimensional energy touching lines of the two mini-bands are located on the top and bottom of the diamond-shaped Brillouin zone with $|q_y| > k/2$, whereas for $V_{\overline{X}} < V_Y$ the lines are located on the left and right of the Brillouin zone with $|q_x| > k/2$ (Fig. 2.16). In the following we consider the case $V_{\overline{X}} > V_Y$. A finite value of V_X then leads to an energy splitting between the two mini-bands, apart from two opposite points located along the vertical line. Here, the two mini-bands still touch and have a linear dispersion relation in the vicinity. As these are non-symmetrical points in the Brillouin zone, these two points are Dirac points with an associated $\pm\pi$ Berry phase. Further increase of V_X shifts the two Dirac points to the outer corner of the Brillouin zone, while at the same time increasing the dispersion slope along the horizontal direction and decreasing the slope along the vertical direction. For a critical value

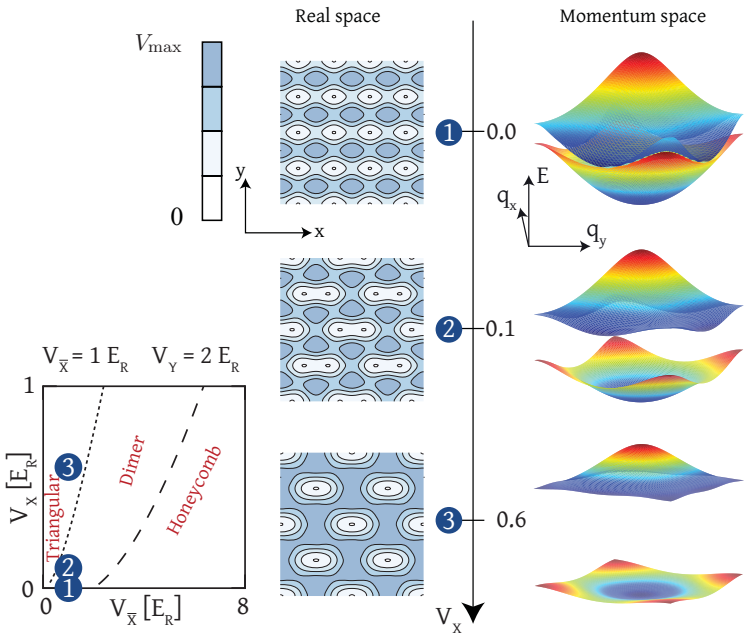

FIGURE 2.15.: **Lattice potential and band structure.** The band structure (right column) is shown along with the real space potential (left column) for different lattice depths V_X and fixed depths $V_{\overline{X},Y} = [1, 2]\ E_\mathrm{R}$. All band structure energies have been normalized to the respective bandwidth of the two lowest bands. For vanishing V_X the two lowest bands touch on two one-dimensional lines located at $|q_x| > k/2$ (see main text). On the bottom left the corresponding position in the topology diagram is shown for each lattice.

of V_X, the Dirac points are located precisely at the corner of the Brillouin zone. Since these are equivalent points in the band structure, the two Dirac points touch and annihilate each other here. Additionally, the dispersion relation along the vertical direction is quadratic, while still being linear along the horizontal direction. For even larger values of V_X a gap opens between the mini-bands at the corner of the Brillouin zone, marking the transition from a honeycomb lattice to a dimerized lattice. The transition line between the two lattice geometries marked in the lattice topology diagram of Figs. 2.15 and 2.16 (dashed line) is calculated by numerically solving for the critical lattice depth V_X where the band gap opens.

For the case $V_{\overline{X}} < V_Y$ a finite value of V_X does not lead to the formation of Dirac points and the lattice is directly in the regime of a dimerized lattice.

Wannier functions and tunnelling

An alternative representation of the lattice Hamiltonian can be obtained using a localized basis of real-valued Wannier functions. This is particularly useful for the regime of deep lattices, where the band structure becomes nearly flat (tight-binding regime). The Wannier functions are maximally localized on the unit cell located at $\mathbf{R_j}$ and are separately calculated in each band n via a basis rotation

$$w_{n,\mathbf{j}}(\mathbf{r}) = w_n(\mathbf{r} - \mathbf{R_j}) = \frac{1}{\sqrt{N}} \sum_{\mathbf{q}} \Psi_{n,\mathbf{q}}(\mathbf{r}) e^{i\mathbf{q}\cdot\mathbf{R_j}}. \tag{2.27}$$

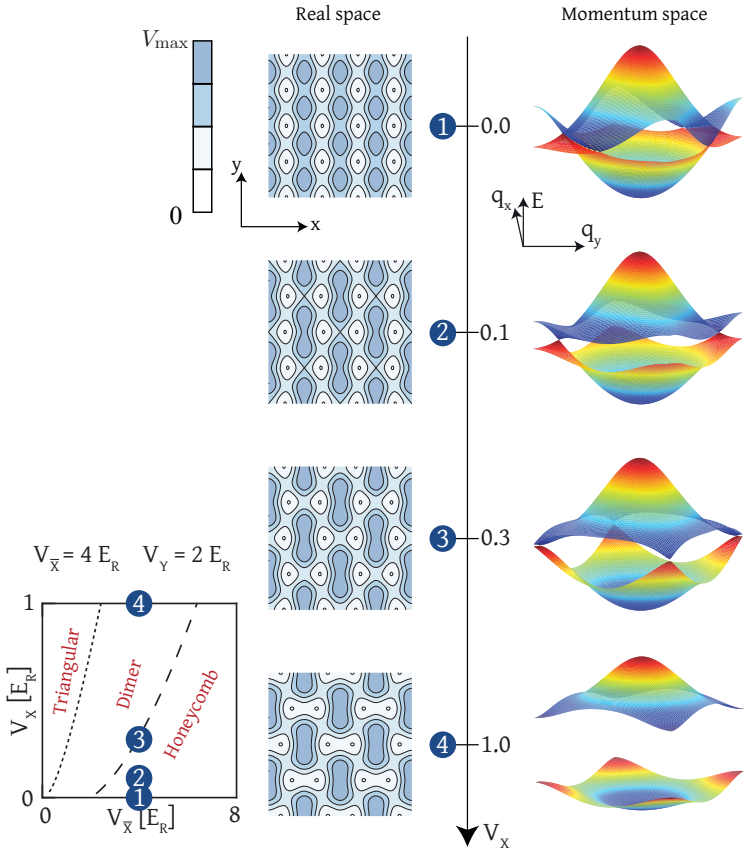

FIGURE 2.16.: **Lattice potential and band structure.** The band structure (right column) is shown along with the real space potential (left column) for different lattice depths V_X and fixed depths $V_{\overline{X},Y} = [4, 2]\ E_\mathrm{R}$. All band structure energies have been normalized to the respective bandwidth of the two lowest bands. For vanishing V_X the two lowest bands touch on two one-dimensional lines located at $|q_y| > k/2$ (see main text). On the bottom left the corresponding position in the topology diagram is shown for each lattice.

Here N is the total number of discrete quasimomentum states $\mathbf{q}$ in the Brillouin zone, corresponding to a real-space lattice with N unit cells. The Wannier functions form a complete orthonormal basis and decay exponentially for large distances to the center $\mathbf{R_j}$. Careful attention has to paid when calculating Wannier functions explicitly, as in the above definition the complex phase of the Bloch states is undefined.

In the dimerized and honeycomb lattice regime, each unit cell contains two sites. While the above defined Wannier functions $w_{n,\mathbf{j}}$ are localized on both sites of a unit-cell, it is also possible to define Wannier functions $w^l_{n,\mathbf{j}}$ and $w^r_{n,\mathbf{j}}$ that are localized on the left and right site respectively. Here l, r denote the left and right Wannier function on the unit cell located at $\mathbf{r} = \mathbf{R_j}$ and $n \in \mathbb{N}$. A correct evaluation of the Wannier functions with all necessary properties requires the adequate choice of these phases, which for the case of the two-dimensional tunable-geometry lattice is not obvious. This has been worked out by Ulf Bissbort and kindly provided to our group [123].

These Wannier functions can now be used to rewrite the many-body lattice Hamiltonian

from Eq. 2.16 in second quantized form and using the fermionic field operators $\hat{\Psi}(\mathbf{r})$

$$\hat{H} = \int \mathrm{d}\mathbf{r}\hat{\Psi}^{\dagger}(\mathbf{r}) \left(-\frac{\hbar^2}{2m}\nabla^2 + V(\mathbf{r}) \right) \hat{\Psi}(\mathbf{r}). \tag{2.28}$$

Here and in the following we omit the spin index $\sigma \in \{\uparrow, \downarrow\}$ for simplicity. With the above definition of the Wannier functions, the fermionic field operator can be rewritten in terms of the Wannier operators $\hat{c}_{l,n,\mathbf{j},\sigma}$ and $\hat{c}_{r,n,\mathbf{j},\sigma}$

$$\hat{\Psi}(\mathbf{r}) = \sum_{n,\mathbf{j}} w^{l}_{n,\mathbf{j}}(\mathbf{r})\hat{c}_{l,n,\mathbf{j}} + w^{r}_{n,\mathbf{j}}(\mathbf{r})\hat{c}_{r,n,\mathbf{j}}. \tag{2.29}$$

After inserting this expression into Eq. 2.28, the many-body Hamiltonian takes the form of a tunnelling Hamiltonian

$$\hat{H} = -\sum_{s,s'}\sum_{n}\sum_{\mathbf{i},\mathbf{j}} t^{s,s'}_{n,\mathbf{i},\mathbf{j}}\hat{c}^{\dagger}_{s,n,\mathbf{i}}\hat{c}_{s',n,\mathbf{j}}. \tag{2.30}$$

Here $t^{s,s'}_{m,n,\mathbf{i},\mathbf{i}}$ denotes the tunnelling matrix element from the $s = l(r)$ Wannier state at the unit cell located at $\mathbf{R_i}$ in band n to the $s' = l(r)$ Wannier state at the unit cell located at $\mathbf{R_j}$ in band n. The tunnelling matrix elements are evaluated according to

$$t^{s,s'}_{n,\mathbf{i},\mathbf{j}} = -\int w^{s}_{n,\mathbf{j}}(\mathbf{r})^* \left(-\frac{\hbar^2}{2m}\nabla^2 + V(\mathbf{r}) \right) w^{s'}_{n,\mathbf{i}}(\mathbf{r})\mathrm{d}\mathbf{r}. \tag{2.31}$$

Owing to the orthogonality of the Wannier functions in different bands, the tunnelling matrix elements between different bands are zero. An alternative way of obtaining the tunnelling matrix elements is from the Fourier transform of the band structure $E_n(\mathbf{q})$, which can be seen by inserting the definition of the Wannier functions in Eq. 2.27 into the expression for the tunnelling matrix elements

$$t^{s,s'}_{n,\mathbf{i},\mathbf{j}} = -\frac{1}{N}\sum_{\mathbf{q}} \frac{E_{2n}(\mathbf{q}) \pm E_{2n+1}(\mathbf{q})}{2} e^{i\mathbf{q}(\mathbf{R_i}-\mathbf{R_j})}. \tag{2.32}$$

In this formula the plus (minus) sign has to be taken for $s = s'$ ($s \neq s'$).

Tight-binding Hamiltonian

If all relevant energies (chemical potential, interaction energy, temperature) are much smaller than the gap between the lowest and first exited band, it is sufficient to consider only the lowest band in the many-body Hamiltonian (that is the two lowest mini-bands). If in addition the lattice is very deep, the localized Wannier functions decay very rapidly with distance. In this situation only the tunnelling terms between neighbouring sites $\langle i, j\rangle$ have to be considered. Neglecting constant energy offsets, this results in the tight-binding Hamiltonian

$$\begin{aligned} \hat{H}_{\mathrm{t.-b.}} &= -t_{i,j}\sum_{\langle i,j\rangle}(\hat{c}^{\dagger}_i\hat{c}_j + \mathrm{h.c.}) \\ &= -t\sum_{\langle i,j\rangle_{\_\_}}(\hat{c}^{\dagger}_i\hat{c}_j + \mathrm{h.c.}) - t_d\sum_{\langle i,j\rangle_{\blacksquare}}(\hat{c}^{\dagger}_i\hat{c}_j + \mathrm{h.c.}) \\ &\quad -t_w\sum_{\langle i,j\rangle_{\cdots}}(\hat{c}^{\dagger}_i\hat{c}_j + \mathrm{h.c.}). \end{aligned} \tag{2.33}$$

Here the tunnelling matrix elements between nearest-neighbours are denoted with t, t_d and t_w with the convention $t_w < t_d$, see Fig. 2.17a. The band structure $E(\mathbf{q})$ of the tight-binding model can be calculated by introducing the Fourier transform of the lowest-band Wannier operators $\hat{c}_{l,\mathbf{j}}$ and $\hat{c}_{r,\mathbf{j}}$ on the left and right sites of the real space unit cell (sometimes also referred to as $\mathcal{A}$ and $\mathcal{B}$ sublattices)

$$\hat{c}_{l,\mathbf{j}} = \sum_{\mathbf{q}} \hat{c}_{l,\mathbf{q}} e^{i\mathbf{q}\mathbf{R}_\mathbf{j}} \qquad \hat{c}_{r,\mathbf{j}} = \sum_{\mathbf{q}} \hat{c}_{r,\mathbf{q}} e^{i\mathbf{q}\mathbf{R}_\mathbf{j}}. \tag{2.34}$$

This results in a matrix-equation for $\hat{c}_{l,\mathbf{q}}$ and $\hat{c}_{r,\mathbf{q}}$, which after diagonalization leads to new momentum modes $\hat{c}_{0,\mathbf{q}}$ and $\hat{c}_{1,\mathbf{q}}$, which are a superposition of the left and right momentum modes and describe the eigenstates at quasi-momentum $\mathbf{q} = (q_x, q_y)$ in the two lowest bands ($a = \lambda/2$)

$$\begin{aligned} \hat{H}_{\text{t.-b.}} &= \sum_{\mathbf{q}} E(\mathbf{q}) \hat{c}^\dagger_{0,\mathbf{q}} \hat{c}_{0,\mathbf{q}} - \sum_{\mathbf{q}} E(\mathbf{q}) \hat{c}^\dagger_{1,\mathbf{q}} \hat{c}_{1,\mathbf{q}} \\ E(\mathbf{q})^2 &= 4\left(t_d + t_w\right)\cos(aq_x)\cos(aq_y) + 4t\cos^2(aq_y) \\ &\quad + 4t_d t_w \cos^2(aq_x) + \left(t_w - t_d\right)^2. \end{aligned} \tag{2.35}$$

The dispersion relation along the central vertical line in the Brillouin zone ($q_x = 0$) is $\pm(2t\cos aq_y + t_d t + t_w t)$. This allows deriving a simple condition for the existence of Dirac points within the tight-binding model

$$\frac{t_w}{t} \leq 2 - \frac{t_d}{t}. \tag{2.36}$$

The two Dirac points are then located at quasi-momentum q_y along the central $q_x = 0$ line according to the condition

$$-2t\cos(aq_y) = t_d + t_w. \tag{2.37}$$

The linear dispersion relation slopes of the two Dirac points along the horizontal and vertical direction are given by

$$\frac{\partial E}{\partial q_x} = a\left(t_d - t_w\right) \qquad \text{and} \qquad \frac{\partial E}{\partial q_y} = a\sqrt{4t^2 - \left(t_d + t_w\right)^2} \tag{2.38}$$

Further properties of the band-structure, energy gaps and position of the Dirac points as a function of the tunnelling ratios t_d/t_y and t_w/t_y are summarized in Fig. 2.17.

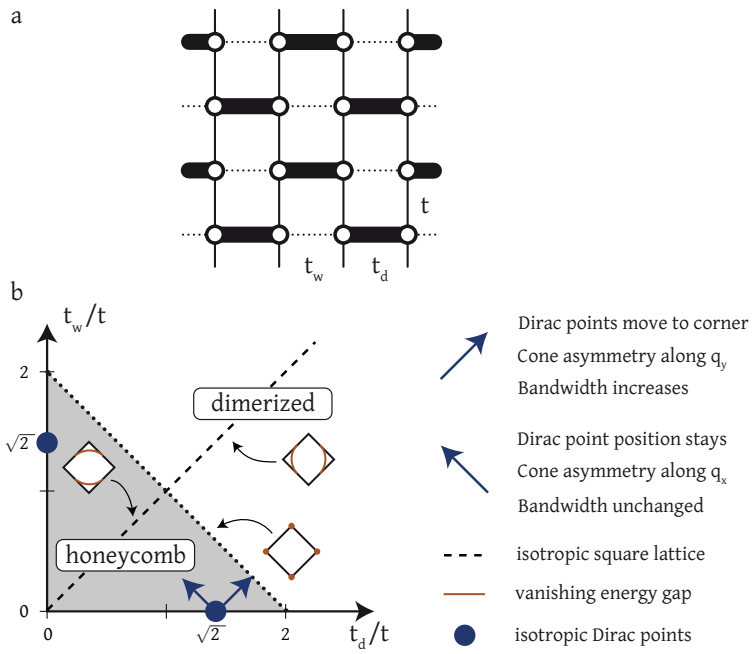

FIGURE 2.17.: **Tight binding model.** (a) Schematic view of the tight-binding model described in Eq. 2.33, which was derived using Wannier functions for the tunable-geometry optical lattice. (b) Summary of the qualitative behaviour of the bandstructure predicted by the tight-binding model. The gray shaded region corresponds to a honeycomb lattice, where two Dirac points are present at opposite points in the Brillouin zone and $q_x = 0$. The white region is the dimerized lattice regime and the dashed line the denotes the isotropic square lattice. The dependence of the dispersion relation at the Dirac points, their position and the total bandwidth of the two lowest bands is indicated in the legend on the right. The orange lines indicate the points where the two lowest bands touch in energy, i.e. a vanishing gap. At the ideal honeycomb point the Dirac points are isotropic and have the same dispersion relation slopes along all directions. Cone asymmetry along q_y means that the ratio of the dispersion relation slopes at the Dirac point along the q_y direction increases as compared to the q_x direction (analogous for the cone asymmetry along q_x).

3 The Fermi-Hubbard model

The first part of this chapter gives a brief overview over the two-particle scattering theory for dilute atomic gases at ultralow temperatures. This is then used to derive the Fermi-Hubbard model, which is a well suited Hamiltonian for describing interacting fermionic particles in an optical lattices. The second part is devoted to methods for evaluating the equation of state and several observables (on-site and nearest-neighbour correlators) within the Fermi-Hubbard model. In particular, a high-temperature series expansion up to second order is developed for bth isotropic and anisotropic simple cubic as well as dimerized lattices – both of which are configurations well accessible with the tunable-geometry optical lattice. The presented theoretical techniques form the basis for the comparison to theory of the measurements presented in the following chapters.

3.1. Interacting ultracold gases

Scattering theory

The scattering between two particles is a standard quantum mechanical textbook problem [124], which is outlined in the following. Denoting the two-particle interaction potential with $V(\mathbf{r})$ of range r_0, where $\mathbf{r}$ is the relative spatial coordinate between the two atoms, the stationary Schrödinger equation reads

$$\left(\frac{\hbar^2}{2m}\nabla^2 + E_{\mathbf{k}}\right)\Psi_{\mathbf{k}}(\mathbf{r}) = V(\mathbf{r})\Psi_{\mathbf{k}}(\mathbf{r}). \tag{3.1}$$

Here the wave-vector of the incoming wave is denoted by $\mathbf{k}$ with the energy $E_{\mathbf{k}}$. For large distances $|\mathbf{r}| \gg r_0$ the wavefunction can be written as a sum of an incoming plane wave and a scattered spherical wave

$$\Psi_{\mathbf{k}}(\mathbf{r}) = e^{i\mathbf{kr}} + \frac{e^{ikr}}{r} f(\mathbf{k}, \mathbf{k}'). \tag{3.2}$$

The wave-vector of the outgoing wave is given by $\mathbf{k}' = \mathbf{kr}/r$. For weak interaction potentials $V(\mathbf{r})$ the scattering amplitude $f(\mathbf{k}, \mathbf{k}')$ can be calculated in the Born-approximation, which gives

$$f(\mathbf{k}, \mathbf{k}') = -\frac{m}{2\pi\hbar^2}\widetilde{V}(\mathbf{k} - \mathbf{k}'), \tag{3.3}$$

where the Fourier transform of the interaction potential is denoted by $\widetilde{V}(\mathbf{k} - \mathbf{k}')$. In many cases the scattering cross section σ is of interest, which describes the effective atomic size seen by the scattered atom during the scattering process. This quantity is given by the integral over the scattering solid angle

$$\sigma = \int \mathrm{d}\Omega |f(\mathbf{k}, \mathbf{k}')|^2 \tag{3.4}$$

For the case of a spherically symmetric interaction potential $V(r)$, the two-body scattering wavefunction is written in spherical coordinates and can be expressed in partial waves using the Legendre polynomials $P_l \cos\theta$ of order $l \in \{0, 1, ...\}$ and the radial wavefunction $u_l(r)/r$. The corresponding radial Schrödinger equation for each l then reads

$$\frac{\hbar^2}{2m}\left(\partial_r^2 + k^2\right) u_l(r) = V_{\text{eff}}(r) u_l(r), \tag{3.5}$$

$$V_{\text{eff}}(r) = V(r) + \frac{\hbar^2 l(l+1)}{2mr^2}. \tag{3.6}$$

The effective interaction potential $V_{\text{eff}}(r)$ includes the centrifugal barrier, which cannot be overcome in the limit of low scattering energies (low temperatures), i.e. $k \to 0$. The remaining partial wave is then the radially symmetric s-wave ($l = 0$) term. In this case the asymptotic solution of Eq. 3.5 is $u_0(r) = r - a$ and the expression for the scattering wavefunction becomes

$$\Psi_{\mathbf{k}\to 0}(\mathbf{r}) \propto \frac{r-a}{r}. \tag{3.7}$$

The entire scattering problem can thus be described by a single parameter, the s-wave scattering length a, which describes the intercept of the asymptotic scattering wavefunction. The scattering is repulsive for a positive intercept $a > 0$ and attractive for a negative intercept $a < 0$, see Fig. 3.1b. Using a low momentum expansion, the scattering length can be related to the scattering amplitude

$$f(k) = -\frac{1}{1/a + ik - k^2 r_e/2}, \tag{3.8}$$

where the effective range of the interaction potential V was introduced [125, 126]. The scattering cross section can be obtained from the optical theorem $\sigma(k) = (4\pi/k)\text{Im}[f(k)]$, which gives for small $k \to 0$

$$\sigma = \frac{4\pi a^2}{1 + a^2 k^2}. \tag{3.9}$$

A further important aspect considers the symmetry. The spatial part of the two-body wavefunction is symmetric for even values of l and antisymmetric for odd values of l. Owing to quantum statistics, two scattering fermions with the same spin thus have a vanishing s-wave scattering length and the lowest partial wave contributing is the p-wave term ($l = 1$). Since this is negligibly small at the ultralow temperatures in cold atoms experiments, an ultracold spin-polarized cloud of fermions can safely be considered non-interacting. This is different for a two-component mixture of fermionic atoms, in which case the s-wave scattering length of two particles with different spins is finite.

Dilute atomic gases at ultralow temperatures

Atomic gases at ultralow temperatures are in fact metastable states. The stability timescale is given by the three-body recombination rate, where a deeply bound molecule and a high-energy atom are created. Owing to the very low densities in ultracold atoms experiments (typically around 10^{14} cm^{-3}), these three-body recombination processes are strongly suppressed and usually comparable to the lifetime of the atomic gas in the vacuum chamber of several seconds. The interaction potential between two neutral atoms at large distances is given by the van der Waals potential $V(r) = -C_6/r^6$, with an effective range of $\beta_6 = (C_6 m/\hbar^2)^{1/4}$ and the

van der Waals parameter C_6. In ultracold Fermi gases the mean particle spacing is typically given by k_F^{-1}, which is much larger than the effective range of the van der Waals potential [127]

$$k_\mathrm{F}\beta_6 \ll 1. \tag{3.10}$$

It is therefore sufficient to describe the interaction in ultracold dilute atomic gases via the two-body scattering process. Additionally, the scattering state is well described by its asymptotic behaviour. The interacting many-body system then depends on a single interaction parameter, the scattering amplitude f, which for low temperatures is only determined by the s-wave scattering length. This requires the scattering between particles to be in the zero-range limit, see Eq. 3.8, where

$$k^2|r_e| \ll |1/a + ik|. \tag{3.11}$$

An exact calculation of the interatomic potential is in most cases complicated and the Born approximation cannot be applied. Using the above introduced s-wave scattering length a, a zero-range pseudo-potential can be introduced [127]

$$V(r) = g\delta(r)\partial_r r, \qquad \text{with} \quad g = \frac{4\pi\hbar^2}{m}a. \tag{3.12}$$

Here we denoted the coupling constant with g and the regularization operator $\partial_r r$ removes the $1/r$ divergence for $r \to 0$. For a small gas parameter $k_\mathrm{F}a \ll 1$, the pseudo-potential can be treated in the Born approximation, which allows a mean-field description for the interaction energy. As will be explained in the following chapter, for deep optical lattices or for very large scattering lengths this approximation breaks down and the scattering is no longer in the zero-range limit.

Feshbach resonances

The presence of Feshbach resonances in ultracold atomic gases allows adjusting the scattering length a to arbitrary values via a magnetic offset field. The underlying idea is a scattering resonance between an open channel and one or several closed channels. In the following we consider two incoming atoms in the hyperfine states $|\mathrm{F}_1, m_{\mathrm{F},1}\rangle$ and $|\mathrm{F}_2, m_{\mathrm{F},2}\rangle$, which are in the open channel as their energy is slightly above the scattering continuum value, see Fig. 3.1a. At small distances the interatomic potential contains an additional spin-dependent interaction term, which leads to a coupling to other hyperfine channels denoted with $|\mathrm{F}'_1, m'_{\mathrm{F}',1}\rangle$ and $|\mathrm{F}'_2, m'_{\mathrm{F}',2}\rangle$. Angular momentum conservation implies $m_{\mathrm{F},1}+m_{\mathrm{F},2} = m'_{\mathrm{F}',1}+m'_{\mathrm{F}',2}$. A Feshbach resonance appears if the open channel scattering continuum couples to an energetically close bound state of the closed channel. In general the open and closed channel have a difference in total magnetic moment $\Delta\mu$. This allows changing the detuning δ between the two channels via a magnetic offset field, where $\hbar\delta = \Delta\mu(B - B_\mathrm{res})$ and B_res is the resonance magnetic field. The entrance of an additional bound state into the scattering process leads to a divergence of the s-wave scattering length, see Fig. 3.1b. This is similar to the textbook scattering problem of an attractive square well potential, where a bound state enters upon increasing the well depth. In the vicinity of the Feshbach resonance, the scattering length can be written as [128]

$$a(B) = a_\mathrm{bg}\left(1 - \frac{\Delta B}{B - B_0}\right), \tag{3.13}$$

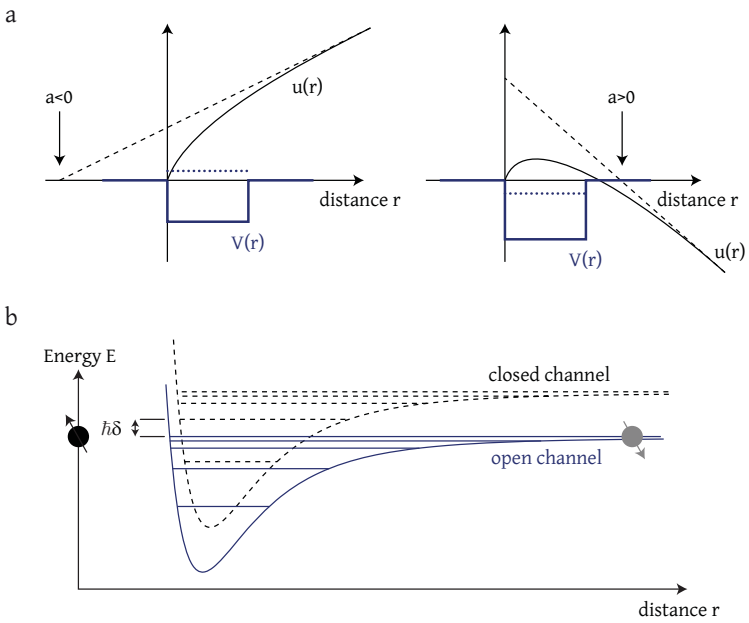

FIGURE 3.1.: **Two-particle scattering and Feshbach resonance.** (a) The two possible cases for low-energy scattering from a spherically symmetric attractive box potential at variable depths. The intercept of the asymptotic behaviour for the radial wavefunction $u_l(r)$ determines the sign and the strength of the scattering length a. As the box potential depth is lowered and an additional bound state enters, the scattering length diverges to $-\infty$ and eventually reduces its value again coming from $+\infty$. (b) Exemplary interatomic van der Waals potential for an open and closed channel as a function of distance r between the two scattering particles. For a finite magnetic offset field both channels have an energy offset owing to their different magnetic moments (see main text). The detuning $\hbar\delta$ between the open channel continuum state and the nearest bound state of the closed channel can be controlled by changing the magnetic offset field.

where a_{bg} denotes the background scattering length and ΔB the width of the Feshbach resonance. The Feshbach resonance position B_0 does not exactly coincide with the energy crossing resonance value B_{res}, owing to an avoided crossing of the highest bound state in the open channel [129]. The width of the resonance is determined by the effective range of the potential r_e with $\Delta\mu\Delta B = 2\hbar^2/mr_e a_{\mathrm{bg}}$ [127]. Feshbach resonances are generally classified into broad and narrow resonances. If the admixture of the closed channel bound state is small as compared to the open channel contribution, resonances are termed broad and can be conveniently modelled by a single-channel model. If the contribution of the closed channel state is large, the resonance is narrow and multi-channel models have to be considered for an accurate description [130]. Experimentally broad Feshbach resonances are more desirable, as they offer easy magnetic field control and are simple to model theoretically. Additionally, the lifetime of the Feshbach molecules is usually very large in this case. These molecular states are adiabatically connected to the free scattering state in the open channel, where the binding energy E_{bind} close to the Feshbach resonance is given by the Wigner formula [124]

$$E_{\mathrm{bind}} = -\frac{\hbar^2}{ma^2}. \tag{3.14}$$

3.2. Constructing the Fermi-Hubbard model

In this section we now consider two-particle scattering in the presence of an optical lattice. The interatomic potential can be modelled by the pseudo-potential from Eq. 3.12 if the spatial extent of the on-site wavefunction on a lattice site is much larger than the van der Waals effective range. For deep lattices the lowest on-site state is close to the harmonic oscillator ground state with an harmonic oscillator length $a_{\mathrm{ho}} = \sqrt{\hbar/m\omega_{\mathrm{site}}}$, where ω_{site} is the on-site trap frequency. The condition for the pseudo-potential is then $\beta_6 \ll a_{\mathrm{ho}}$. This regime is called the asymptotic regime, where the scattering length is energy/momentum independent. The problem of two particles in a three-dimensional harmonic trap interacting via a pseudo-potential can in fact be solved analytically for arbitrary values of the s-wave scattering length [131].

The interaction part of the many-body Hamiltonian in the presence of two-particle interactions can be written using the fermionic field operator $\hat{\Psi}$, similar to the kinetic energy expression from Eq. 2.28

$$\begin{aligned}\hat{H}_{\mathrm{int}} &= \frac{1}{2}\sum_{\sigma,\sigma'\in\{\uparrow,\downarrow\}}\int \mathrm{d}\mathbf{r}\mathrm{d}\mathbf{r}'\hat{\Psi}^\dagger_{\sigma'}(\mathbf{r}')\hat{\Psi}^\dagger_{\sigma}(\mathbf{r})V(\mathbf{r}-\mathbf{r}')\hat{\Psi}_{\sigma}(\mathbf{r})\hat{\Psi}_{\sigma'}(\mathbf{r}') \\ &= \frac{1}{2}\sum_{\sigma,\sigma'\in\{\uparrow,\downarrow\}}\int \mathrm{d}\mathbf{r}\hat{\Psi}^\dagger_{\sigma'}(\mathbf{r})\hat{\Psi}^\dagger_{\sigma}(\mathbf{r})\hat{\Psi}_{\sigma}(\mathbf{r})\hat{\Psi}_{\sigma'}(\mathbf{r}). \end{aligned} \tag{3.15}$$

In the second line we inserted the expression of the pseudo-potential for the interatomic interaction $V(\mathbf{r}-\mathbf{r}') = g\delta(\mathbf{r}-\mathbf{r}')$.

As the case in section 2.3, the field operator can be expressed using Wannier functions, see Eq. 2.29. This generally results in various cross-terms between Wannier states in different bands and on different sites. If all energy scales (temperature, chemical potential, interaction energy) are much smaller than the separation between the two lowest bands, it is sufficient to consider only the lowest band states (that is the two lowest mini-bands, see section 2.3). If additionally the nearest-neighbour interaction terms are much smaller than the on-site interaction terms, the many-body interaction Hamiltonian is given by the on-site term

$$\hat{H}_{\mathrm{on-site}} = U\sum_{s,\mathbf{i}}\hat{n}_{s,0,\mathbf{i},\uparrow}\hat{n}_{s,0,\mathbf{i},\downarrow}. \tag{3.16}$$

The summation runs over left and right sites $s \in \{l, r\}$ and all real space unit cells located at $\mathbf{R_i}$, see Eq. 2.27. The operator $\hat{n}_{s,0,\mathbf{i},\sigma} = \hat{c}^\dagger_{s,0,\mathbf{i},\sigma}\hat{c}_{s,0,\mathbf{i},\sigma}$ counts whether or not a particle with spin σ is present in the lowest band on the left or right site of the unit cell located at $\mathbf{R_i}$. The Hubbard interaction parameter U is given by

$$U = g\int |w^s_{0,\mathbf{i}}(\mathbf{x})|^4\mathrm{d}\mathbf{x}. \tag{3.17}$$

Here the value for the interaction energy U is independent of the unit cell $\mathbf{i}$ and whether or not the left or right site of the unit cell is considered. If an energy offset between neighbouring sites is present (i.e. an energy difference between $\mathcal{A}$ and $\mathcal{B}$ sublattice, see section 2.3), this is no longer true and two different on-site interaction energies have to be considered.

The full Hamiltonian including the kinetic energy in the tight-binding approximation from Eq. 2.33 and the on-site interaction term from Eq. 3.16 then corresponds to the single-band

Fermi-Hubbard model

$$\hat{H}_{\mathrm{FH}} = -t_{i,j} \sum_{\langle i,j\rangle,\sigma} (\hat{c}^{\dagger}_{i,\sigma}\hat{c}_{j,\sigma} + \mathrm{h.c.}) + U \sum_{i} \hat{n}_{i,\uparrow}\hat{n}_{i,\downarrow}. \tag{3.18}$$

Here $\langle i,j\rangle$ denotes any neighbouring sites and $\sigma \in \{\uparrow,\downarrow\}$ the spin. This Hamiltonian is an accurate description for the experiments presented in this thesis with interacting two-component spin mixtures of ultracold fermionic gases in the tunable-geometry optical lattice. The underlying harmonic confinement can be included by adding the $\hat{H}_{\mathrm{trap}}$ term to the Fermi-Hubbard model

$$\hat{H}_{\mathrm{trap}} = \sum_{i,\sigma} \epsilon_i \hat{n}_{i,\sigma}, \tag{3.19}$$

where the site-dependent energy offset is denoted with ϵ_i.

Extended Hubbard-model

In the above treatment the nearest-neighbour interaction terms were neglected. If the barrier height between neighbouring sites on the unit cell is small, the overlap between adjacent Wannier functions on this double-well becomes large and additional terms have to be taken into account. To lowest order this can be done by including in the Wannier function expansion of the full interaction term in Eq. 3.15 only those cross-terms, which represent left and right sites within the same unit cell. This leads to several additional diagonal terms in the Fermi-Hubbard model, which are beyond the usual on-site interaction terms on the left and right site [60]. For clarity, we list the different types of terms and their physical meaning (omitting for the moment the unit cell index $\mathbf{i}$):

- on-site interaction: $U\Big(\hat{n}_{l,\uparrow}\hat{n}_{l,\downarrow} + \hat{n}_{r,\uparrow}\hat{n}_{r,\downarrow}\Big)$
- nearest-neighbour interaction: $U_{lr}\Big(\hat{n}_{l,\uparrow}\hat{n}_{r,\downarrow} + \hat{n}_{l,\uparrow}\hat{n}_{r,\downarrow}\Big)$
- direct exchange process: $U_{lr}\left(\hat{c}^{\dagger}_{l,\downarrow}\hat{c}^{\dagger}_{r,\uparrow}\hat{c}_{l,\uparrow}\hat{c}_{r,\downarrow} + \mathrm{h.c.}\right)$
- doublon tunnelling: $U_{lr}\left(\hat{c}^{\dagger}_{l,\uparrow}\hat{c}^{\dagger}_{l,\downarrow}\hat{c}_{r,\uparrow}\hat{c}_{r,\downarrow} + \mathrm{h.c.}\right)$
- density-assisted tunnelling: $\Delta t \sum_{\sigma\neq\overline{\sigma}} \Big(\hat{n}_{l,\sigma} + \hat{n}_{r,\sigma}\Big)\left(\hat{c}^{\dagger}_{l,\overline{\sigma}}\hat{c}_{r,\overline{\sigma}} + \mathrm{h.c.}\right)$

Here we used abbreviations for the nearest-neighbour interaction energy U_{lr} and the density-assisted tunnelling renormalization Δt assuming purely real-valued Wannier functions

$$U_{lr} = g \int w^{l}_{0,\mathbf{i}}(\mathbf{x})^2 w^{r}_{0,\mathbf{i}}(\mathbf{x})^2 \mathrm{d}\mathbf{x} \tag{3.20}$$

$$\Delta t = g \int w^{l}_{0,\mathbf{i}}(\mathbf{x}) w^{r}_{0,\mathbf{i}}(\mathbf{x})^3 \mathrm{d}\mathbf{x}. \tag{3.21}$$

We also omitted terms, which only lead to a small shift in the energies of the localized states. For an exact derivation of the extended Fermi-Hubbard Hamiltonian, careful attention to the fermion minus-sign has to be paid. As the two correction energy scales U_{lr} and Δt are usually much smaller than the energies of the simple double-well model [60], these terms merely lead to corrections on a quantitative level but do not change the qualitative behavior.

3.3. High-temperature expansion in cubic lattices

Series expansions are a possible approach for evaluating the thermodynamics and observables for generic lattice models and is applicable to a variety of systems with spin and charge degrees of freedom. Depending on the lattice system and parameter regime of interest, various methods exist. Examples range from a low-temperature series, which can be applied to the Ising model, or zero-temperature interaction expansions, where a perturbative part is split off from the main Hamiltonian [132]. In this work a high-temperature series for Hubbard-type models is used, which is obtained by splitting the Hamiltonian $\hat{H}_{\mathrm{FH}}$ into an on-site interaction term $\hat{H}_0$ and a tunnel coupling $\hat{H}_c$

$$\hat{H}_{\mathrm{FH}} = \hat{H}_0 + \hat{H}_c. \tag{3.22}$$

The central idea is to evaluate the partition function $\mathcal{Z}$ by treating the tunnelling term as a perturbation. This results in an expansion of the partition function in powers of βt, where $\beta = 1/k_{\mathrm{B}}T$ is the reduced temperature and t is the tunnel energy of the coupling term H_c [132]

$$\begin{aligned} \mathcal{Z} &= \mathrm{Tr}\{e^{-\beta\hat{H}}\} \\ &= \mathcal{Z}_0 + \mathcal{Z}_0 \sum_{n=1}^{\infty}(-1)^n \int_0^{\beta} \mathrm{d}\tau_1 \int_0^{\tau_1} \mathrm{d}\tau_2 ... \int_0^{\tau_{n-1}} \mathrm{d}\tau_n \\ &\quad \langle \hat{H}_c'(\tau_1)\hat{H}_c'(\tau_2)...\hat{H}_c'(\tau_n)\rangle_0. \end{aligned} \tag{3.23}$$

Here $\mathcal{Z}_0$ denotes the unperturbed partition function and we make use of the interaction representation for the tunnelling operators

$$\mathcal{Z}_0 = \mathrm{Tr}\{e^{-\beta\hat{H}_0}\} \tag{3.24}$$

$$\hat{H}_c'(\tau) = e^{\tau\hat{H}_0}\hat{H}_c e^{-\tau\hat{H}_0}. \tag{3.25}$$

The average $\langle ... \rangle_0$ is evaluated in the unperturbed Hamiltonian

$$\langle \hat{H}_c'(\tau_1)\hat{H}_c'(\tau_2)...\hat{H}_c'(\tau_n)\rangle_0 = \mathrm{Tr}\{e^{-\beta\hat{H}_0}\hat{H}_c'(\tau_1)\hat{H}_c'(\tau_2)...\hat{H}_c'(\tau_n)\}/\mathcal{Z}_0. \tag{3.26}$$

3.3.1. Thermodynamic quantities

In the following section we apply this formalism to the single-band Fermi-Hubbard model on a simple cubic lattice, see Fig. 3.2. For simplicity we work in the isotropic model where all spatial tunnellings are equal $t_x = t_y = t_z = t$. The Hamiltonian is decomposed as $\hat{H} = \hat{H}_0 + \hat{H}_c$ in the grand canonical ensemble with

$$\begin{aligned} \hat{H}_0 &= U\sum_i \hat{n}_{i\uparrow}\hat{n}_{i\downarrow} - \mu\sum_i(\hat{n}_{i\uparrow} + \hat{n}_{i\downarrow}) \\ \hat{H}_c &= -t\sum_{\sigma,\langle i,j\rangle}(\hat{c}_{i,\sigma}^{\dagger}\hat{c}_{j,\sigma} + \mathrm{h.c.}). \end{aligned}$$

The series expansion is valid in the regime $t \ll k_{\mathrm{B}}T \ll U$ [132]. Thermodynamic quantities are obtained by evaluating the grand canonical potential $-\beta\Omega = \log\mathcal{Z}$ from the partition

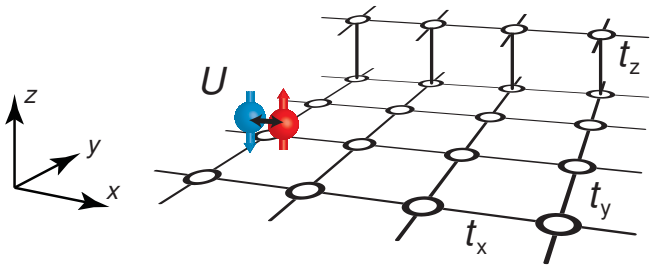

FIGURE 3.2.: **Fermi-Hubbard model on a simple cubic lattice** Two fermionic spin-components (red spin-up and blue spin-down) can delocalize over the lattice via tunnelling to nearest-neighbours. The tunnelling matrix elements t_x, t_y and t_z can be different along the three spatial directions. Two particles of opposite spin share an interaction energy U, whereas in the single-band approximation two particles with the same spin can never occupy the same site due to Pauli's principle.

function

$$-\beta\Omega = \log\mathcal{Z}_0 + \sum_{n=1}^{\infty}(-1)^n \int_0^\beta \mathrm{d}\tau_1 \int_0^{\tau_1} \mathrm{d}\tau_2 ... \int_0^{\tau_{n-1}} \mathrm{d}\tau_n \langle \hat{H}'_c(\tau_1)\hat{H}'_c(\tau_2)...\hat{H}'_c(\tau_n)\rangle_0. \tag{3.27}$$

From this several thermodynamic quantities, such as the density n, entropy per site s and double occupancy d (probability for a doubly occupied site), can be obtained from derivatives of the grand potential per site $\Omega^s = \Omega/l$, where l is the number of sites in the system

$$n = -\frac{\partial\Omega^s}{\partial\mu}, \qquad s = -\frac{\partial\Omega^s}{\partial T}, \qquad d = \frac{\partial\Omega^s}{\partial U}. \tag{3.28}$$

The sum in Eq. 3.27 is evaluated by determining the contribution of every order n separately. If the series is convergent, the calculation can be truncated at a suitable order n and the result is then very close to the exact answer. The determination of the contributions within any order n amounts to the evaluation of a trace, multiple integration and a sum over all possible tunnel operations $\hat{H}'_c(\tau_1)\hat{H}'_c(\tau_2)...\hat{H}'_c(\tau_n)$. A tractable approach of grouping these tunnelling configurations for any order n is the use of graph theory [132, 133, 134]. This is a very powerful technique when calculating extensive expressions, such as thermodynamic potentials, as the various contributions can then be simply added up. The main idea is a graphical representation of the possible tunnelling operations, which are drawn as lines between neighbouring sites, whereas dots indicate lattice sites. In second order only one graph contributes to the evaluation of thermodynamic quantities, which is shown in Tab. 3.1. The thermal average $\langle ... \rangle_0$ in Eq. 3.27 (i.e. the trace) is evaluated in a configuration space, which is spanned by the unperturbed eigenstates of the system $|\Psi_i\rangle$. For the case of a single-band Fermi-Hubbard model on a simple cubic lattice, this basis is formed by a tensor product of all sites, where each site has four possible configurations $|0\rangle$, $|\uparrow\rangle$, $|\downarrow\rangle$ and $|\uparrow\downarrow\rangle$. The contribution X_g of each graph in order n to the total sum is then evaluated in a basis with $l_g \leq l$ sites.

This allows rewriting the total sum as

$$-\beta\Omega^s = \log z_0 + \sum_{n=1}^{\infty}(-1)^n(\beta t)^n \left(\sum_g \frac{c_g}{z_0^{l_g}} \mathrm{X}_g\right). \tag{3.29}$$

Owing to the trace in Eq. 3.27, each graph contribution needs to be divided by $z_0^{l_g}$, which is the unperturbed partition function on l_g sites. Here the single site partition function is denoted with z_0, which reads after introducing the fugacity $\zeta = \exp(\beta\mu)$ and the scaled interaction $w = \exp(-\beta U)$

$$z_0 = 1 + 2\zeta + \zeta^2 w. \tag{3.30}$$

We have furthermore introduced the weak lattice constant c_g for each graph, which is necessary for correct counting of all graph contributions in the global system and correctly taking into account the contribution per site to the extensive quantity of interest (here this is the grand canonical potential per site). The exact value depends for example on the number of nearest-neighbours [133]. An overview of the weak lattice constants for different graphs in the square and cubic lattice is shown in Tab. 3.1.

graph	square	cubic
•—•	2	3

graph	square	cubic
○—•	4	6
○—○	1	1
•—○ ○	6	10

TABLE 3.1.: **Lattice constants** Weak lattice constants for different graphs for the square and cubic lattice. On the left the only contributing graph in second order for evaluation of thermodynamic quantities is shown. On the right the relevant graphs up to second order are shown for evaluating single and two-site observables indicated by the open circles, see section 3.3.2.

The determination of the graph weights X_g basically amounts to the evaluation of a trace, which is done by summing over matrix elements for all possible eigenstates of the unperturbed Hamiltonian $|\Psi_i\rangle$ defined on the lattice sites l_g of each graph and subsequent integration

$$\begin{aligned} X_g &= \frac{1}{\beta^n}\sum_{|\Psi_i\rangle}\int_0^\beta \mathrm{d}\tau_1 \int_0^{\tau_1}\mathrm{d}\tau_2 ... \int_0^{\tau_{n-1}}\mathrm{d}\tau_n \\ &\quad \langle\Psi_i|e^{-\beta\hat{H}_0}\hat{T}'(\tau_1)\hat{T}'(\tau_2)...\hat{T}'(\tau_n)|\Psi_i\rangle_g. \end{aligned} \tag{3.31}$$

Here we abbreviated $\hat{H}_c' = t\hat{T}'$ and the matrix element $\langle ...\rangle_g$ is evaluated using the tunnelling bonds of the corresponding graph. All calculations are done up to second order. Denoting $\hat{H}_c = t\hat{T}$, the generic graph weight then reads

$$X_{g,2} = \frac{1}{\beta^2}\sum_{|\Psi_i\rangle}\int_0^\beta \mathrm{d}\tau_1 \int_0^{\tau_1}\mathrm{d}\tau_2 \langle\Psi_i|e^{(\tau_1-\beta)\hat{H}_0}\hat{T}e^{(\tau_2-\tau_1)\hat{H}_0}\hat{T}e^{-\tau_2\hat{H}_0}|\Psi_i\rangle_g. \tag{3.32}$$

The correct counting thus includes the number of states, the number of tunnelling processes on the graph bonds and the integral contribution of the weighted energies. A general expression for the above matrix element with the double integral can be found using

$$\hat{H}_0|\Psi_i\rangle = E_o|\Psi_i\rangle, \qquad \hat{H}_0\,|\Psi_u\rangle = E_u|\Psi_u\rangle, \tag{3.33}$$

where $|\Psi_u\rangle$ denotes any possible state in the unperturbed basis after applying the tunnelling operator $\hat{T}$ on $|\Psi_i\rangle$, i.e. $\langle\Psi_u|\hat{T}|\Psi_i\rangle \neq 0$. The contribution to the graph weight $X_{g,2}$ omitting for the moment the amount of tunnelling processes then reads for every state $|\Psi_i\rangle$

$$\begin{aligned} \frac{e^{-\beta E_o}}{\beta(E_u - E_o)}\left(1 + \frac{e^{-\beta(E_u-E_o)} - 1}{\beta(E_u - E_o)}\right) \quad &\text{if} \quad E_o \neq E_u \\ \frac{1}{2}e^{-\beta E_o} \quad &\text{if} \quad E_o = E_u \end{aligned} \tag{3.34}$$

Tab. 3.2 summarizes the evaluation of the relevant graph weight X_2 in second order for the grand potential, which amounts to

$$X_2 = 2\zeta(1 + \zeta^2 w) + \frac{4\zeta^2}{\beta U}(1 - w). \tag{3.35}$$

The total expression for the grand potential up to second order in βt then reads

$$-\beta\Omega^s = \log(z_0) + (\beta t)^2 \frac{c}{z_0^2} X_2, \tag{3.36}$$

where $c = 2$ for the square lattice and $c = 3$ for the cubic lattice.

state $\|\Psi_i\rangle$	$\frac{1}{\beta^2}\int\int\langle\Psi_i\|...\|\Psi_i\rangle$
$\|\uparrow,0\rangle, \|\downarrow,0\rangle, \|0,\downarrow\rangle, \|0,\uparrow\rangle$	$4 \times 1 \times \frac{1}{2}\zeta$
$\|\uparrow,\downarrow\rangle, \|\downarrow,\uparrow\rangle$	$2 \times 2 \times \zeta^2(\frac{1}{\beta U} + \frac{w-1}{(\beta U)^2})$
$\|\downarrow\uparrow,0\rangle, \|0,\downarrow\uparrow\rangle$	$2 \times 2 \times \zeta^2 w(-\frac{1}{\beta U} + \frac{1/w-1}{(\beta U)^2})$
$\|\downarrow\uparrow,\downarrow\rangle, \|\downarrow\uparrow,\uparrow\rangle, \|\downarrow,\downarrow\uparrow\rangle, \|\uparrow,\downarrow\uparrow\rangle$	$4 \times 1 \times \frac{1}{2}\zeta^3 w$

TABLE 3.2.: **Grand potential** Second order graph contributions to the grand canonical potential in the Fermi-Hubbard model. The matrix element is multiplied by the number of states (first number) and the amount of tunnelling processes (second number), whereas the last number is the weight contribution according to Eq. 3.34. States that do not contribute are omitted here. The total graph weight X_2 is obtained by the sum of all contributions.

In the case of an anisotropic simple cubic lattice with direction-dependent tunnellings t_x, t_y and t_z, an effective tunnelling $\bar{t}$ can be used in the expression for the grand potential to obtain all thermodynamic quantities

$$3\bar{t}^2 = t_x^2 + t_y^2 + t_z^2.$$

3.3.2. Observable evaluation technique

The evaluation of the series expansion for an observable $\hat{\mathcal{O}}$ is more complicated than the direct calculation of the grand potential, as it requires expanding the expression in the numerator

and denominator

$$\langle\hat{\mathcal{O}}\rangle = \frac{\mathrm{Tr}\left\{\hat{\mathcal{O}}e^{-\beta(\hat{H}_0+\hat{H}_c)}\right\}}{\mathrm{Tr}\left\{e^{-\beta(\hat{H}_0+\hat{H}_c)}\right\}}. \tag{3.37}$$

While there are several approaches to this problem - some of which directly sort the terms of the entire expression into different graphs, which then requires a sub-cluster subtraction due to multiple counting of graph contributions [133] - we will use here a simplified version, where the numerator and denominator are expanded separately. This approach is well suited for calculations up to second order, but becomes significantly more complicated for higher orders. The denominator series has already been carried out in the previous section, see Eq. 3.23. To obtain the numerator series, we start by introducing a fictitious auxiliary field Φ associated to the observable $\hat{\mathcal{O}}$. This allows reducing the problem to the expansion of a new grand canonical potential $\Omega^{\hat{\mathcal{O}}}$ [135]

$$\begin{aligned} \langle\hat{\mathcal{O}}\rangle &= \partial_\Phi \Omega^{\hat{\mathcal{O}}}\Big|_{\Phi=0} \\ -\beta\Omega^{\hat{\mathcal{O}}} &= \log\left(\mathrm{Tr}\left\{e^{-\beta(\hat{H}_0+\hat{H}_c+\Phi\hat{\mathcal{O}})}\right\}\right). \end{aligned} \tag{3.38}$$

The central idea is thus to evaluate the partition function series with a more complicated unperturbed Hamiltonian given by $\hat{H}_0 + \Phi\hat{\mathcal{O}}$ and subsequently take the derivative. A more suitable form of Eq. 3.38 for evaluation is

$$\langle\hat{\mathcal{O}}\rangle = \frac{\mathrm{Tr}\left\{\hat{\mathcal{O}}e^{-\beta\hat{H}_0}\right\} - \frac{1}{\beta}\partial_\Phi\mathcal{A}\Big|_{\Phi=0}}{\mathrm{Tr}\left\{e^{-\beta(\hat{H}_0+\hat{H}_c)}\right\}}. \tag{3.39}$$

Here we used the abbreviation

$$\begin{aligned} \mathcal{A} &= \sum_{n=1}^{\infty}(-1)^n \int_0^\beta \mathrm{d}\tau_1 \int_0^{\tau_1} \mathrm{d}\tau_2 ... \int_0^{\tau_{n-1}} \mathrm{d}\tau_n \\ &\quad \mathrm{Tr}\left\{e^{-\beta(\hat{H}_0+\phi\hat{\mathcal{O}})}\hat{H}_c'(\tau_1)\hat{H}_c'(\tau_2)...\hat{H}_c'(\tau_n)\right\} \\ \hat{H}_c'(\tau) &= e^{\tau(\hat{H}_0+\Phi\hat{\mathcal{O}})}\hat{H}_c e^{-\tau(\hat{H}_0+\Phi\hat{\mathcal{O}})}. \end{aligned}$$

The second term in the numerator is hence the correction, whereas the first term is the unperturbed part. After both the numerator and denominator terms are expanded, the entire fraction needs to be re-expanded again and the terms ordered in powers of βt. While this procedure becomes quite complicated for higher orders, we restrict the calculation to second order in βt here. Neglecting fourth order terms, the symbolic result is

$$\frac{A + B(\beta t)^2}{C + D(\beta t)^2} = \frac{A}{C} + \left(\frac{B}{C} - \frac{AD}{C^2}\right)(\beta t)^2. \tag{3.40}$$

The same graph technique as explained in the previous section is used for evaluating the series expression in Eq. 3.39. All possible tunnelling configurations are graphically represented by lines and the trace is evaluated in an unperturbed eigenbasis $|\Psi_i\rangle$ defined on a l-site basis. An important difference to the usual graphs used for evaluating thermodynamic quantities

is the presence of marked sites (open symbols), which indicate the sites at which the observable $\hat{\mathcal{O}}$ is evaluated. In this work only single-site and neighbouring two-site observables are considered, such that in second order only a very small number of graphs contribute, see Tab. 3.2. The number of sites for the evaluation basis is then either $l = 2$ or $l = 3$. If multiple graphs are present in the calculation, the second order contribution of each graph to the observable is calculated separately and only at the end all contributions are added up. Also, it is important that the same number of sites for the basis is used when evaluating the numerator and denominator for the contribution of a single contributing graph. The expression for the second order expansion of the partition function in the denominator on l sites then reads for given graph with weak lattice constant c_g (definitions as in Eq. 3.36)

$$l = 2 : \; z_0^2 + c_g X_2 (\beta t)^2, \qquad l = 3 : \; z_0^3 + c_g z_0 X_2 (\beta t)^2. \tag{3.41}$$

Using the relation $[\hat{H}_0, \hat{\mathcal{O}}] = 0$, which holds for all observables calculated in the following (on-site density, nearest-neighbour density and spin correlator), the expression for the second order correction in the numerator can be calculated. As in the previous section, all terms are grouped into graph contributions X_g with weak lattice constants c_g and site number l_g, and we find for the sum of all enumerator contributions

$$-\frac{1}{\beta}\partial_\Phi \mathcal{A}\Big|_{\phi=0} = (\beta t)^2 \sum_g c_g X_{g,2} z_0^{l-l_g}. \tag{3.42}$$

The addition $z_0^{l-l_g}$ is necessary to ensure that the entire expression is in a l-site basis[1]. Similar to Eq. 3.32, the graph weight is written as

$$\begin{aligned} X_{g,2} \;=\; & \frac{1}{\beta^2} \sum_{|\Psi_i\rangle} \int_0^\beta \mathrm{d}\tau_1 \int_0^{\tau_1} \mathrm{d}\tau_2 \\ & (1 - \frac{\tau_1}{\beta} + \frac{\tau_2}{\beta}) \langle \Psi_i | \hat{\mathcal{O}} e^{(\tau_1-\beta)\hat{H}_0} \hat{T} e^{(\tau_2-\tau_1)\hat{H}_0} \hat{T} e^{-\tau_2 \hat{H}_0} | \Psi_i \rangle_g + \\ & (\frac{\tau_1}{\beta} - \frac{\tau_2}{\beta}) \langle \Psi_i | e^{(\tau_1-\beta)\hat{H}_0} \hat{T} e^{(\tau_2-\tau_1)\hat{H}_0} \hat{\mathcal{O}} \hat{T} e^{-\tau_2 \hat{H}_0} | \Psi_i \rangle_g. \end{aligned} \tag{3.43}$$

As in the case for the expansion of the grand potential in the previous section, the correct counting includes the number of states, the number of tunnelling processes on the graph bonds and the integral contribution of the weighted energies. We use

$$\begin{aligned} \hat{H}_0 |\Psi_i\rangle &= E_o |\Psi_i\rangle, \qquad \hat{H}_0 |\Psi_u\rangle = E_u |\Psi_u\rangle \\ \hat{\mathcal{O}} |\Psi_i\rangle &= O_o |\Psi_i\rangle, \qquad \hat{\mathcal{O}} |\Psi_u\rangle = O_u |\Psi_u\rangle. \end{aligned}$$

The states $\{|\Psi_i\rangle\}$ are chosen to be common eigenvectors of $\hat{H}_0$ and $\hat{\mathcal{O}}$ with eigenvalues E_o, E_u, O_o, O_u. Again $|\Psi_u\rangle$ denotes any possible state in the unperturbed basis after applying the tunnelling operator $\hat{T}$ on $|\Psi_i\rangle$, i.e. $\langle \Psi_u | \hat{T} | \Psi_i \rangle \neq 0$. The contribution to the graph weight $X_{g,2}$, omitting for the moment the amount of tunnelling processes, then reads for every state $|\Psi_i\rangle$

$$\begin{aligned} O_o \frac{e^{-\beta E_o}}{\beta(E_u - E_o)} \left(1 + \frac{e^{-\beta(E_u - E_o)} - 1}{\beta(E_u - E_o)} \right) \quad & \text{if} \quad E_o \neq E_u \\ (O_u + 2O_o) \frac{e^{-\beta E_o}}{6} \quad & \text{if} \quad E_o = E_u. \end{aligned} \tag{3.44}$$

[1] This result holds in second order, whereas for higher orders different techniques become necessary.

3.3.3. Results for the homogeneous cubic lattice

We now use the high-temperature series calculations to investigate the phase diagram of the repulsive Fermi-Hubbard model on a homogeneous cubic lattice. For the temperature regime accessible by the series, no real phase transitions are expected, as all thermodynamic potentials are analytic functions in the system variables. The accessible phases are rather connected by crossovers, where each quantity changes smoothly as the system parameters are varied. The relevant parameters are (in normalized units) the interaction energy U/t, the temperature T/t and the chemical potential μ/t. Using the techniques explained in the previous section, we investigate in the following the behaviour of various observables and characterize the different phases.

- Entropy per site s
- On-site density $n = \langle \hat{n}_{i,\uparrow} + \hat{n}_{i,\downarrow} \rangle$
- Density-density correlator $C_{dd} = \sum_{\sigma,\sigma'} \langle \hat{n}_{i,\sigma}(1 - \hat{n}_{i,\bar{\sigma}}) \hat{n}_{i+1,\sigma'}(1 - \hat{n}_{i+1,\bar{\sigma'}}) \rangle$
- Spin correlator $C_{ss} = \langle \hat{S}^z_i \hat{S}^z_{i+1} \rangle = \frac{1}{4} \langle (\hat{n}_{i,\uparrow} - \hat{n}_{i,\downarrow})(\hat{n}_{i+1,\uparrow} - \hat{n}_{i+1,\downarrow}) \rangle$

Here $\sigma, \sigma' \in \{\downarrow, \uparrow\}$ denote the spin and $\bar{\sigma}, \bar{\sigma'}$ the opposite spin and $\hat{S}^z_i = (\hat{n}_{i,\uparrow} - \hat{n}_{i,\downarrow})/2$ is the spin-projection operator along the z-axis. The density-density correlator C_{dd} counts the probability for two particles with arbitrary spin to be located next to each other on neighbouring sites $i, i+1$. The spin correlator C_{ss} compares the chance of finding two particles with opposite spins on neighbouring sites with two particles of the same spin. The contributions to the graph weights for the numerator are summarized in Tab. A.1 and A.2 in the Appendix A. All contributions in the numerator are summed using the weak lattice constants from Tab. 3.1, whereas the denominator expression is taken from Eq. 3.41. The entire fraction is then expanded as in Eq. 3.40. The final expressions for all observables can be found in the Appendix A[2]. The entropy is evaluated from a derivative of the grand potential, see Eq. 3.28.

In total three different phases are possible for a repulsive homogeneous Fermi-Hubbard model at not too low temperatures: a metallic, band-insulating and Mott-insulating phase. A simple understanding of how these different phases are connected is obtained by investigating the dependence of the density on chemical potential for different interactions and temperatures, see Fig. 3.3a. For very large chemical potentials a band insulating state forms, where two particles are located on the same site and the compressibility $\kappa = \partial n / \partial \mu$ is strongly reduced. This state appears for all interactions and temperatures at sufficiently high values of the chemical potential. Only for low temperatures and very strong repulsive interactions a Mott-insulating state appears at half-filling (one particle per site), which is characterized by a vanishing compressibility and a very small number of density fluctuations. As compared to the band insulator, the incompressibility is in this case interaction-driven. For weaker interactions the Mott state is destroyed and transforms to a metallic state with a finite value of the compressibility. At intermediate fillings other than one or two particles per site, the system is also metallic.

[2] When evaluating the spin correlator C_{ss} in the anisotropic cubic lattice with direction dependent tunnellings t_x, t_y and t_z, the tunnelling between the neighbouring sites $i, i+1$ needs to be used in the expression $(\beta t)^2$.

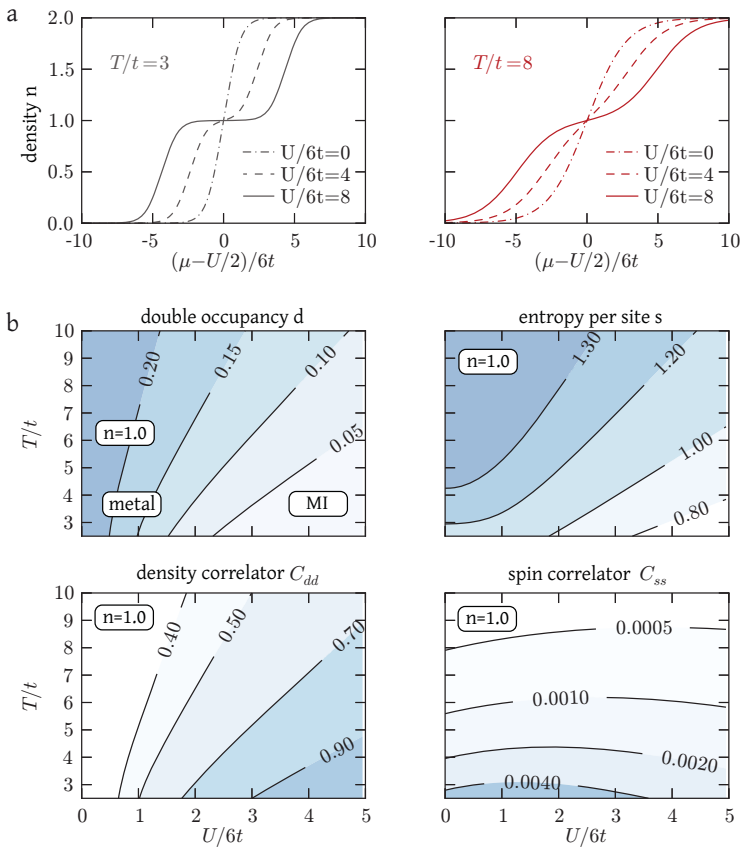

FIGURE 3.3.: **Second order high-temperature series for the Fermi-Hubbard model on a simple cubic lattice** (a) Dependence of density on chemical potential for various interactions and temperatures. The Mott plateau appears at half-filling for large interactions and low temperatures. (b) Phase-diagram with several observables as a function of normalized interaction U/t and temperature T/t at half filling. For each point the chemical potential corresponding to a density of one particle was obtained. The Mott-insulating region is denoted with MI and $k_\mathrm{B} = 1$.

The crossover from a metallic to Mott-insulating state at half-filling can also be seen in the phase-diagram shown in Fig. 3.3b as a function of interaction and temperature, which was obtained for a filling of one particle per site. Only for low temperatures and large repulsive interactions the double occupancy is strongly suppressed, which is a characteristic signal of the Mott state. Large temperatures at fixed interaction create thermal excitations in form of additional doubly occupied sites. The entropy per site decreases for large interactions, as the doubly occupied sites costs an additional energy U and are thus no longer energetically populated. For very large interactions all density fluctuations have disappeared from the system and only the spin degree of freedom remains. The system is then in a paramagnetic Mott state, where the entropy saturates to $k_\mathrm{B}\log 2$, which is the spin entropy per site for a two-component paramagnet. Here k_B denotes the Boltzmann constant.

Investigation of the nearest-neighbour density correlator C_{dd} confirms the above picture: only at large interactions and low enough temperature a Mott-state can form with a small

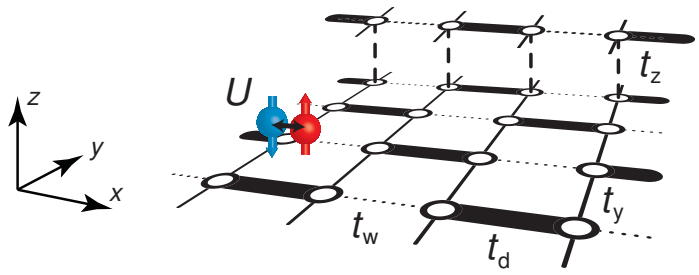

FIGURE 3.4.: **Fermi-Hubbard model on a dimerized lattice** Two fermionic spin-components (red spin-up and blue spin-down) can delocalize over the lattice via tunnelling to nearest-neighbours. The tunnellings along the x direction are dimerized with a strong tunnelling t_d and a much weaker coupling t_w. Along the y and z axis the tunnelling matrix elements are denoted with t_y and t_z. The dimerization is arranged in a chequerboard pattern in the x-y plane, which replicates along the vertical z axis. Two particles of opposite spin share an interaction energy U, whereas two particles with the same spin can never occupy the same site due to Pauli's principle.

number of holes, i.e. a correlator value close to one. For large temperatures excitations in form of double occupancies and holes reduce this value. At the temperatures accessible by the high-temperature series, the nearest-neighbour spin correlator C_{ss} already shows a small signal, indicating the onset of magnetic ordering. However, to access the low-temperature regime, where a true phase transition to a long-range ordered antiferromagnetic state occurs (maximum critical temperature T_c/t 0.35 [136]), more involved calculation techniques are necessary, such as for example determinental quantum Monte-Carlo or dynamical mean field theory or extended variants of the latter [136, 137, 138]. Interestingly, the maximum spin correlator at constant temperature occurs at an interaction, which is close to where the critical temperature has its maximum value. Further details on the high-temperature phase diagram and the extension to the attractive regime can be found for example in [102].

3.4. High-temperature expansion in dimerized lattices

In this and the following section we determine the partition function and grand potential for a Fermi-Hubbard model on a dimerized simple cubic lattice in a high-temperature series expansion up to second order. We start with the definition of the homogeneous single-band Hubbard Hamiltonian with different tunnelling links between nearest neighbours $\langle i,j\rangle_{\_}$, $\langle i,j\rangle_{\_\_}$, $\langle i,j\rangle_{\_\_\_}$ and $\langle i,j\rangle_{...}$ respectively, see Fig. 3.4,

$$\begin{aligned}
\hat{H}_0 &= -t_d \sum_{\sigma,\langle i,j\rangle_{_}} (\hat{c}^\dagger_{i,\sigma}\hat{c}_{j,\sigma} + \text{h.c.}) + U\sum_i \hat{n}_{i\uparrow}\hat{n}_{i\downarrow} - \mu\sum_i(\hat{n}_{i\uparrow}+\hat{n}_{i\downarrow}) \qquad (3.45)\\
\hat{H}_c &= -t_y \sum_{\sigma,\langle i,j\rangle_{__}} (\hat{c}^\dagger_{i,\sigma}\hat{c}_{j,\sigma} + \text{h.c.}) - t_z \sum_{\sigma,\langle i,j\rangle_{___}} (\hat{c}^\dagger_{i,\sigma}\hat{c}_{j,\sigma} + \text{h.c.})\\
&\quad -t_w \sum_{\sigma,\langle i,j\rangle_{...}} (\hat{c}^\dagger_{i,\sigma}\hat{c}_{j,\sigma} + \text{h.c.}).
\end{aligned}$$

We have split the Hamiltonian into the dimer part $\hat{H}_0$ and the coupling between dimers $\hat{H}_c$, similar to Eq. 3.22, where the term dimer denotes two neighbouring sites with strong tunnelling between them. The on-site interaction energy is given by U, the tunnelling matrix elements between nearest neighbours by t_d, t_y, t_z and t_w and the chemical potential is parametrized with μ. For most parameter regimes considered in this work, the tunnelling between dimers is much stronger than all other tunnellings $t_d \gg t_y, t_z, t_w$. The coupling between neighbouring dimers can then be treated as a perturbation in a high-temperature series. The series is expected to converge in the parameter regime

$$t_y, t_z, t_w \ll k_\mathrm{B}T \ll U, t_d. \tag{3.46}$$

3.4.1. Lowest order: atomic limit

The evaluation of the grand potential per dimer Ω^d to lowest order (atomic limit) merely requires the evaluation of the isolated dimer Hamiltonian $\hat{H}_d$ defined on two sites

$$-\beta\Omega^d = \log z_0^d \qquad z_0^d = \mathrm{Tr}\{e^{-\beta(\hat{H}_d - \mu\hat{N})}\} \tag{3.47}$$

For clarity we have denoted with $\hat{H}_d$ the Hamiltonian in the canonical ensemble with the energy eigenvalues $\{E_i\}$ and particles numbers $\{N_i\}$. Using left and right creation and annihilation operators $\hat{c}^\dagger_{l(r),\sigma}$ and $\hat{c}_{l(r),\sigma}$ of spin σ, the two-site dimer Hamiltonian $\hat{H}_d$ reads

$$\hat{H}_d = -t_d \sum_\sigma (\hat{c}^\dagger_{l,\sigma}\hat{c}_{r,\sigma} + \mathrm{h.c.}) + U \sum_{i=l,r} \hat{n}_{i\uparrow}\hat{n}_{i\downarrow}. \tag{3.48}$$

The particle number per dimer and entropy per dimer can then be obtained from derivatives of the potential, see Eq. 3.28 (division by 2 then gives the on-site density and entropy per site). The trace is evaluated in the eigenenergy basis containing 16 states

$$\mathrm{Tr}\{e^{-\beta(\hat{H}_d - \mu\hat{N})}\} = \sum_{i=1\ldots16} \langle\Psi_i^d|e^{-\beta\hat{H}_d}|\Psi_i^d\rangle = \sum_{i=1\ldots16} e^{-\beta(E_i - \mu N_i)}. \tag{3.49}$$

The corresponding eigenstates and eigenvectors obtained after diagonalization are given in Tab. 3.3, whereas the complete expression for the single site grand potential can be found in the Appendix B. We abbreviate the states $|\Psi_\mathrm{singlet}\rangle$ and $|\Psi_\mathrm{double}\rangle$ and set $u = U/(4t_d)$

$$|\Psi_\mathrm{singlet}\rangle = \frac{(|\uparrow,\downarrow\rangle - |\downarrow,\uparrow\rangle)(u + \sqrt{u^2+1}) + |\uparrow\downarrow,0\rangle + |0,\uparrow\downarrow\rangle}{2\sqrt{u^2+1+u\sqrt{1+u^2}}} \tag{3.50}$$

$$|\Psi_\mathrm{double}\rangle = \frac{(|\uparrow,\downarrow\rangle - |\downarrow,\uparrow\rangle)(u - \sqrt{u^2+1}) - |\uparrow\downarrow,0\rangle - |0,\uparrow\downarrow\rangle}{2\sqrt{u^2+1-u\sqrt{1+u^2}}}. \tag{3.51}$$

The evaluation of observables $\hat{\mathcal{O}}$ on a dimer other than the density and entropy, such as for example the singlet and triplet probability or the double occupancy per site, is done by determining the expression $\mathrm{Tr}\{\hat{\mathcal{O}}\exp(-\beta(\hat{H}_d - \mu\hat{N}))\}$ and using Eq. 3.37. If the observable $\hat{\mathcal{O}}$ commutes with the dimer Hamiltonian $\hat{H}_d$ and $\hat{N}$, the evaluation becomes particularly simple, as only the relevant dimer eigenstates $|\Psi_i^d\rangle$ have to be counted and weighted with the value of the observable. While this is the case for the singlet and triplet probabilities, the evaluation of the double occupancy for example is slightly more complicated, as the measurement operator

eigenenergy E_i/t_d	eigenstate $\|\Psi_i^d\rangle$
0	$\|0,0\rangle$
-1	$(\|\uparrow,0\rangle + \|0,\uparrow\rangle)/\sqrt{2}$
-1	$(\|\downarrow,0\rangle + \|0,\downarrow\rangle)/\sqrt{2}$
1	$(\|\uparrow,0\rangle - \|0,\uparrow\rangle)/\sqrt{2}$
1	$(\|\downarrow,0\rangle - \|0,\downarrow\rangle)/\sqrt{2}$
0	$\|\uparrow,\uparrow\rangle$
0	$\|\downarrow,\downarrow\rangle$
$2(u-\sqrt{u^2+1})$	$\|\Psi_{\text{singlet}}\rangle$
0	$(\|\uparrow,\downarrow\rangle + \|\downarrow,\uparrow\rangle)/\sqrt{2}$
$4u$	$(\|\uparrow\downarrow,0\rangle - \|0,\uparrow\downarrow\rangle)/\sqrt{2}$
$2(u+\sqrt{u^2+1})$	$\|\Psi_{\text{double}}\rangle$
$4u-1$	$(\|\uparrow\downarrow,\uparrow\rangle - \|\uparrow,\uparrow\downarrow\rangle)/\sqrt{2}$
$4u+1$	$(\|\uparrow\downarrow,\uparrow\rangle + \|\uparrow,\uparrow\downarrow\rangle)/\sqrt{2}$
$4u-1$	$(\|\uparrow\downarrow,\downarrow\rangle - \|\downarrow,\uparrow\downarrow\rangle)/\sqrt{2}$
$4u+1$	$(\|\uparrow\downarrow,\downarrow\rangle + \|\downarrow,\uparrow\downarrow\rangle)/\sqrt{2}$
$8u$	$\|\uparrow\downarrow,\uparrow\downarrow\rangle$

TABLE 3.3.: **Fermi-Hubbard model on a double-well** Eigenvalues E_i and eigenvectors $|\Psi_i^d\rangle$ for the isolated single dimer Hamiltonian $\hat{H}_d$ with the abbreviation $u = U/(4t_d)$.

$\hat{n}_{i,\uparrow}\hat{n}_{i,\downarrow}$ on site i does not commute with $\hat{H}_d$. In this case a transformation to the diagonal basis $\{|\Phi_i^d\rangle\}$ of the observable is necessary with the eigenvalues $\{O_i\}$ $(i = 1...16)$. The result can then be formally written as the trace over a 16×16 matrix

$$\mathrm{Tr}\{\hat{\mathcal{O}}e^{-\beta\hat{H}_d}\} = \mathrm{Tr}\{S^*\mathcal{O}SE\} \tag{3.52}$$
$$S_{i,j} = \langle\Phi_i^d|\Psi_j^d\rangle, \quad \mathcal{O}_{i,j} = \delta_{i,j}O_i, \quad E_{i,j} = \delta_{i,j}e^{-\beta(E_i-\mu N_i)}$$

Here $S, \mathcal{O}$ and E are 16×16 matrices, where $\mathcal{O}$ and E contain only diagonal entries. For all non-commuting observables investigated in this work a localized basis is well suited for $\{|\Phi_i^d\rangle\}$. The two-site basis vectors can be constructed from a tensor product of single-site states $\{|\Phi_i^{l(r)}\rangle\}$ on the left and right well respectively

$$|\Phi_i^d\rangle = |\Phi_m^l\rangle \otimes |\Phi_n^r\rangle, \qquad m,n = 1,2,3,4 \quad i = 4(m-1)+n \tag{3.53}$$
$$\{|\Phi_m^{l(r)}\rangle\} = \{|0\rangle, |\uparrow\rangle, |\downarrow\rangle, |\uparrow\downarrow\rangle\}. \tag{3.54}$$

In this notation $|\Phi_8\rangle = |\uparrow,\uparrow\downarrow\rangle$ for example, where the first (second) entry denotes the left (right) site. The projection of the eigenvectors of $\hat{H}_d$ shown in Tab. 3.3 onto the basis $\{|\Phi_i^d\rangle\}$ then gives the entries for S. The observable matrix D for the double occupancy probability per site (here written for the left site) is for example given by

$$D = \mathrm{diag}(\underbrace{0,...,0}_{12},1,1,1,1). \tag{3.55}$$

3.4.2. Series expansion technique

In this section we couple the dimers perturbatively and evaluate the second order high-temperature series expression for the grand potential. The calculation is in principle anal-

ogous to the strategy presented in 3.3.1, with two important differences: the number of relevant states is increased from 4 per site to 16 per dimer. In addition, the tunnelling operator is no longer diagonal in the atomic basis of isolated particles (as the case for the simple cubic lattice). These two points significantly increase the number of terms in the calculation. The development of a suitable automatic evaluation hence becomes necessary, which will be outlined in the following.

We begin with the graph expression for the grand potential per dimer, similar to Eq. 3.36

$$-\beta\Omega^d = \log z_0^d + \frac{(\beta t_y)^2}{(z_0^d)^2}\sum_g c_g X_g, \tag{3.56}$$

where the single dimer partition function is denoted by z_0^d. For simplicity we choose an explicit expansion in βt_y here, such that the tunnelling ratios t_z/t_y and t_w/t_y appear in the weak lattice constants of the graphs. The expression for the graph weights X_g is the same as in Eq. 3.32. Since in second order only two tunnelling operations are present – which after application need to lead back to the same initial state – always two dimers are coupled to each other. These two dimers are indicated by the upper and lower dimer in the graphs. All contributing graphs with their weak lattice constant are shown in Tab. 3.4.

graph	weak lattice constant	graph	weak lattice constant
	$(\frac{t_z}{t_y})^2$		$1+\frac{1}{2}(\frac{t_w}{t_y})^2$
	$(\frac{t_z}{t_y})^2$		$1+\frac{1}{2}(\frac{t_w}{t_y})^2$
	$(\frac{t_z}{t_y})^2$		

TABLE 3.4.: **High-temperature series graphs in the dimerized lattice** Summary of all graphs contributing to the partition function in second order for a Fermi-Hubbard model on a dimerized cubic lattice. The weak lattice constants contain ratios of tunnellings, as the tunnel coupling is in general different for all directions. The upper and lower bubble denotes the upper and lower dimer, each consisting of two neighbouring sites. The solid lines represent the tunnel coupling.

The number of graphs can be reduced by exploiting the symmetry between the two sites of a dimer (no bias energy offset)

The value for the graph weight X_g is evaluated in an unperturbed double-dimer basis, which is constructed from a tensor product of single dimer eigenstates $\{|\Psi^u\rangle\}$ and $\{|\Psi^l\rangle\}$ of the upper and lower dimer

$$\begin{aligned} &\text{  } = |\Psi^u,\Psi^l\rangle = |\Psi^u\rangle\otimes|\Psi^l\rangle \\ &\hat{H}_0|\Psi^{u,l}\rangle = E^{u,l}|\Psi^{u,l}\rangle \quad \hat{N}|\Psi^{u,l}\rangle = N^{u,l}|\Psi^{u,l}\rangle. \end{aligned} \tag{3.58}$$

This gives in total 16^2 basis vectors. By introducing another "intermediate" double-dimer basis $|\widetilde{\Psi}^u,\widetilde{\Psi}^l\rangle$ with eigenenergies $\widetilde{E}^{u,l}$, the integral and matrix element part in the generic

expression for the graph weight can be recast into a more convenient form

$$\begin{aligned} X_g &= \frac{1}{\beta^2} \sum_{\substack{|\Psi^u,\Psi^l\rangle, \\ |\widetilde{\Psi}^u,\widetilde{\Psi}^l\rangle}} \int_0^\beta \mathrm{d}\tau_1 \int_0^{\tau_1} \mathrm{d}\tau_2 \\ & e^{(\tau_1-\tau_2+\beta)(E^u+E^l)} e^{\beta\mu(N^u+N^l)} e^{(\tau_2-\tau_1)(\widetilde{E}^u+\widetilde{E}^l)} \times \\ & \langle \Psi^u,\Psi^l|\hat{T}_g|\widetilde{\Psi}^u,\widetilde{\Psi}^l\rangle\langle\widetilde{\Psi}^u,\widetilde{\Psi}^l|\hat{T}_g|\Psi^u,\Psi^l\rangle. \end{aligned} \tag{3.59}$$

Here the tunnelling operator $\hat{T}_g$ is taken along the bonds of the corresponding graph, see Tab. 3.4. All terms are now grouped by introducing the Hadamard product[3] of an energy weight matrix W and a tunnelling matrix T_g and summing over all entries

$$X_g = \sum_{i,j} (W \circ T_g^* \circ T_g)_{i,j}. \tag{3.60}$$

The entries of the $16^2 \times 16^2$ energy weight and tunnelling matrix are determined by the matrix elements in the two double-dimer bases $|\Psi^u,\Psi^l\rangle$ and $|\widetilde{\Psi}^u,\widetilde{\Psi}^l\rangle$. Using the abbreviations $\widetilde{E} = \widetilde{E}^u + \widetilde{E}^l$ and $E = E^u + E^l$ the expressions are (see also Eq. 3.34)

$$(W)_{i,j} = e^{-\beta E} e^{\beta\mu(N^u+N^l)} \begin{cases} \frac{1}{\beta(\widetilde{E}-E)} + \frac{e^{-\beta(\widetilde{E}-E)}-1}{\beta^2(\widetilde{E}-E)^2} & \text{if} \quad E \neq \widetilde{E} \\ \frac{1}{2} \quad \text{if} \quad E = \widetilde{E} \end{cases} \tag{3.61}$$

$$(T_g)_{i,j} = \langle \widetilde{\Psi}^u,\widetilde{\Psi}^l|\hat{T}_g|\Psi^u,\Psi^l\rangle \tag{3.62}$$

A suitable evaluation of the tunnelling matrix can be done using a basis transformation to localized states $\{|\Phi^{loc}\rangle\}$, similar to the method in the previous section. The localized basis is defined as a tensor product of states on the four isolated sites corresponding to the left and right site of the lower and upper dimer. Using the transformation matrix S between the double-well eigenstates and isolated states, see Eq. 3.52, the tunnelling matrix can then be written as

$$\begin{aligned} T_g &= (S \otimes S)^{-1} T_g^{loc} (S \otimes S) \\ (T_g^{loc})_{i,j} &= \langle \Phi^{loc}|\hat{T}_g|\Phi^{loc}\rangle. \end{aligned} \tag{3.63}$$

Here $S \otimes S$ denotes the Kronecker product of two matrices. The tunnelling operator in the localized basis T_g^{loc} for each graph can be efficiently constructed from single site creation and annihilation matrix representations and subsequent multiple Kronecker products. At this point careful attention has to be paid to the appearance of possible fermion minus signs in the matrix elements. For all graphs with double lines, see Tab. 3.4, this never occurs, since the second tunnelling operator exactly reverses the tunnelling process of the first operator and acts on the same particle. For the graph with single lines this is no longer the case and the tunnelling matrix minus signs need to be included manually.

The presented recipe allows the calculation of the second order correction to the grand potential, which gives access to the density and entropy via derivatives (normalized per site

[3]The Hadamard product of two matrices A and B is defined as element-wise multiplication $(A \circ B)_{i,j} = A_{i,j}B_{i,j}$.

after division by a factor of 2), see Eq. 3.28. For the correction terms of other observables $\hat{\mathcal{O}}$ defined on a dimer, the numerator and denominator traces need to be expanded separately and the total fraction re-expanded again (see section 3.3.2). For simplicity we restrict the calculation to observables, which commute with the single dimer Hamiltonian $\hat{H}_d$ and $\hat{N}$. In this case, only the contributing states have to be counted and weighted with the value of the observable. The evaluation is then analogous to the second order calculation for the grand potential, with the inclusion of a suitable observable matrix $\mathcal{O}$ into the new graph weight $X_g^{\mathcal{O}}$

$$X_g^{\mathcal{O}} = \sum_{i,j} (W \circ T_g^* \circ T_g \circ \mathcal{O})_{i,j}. \tag{3.64}$$

Using Eq. 3.40 the full expression for the thermal average of the observable $\hat{\mathcal{O}}$ in second order then reads

$$\langle \hat{\mathcal{O}} \rangle^{\text{2nd}} = \langle \hat{\mathcal{O}} \rangle^{\text{0th}} + \frac{2(\beta t_y)^2}{(z_0^d)^2} \left(\sum_g c_g X_g^{\mathcal{O}} - \frac{\langle \hat{\mathcal{O}} \rangle^{\text{0th}}}{(z_0^d)^2} \sum_g c_g X_g \right). \tag{3.65}$$

3.4.3. Results for the homogeneous dimerized lattice

In the following we briefly discuss the different possible phases for the repulsive Fermi-Hubbard model on a dimerized lattice predicted by the second order high-temperature series expansion. The behaviour of different observables is investigated to characterize and understand these phases. For the temperature regimes accessible by the series, the system contains in principle the same phases than for the cubic lattice: metallic, band-insulating and Mott-insulating. In the scanned parameter range no phase transitions occur and all phases are connected by crossovers, where all quantities change smoothly. The addition of a dimerization essentially changes the energy level structure for states on neighbouring sites. This alters the dependence of the thermodynamic quantities and can lead to surprising behaviour depending on the parameters, such as for example very low local entropies.

The number of parameters are reduced by setting all weak tunnelling links equal $t_y = t_z = t_w$ and denoting their value by t. The relevant energy scales in the system are then

- temperature T/t
- on-site interaction U/t
- dimerization t_d/t
- filling/on-site density n (or chemical potential μ/t)

For weak dimerizations the entropy per site s shows a very similar behavior on chemical potential and filling than in the cubic lattice, see Fig. 3.5a. For strong interactions and at temperatures comparable to the weak tunnelling, the half-filled system forms a Mott-insulating state with one particle per site and only a few holes and double occupancies in the system. The entropy per site is still above log2, which corresponds to the spin-entropy per site of a two component system. At the same time the amount of singlets in the lattice is very small. For very large chemical potentials the system forms a band-insulator with again a reduced compressibility.

The situation is different for strong dimerizations, see Fig. 3.5b, as the superposition states on a dimer now start to play a significant role. Due to the increased dimer tunnelling t_d the splitting $\Delta E = 4t_d^2/U$ ($U \gg t_d$) between the lower-lying singlet state (see Eq. 3.50) and the triplet states $|\uparrow,\uparrow\rangle$, $|\downarrow,\downarrow\rangle$ and $(|\uparrow,\downarrow\rangle + |\downarrow,\uparrow\rangle)/\sqrt{2}$ becomes much larger than the temperature. At half filling the number of available states hence reduces from initially four to only the singlet configuration, which is signalled by a large singlet probability accompanied by a strong reduction of the entropy per site at half-filling. The entropy increases again away from half-filling, as more configurations become available, while the singlet fraction decreases. Investigation of the density dependence on the chemical potential reveals two additional plateaus as compared to the weak dimerization case. The plateaus are located at a density of 0.5 (i.e. one particle per dimer) and 1.5 (i.e. three particles per dimer). The origin of this feature is the energy splitting of $2t_d$ between the symmetric and antisymmetric superposition state of a single particle (or equivalently three particles) located on the two neighbouring sites of a dimer. The presence of a plateau signals an incompressible phase, which in this case is a band insulator, as the splitting is a pure band effect. Additionally, the entropy dependence on filling shows the expected reduction at these densities.

For a more thorough understanding of the phases we now investigate the half-filled phase diagram as a function of interaction and temperature for a strongly dimerized lattice with $t_d/t = 10$, see Fig. 3.6. While for the cubic lattice the double occupancy shows a monotonous behaviour with increasing temperature for different interactions, this is no longer the case in the dimerized lattice. This is a direct consequence of the energy level structure of the double-well system: for small temperatures only the singlet and triplet states are seen, where the singlet state has a small admixture of a double occupancy. This causes the reduction of double occupancy with increasing temperature. For larger temperatures the higher lying double occupancy states become relevant, thus leading to a re-increase in the number of doubly occupied sites.

This can also be seen in the dependence of the entropy per site for increasing interaction at constant temperature. For high temperatures the entropy decreases - analogous to the cubic lattice - since the double occupancy states become too high in energy and are no longer thermally populated, thus reducing the number of available states. For very low temperatures however, the doubly occupied states no longer play a role and only the decreasing splitting with interaction between the singlet and triplet states remains. In this case, more states are in fact populated at constant temperature and the entropy hence increases for larger interactions. In the limit $U \gg t_d$ the splitting energy scale between the singlet and the triplet state becomes negligible compared to all other scales. The behaviour of the double occupancy and entropy then approaches the atomic-limit prediction of the cubic lattice.
The highest singlet and lowest triplet probabilities are obtained for low temperatures and low interactions. This is again a consequence of the energy-splitting between the singlet and the triplet states, which becomes larger for smaller interactions. Even at temperatures larger than the strong dimer tunnelling $T > t_d$, a strong imbalance in the singlet and triplet probabilities is observed.

The second order correction terms are expected to become important if the temperature approaches the tunnelling. While these corrections can be quite large in the cubic lattice, this is no longer the case for strongly dimerized systems. The reason is the large tunnelling energy scale on the dimer as compared to the weak tunnelling between the dimers, which

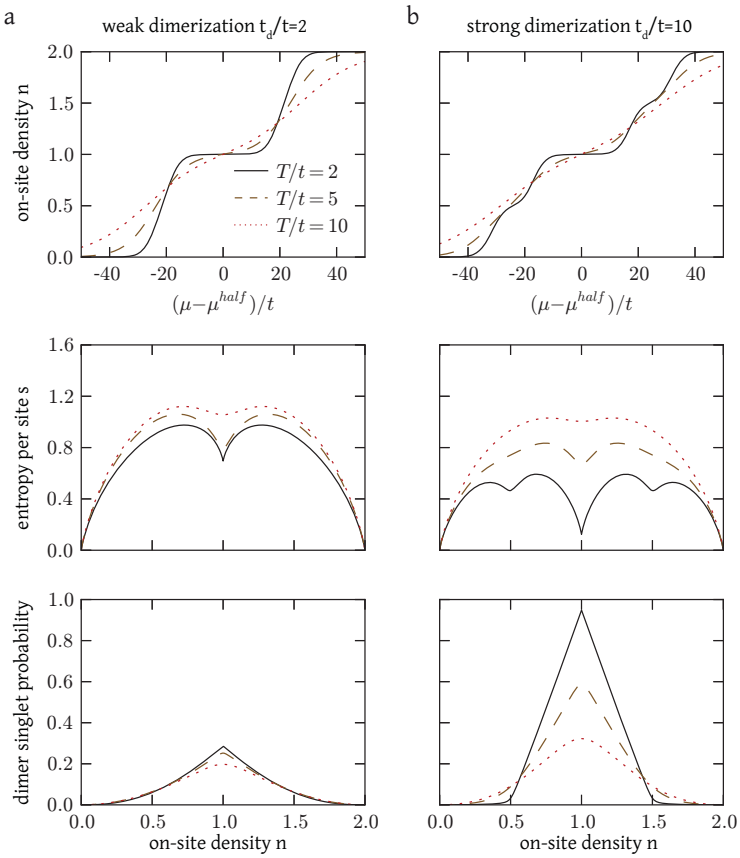

FIGURE 3.5.: **High-temperature series in the dimerized lattice** Density as a function of chemical potential (top row) and entropy per site and singlet probability versus density (bottom two rows) are shown. The dependencies are shown for three different temperatures T/t and additionally for weak (a) and strong (b) dimerizations t_d/t. The chemical potential at half filling is denoted with μ^{half}, whereas the singlet state is defined in Eq. 3.50. The interaction energy is set to $U/t = 40$ and $k_{\mathrm{B}} = 1$.

additionally increases the weight of the 0th order part of the partition function as compared to the second order correction. This leads to a small relative correction in the temperature range where the series still converges, see Fig. 3.7.

3.5. The harmonic trap and local density approximation

The effect of the harmonic trap is included in a local density approximation, which is expected to be a good approximation away from phase boundaries and if the energy scale between neighbouring sites is much smaller than all other energy offset in the homogeneous system. The harmonic confinement leads to a quadratically varying chemical potential

$$\mu(r) = \mu_0 - \frac{1}{2} m \overline{\omega}^2 (\frac{\lambda}{2})^2 r^2, \tag{3.66}$$

where $\overline{\omega}$ is the geometric mean of the trapping frequencies, μ_0 the chemical potential in the center of the trap and r the normalized distance of a site to the trap center. Any trap

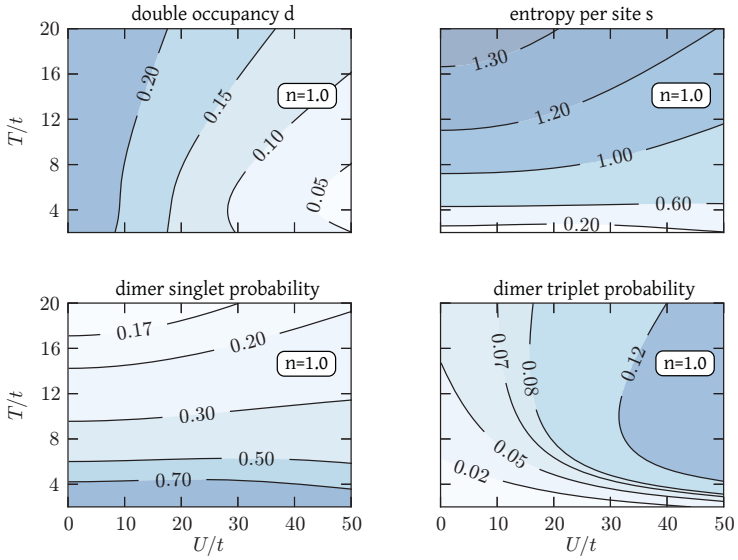

FIGURE 3.6.: **Theoretical predictions in the half-filled dimerized lattice** Double occupancy d, entropy per site s, singlet and triplet (consisting of two particles with opposite spins) probabilities versus interaction and temperature at half-filling. For each datapoint the chemical potential was determined such that the on-site density is one. The dimerization is set to $t_d/t = 10$ and $k_\mathrm{B} = 1$. The shown results are calculated in the atomic limit.

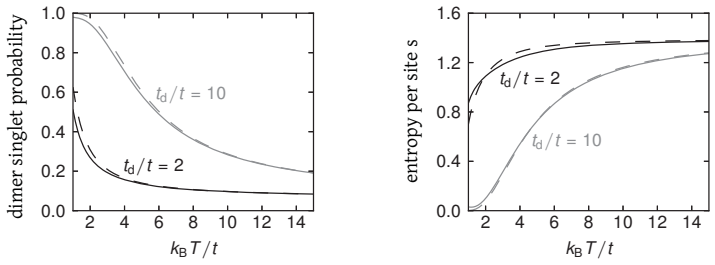

FIGURE 3.7.: **Second order corrections in the dimerized lattice** The atomic limit (dashed line) and second order high-temperature series prediction (solid line) are compared in a homogeneous dimerized lattice. The singlet probability and entropy per site are shown as a function of temperature at half-filling with an interaction $U/t = 5$.

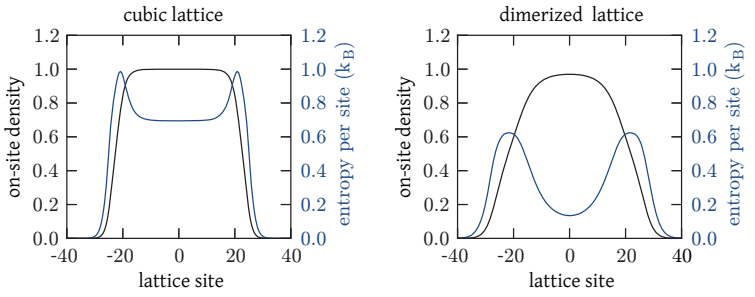

FIGURE 3.8.: **Effects of the harmonic trap** Density and entropy distribution in a trapped system for a cubic lattice with $U/6t = 6.7$ and a dimerized lattice with $U/6t = 3.3$ and $t_d/t = 30$. The geometric mean trap frequency is set to $2\pi \times 60$Hz, the atom number is $50'000$ and the average entropy per particle $S/N = 1.2k_B$. In the cubic lattice a Mott-insulator forms in the center of the trap with metallic regions around it, whereas for the dimerized case the cloud is mostly metallic due to the large dimer tunnelling energy $t_d > U$. The local entropy of the Mott-insulator is limited to log2, corresponding to the spin entropy per site for two spin components.

averaged observable $\mathcal{O}^{\text{trap}}$ is then obtained from integration of the contributions per site $\mathcal{O}^{\text{hom}}(\mu)$

$$\mathcal{O}^{\text{trap}} = \int_0^\infty 4\pi r^2 \mathcal{O}^{\text{hom}}(\mu(r))\mathrm{d}r. \tag{3.67}$$

Motivated by the experimentally accessible quantities, the usual starting point for theoretical calculations is a given atom number N and entropy per particle S/N in the entire trapped system. From these numbers the system temperature T and chemical potential μ_0 in the center of the trap are obtained by inverting the equations

$$N = \int_0^\infty 4\pi r^2 n(\mu(r), T)\mathrm{d}r$$
$$S = \int_0^\infty 4\pi r^2 s(\mu(r), T)\mathrm{d}r.$$

Fig. 3.8 compares exemplary situations for the density and entropy distribution in a cubic and dimerized lattice with harmonic confinement. In general the harmonic confinement leads to a coexistence of several different phases within the trap (for example metallic, Mott-insulating and band-insulating), which are located at different radial distances from the center and are assumed to be in global thermal equilibrium. The distribution of different phases in the trap additionally determines the entropy distribution over the cloud size and, for the case of a strongly dimerized lattice, can lead to very low local entropies in the trap center. For a given fixed total entropy per particle S/N in the entire system, the entropy is then stored in metallic excitations located in the outer parts of the density distribution.

4 The experimental apparatus

This chapter gives an overview of the experimental apparatus used for performing experiments with ultracold Fermi gases in optical lattices. Since its initial construction in 2001, the setup has continuously changed and evolved several times. In the following a very brief explanation of the preparation cycle of the quantum degenerate Fermi gas is given. More experimental details can be found in the PhD theses of T. Stöferle, H. Moritz and K. Günther [103, 104, 139].

The general setup consists of two optical tables. On the laser table the laser beams necessary for cooling, trapping, manipulating and imaging the atoms is produced, including various electronic equipment for control and stabilization of the beams. In the setup either commercial solid state and diode-lasers or home-built diode-lasers are used with external grating designs and tapered amplifiers [140]. The frequency of the lasers is stabilized via frequency modulation spectroscopy [141] or by stabilizing the beat frequency between two lasers [142]. The laser light is then guided to the experiment table via optical fibres, which also serve as spatial filters of the mode profile. On the experiment table the vacuum system with the magnetic field coils and control circuitry is installed including various beam shaping optics and intensity regulation electronics. Additionally, several imaging systems are present along all spatial directions, where the atomic distribution is imaged onto CCD cameras for final data readout.

4.1. Preparation cycle of the ultracold Fermi gases

The preparation of the ultracold fermionic quantum gas takes in total approximately 50 s. After the preparation cycle, experiments with the atomic cloud can be done for at most a few seconds, as atomic losses and heating processes (for example due to collisions with background atoms in the vacuum chamber) then start to play a significant role. In addition, the detection of the atomic gas is done via absorption imaging of a resonant laser beam, where the shadow profile is imaged onto a CCD chip of a camera. This method is destructive and leads to a loss of the entire atomic cloud. For each new experiment an entirely new atomic cloud is therefore produced, which is done repeatedly in a continuous cycle approximately every minute. The capability of reproducing the same atomic cloud in every experimental cycle is therefore of vital importance for reliable experiments. Cold atoms experiments are typically able to produce the same atomic cloud with fluctuations in atom number and temperature of around a few percent. This allows a systematic investigation of the system dependence on various parameters, which can be changed in a controlled way every experimental cycle. The entire experimental sequence is timed and controlled with a custom-made software program [103].

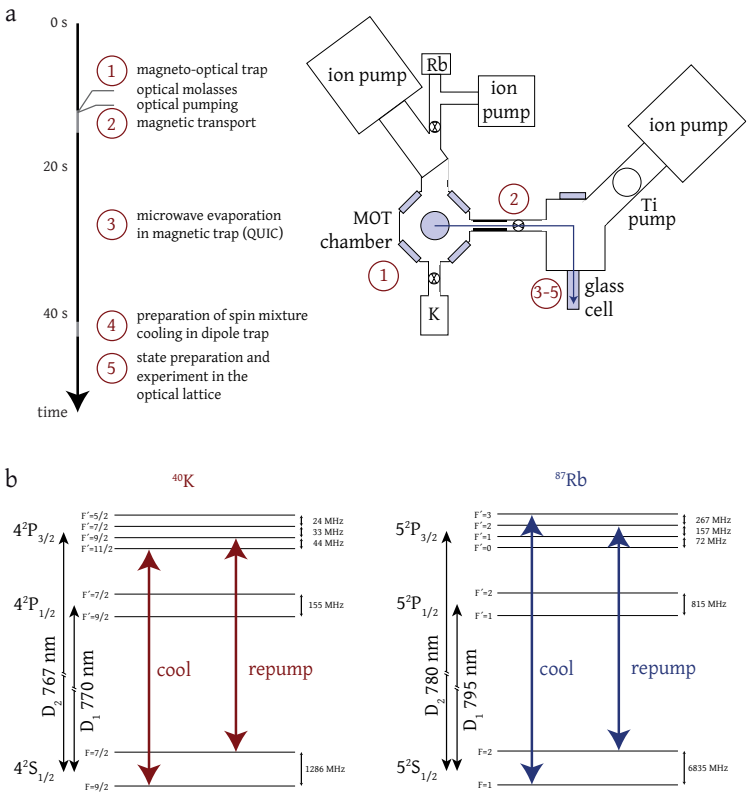

FIGURE 4.1.: **Vacuum system and atomic level schemes.** (a) Overview of the experimental cycle used to produce a quantum degenerate Fermi gas with a schematic view of the vacuum system. The sequence begins with laser cooling and trapping in the MOT chamber, followed by magnetic transport to the UHV section and finally into the glass. Here, further evaporative cooling takes place until the gas is finally loaded into the optical lattice. (b) Energy level diagram for ^{40}K and ^{87}Rb including the D_1 and D_2 transition lines. Values are taken from [143, 144]. Both the cooling and repumping lasers are red-detuned with respect to the atomic transition.

Laser cooling

An outline of the timing sequence for the experimental cycle and a schematic view of the vacuum chamber is shown in Fig. 4.1a. Each experimental cycle begins with laser cooling and trapping of both bosonic ^{87}Rb and fermionic ^{40}K in a magneto-optical trap (MOT), which is loaded for 12 s from the background pressure of around 10^{-8} mbar in the vacuum chamber. The relevant atomic level schemes including the laser cooling and repumping transitions for both elements are shown in Fig. 4.1b. The atomic sources are ampules, where the element exists in solid form and the background pressure is determined by the vapour pressure of the two elements (4×10^{-7} mbar for ^{40}K heated to 50°C and 3×10^{-7} mbar for ^{87}Rb at room temperature). The potassium sample is enriched from 0.012% natural abundancy to 14% and the entire atomic sample contains a few mg of potassium in various isotopes. The MOT allows capturing $\sim 10^9$ ^{87}Rb atoms and $\sim 10^7$ ^{40}K atoms at temperatures close to 1 mK. This first step is followed by Sub-Doppler cooling of ^{87}Rb in an optical molasses

configuration [145] and optical pumping of ^{40}K to the $|F = 9/2, m_\mathrm{F} = 9/2\rangle$ state and ^{87}Rb to the $|F = 2, m_\mathrm{F} = 2\rangle$ state. As both states are low-field seekers, both elements can be loaded into a quadrupole trap formed by two coils in anti-Helmholtz configuration.

Magnetic transport

The rather high background pressure of about 10^{-8} mbar limits the lifetime of the atomic cloud in the quadrupole trap to at most a few seconds. Although the laser cooling leads to a very large increase in phase-space density, additional cooling steps are necessary to reach quantum degeneracy. For that purpose, both atomic clouds are transported to a ultra-high vacuum (UHV) section with a pressure below 10^{-11} mbar into a glass cell, which allows convenient optical access. The MOT and the UHV pressure regions in the vacuum chamber are connected via a differential pumping tube, which allows maintaining a large pressure difference of more than three orders of magnitude. Both atomic clouds are transported via a conveyor belt of quadrupole traps, which are sequentially turned on and off to drag the gas from the MOT chamber to the glass cell [105].

Evaporative cooling

After the magnetic transport both atomic clouds are loaded into a magnetic QUIC trap [146] in the glass cell, which has a finite bias field at the trap minimum and therefore prevents Majorana spin-flips at low temperatures [147, 148]. The temperature is lowered even further by evaporative cooling of ^{87}Rb, which is performed over a duration of about 30 s. Owing to the large inter-species scattering length between ^{40}K and ^{87}Rb, both clouds are constantly in thermal contact and the ^{40}K cloud lowers its temperature as the evaporative cooling on ^{87}Rb proceeds (sympathetic cooling). This has the advantage that nearly no fermionic atoms are lost and the bosonic species serves as a cooling agent. The evaporation is achieved by continuously exposing the atoms to a microwave signal resonant to the $|F = 2, m_\mathrm{F} = 2\rangle \rightarrow |F = 1, m_\mathrm{F} = 1\rangle$ transition of ^{87}Rb, where the spin-flip frequency is exponentially decreased over time. Careful attention is paid to the removal of the parasite non-stretched states $|F = 2, m_\mathrm{F} = 1\rangle$ and $|F = 1, m_\mathrm{F} = -1\rangle$ of ^{87}Rb, which are also magnetically trappable and would lead to drastic losses of ^{40}K. This is achieved by adding corresponding microwave cleaning frequencies. Since the hyperfine splitting of both elements is different, the ^{40}K atoms are essentially unaffected by the present microwave radiation and no spin-flip transitions are driven. At the end of the evaporation the ^{87}Rb atoms are completely removed by lowering the microwave frequency through the trap bottom formed by the magnetic QUIC trap. The remaining pure fermionic gas contains about 2×10^6 atoms in the stretched $|F = 9/2, m_\mathrm{F} = 9/2\rangle$ state and is deep in the quantum degenerate regime with a temperature of $T = 0.2\ T_\mathrm{F}$, where T_F is the Fermi-temperature. Fig. 4.2 shows an overview of how the ^{40}K and ^{87}Rb change during the evaporative cooling.

Crossed beam dipole trap

Clean access to Feshbach resonances of two-component spin mixtures in purely magnetic traps is not possible, as the relevant bias field would change over the cloud size and would lead to a spatially dependent scattering length. In addition, owing to the difference in magnetic moments, the trap potential for both spin states would be slightly different. This can be

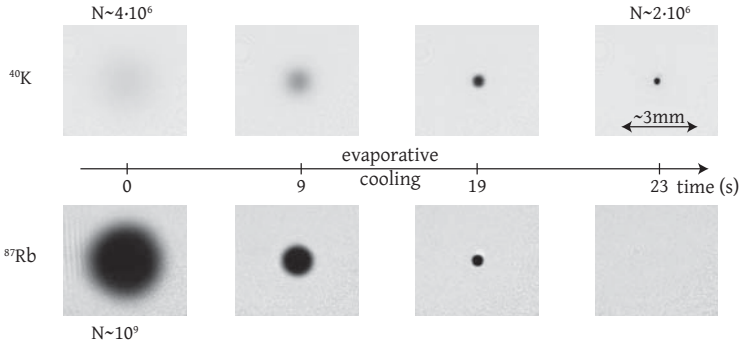

FIGURE 4.2.: **Evaporative cooling.** Absorption images at different times during the evaporation in the magnetic QUIC trap are shown for ^{40}K (top row) and ^{87}Rb (bottom row). The images were obtained after a short time-of-flight release of a few ms from the magnetic trap. As the evaporation proceeds, the ^{87}Rb cloud reduces both in temperature and atom number. At the same time the ^{40}K cloud is sympathetically cooled while only very few atoms are lost. After the evaporation and final removal of all ^{87}Rb atoms a spin-polarized Fermi gas at temperatures $T = 0.2\ T_{\mathrm{F}}$ remains.

circumvented by loading the spin-polarized fermionic gas into a crossed beam dipole trap, which creates the same harmonic potential for all spin components owing to the light-shift. The dipole trap is formed by two perpendicularly intersecting laser beams along the x and z axis (gravity along y) operating at 826.05 nm, which is red-detuned with respect to the atomic D_1 and D_2 lines. The laser light is derived from a Ti:Sa laser with an output power of 4 W. Both beams are guided via optical fibers to the experiment and have at the location of the atoms a Gaussian TEM_{00} beam profile with a horizontal beam waist ($1/e^2$ radius) of 150 μm and a vertical beam waist of 50 μm to compensate the gravitational sag. After the evaporation and removal of all ^{87}Rb atoms, the spin-polarized Fermi gas is directly loaded from the magnetic QUIC trap into the center of the Gaussian beams of the dipole trap, which creates a harmonic confinement along all directions. In the presence of a small bias field of a few Gauss the atoms are then transferred from $|F = 9/2, m_{\mathrm{F}} = 9/2\rangle$ into their magnetic ground state $|F = 9/2, m_{\mathrm{F}} = -9/2\rangle$ via a Landau-Zener sweep across the entire hyperfine manifold [149]. The offset field is then increased to about 220 G, which allows selective driving of $\Delta m_{\mathrm{F}} = \pm 1$ transitions within the $F = 9/2$ hyperfine manifold (at these magnetic fields ^{40}K is in the Zeeman to Paschen-Back crossover regime). A balanced incoherent spin mixture of $|F = 9/2, m_{\mathrm{F}} = -9/2\rangle$ and $|F = 9/2, m_{\mathrm{F}} = -7/2\rangle$ is created by driving several fast Landau-Zener transfers from $m_{\mathrm{F}} = -9/2 \rightarrow m_{\mathrm{F}} = -7/2$. Collisions and inhomogeneities of the bias field then ensure the decoherence necessary for a balanced incoherent spin mixture.

After this procedure the temperature of the gas has increased to around $T = T_{\mathrm{F}}$, mainly caused by the non-adiabatic loading from the magnetic to the dipole trap. At this point the Feshbach resonances of the $m_{\mathrm{F}} = -9/2, -7/2$ spin mixture can be exploited, see Fig. 4.3. After setting the bias field to 202.1 G, which results in a very large attractive scattering length of $a = -1700 a_0$, evaporative cooling on the fermionic spin mixture is performed to further lower the temperature. This is achieved by an exponential decrease of the dipole trap beam powers, which allows the hottest atoms to escape the trap, thus reducing the sample temperature. After a few seconds of evaporation an ultracold Fermi gas is created at

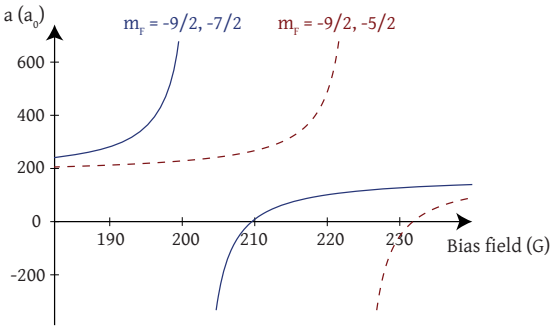

spin mixture	position B (G)	width ΔB (G)	a (a_0)
m_F = -9/2, -7/2	202.10(7)	7.5(1)	174
m_F = -9/2, -5/2	224.21(5)	7.6(1)	174

FIGURE 4.3.: **Feshbach resonance.** The two Feshbach resonances accessed in the experiment for ^{40}K in the $4^2S_{1/2}$ ground state and different spin mixtures in the $F = 9/2$ hyperfine manifold. The parameters are either taken from [150, 25] or measured in the experiment [102].

temperatures $T < 0.1\ T_F$, where the atom number can be chosen to be between 20×10^3 and 200×10^3 by adjusting the evaporation end point. After the evaporation the desired scattering length can be set by ramping the bias field to the corresponding value. Alternatively, a Landau-Zener sweep from $m_F = -7/2 \rightarrow m_F = -5/2$ can be done to create a balanced $m_F = -9/2, -5/2$ spin mixture. This configuration also has a Feshbach resonance close to 200 G, which allows setting the scattering length to large repulsive values up to $a = 600a_0$. After the preparation the ultracold Fermi gas is loaded into the tunable-geometry optical lattice.

4.2. Measurement techniques and accessible observables

4.2.1. Double occupancy

In this section the measurement of double occupancies is explained. The starting point is a two-component spin mixture of ^{40}K with $|F = 9/2, m_F = -9/2\rangle$ and $|F = 9/2, m_F = -7/2\rangle$ in a deep simple cubic lattice with lattice depths around $30 - 40E_R$. Each lattice site is either occupied by one atom of any spin or two atoms with opposite spins in the lowest band (or not occupied at all). The double occupancy is defined as the fraction of atoms residing on doubly occupied lattice sites.

The measurement protocol begins with sweeping the magnetic bias field from above across the $m_F = -9/2, -7/2$ Feshbach resonance to 201.3 G. This leads to the formation of Feshbach molecules on the doubly occupied sites. The binding energy of these molecules is around 110 kHz. At this bias field the single particle transition frequency $m_F = -7/2 \rightarrow m_F = -5/2$ is $\nu_{\text{single}} = 47.072$ MHz. Owing to the binding energy of the Feshbach molecule, the corresponding transition frequency for the case of two atoms on a site is shifted $\nu_{\text{double}} = \nu_{\text{single}} + \nu_{\text{shift}}$, with $\nu_{\text{shift}} \approx 120$ kHz. This frequency shift is the sum of the Feshbach molecule

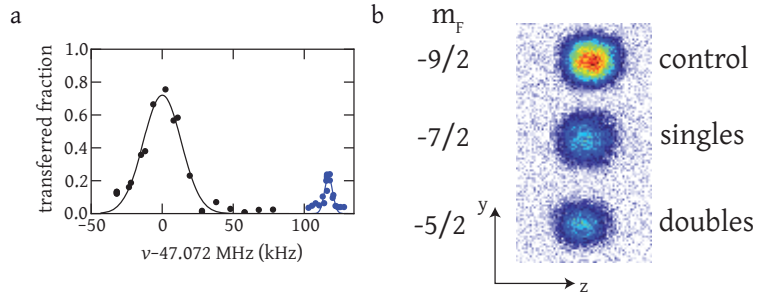

FIGURE 4.4.: **Double occupancy detection.** (a) Radio-frequency spectrum of a two-component fermionic spin mixture in a deep simple cubic lattice (image taken from [102]). The left peak corresponds to the singly occupied sites with a π pulse time of 35 μs, whereas the right peak are the doubly occupied sites with a π pulse time of 130 μs. (b) Typical absorption image obtained after the radio-frequency spectroscopy, Stern-Gerlach separation and free expansion. In this case a $m_F = -9/2, -7/2$ attractive mixture was prepared in a simple cubic lattice with a large double occupancy, which is encoded into the $m_F = -5/2$ population. The atomic distributions of each spin component are fitted with a Gaussian distribution.

binding energy and the repulsive interaction shift of about 10 kHz of the $m_F = -9/2, -5/2$ mixture at the used bias field (here the $m_F = -9/2, -5/2$ mixture is far away from its Feshbach resonance and the scattering length is weakly repulsive).

After the Feshbach molecule formation a radio-frequency π pulse is applied, where the frequency is set to ν_{double}. This converts the $m_F = -7/2$ atoms on doubly occupied sites to $m_F = -5/2$ atoms. If initially a $m_F = -9/2, -5/2$ spin mixture is prepared, the double occupancy is detected in the same way, simply with the reverse rf π pulse from the free state to the Feshbach molecule, which is subsequently dissociated. Owing to the different Franck-Condon overlaps, the π pulse takes 130 μs for the double occupancy rf transfer and 35 μs for the single occupancy transfer. Fig. 4.4a shows a comparison of the single and double occupancy transfer spectra. After the transfer, the bias field is increased again to values well above the $m_F = -9/2, -7/2$ Feshbach resonance and the lattice is subsequently ramped down within a few ms. This is followed by a removal of the optical dipole trap and the bias field, which allows a free expansion of the atoms. The population of the different spin components are detected by applying an additional magnetic field gradient for 2 ms during the initial expansion. Owing to the different Zeeman magnetic field dependencies of the spin states, this leads to different accelerations, which allows the spatial separation of the spin states after a few ms of free expansion. The atomic profiles are then recorded by shining a resonant laser beam onto the atoms and imaging the shadow profile onto a CCD camera. A typical image obtained after this procedure is shown in Fig. 4.4b. Denoting the atomic populations in the different spin states with $N^{|-9/2\rangle}$, $N^{|-7/2\rangle}$ and $N^{|-5/2\rangle}$, the double occupancy D is

$$D = \frac{2N^{|-5/2\rangle}}{N}, \tag{4.1}$$

where $N = N^{|-9/2\rangle} + N^{|-7/2\rangle} + N^{|-5/2\rangle}$ is the total atom number.

The detection efficiency of double occupancies is determined by the transfer efficiency of the radio-frequency π pulse. This is finite due to magnetic field fluctuations originating from

the current stability of the connected power supply. An additional limitation is the residual variation of the bias field over the cloud size, which is mainly created due to imperfect alignment of the bias field coils in Helmholtz configuration with respect to the precise atomic position. Both mechanisms lead to a dephasing of the Rabi-oscillations when driving the $m_F = -7/2 \rightarrow m_F = -5/2$ transition. The transfer efficiency of the π pulse, which ideally transfers all $m_F = -7/2$ on doubly occupied sites to $m_F = -5/2$ atoms, can be calibrated with two independent methods:

- Measurement of the single and double occupancy in a two-component mixture. Ideally the sum of both fractions should be one. After separately measuring the single occupancy transfer efficiency by preparing a spin-polarized cloud and detecting how many atoms are transferred, the double occupancy detection efficiency can be extracted.
- Measurement of the double occupancy from the number of associated molecules. This can be done by associating Feshbach molecules and directly releasing the gas from all confining potentials. When imaging only the single atoms are detected, whereas the Feshbach molecules are not detected as their imaging transition frequency is shifted. The difference in detected atom number with and without Feshbach molecule association then gives the double occupancy.

Using both methods a double occupancy detection efficiency of 89(2)% is found.

4.2.2. Quasi-momentum distribution

The momentum distribution of an ultracold gas in an optical lattice can be measured by abruptly turning off the lattice potential (i.e. on a timescale much faster than the tunnelling time between neighbouring sites). The Bloch eigenstates in the lattice are then projected onto free plane wave states $e^{i\mathbf{kr}}$, which then propagate during the free expansion according to their momentum $\mathbf{p} = \hbar\mathbf{k}$. After a sufficiently long free expansion the resulting density distribution then corresponds to the momentum distribution of the atoms before suddenly turning off the lattice potential.

A different situation occurs if the lattice is ramped down adiabatically with respect to the band separation energy, but still faster than the timescale for collisional processes, which would lead to a change of the quasi-momentum [42]. In this case the single-particle states follow the evolution of the eigenstates during the ramping down from Bloch states to free plane wave states. As a result of this method the quasi-momentum is mapped to real momentum. When measuring after subsequent free expansion, the density distribution then directly corresponds to the quasi-momentum distribution of the atoms in the optical lattice. Fig. 4.5 shows an exemplary case in a diagonal lattice.

4.2.3. Trap frequencies

The red-detuned crossed beam dipole trap creates a harmonic confinement for the gas, where the trap frequencies along the different directions depend on the power of the beams. Tab. 4.1 shows the measured trap frequencies for the two possible powers used for the measurements in this work. Their values were obtained by inducing a dipole oscillation of a non-interacting gas of ^{40}K [102] in the harmonic trap and measuring the momentum oscillation after free expansion of the gas.

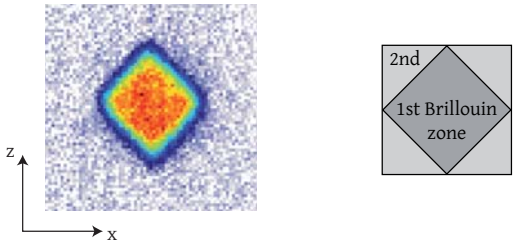

FIGURE 4.5.: **Quasi-momentum distribution.** The quasi-momentum distribution of a Fermi gas loaded into the lowest band of a diagonal lattice with $V_{\overline{X},X,Y,Z} = [0, 3, 3, 7]E_{\mathrm{R}}$ is shown using the bandmapping technique explained in the main text. As shown on the right panel, the Brillouin zone is a square rotated by 45°, see also chapter 2.3.

Owing to the finite beam waists, the red-detuned tunable-geometry optical lattice creates

$\mathrm{P}_{\mathrm{dipole}}$ (mW)	$\omega_x(1/\mathrm{s})$	$\omega_y(1/\mathrm{s})$	$\omega_z(1/\mathrm{s})$
39	$2\pi \times 28.1$	$2\pi \times 90.1$	$2\pi \times 31.6$
43	$2\pi \times 30.7$	$2\pi \times 106.0$	$2\pi \times 34.6$

TABLE 4.1.: **Dipole trap frequencies.** Summary of the trap frequencies in the red-detuned crossed beam dipole trap at 826 nm for different trap laser beam powers $\mathrm{P}_{\mathrm{dipole}}$.

an additional harmonic confinement $\omega_{\mathrm{lattice}}$ to that of the dipole trap with frequency ω_{dipole}. The total trap frequency ω_{total} along any axis is then given by the sum of the square values

$$\omega_{\mathrm{total}}^2 = \omega_{\mathrm{dipole}}^2 + \omega_{\mathrm{lattice}}^2. \tag{4.2}$$

The squared trap frequency contribution along any axis perpendicular to a single lattice beam is proportional to the lattice depth [105]. For example a lattice beam of depth V_x along the x axis creates a lattice trap frequency contribution ω_y^x along the y axis of

$$\omega_y^2 = c_y^x V_x. \tag{4.3}$$

We experimentally measure the lattice to frequency calibration slopes c by adding a single lattice beam to the harmonic trap of the dipole trap and measuring the resulting oscillation frequencies in the perpendicular directions for a non-interacting gas of ^{40}K [102]. The total trap frequency is then given by the summed square values of the trap frequency contributions from the dipole trap and the lattice. Tab. 4.2 shows a summary of all relevant calibration slopes c. If all lattice beams are turned on, the general expression for the lattice trap frequency along any axis is not just the sum of the squared lattice contributions, as the x and y lattice beam interfere. Denoting the lattice depths of all four beams with $V_{\overline{x}}$, V_x, V_y and V_z and the

direction	slope $(1/\mathrm{s}^2 E_\mathrm{R})$	direction	slope $(1/\mathrm{s}^2 E_\mathrm{R})$
c_x^y	$4\pi^2 \times 162.6$	c_y^z	$4\pi^2 \times 137.8$
c_x^z	$4\pi^2 \times 107.1$	c_z^x	$4\pi^2 \times 113.6$
c_y^x	$4\pi^2 \times 105.2$	c_z^y	$4\pi^2 \times 127.8$

TABLE 4.2.: **Lattice beam trap frequency contributions.** Calibration slopes for the contributions to the trap frequency of single lattice beams according to Eq. 4.3. Their values were obtained from dipole oscillations after turning on a single lattice beam and oscillating in perpendicular directions.

visibility with α, we obtain for the lattice trap frequencies after a brief calculation

$$\begin{aligned}
\omega_x^2 &= \left(1 + \frac{\alpha^2 V_x}{V_{\overline{x}} - V_x}\right) c_x^y V_y + c_x^z V_z \\
\omega_y^2 &= \left(1 - \frac{\alpha^2 V_x V_{\overline{x}}}{(V_{\overline{x}} - V_x)^2}\right) c_y^x V_{\overline{x}} + \frac{\alpha^2 V_y}{V_{\overline{x}} - V_x}\left(1 + \frac{V_x}{V_{\overline{x}} - V_x}\right) c_y^x V_x + c_y^z V_z \\
\omega_z^2 &= \left(1 - \frac{\alpha^2 V_x V_y}{(V_{\overline{x}} - V_x)^2}\right) c_z^x V_{\overline{x}} + \frac{\alpha^2 V_y}{V_{\overline{x}} - V_x}\left(1 + \frac{V_x}{V_{\overline{x}} - V_x}\right) c_z^x V_x + \\
&\quad \left(1 + \frac{\alpha^2 V_x}{V_{\overline{x}} - V_x}\right) c_z^y V_y
\end{aligned}$$

These expressions include the changing potential minimum of single lattice sites due to the finite beam waists. The changing zero-point energy of the lowest harmonic oscillator state originating from a change in the on-site frequency is neglected. This effect changes the trap frequency by at most a few percent as determined from an exact calculation of the trap frequency expressions from the lattice.

5 Probing nearest-neighbour correlations

The realization of ultracold fermions in optical lattices gives access to a controlled and very clean study of the Fermi-Hubbard model [29, 30]. After the recent realization of the metal to Mott-insulator transition [55, 56], reaching the low-temperature regime of quantum magnetism has been considered as one of the next major milestones on the road of *quantum simulation* of strongly correlated electron systems. In this context the realization of a sensitive lattice thermometer is of paramount importance for quantifying the approach to the antiferromagnetically ordered state. While in the weakly interacting regime the double occupancy has been shown to be well a suited quantity [95], the sensitivity reduces in the Mott-insulating regime of strong interactions. An alternative temperature dependent observable is the nearest-neighbour correlator, which is expected to show a strong dependence on temperature in the lattice owing to the additional harmonic confinement.

In this chapter we implement and study a newly developed probe for nearest-neighbour correlations of fermionic quantum gases in optical lattices, which gives access to configurations with opposite spins on adjacent sites. The correlation function is given by

$$\mathcal{P}_{i,i+1} = \sum_{\sigma} \langle n_{i,\sigma} n_{i+1,\bar{\sigma}} \left(1 - n_{i,\bar{\sigma}}\right) \left(1 - n_{i+1,\sigma}\right) \rangle, \tag{5.1}$$

where $\sigma = \{\uparrow, \downarrow\}$, $\bar{\sigma}$ are opposite spins and $i, i+1$ adjacent sites. This probe hence determines the probability of finding singly occupied neighbouring sites with opposite spins. The experimental strategy for detecting the correlator $\mathcal{P}_{i,i+1}$ relies on exciting the system by a periodic modulation of the lattice depth [78]. The corresponding modulation in kinetic energy leads to tunnelling of particles to adjacent sites. If two particles of opposite spin are located on neighbouring sites, additional double occupancies (doublons) are created as shown in Fig. 5.1. The resulting doublon production rate is sensitive on the nearest-neighbour density and spin correlator $\mathcal{P}_{i,i+1}$. In the following we describe and characterize this experimental method and show that in the perturbative regime the frequency integrated doublon production rate is given by $\mathcal{P}_{i,i+1}$ [79, 80, 81, 82]. We then use this technique to measure nearest-neighbour correlations as a function of temperature covering the regime from a paramagnetic Mott insulator to a strongly interacting metallic state. The results are in good agreement with the predictions of an *ab initio* theory without any fitting parameters. This probe opens new prospects for studying the approach to magnetically ordered phases [1].

5.1. Experimental preparation and detection

The experimental sequence used to produce a quantum degenerate Fermi gas has been described in detail in previous work [97, 95]. In brief, a balanced spin mixture of ^{40}K atoms

[1] Parts of this chapter have been published in [77].

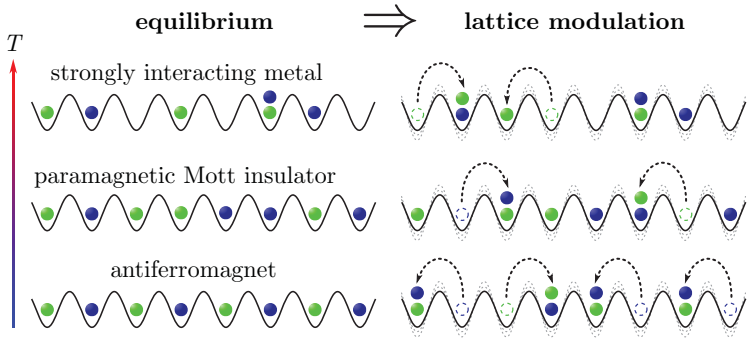

FIGURE 5.1.: Probing nearest-neighbour correlations for different phases. A periodic lattice modulation causes tunnelling of particles to neighbouring sites. The number of created doublons strongly depends on the state of the many-body system (strongly interacting metal, paramagnetic Mott insulator or antiferromagnet) and can be used to determine the nearest-neighbour correlator $\mathcal{P}_{i,i+1}$ [79].

in the $m_F = -9/2$ and $-5/2$ magnetic sublevels of the $F = 9/2$ hyperfine manifold is evaporatively cooled in an optical dipole trap. For samples of $N = 80(7) \times 10^3$ atoms we reach temperatures as low as 14% of the Fermi temperature T_F. Subsequently we ramp up a three-dimensional optical lattice of simple cubic geometry and lattice constant $d = 532\,\mathrm{nm}$. The lattice depth is increased in 0.2 s to final values of $7.0(7)\,E_\mathrm{R}$ or $10(1)\,E_\mathrm{R}$. The hopping t is inferred from Wannier functions [32] and the on-site interaction energy U is obtained from lattice modulation spectroscopy [55]. The underlying trapping potential has a mean frequency of $\omega/2\pi = 70.1(5)\,\mathrm{Hz}$ for $7\,E_\mathrm{R}$ and $\omega/2\pi = 77.3(7)\,\mathrm{Hz}$ for $10\,E_\mathrm{R}$. With this procedure we create samples where the core is in the Mott insulating regime [95].

After this preparation, the lattice depth is modulated by δV along all three axes in time τ according to $V(\tau) = V + \delta V \sin(2\pi\nu\tau)$. This results in a modulation of both the hopping and the on-site interaction with amplitudes δt and δU respectively, creating additional doubly occupied sites as compared to the initial state. The increase in the number of doublons is maximal when the modulation frequency ν coincides with the doublon energy (resonant excitation at $\nu = U/h$). After the lattice modulation, the fraction of atoms on doubly occupied sites $D = 2\sum_i \langle n_{i,\uparrow} n_{i,\downarrow}\rangle / N$ is measured by mapping doublons into a different spin state, subsequent Stern-Gerlach separation and absorption imaging [55], see section 4.2.

Fig. 5.2 (a) shows the evolution of double occupancy as a function of lattice modulation time for resonant excitation. After a steep initial rise, we observe a saturation of the induced double occupancy on a timescale on the order of the tunnelling time h/t. The saturation value depends only weakly on the modulation strength and reaches typical values of $20-30\%$. In contrast to previous work, where only this saturation regime was considered [55, 97], our high accuracy in the determination of double occupancy allows us to perform measurements in the weak excitation limit. Here we find that double occupancy increases linearly with time as shown in Fig. 5.2(b). We extract the normalized doublon production rate Γ from the slope $\Delta D/\Delta\tau$ of a linear fit to the data

$$\Gamma = \frac{h}{t}\frac{\Delta D}{\Delta \tau}. \tag{5.2}$$

On shorter timescales an underlying oscillatory response at the modulation frequency ν is observed, Fig. 5.2(c).

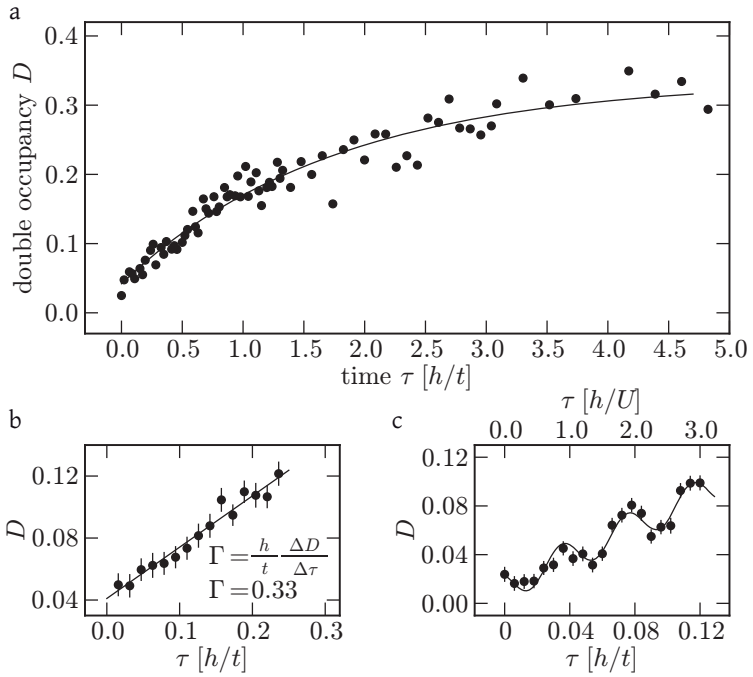

FIGURE 5.2.: Evolution of double occupancy as a function of the lattice modulation time τ for resonant excitation. The lattice depth is set to $7\,E_{\mathrm{R}}$ ($U/6t = 4.1$) and the modulation strength is $\delta V/V = 0.1$. (a) The induced double occupancy saturates for large times, which is well captured by an exponential fit (solid line). (b) At low modulation times D increases linearly, from which the doublon production rate Γ is obtained by a linear fit. The lattice depth was set to $10\,E_{\mathrm{R}}$ for this measurement ($U/6t = 10.6$). (c) On the timescale of the modulation period h/U the double occupancy shows an underlying low amplitude sinusoidal modulation. The solid line is a fit with fixed frequency U/h. For clarity, $\delta V/V$ was increased to 0.2. Error bars in double occupancy denote statistical errors from multiple measurements.

5.2. Theoretical modelling

5.2.1. Perturbation theory

The experiment can be well understood in the framework of time-dependent perturbation theory, which we outline below. The main result is that the frequency integrated doublon production rate is proportional to the nearest-neighbour correlator $\mathcal{P}_{i,i+1}$. We begin by considering a periodic modulation in time τ of the tunnelling, which originates from a periodic lattice depth modulation $V(\tau) = V_0 + \delta V \sin(\omega\tau)$. The Hamiltonian of the homogeneous system is written as

$$\begin{aligned} H(\tau) &= H_0 + W(\tau) \\ H_0 &= -tH_t + UH_U \\ W(\tau) &= -\delta t \sin(\omega\tau) H_{\mathrm{t}}. \end{aligned}$$

Here H_0 is the Fermi-Hubbard Hamiltonian [13] and the time-dependent perturbation is given by $W(\tau)$, where $\omega = 2\pi\nu$ is the modulation frequency and δt the modulation strength.

Note that in this notation the tunnelling H_t and on-site interaction H_U are dimensionless, whereas $W(\tau)$ has units of energy. The time-dependent double occupancy $p_d(t)$ is written as [2]

$$p_d(\tau) = \frac{\mathrm{Tr}\{e^{-\beta H(\tau)} H_U\}}{\mathrm{Tr}\{e^{-\beta H(\tau)}\}} = p_d^{(0)} + p_d^{(1)}(\tau) + p_d^{(2)}(\tau). \tag{5.3}$$

Here $p_d^{(0)}$ is the double occupancy without perturbation, whereas $p_d^{(1)}(\tau)$ and $p_d^{(2)}(\tau)$ are the first and second order terms in perturbation theory and are given by

$$\begin{aligned} p_d^{(1)}(\tau) &= -\frac{i}{\hbar}\int_{-\infty}^{\tau} d\tau' \langle \big[H_U^H(\tau), W^H(\tau')\big]\rangle_0 \qquad (5.4)\\ p_d^{(2)}(\tau) &= \left(\frac{i}{\hbar}\right)^2 \int_{-\infty}^{\tau} d\tau' \int_{-\infty}^{\tau'} d\tau'' \langle \big[[H_U^H(\tau), W^H(\tau')], W^H(\tau'')\big]\rangle_0. \end{aligned}$$

In this notation $\langle\hat{\mathcal{O}}\rangle_0$ denotes the unperturbed thermal average and $\hat{\mathcal{O}}^H$ the Heisenberg picture

$$\langle\hat{\mathcal{O}}\rangle_0 = \frac{\mathrm{Tr}\{e^{-\beta H_0}\hat{\mathcal{O}}\}}{\mathrm{Tr}\{e^{-\beta H_0}\}} \qquad \hat{\mathcal{O}}^H(\tau) = e^{i\frac{\tau}{\hbar}H_0}\hat{\mathcal{O}}(\tau)e^{-i\frac{\tau}{\hbar}H_0}. \tag{5.5}$$

First order response

The first order (or linear) response is proportional to the perturbation parameter δt and gives an oscillatory contribution at the modulation frequency ω. A convenient representation of the linear response is

$$p_d^{(1)}(\tau) = -\delta t \frac{t}{\hbar U}\int_{-\infty}^{\infty} d\tau' \sin(\omega\tau')\chi^{(1)}(\tau-\tau'). \tag{5.6}$$

Here we introduced the first order susceptibility $\chi^{(1)}(\tau-\tau')$, which is essentially the kinetic energy correlator

$$\chi^{(1)}(\tau-\tau') = -i\theta(\tau-\tau')\langle\big[H_t^H(\tau-\tau'), H_t^H(0)\big]\rangle_0, \tag{5.7}$$

and $\theta(\tau)$ is the Heavyside step function. From this the oscillatory response of the first order term is immediately seen using the Fourier transform $\chi^{(1)}(\omega)$ of the first order susceptibility

$$\begin{aligned} p_d^{(1)}(\tau) = &- \delta t\frac{t}{\hbar U}\mathrm{Re}\left(\chi^{(1)}(\omega)\right)\sin(\omega\tau) \qquad (5.8)\\ &\delta t\frac{t}{\hbar U}\mathrm{Im}\left(\chi^{(1)}(\omega)\right)\cos(\omega\tau). \qquad (5.9) \end{aligned}$$

Second order response

The calculation of the second order term is more tedious. After a lengthy calculation several oscillatory contributions can be identified [151]. Additionally, a term can be found, which leads to a linear increase of the double occupancy probability in time. This response is

[2] To get the double occupancy D (fraction of atoms on doubly occupied sites), this number needs to be multiplied by 2 and divided by the total atom number.

proportional to $(\delta t)^2$ and can be related to the first order susceptibility [79, 151]. The total quadratic response can then be written as

$$p_d^{(2)}(\tau) = (\delta t)^2 \left(-\frac{\omega}{2\hbar U} \mathrm{Im}(\chi^{(1)}(\omega))\tau + \text{osc.terms} \right). \tag{5.10}$$

The rate of change of the double occupancy (doublon production rate) is given by [3]

$$\frac{\Delta p_d}{\Delta \tau} = (\delta t)^2 \left(-\frac{\omega}{2\hbar U} \right) \mathrm{Im} \left(\chi^{(1)}(\omega) \right) \tag{5.11}$$

Energy absorption rate

At this point it is interesting to investigate the time-dependence of the total energy $E(\tau)$, which can be found by evaluating the expectation value of $H(\tau)$

$$E(\tau) = \frac{\mathrm{Tr}\{e^{-\beta H(\tau)} H(\tau)\}}{\mathrm{Tr}\{e^{-\beta H(\tau)}\}}. \tag{5.12}$$

A perturbative calculation up to first order leads to several oscillatory terms in the modulation frequency ω and an additional contribution increasing linearly in time. The energy absorption rate $\Delta E/\Delta\tau$ is again related to the first order susceptibility [151]

$$\frac{\Delta E}{\Delta \tau} = (\delta t)^2 \left(-\frac{\omega}{2\hbar} \right) \mathrm{Im} \left(\chi^{(1)}(\omega) \right). \tag{5.13}$$

The energy absorption is hence the same than the production rate of doublons up to factor of U

$$\frac{\Delta E}{\Delta \tau} = U \frac{\Delta p_d}{\Delta \tau}. \tag{5.14}$$

Although the calculation is done in first order of δt, the energy absorption rate scales quadratically with δt. This originates from the evaluation of the correlator $\langle [H^H(\tau), W^H(\tau)] \rangle_0$, see Eq. 5.4, where the total Hamiltonian $H^H(\tau)$ already includes the perturbation term $W^H(\tau)$.

5.2.2. Relation to nearest-neighbour correlator

In the experiment the lattice depth is periodically modulated in time. This not only leads to a modulation of the tunnelling, but also of the interaction. The total perturbation part of the Hamiltonian is then

$$W(\tau) = -\delta t \sin(\omega\tau) H_t + \delta U \sin(\omega\tau) H_U. \tag{5.15}$$

In this notation $\delta t, \delta U > 0$. Since the unperturbed Hamiltonian only depends on the ratio U/t, the modulation of both the kinetic and interaction part can be rewritten as a perturbation in the tunnelling with a rescaled amplitude $\widetilde{\delta t}$ [152, 153, 154]

$$\frac{\widetilde{\delta t}}{t} = \frac{\delta t}{t} + \frac{\delta U}{U}. \tag{5.16}$$

[3] A possible definition of this rate is $\Delta p_d/\Delta\tau = (p_d(\tau + T) - p_d(\tau))/T$, where $T = 2\pi/\omega$ is the oscillation period.

Using Eq. 5.11 the doublon production rate Γ defined in Eq. 5.2 (which counts the production rate of the fraction of atoms on doubly occupied sites normalized to the tunnelling time) then reads

$$\Gamma(\nu) = \left(\frac{\widetilde{\delta t}}{t}\right)^2 \left(\frac{-4\pi^2\nu t}{NU}\right) \mathrm{Im}\left(\chi^{(1)}(\nu)\right), \tag{5.17}$$

where the total atom number is denoted with N.

The susceptibility $\chi^{(1)}(\nu)$ hence determines the frequency-dependent excitation spectrum of the system. While there are numerous strategies for theoretical evaluation [154, 153, 80, 82, 81, 155, 156, 157, 158, 159, 160], we will use a different approach via Fermi's Golden rule, which allows an alternative representation of the doublon production [80]

$$\Gamma(\nu) = \left(\frac{\widetilde{\delta t}}{t}\right)^2 \frac{2\pi^2 t}{Nh} \sum_n \langle n|\delta H_U|n\rangle \left|\langle n|H_t|0\rangle\right|^2 \delta(\nu - \nu_{n0}). \tag{5.18}$$

Here $|0\rangle$ and $|n\rangle$ denote the unperturbed and excited states of H_0, $h\nu_{n0}$ is their energy difference and δH_U counts the number of additionally created doublons. While a full evaluation of the spectral function seems too complicated, information can be extracted from the normalized frequency integrated response R

$$R = \frac{h}{U}\int \mathrm{d}\nu\Gamma(\nu) = \left(\frac{\widetilde{\delta t}}{t}\right)^2 \frac{2\pi^2 t}{NU} \sum_n \langle n|\delta H_U|n\rangle \left|\langle n|H_t|0\rangle\right|^2 \tag{5.19}$$

We now evaluate the matrix elements in the atomic limit ($U \gg t$), where the eigenbasis is given by localized states. The only contributing matrix elements in Eq. 5.19 are then configurations, where two particles with opposite spins are located on neighbouring sites. The sum over the matrix elements is thus directly related to the nearest-neighbour correlator

$$z\sum_i \mathcal{P}_{i,i+1} = \sum_n \langle n|\delta H_U|n\rangle \left|\langle n|H_t|0\rangle\right|^2. \tag{5.20}$$

Here we denoted the connectivity of the lattice with z and the summation runs over all lattice sites i. The connectivity enters into the expressions as the lattice modulation is done along all three spatial axes. The frequency integrated response R can now be rewritten to

$$R = 2\pi^2 \left(\frac{\widetilde{\delta t}}{t}\right)^2 z\frac{t}{U}\mathcal{P}, \tag{5.21}$$

where $\mathcal{P} = \sum_i \mathcal{P}_{i,i+1}/N$ is the system averaged correlator. In the perturbative regime R therefore gives direct access to the nearest-neighbour correlator $\mathcal{P}$ of the unperturbed initial state.

5.3. Experimental results

We validate that the experiments are performed in the weak excitation regime by studying the scaling of R with the relative modulation amplitude $\widetilde{\delta t}/t$ [4]. We measure the doublon

[4] We use $\widetilde{\delta t}/t = -\sqrt{V/E_\mathrm{R}}\delta V/V$, which is accurate to a few percent for the lattice depths used in the experiment.

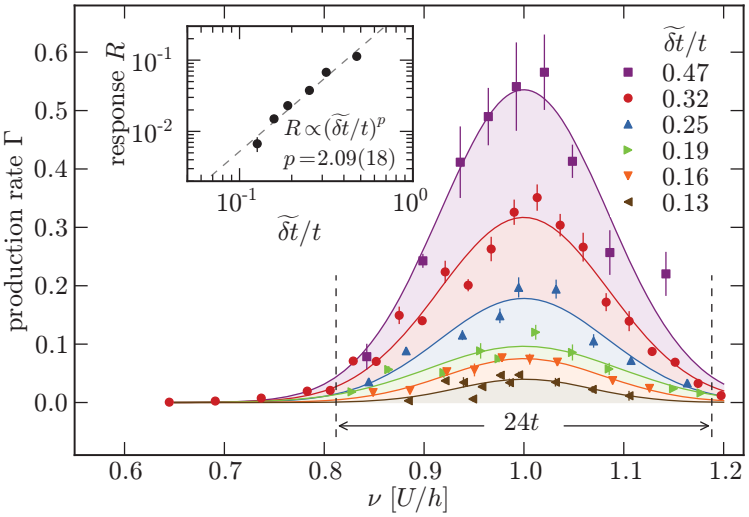

FIGURE 5.3.: Doublon production rate Γ as a function of the lattice modulation frequency ν, measured for different modulation amplitudes $\widetilde{\delta t}/t$. The experiments are performed at $U/6t = 10.6$ and $V = 10E_R$. The shaded areas are Gaussian fits to the spectra, which are used to extract the frequency integrated response R. The two vertical dashed lines denote twice the three-dimensional bandwidth $4zt$ (with $z = 6$). The inset is a double-logarithmic plot of R for various modulation amplitudes, where the dashed line is a power law fit. Error bars denote the fit errors.

production rate as a function of the modulation frequency, from which the modulation spectra in Fig. 5.3 are obtained. The frequency integrated response is then determined by a Gaussian fit to each spectrum. The result is plotted as a function of the lattice modulation amplitude $\widetilde{\delta t}/t$ (inset of Fig. 5.3). We find a scaling exponent of 2.09(18), in very good agreement with the expected value of 2 predicted by second order perturbation theory. We can thus infer the nearest-neighbour correlator $\mathcal{P}$ from the frequency integrated response.

Further information can be obtained from the lineshape of the modulation spectra, which reveals the density of states of the excitations. At half filling and temperatures well above the Néel transition, the density of states has an approximately triangular shape of full width $\sim 3zt$ [81]. However, the trapping potential is expected to broaden the spectrum and introduce deviations to the lineshape [79]. This is consistent with the experimental data, which is well captured by Gaussian fits with $1/e^2$ diameters of $4zt$. The doublon production rate on resonance shows the same scaling behaviour as the integrated response R, with a scaling exponent of 1.98(11). This allows us to determine $\mathcal{P}$ from the resonant doublon production rate alone assuming a Gaussian density of states as in Fig. 5.3 [5].

We now use doublon production rate measurements to determine the nearest-neighbour correlator $\mathcal{P}$ as a function of entropy for $U/6t = 4.1$. We prepare samples with different entropies per particle by adding a variable waiting time in the optical dipole trap of up to 2 s, which results in heating due to inelastic scattering processes. The entropy per particle s_{in} before loading into the lattice is inferred from Fermi fits to the momentum distribution

[5] We have verified this assumption by inferring the value of the nearest-neighbour correlator from the inset of Fig. 5.3, which is in good agreement with the model.

of the cloud after expansion. This is a lower bound for the specific entropy in the lattice, as non-adiabatic processes take place during the loading. An upper bound s_{out} is given by the entropy measured after reversing the loading procedure.

The nearest-neighbour correlator rapidly decreases with increasing entropy, as shown in Fig. 5.4(a). This behaviour has a simple physical interpretation: in a harmonically trapped lattice system higher temperatures lead to an increased cloud size, which results in a large number of empty sites. The probability of finding two neighbouring singly occupied sites is therefore strongly reduced. This qualitative picture is confirmed by *ab initio* calculations of the nearest-neighbour correlator using the high-temperature series expansion up to second order, see chapter 3.3.3. The nearest-neighbour correlator $\mathcal{P}_{i,i+1}$ can be directly obtained from the expressions for the density and spin correlators C_{dd} and C_{ss}

$$\mathcal{P}_{i,i+1} = \frac{C_{dd} - 4C_{ss}}{2}. \tag{5.22}$$

Owing to the harmonic confinement the trap averaged correlator $\mathcal{P} = \sum_i \mathcal{P}_{i,i+1}/N$ needs to be evaluated. This is done using a local density approximation, which is an excellent assumption in this temperature regime [161]. The system parameters are calibrated by independent methods [95]. The results of this calculation are shown in Fig. 5.4(a).

We find quantitative agreement between the measured nearest-neighbour correlator and the theoretical predictions without any fitting parameters. The theoretical entropies s corresponding to the measured values of $\mathcal{P}$ lie in between the lower and upper experimental bounds s_{in} and s_{out}. Nearest-neighbour correlation measurements thus allow us to determine entropy and temperature in the lattice for regimes where theory is still reliable and a quantitative comparison is possible. In contrast to thermometry in the optical dipole trap, the correlator $\mathcal{P}$ is a direct observable in the lattice and does not rely on adiabaticity assumptions during the loading procedure. A comparison of these two methods suggests increased heating during the loading of the lattice for colder initial temperatures.

Further insight can be obtained from the theoretical model by investigating the spatial distribution of the nearest-neighbour correlator over the trap. From the inferred entropies s we calculate the profiles shown in Fig. 5.4(b) and (c) for the parameters of our system [6]. At half filling and deep in the Mott insulating regime $\mathcal{P}_{i,i+1}$ is expected to be close to 0.5, whereas thermal excitations reduce this number in the metallic phase. This is confirmed by the values in the core of the system, with 0.44 for the coldest and 0.17 for the hottest point. The decrease in $\mathcal{P}_{i,i+1}$ thus signals the transition from a paramagnetic Mott insulator to a strongly interacting metal. As the onset of local spin correlations corresponds to an increase of $\mathcal{P}_{i,i+1}$ above 0.5, nearest-neighbour correlation measurements are a promising tool for studying the approach to the antiferromagnetic phase [74].

5.4. Conclusion

In conclusion, we have measured nearest-neighbour correlations of ultracold fermions in optical lattices by determining the response of the system to a weak lattice modulation. This observable is well suited for thermometry in the lattice and can be used to explore novel

[6] The local value of the nearest-neighbour correlator is obtained by combining the HTSE result with a local density approximation. The average over all sites then yields the values of $\mathcal{P}$ shown in Fig. 4(a).

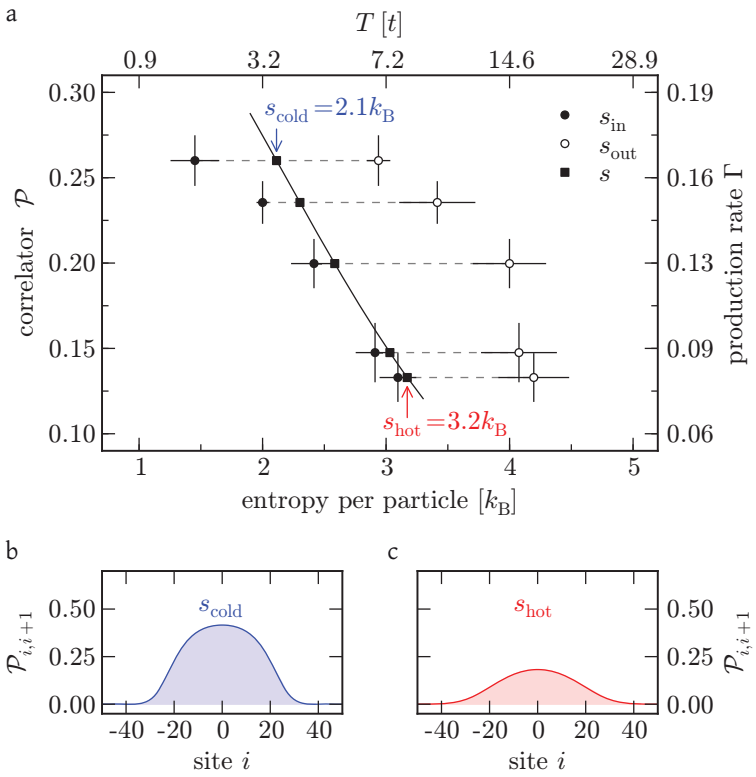

FIGURE 5.4.: Measurement of the nearest-neighbour correlator $\mathcal{P}$. (a) Dependence on entropy per particle in a trapped lattice system for $U/6t = 4.1$, $V = 7E_{\mathrm{R}}$ and $\widetilde{\delta t}/t = 0.26$. Solid and open circles denote lower and upper bounds s_{in} and s_{out} for the entropy per particle in the lattice for each measured value of $\mathcal{P}$. The black solid line is the calculated nearest-neighbour correlator obtained from second order HTSE without any fitting parameters. The entropy s inferred from comparing each measured value of $\mathcal{P}$ to theory lies in between the experimental bounds. For clarity the correspoding lattice temperatures T and measured doublon production rates Γ are also included. Error bars denote statistical errors from several measurements. (b) and (c) show the calculated distribution of $\mathcal{P}_{i,i+1}$ in the trap for the lowest and highest entropies s_{cold} and s_{hot}, while the area under these curves corresponds to the measured correlator $\mathcal{P}$.

cooling schemes [74]. The technique opens new prospects for studying the approach to the antiferromagnetic phase, since the regime between a paramagnetic Mott insulator and an antiferromagnet is governed by the formation of short-range magnetic correlations. In the future, nearest-neighbour correlation measurements might give insight into resonating valence bond ground states, where singlet correlations on neighbouring sites are expected to occur in the absence of long range ordering [162].

6 Detecting spin correlations

As the temperature of a fermionic two-component quantum gas in a simple cubic lattice with repulsive interactions is lowered and approaches the magnetic exchange energy scale, spins on neighouring sites start to align antiferromagnetically [6]. For even lower temperatures, the spin correlation length increases over several sites, until long-range antiferromagnetic order appears below a certain critical temperature. Reaching the regime of quantum magnetism for fermions, where the ordering of spins emerges in a thermalized many-body quantum state, has been a long-standing goal in the cold atoms community. In this chapter the detection technique for measuring spin correlations on neighbouring sites is presented, which is achieved by the use of the tunable-geometry optical lattice.

The detection of spin correlations on neighbouring sites relies fundamentally on the ability to coherently control and detect superposition states of two fermionic particles of opposite spin on adjacent sites. In a first step, this is done on an array of isolated double-wells, where coherent singlet-triplet oscillations (STO) are observed. The initial state contains a large number of singlets, which is prepared in a deep optical lattice by splitting sites with double-occupancies into a double-well, where each site then contains one particle. The experimental detection technique is an extension of a previously developed method used for detecting STO in bosonic systems [76]. While this is an important ingredient, the detection of spin correlations for a system prepared in thermal equilibrium requires additional steps, including a rapid lattice ramp to a detection lattice and the removal of double occupancies. These points are discussed in the second part of this chapter. The measured magnetic spin correlations in different lattice geometries are presented in chapter 7. To avoid confusion in the notation, the tunnelling is denoted with t and time is τ.

6.1. Singlet-triplet oscillations on isolated double-wells

6.1.1. Two-state picture

The tunable-geometry optical lattice offers the possibility of creating several copies of isolated double-wells using the dimerized lattice geometry. This is achieved by going to very deep lattices, where all tunnellings become negligibly small (i.e. the tunnelling times becomes on the order of the lifetime of the system, which is typically a few seconds), except for the intra-dimer tunnelling t_d. In the limit of very large on-site interactions $U \gg t_d$, only two states remain for two fermions with opposite spins on a double-well, which are the singlet $|s\rangle$

and triplet state $|t_0\rangle$, see Tab. 3.3 in chapter 3,

$$\begin{aligned} |s\rangle &= \frac{|\uparrow,\downarrow\rangle - |\downarrow,\uparrow\rangle}{\sqrt{2}} \\ |t_0\rangle &= \frac{|\uparrow,\downarrow\rangle + |\downarrow,\uparrow\rangle}{\sqrt{2}}. \end{aligned}$$

A coherent oscillation between these two states can be induced by lifting the energy degeneracy of the $|\uparrow,\downarrow\rangle$ and $|\downarrow,\uparrow\rangle$ states $E(|\downarrow,\uparrow\rangle) = E(|\uparrow,\downarrow\rangle) + 2\Delta$. The time-evolution of the two states is then (up to a global phase-factor)

$$\begin{aligned} |s\rangle(\tau) &= \frac{|\uparrow,\downarrow\rangle - |\downarrow,\uparrow\rangle\, e^{-2\pi i \frac{2\Delta}{h}\tau}}{\sqrt{2}} \\ |t_0\rangle(\tau) &= \frac{|\uparrow,\downarrow\rangle + |\downarrow,\uparrow\rangle\, e^{-2\pi i \frac{2\Delta}{h}\tau}}{\sqrt{2}}. \end{aligned}$$

The singlet state hence coherently evolves into a triplet state and the triplet state coherently evolves into a singlet state. The frequency of the singlet-triplet oscillation is determined by the energy splitting and is given by $\nu_{\mathrm{STO}} = 2\Delta/h$.

6.1.2. The tilted double-well

Eigenenergies

The above simple picture assumes a large interaction $U \gg t_d$ and an energy offset Δ much greater than the energy splitting $4t_d^2/U$ between the singlet and triplet state. In addition, doubly occupied sites are neglected, which requires $U \gg \Delta$. In the following we study the full double-well system of two fermionic particles with opposite spin (in total four states) and investigate the dependence of the singlet-triplet oscillations on the relevant system parameters. The double-well Hamiltonian is given by

$$\begin{aligned} \hat{H}_\Delta &= -t_d \sum_\sigma (\hat{c}^\dagger_{l,\sigma}\hat{c}_{r,\sigma} + \mathrm{h.c.}) + U(\hat{n}_{l,\uparrow}\hat{n}_{l,\downarrow} + \hat{n}_{r,\uparrow}\hat{n}_{r,\downarrow}) + \\ &\quad \frac{\Delta_\uparrow}{2}(\hat{n}_{l,\uparrow} - \hat{n}_{r,\uparrow}) + \frac{\Delta_\downarrow}{2}(\hat{n}_{l,\downarrow} - \hat{n}_{r,\downarrow}). \end{aligned} \tag{6.1}$$

Here $\hat{c}^\dagger_{l(r),\sigma}$ denotes the fermionic creation operator of a particle on the left (right) site of the double-well and $\sigma \in \{\uparrow,\downarrow\}$ denotes the spin. The energy offset $2\Delta = \Delta_\uparrow - \Delta_\downarrow$ is created experimentally via a magnetic field gradient. This leads to a fixed ratio of the different energy offsets for the spin states $(\Delta_\uparrow + \Delta_\downarrow)/(\Delta_\uparrow - \Delta_\downarrow) = \gamma$, which originates from the magnetic field dependence of the two Zeeman states $|\uparrow\rangle \mathrel{\widehat{=}} |\mathrm{F} = 9/2, \mathrm{m_F} = -9/2\rangle$ and $|\downarrow\rangle \mathrel{\widehat{=}} |\mathrm{F} = 9/2, \mathrm{m_F} = -7/2\rangle$. In the experiment a magnetic offset field of 221.4 G is used[1], which fixes the ratio to $\gamma = 18$. All relevant parameters U, t_d and Δ can be tuned freely in the experiment.

[1] At this offset field the Zeeman energy level dependencies are -1.40 MHz/G for the $|-9/2\rangle$ atoms and -1.25 MHz/G for the $|-7/2\rangle$ atoms.

Using the localized basis $\{|\uparrow,\downarrow\rangle, |\downarrow,\uparrow\rangle, |\uparrow\downarrow,0\rangle, |0,\uparrow\downarrow\rangle\}$ the Hamiltonian is written in matrix-form and diagonalized to obtain the energy eigenvalues and eigenvectors[2]

$$\hat{H}_\Delta = \begin{pmatrix} \Delta & 0 & -t_d & -t_d \\ 0 & -\Delta & t_d & t_d \\ -t_d & t_d & U+\gamma\Delta & 0 \\ -t_d & t_d & 0 & U-\gamma\Delta \end{pmatrix}. \tag{6.2}$$

The eigenenergies for a vanishing offset $\Delta = 0$ are shown in Fig. 6.1a. For very large interactions $U \gg t_d$ the two lowest states are the above mentioned singlet $|s\rangle$ and triplet $|t_0\rangle$ state separated by an energy $4t_d^2/U$. In this regime, the two upper states $|d\rangle$ and $|d_{\mathrm{mix}}\rangle$ have an energy offset of U as compared to the other states and both have a large double occupancy admixture $|\uparrow\downarrow,0\rangle$ and $|0,\uparrow\downarrow\rangle$. If the interaction value is lowered, the singlet state contains an increasing admixture of doubly occupied sites, whereas the high energy state $|d_{\mathrm{mix}}\rangle$ reduces its double occupancy admixture. The other two states $|t_0\rangle$ and $|d\rangle$ do not change their matrix element. For vanishing interactions the energies are determined by the symmetric and anti-symmetric state for each particle, which are separated in energy by $2t_d$.

The application of an offset energy Δ leads to a tilting of the energy levels with avoided crossings between them. A simple intuitive understanding is possible for the case $\gamma = 0$, which corresponds to the situation of opposite gradients for the two spin components, see Fig. 6.1b. For very small energy offsets, the singlet and triplet states mix and eventually change to $|\uparrow,\downarrow\rangle$ and $|\downarrow,\uparrow\rangle$ with an energy slope of $\pm\Delta$. In this regime the double occupancy admixture d_Ψ of these two states is negligible

$$d_\Psi = |\langle\uparrow\downarrow,0|\Psi\rangle|^2 + |\langle 0,\uparrow\downarrow|\Psi\rangle|^2. \tag{6.3}$$

This changes at $\Delta = U$, where the three states $|\uparrow,\downarrow\rangle$, $|\uparrow\downarrow,0\rangle$ and $|0,\uparrow\downarrow\rangle$ have the same energy and an avoided crossing occurs. At this point the double occupancy admixture of the two lowest energy states rises significantly. The width of the avoided crossing is determined by the ratio U/t_d. In the limit of very large offsets $\Delta \gg U$, all eigenstates are given by localized states with an energy of either 0 or $\pm\Delta$.

The situation is more complicated for a finite value of γ, which is the case in the experiment, see Fig. 6.1c. For small energy offsets the behaviour is similar to before and the singlet and triplet states smoothly change to $|\uparrow,\downarrow\rangle$ and $|\downarrow,\uparrow\rangle$ with an energy slope of $\pm\Delta$. Additional avoided crossings appear at $\Delta = U/(\gamma \pm 1)$, where either the two states $|\uparrow\downarrow,0\rangle$ and $|\uparrow,\downarrow\rangle$ or $|0,\uparrow\downarrow\rangle$ and $|\downarrow,\uparrow\rangle$ have the same energy. At this point the double occupancy admixture of the two lowest states rises significantly. For very large energy offsets $\Delta \gg U$ the eigenstates correspond to localized states with energy slopes of $\pm\Delta$ and $U \pm \gamma\Delta$.

Time evolution

Knowledge over the eigenenergy and eigenvector structure of the tilted double-well system simplifies the understanding of the requirements for a coherent large-amplitude singlet-triplet oscillation. The generic STO protocol is as follows:

- Preparation of the system in the lowest energy state (singlet $|s\rangle$) in the absence of an offset Δ

[2] Careful attention has to be paid to the fermion minus-sign arising from the anti-commutation relations.

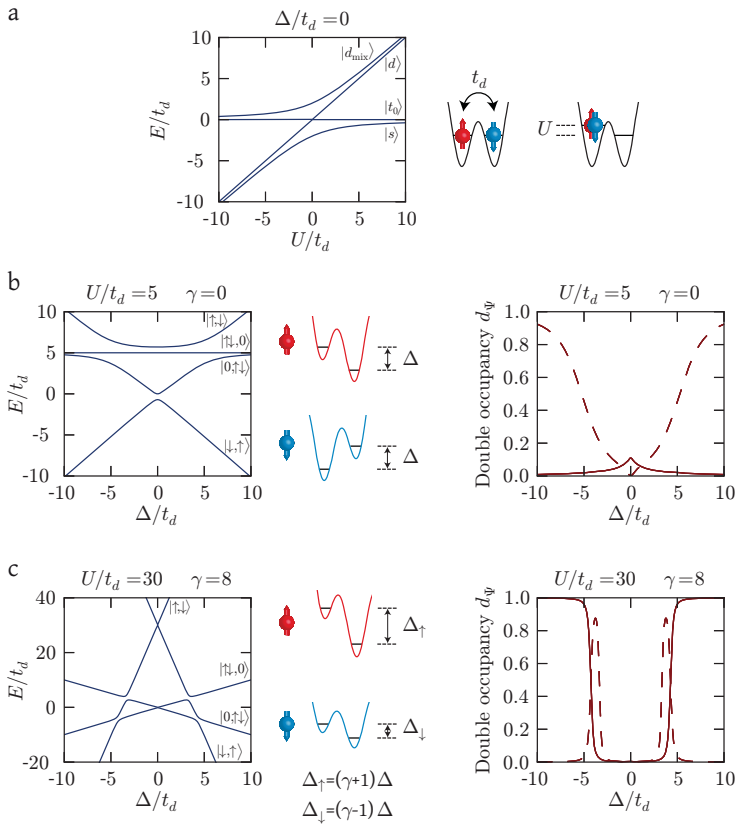

FIGURE 6.1.: **The Fermi-Hubbard model on a tilted double-well.** (a) Eigenenergies for the balanced case $\Delta = 0$ with a schematic view of the origin of the tunnelling energy t_d and on-site interaction U. For $U \gg t_d$ the splitting between the singlet and triplet state is $4t_d^2/U$. An explicit representation for all eigenstates is given in Tab. 3.3 in chapter 3. (b) Energies for the symmetrically tilted double-well, where the tilt is opposite for the two spin components. On the right panel the double occupancy overlap $d_\Psi = |\langle\uparrow\downarrow, 0|\Psi\rangle|^2 + |\langle 0, \uparrow\downarrow|\Psi\rangle|^2$ is shown for the energetically lowest (solid line) and second lowest state (dashed line). (c) Asymmetrically tilted double-well with asymmetry parameter $\gamma = 8$ and different energy offsets $\Delta_\uparrow$ and $\Delta_\downarrow$.

- Sudden application of an energy offset Δ for a variable time

- Sudden removal of the energy offset and measurement of the number of singlets and triplets

The largest amplitudes are achieved if the offset Δ is much larger than the singlet-triplet avoided crossing at $\Delta = 0$, which has an energy spacing of $4t_d^2/U$. At the same time the energy offset needs to be much smaller than the energy offset at the avoided crossing point with the higher energy states, which is located at $U/(\gamma + 1)$. Only in this regime the admixture of double occupancies remains small during the time evolution, such that the simple two-state picture for the singlet-triplet oscillation presented in the beginning of this section is valid. As explained in the following, only in this regime a reliable extraction of the singlet and triplet

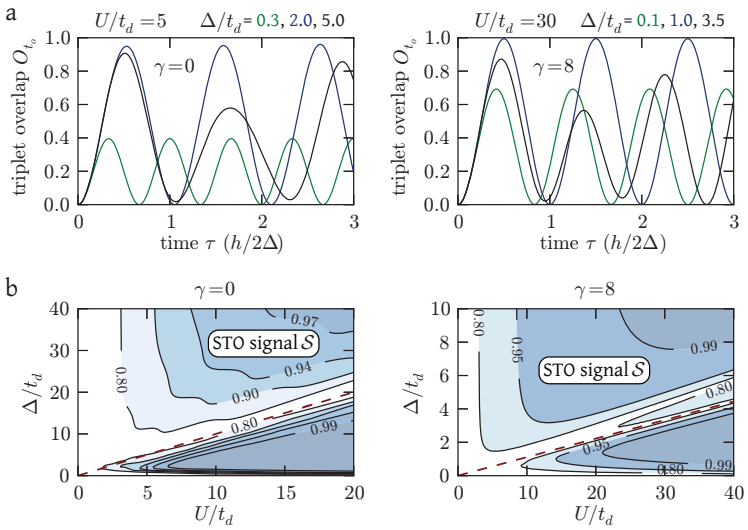

FIGURE 6.2.: **Singlet-triplet oscillation on a double-well.** (a) Overlap with triplet state t_0 after time evolution in a tilted double-well for different parameters with symmetric ($\gamma = 0$, left panel) and asymmetric tilt ($\gamma = 8$, right panel). (b) Parameter scan of the STO signal strength $\mathcal{S}$ as a function of interaction U/t_d and offset Δ/t_d, see Eq. 6.5. Values close to one correspond to a singlet-triplet oscillation with full contrast. The red dashed line depicts $\Delta = U/(1+\gamma)$ and separates the optimum region located on the bottom right, see Eq. 6.4.

populations from the singlet-triplet oscillation signal is possible:

$$\frac{4t_d^2}{U} \ll \Delta \ll \frac{U}{\gamma+1}. \tag{6.4}$$

In addition, the double occupancy admixture of the initial state should be as small as possible, since this would additionally reduce the amplitude. This requirement corresponds to $U \gg t_d$.

The above condition can be verified by performing a time evolution with the double-well Hamiltonian $\hat{H}_\Delta$ of the initially unperturbed singlet state in the presence of an offset field. After a variable time the overlaps $O_s(\tau)$ and $O_{t_0}(\tau)$ of the final state with the unperturbed singlet and triplet states are calculated according to

$$\begin{aligned} O_s(\tau) &= \left|\langle s|e^{-\frac{i}{\hbar}\hat{H}_\Delta \tau}|s\rangle\right|^2 \\ O_{t_0}(\tau) &= \left|\langle t_0|e^{-\frac{i}{\hbar}\hat{H}_\Delta \tau}|s\rangle\right|^2. \end{aligned}$$

The results are shown in Fig. 6.2a. Too small offset values lead to a strong reduction of the oscillation amplitude and additionally increase the frequency beyond $2\Delta/h$. For very large offsets close to $U/(\gamma+1)$ additional frequency components appear, which originate from the additionally present states close to the avoided crossing, see Fig. 6.1. The amplitude of the STO can be quantified by the long-term time average

$$\mathcal{S} = 2\int \mathrm{d}\tau' O_{t_0}(\tau'). \tag{6.5}$$

Values close to one corresponds to a singlet-triplet oscillation with full contrast. A scan of the STO strength for different interactions U/t_d and offset energies Δ/t_d confirms the above qualitative picture, see Fig. 6.2b. While the ideal region is given by Eq. 6.4, offset energies much larger than the critical value (red dashed line) also give high contrast oscillations. This regime is however experimentally not easily accessible, as this requires a rapid quench of the offset energy across the avoided crossings. For the spin-correlation measurements presented in chapter 7, the singlet-triplet oscillations are done at $U/t_d = 585$, $\Delta/t_d = 15$ and $\gamma = 18$, for which a STO signal strength of more than 99.8% is expected.

6.1.3. Merging adjacent sites and singlet-triplet mapping

The experimental detection of the singlet and triplet states is done by merging two adjacent sites to a single site, which essentially maps the populations into higher-band states [76], see Fig. 6.3. The basic mechanism relies on the different symmetries of the spatial wavefunction, which is symmetric for the lowest-lying singlet state $|s\rangle$ and anti-symmetric for the triplet state $|t_o\rangle$ [3]. This necessarily implies an evolution of the singlet and triplet states into states with the same symmetry of the spatial wavefunction on the merged site. For the case of a singlet, both atoms are in the lowest band in the final state, whereas one atom is in the first excited band and one in the lowest band for the case of the triplet.

- singlet $|s\rangle \rightarrow$ both atoms in lowest band
- triplet $|t_0\rangle \rightarrow$ one atom in higher band, one in lowest band

Simple model

The merging of adjacent sites is done in the experiment by reducing the lattice depth $V_{\overline{X}}$ within 10 ms to zero, while at the same time increasing the depth V_X in a way that the overall potential depth $V_{\overline{X}} + V_X$ is constant. As shown in Fig. 6.3, this removes the potential barrier between neighbouring sites on a double-well until they merge into a single site in the final state. For a Hilbert-space of two fermions with opposite spins, the full system during merging is well described by the double-well Hamiltonian in Eq. 6.1 without tilt. Even in the absence of a potential barrier, a well-defined left and right localized Wannier function can be constructed, see chapter 2.3. In this regime the spatial separation of these two states is determined by the harmonic oscillator length of the remaining site after merging. While for a detailed quantitative comparison additional terms have to be taken into account in form of an extended double-well Hamiltonian (see chapter 3.2), the important qualitative features are already well captured by the simple double-well system [60]. In brief, as the two sites are being merged, the nearest-neighbour tunnelling t_d increases dramatically, while the on-site interaction U reduces. This leads to an evolution of the energies for the singlet and triplet state, which is accompanied by a change of the states. In Fig. 6.4 a representative overview of the energies for all states during the merging is shown, starting from $U/t_d = 10^3$ and ending with $U/t_d = 10^{-3}$. The final states after merging then correspond to the states of two non-interacting particles with opposite spins in the two lowest harmonic oscillator states of the merged site, see Tab. 6.1.

[3] For bosonic atoms the opposite is the case.

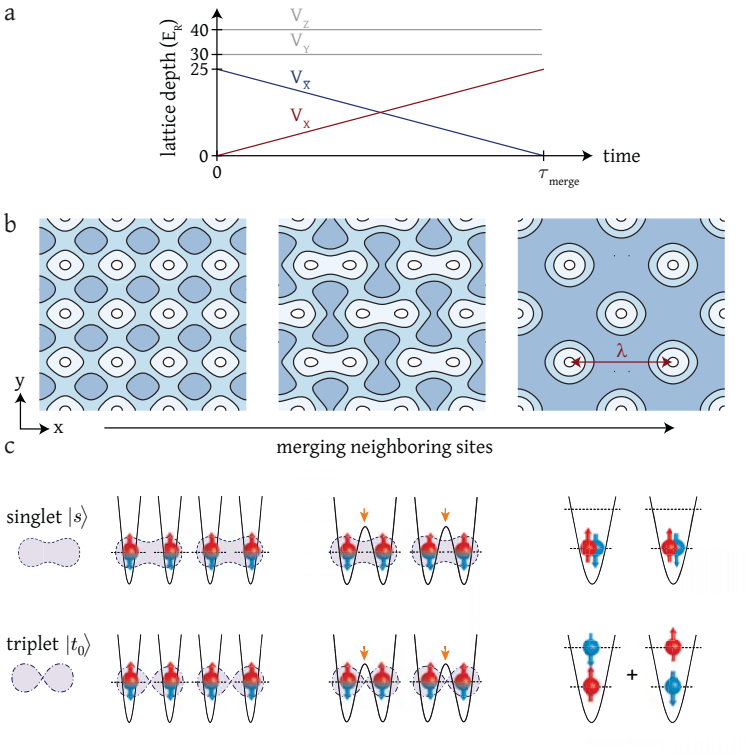

FIGURE 6.3.: **Merging neighbouring sites.** The singlet and triplet states are mapped into higher band population states by merging two adjacent sites to a single one. This is experimentally realized by ramping in $\tau_{\mathrm{merge}} = 10\,\mathrm{ms}$ the laser beam powers $V_{\overline{X}}$ and V_X, while keeping V_Y and V_Z constant (a). The corresponding potential profile is shown in (b) for $V_{\overline{X},X} = [(25,0),(23,2),(0,25)]E_{\mathrm{R}}$ from left to right. White areas denote the potential minima for the atoms. The different symmetry of the spatial wavefunction for the singlet and triplet states ensures a clean mapping into higher band states (c).

While the representation in a basis of localized states on left and right wells is well suited for the large U/t_d regime of two separated sites, the evaluation of the band occupation requires a basis change to the two lowest band Wannier states. While the general relation between these Wannier states is not easily obtained, in the limit of deep lattices they are expected to be related simply by symmetric and antisymmetric combinations

$$\begin{aligned} |\sigma,0\rangle &= \frac{1}{2}\left(\left|\sigma^l\right\rangle - \left|\sigma^h\right\rangle\right), \quad \sigma \in \{\uparrow,\downarrow\} \\ |0,\sigma\rangle &= \frac{1}{2}\left(\left|\sigma^l\right\rangle + \left|\sigma^h\right\rangle\right), \quad \sigma \in \{\uparrow,\downarrow\}. \end{aligned}$$

In this notation the state $\left|\sigma^{l,h}\right\rangle$ denotes an atom with spin $\sigma \in \{\uparrow,\downarrow\}$ in the Wannier function of the lowest band l or first excited band h. This allows rewriting the final states in terms of the higher band population, which is carried out in Tab. 6.1. Additionally, the final states can be written as a product of a spatial and spin wavefunction, where only the triplet state $|t_0\rangle$ contains an anti-symmetric spatial wavefunction with a symmetric (triplet) spin wavefunction. During the merging the triplet state is thus protected from the other three states. In fact, only the singlet $|s\rangle$ and mixed doublon $|d_{\mathrm{mix}}\rangle$ states couple during the merging,

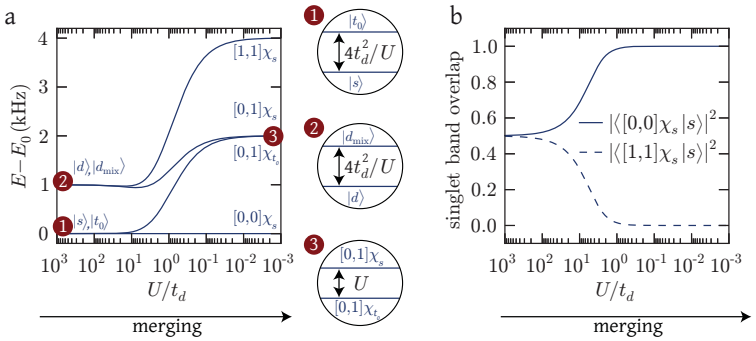

FIGURE 6.4.: **Energy eigenstates during merging.** Calculated difference of eigenenergies E as compared to the energy of the lowest eigenstate E_0 during merging for a Fermi-Hubbard model on a double-well (a). Representative values were chosen for the gradually changing interaction and tunnelling energies during merging, with initial and final values of $U/h = 1\,\mathrm{kHz}$, $t_d/h = 0.001\,\mathrm{kHz}$, and $U/h = 0.001\,\mathrm{kHz}$, $t_d/h = 1\,\mathrm{kHz}$. For large U/t_d the four states are best represented in a localized basis of left and right Wannier functions, whereas for vanishing U/t_d a band occupation basis is more suitable, see Tab. 6.1. The splitting between the energetically close states before merging is given by the exchange energy $4t_d^2/U$, while being U after merging. The spin singlet wavefunction χ_s is anti-symmetric, whereas the spin triplet χ_{t_0} is symmetric. (b) Overlap of the lowest energy state with two different band occupation states. The overlap with the other two possible states is always zero.

while neither the doublon state $|d\rangle$ nor the triplet state $|t_0\rangle$ change their representation. Rapid non-adiabatic merging thus leads to an imperfect mapping of the singlet state partially into higher band population. The timescale for this process is given by the initial value of the singlet-doublon energy splitting of about U. In the experiment this value is $U/h = 0.4\,\mathrm{ms}$, which is much smaller than the total merging time of 10 ms.

Band crossing during merging

So far the higher band states in the x-y plane where considered for the dynamics during the merging of neighbouring sites along the x-direction, whereas the lattice beam along the vertical z-axis was ignored. This is a safe assumption if the z-axis lattice direction is exactly orthogonal to the x-y plane, as the Hamiltonian then separates into two parts and the total Wannier function can be written as a product of two wavefunctions defined in the x-y plane and along the z direction

$$\begin{aligned} w_{[1_{xy},0_z]}(x,y,z) &= w_1^{x,y}(x,y)w_0^z(z) \\ w_{[0_{xy},1_z]}(x,y,z) &= w_0^{x,y}(x,y)w_1^z(z). \end{aligned}$$

In this case there is no coupling between the two coordinate sets and the higher band population from an initial triplet state appears in the x-y plane.

In the experiment the z-axis has a 90° angle deviation with the x- and y-axes of $\alpha = 3°$ and $\beta = 1.2°$ [4]. This leads to a Hamiltonian $\hat{H}_{\rm tilt}$, where the x-y plane and z-axis are weakly

[4] The 90° angle deviation between the x and y beams is measured to be 0.7°

$\|i\rangle$	final state $\|f\rangle$ localized basis	final state $\|f\rangle$ band basis	final state $\|f\rangle$ spin symmetry
$\|s\rangle$	$\frac{1}{2}(\|\uparrow,\downarrow\rangle - \|\downarrow,\uparrow\rangle + \|\uparrow\downarrow,0\rangle + \|0,\uparrow\downarrow\rangle)$	$\left\|\uparrow^l\downarrow^l\right\rangle$	$[0,0]\otimes\chi_s$
$\|t_0\rangle$	$\frac{1}{\sqrt{2}}(\|\uparrow,\downarrow\rangle + \|\downarrow,\uparrow\rangle)$	$\frac{1}{\sqrt{2}}\left(\left\|\uparrow^l\downarrow^h\right\rangle + \left\|\uparrow^h\downarrow^l\right\rangle\right)$	$[0,1]\otimes\chi_{t_0}$
$\|d\rangle$	$\frac{1}{\sqrt{2}}(\|\uparrow\downarrow,0\rangle - \|0,\uparrow\downarrow\rangle)$	$\frac{1}{\sqrt{2}}\left(\left\|\uparrow^l\downarrow^h\right\rangle - \left\|\uparrow^h\downarrow^l\right\rangle\right)$	$[0,1]\otimes\chi_s$
$\|d_{\mathrm{mix}}\rangle$	$\frac{1}{2}(-\|\uparrow,\downarrow\rangle + \|\downarrow,\uparrow\rangle + \|\uparrow\downarrow,0\rangle + \|0,\uparrow\downarrow\rangle)$	$\left\|\uparrow^h\downarrow^h\right\rangle$	$[1,1]\otimes\chi_s$

TABLE 6.1.: **Merging adjacent sites.** Initial states $|i\rangle$ and final states $|f\rangle$ before and after merging adjacent sites for the Fermi-Hubbard model on a double-well. For clarity, different representations are chosen for the final state. The lowest band is denoted with l and the first excited band with h. The band occupation of the first and second particle is denoted by $[0,0]$. The spin singlet wavefunction χ_s is anti-symmetric, such that the corresponding spatial wavefunction is symmetric, whereas the opposite is the case for the spin triplet χ_{t_0}. During merging only the singlet $|s\rangle$ and mixed doublon $|d_{\mathrm{mix}}\rangle$ change their matrix elements.

coupled by tilting of the z-axis

$$\hat{H}_{\mathrm{tilt}} = -\frac{\hbar^2}{2m}\left(\frac{d^2}{dx^2}+\frac{d^2}{dy^2}+\frac{d^2}{dz^2}\right) + V_{at}(x,y) + V_z\cos^2(k\alpha x + k\beta y + kz) \tag{6.6}$$

Here we used the two-dimensional superlattice potential $V_{at}(x,y)$ from Eq. 2.6 and assume $\alpha,\beta \ll 90°$. Due to the tilting the Wannier states $|1_{xy},0_z\rangle$ and $|0_{xy},1_z\rangle$ defined on the double-well are no longer energy eigenstates in the limit of deep lattices. Using the abbreviations

$$\begin{aligned} E_{1,0} &= \langle 1_{xy},0_z|\,\hat{H}_{\mathrm{tilt}}\,|1_{xy},0_z\rangle \\ E_{0,1} &= \langle 0_{xy},1_z|\,\hat{H}_{\mathrm{tilt}}\,|0_{xy},1_z\rangle \\ \Delta E/2 &= \langle 1_{xy},0_z|\,\hat{H}_{\mathrm{tilt}}\,|0_{xy},1_z\rangle\,, \end{aligned}$$

the system can be considered as a two-level system with the energy matrix

$$\begin{pmatrix} E_{1,0} & \Delta E/2 \\ \Delta E/2 & E_{0,1} \end{pmatrix}. \tag{6.7}$$

This leads to an avoided crossing between the two possible higher-band states in the x-y plane and the z-axis with an energy splitting of ΔE. For cubic lattices the energy splitting of the avoided crossing between higher band states along different directions is on the order of a few kHz in deep lattices and for small angles [163]. As shown in Fig. 6.5, the non-interacting energy levels of the two band states cross for the merging ramp employed in the experiment. As discussed in the following section, all higher band populations after merging are observed along the z-axis, i.e. the triplets traverse the avoided crossing adiabatically. From the merging timescale of 10 ms a splitting energy of at least 100 Hz is expected, which can be calculated exactly from the Wannier functions in the x-y plane.

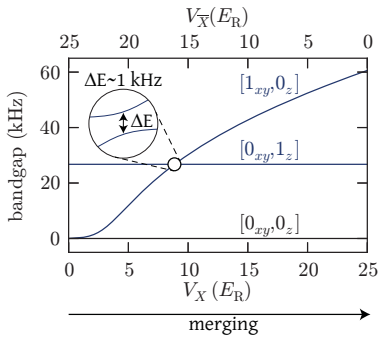

FIGURE 6.5.: **Crossing of higher-band states during merging.** Calculated band energies obtained from direct diagonalization of the untilted Hamiltonian from Eq. 6.6 in the x-y plane and z-axis ($\alpha = \beta = 0$). The notation $[0_{xy}]$ and $[1_{xy}]$ denote the lowest and first excited band state in the x-y plane. The zoom shows qualitatively the expectation for the zero-crossing.

6.1.4. Singlet-triplet oscillations

In this section measurements of singlet-triplet oscillations on isolated double-wells are presented. We prepare a large number of singlets by loading an attractively interacting gas into the merged lattice configuration (diagonal lattice, see Fig. 2.3). This leads to a large number of double occupancies, which are converted into singlets after splitting one site into two adjacent sites. In this configuration the singlet-triplet oscillations are induced with a magnetic field gradient and detected via merging of neighbouring sites.

Preparation and detection

An overview of the preparation and detection scheme is given in Fig. 6.6. A balanced $m_F = -9/2$, $m_F = -7/2$ spin mixture with approximately $100'000$ atoms is evaporatively cooled in the optical dipole trap to temperatures around $0.1\,T_F$. After setting the scattering length to $-770\,a_0$ ($B = 203.5\,\mathrm{G}$), the lattice is turned on with a spline-shaped ramp in 200 ms to a diagonal lattice configuration (symmetry phase $\theta = \pi$, interference phase $\phi = 0$). The preparation is followed by a rapid increase of the lattice depth within 500 μs, which freezes out the atomic motion and prevents further tunnelling between neighbouring sites. In this configuration double occupancies (fraction of atoms on doubly occupied sites) of $D \approx 70\%$ are achieved. After ramping the scattering length to $106\,a_0$ ($B = 221.4\,\mathrm{G}$), singlets are created by splitting sites into two neighbouring sites within 10 ms. This process is found to be adiabatic, as a direct merging returns double occupancy values within a few percent of the initial value. An energy splitting 2Δ between $|\uparrow,\downarrow\rangle$ and $|\downarrow,\uparrow\rangle$ is then applied using a magnetic field gradient, which is created by a current of a few Amperes through the right Ioffe coil. Transient effects during the switching of the coil are expected to play a small role, as the turn-on time of < 1 ms is much smaller than the typical singlet-triplet oscillation period. After a variable STO oscillation time τ_{STO}, the gradient is removed and neighbouring sites are merged. The number of singlets is obtained from the double occupancy after merging, which is measured from molecule formation and RF-spectroscopy from $m_F = -7/2$ to $m_F = -5/2$, see section 4.2. The number of triplets is detected via bandmapping, where the lattice intensities

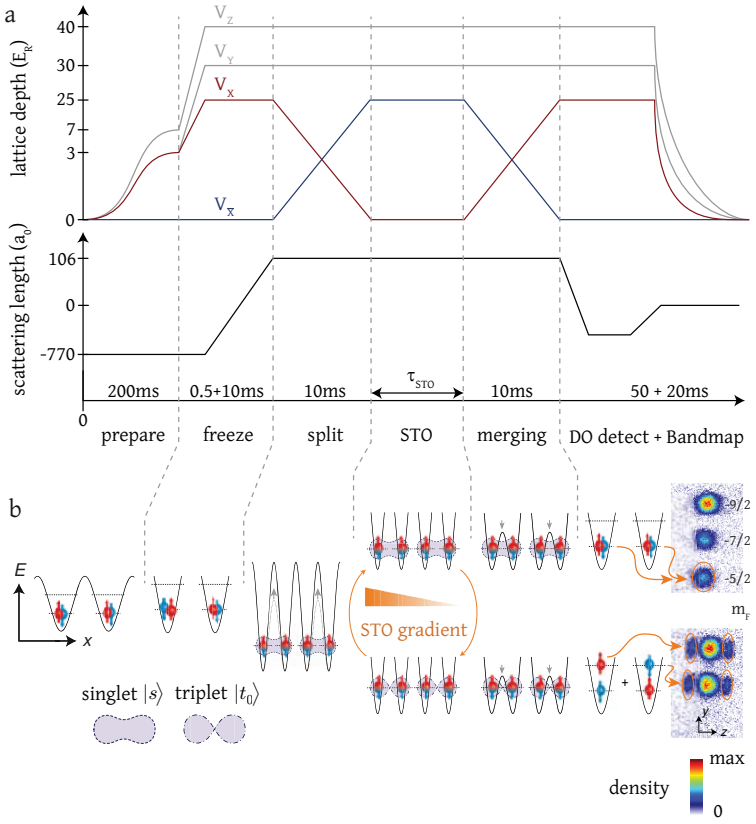

FIGURE 6.6.: **Singlet-triplet oscillation detection scheme on isolated double-wells.** (a) The various lattice and interaction ramps with the different sequence steps. A balanced $m_F = -9/2$, $m_F = -7/2$ spin mixture is initially loaded into a diagonal lattice configuration ($\theta = \pi$ and $\phi = 0$). During the STO a magnetic field gradient is applied for a variable time, which creates a differential gradient between the two spin components and causes an oscillation between the singlet and triplet states. (b) Potential cut along the spatial x-axis for the different configurations. Exemplary absorption images after time-of-flight are shown for different oscillation times with either a large number of singlets or triplets. For details on the detection of double occupancies and the band-mapping procedure, see chapter 4.2.

are ramped down exponentially within 20 ms, and subsequent time-of flight expansion for 8 ms after Stern-Gerlach separation of the spin components. For more details on these two detection techniques, see chapter 4.2.

Figure 6.7 shows an exemplary STO measurement together with three experimental absorption images corresponding to different oscillation times τ_{STO}. The double occupancy after merging η_{D} and the higher band fraction η_{HB} are extracted from such images by evaluating the lowest and first excited band population N_0 and $N_{-1} + N_1$ for each spin component from Gaussian fits and taking the fractions

$$\eta_{\mathrm{D}} = \frac{2N_0^{|-5/2\rangle}}{N_{\mathrm{total}}} \qquad \eta_{\mathrm{HB}} = \frac{2(N_{-1}^{|-9/2\rangle} + N_1^{|-9/2\rangle})}{N_{\mathrm{total}}}, \tag{6.8}$$

where we denoted the total atom number with N_{total}. The factors of two in Eq. 6.8 result

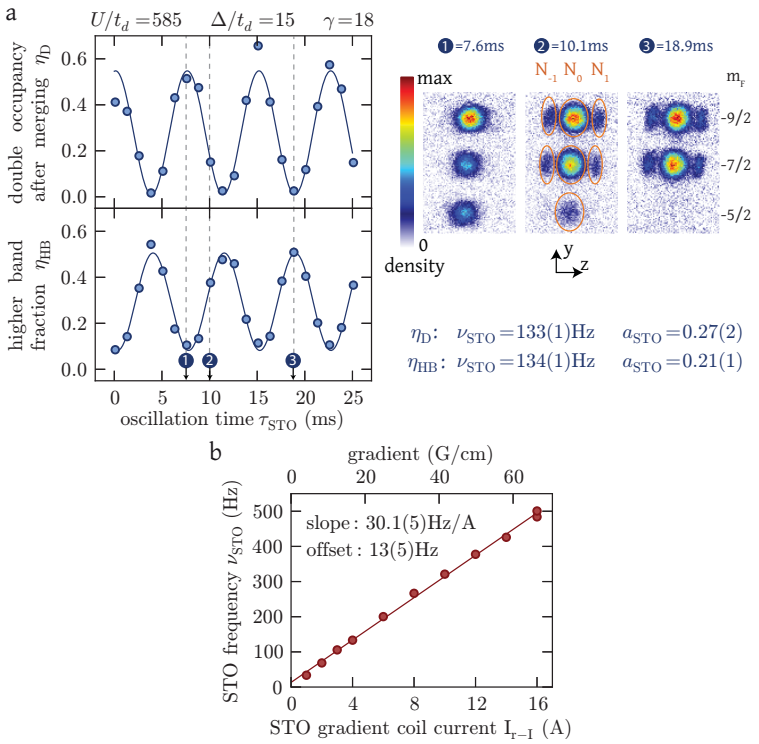

FIGURE 6.7.: **Singlet-triplet oscillations on isolated double-wells.** (a) The double occupancy after merging η_D and the higher band fraction η_{HB} are shown versus singlet-triplet oscillation time τ_{STO}. The oscillations are induced by a magnetic field gradient of 8.7 G/cm, which is created by a current of 4.0 A through the right Ioffe coil. Sinusoidal fits to the experimental data are indicated as solid lines with the fitted frequencies ν_{STO} and amplitudes a_{STO}. Absorption images after Stern-Gerlach separation and 8 ms time-of-flight expansion are shown for variable numbers of singlets and triplets. (b) Measured STO frequency for different currents through the right Ioffe coil I_{r-I}, which changes the field gradient proportionally. The slope of a linear fit is close to the expected value of 32.4 Hz/A obtained by independent calibration of the magnetic field gradient using Bloch oscillations. This calibration is also used to obtain the field gradient values on the top axis (4.2 G/cmA).

from the fact that η_D and η_{HB} denote fractions of atoms [5].

Both η_D and η_{HB} are found to oscillate with the same frequency but opposite amplitudes. The low minima values of the double-occupancy oscillation show a close to unity conversion efficiency of singlets into triplets. Additionally, the vanishing minima values confirm that no triplet states are detected as double occupancies, which is prevented by the difference in molecular binding energy after sweeping across the Feshbach resonance between the two configurations. The observed oscillations show a very high contrast of above 90% as compared to the initial number of double occupancy before splitting. Fitting a sinusoidal oscillation

[5] Due to the presence of a small residual offset field during the imaging, the atomic cross-sections slightly vary by a few percent for the different spin-components. This is taken into account by including correction factors of 1.007, 1.025 and 1.107 for $m_F = -9/2$, $-7/2$ and $-5/2$ respectively, which were obtained by scanning the imaging laser across the atomic resonance.

allows extracting the STO frequency ν_{STO}, which agrees with the expected value Δ/h corresponding to the applied magnetic field gradient. The oscillation amplitude of η_{HB} is found to be lower than η_{D}, which is probably caused by decay of higher band populations after merging adjacent sites, see section 6.1.5.

A systematic investigation of the STO frequency is done by experimentally determining the dependence of ν_{STO} on the current $I_{\mathrm{r-I}}$ through the right Ioffe coil, which proportionally changes the magnetic field gradient and thus the energy offset Δ/h. Excellent agreement is found between the measured and theoretically expected STO frequencies over a broad range, see Fig. 6.7b.

Lifetime of singlets

When investigating the long-time behaviour of the singlet-triplet oscillations, an exponential damping on a timescale of about $\tau_L = 0.2\,\mathrm{s}$ is found, see Fig. 6.8a. This finite lifetime of the singlets originates from a residual magnetic field curvature of the offset coils, which is already present even without the additional STO field gradient created by the right Ioffe coil. This curvature creates a spatially varying magnetic field gradient, which leads to a distribution of STO frequencies over the cloud size. Since the total signal observed in the experiment is the average over all double-wells in the system (which oscillate at slightly different frequencies), this leads to a dephasing on a time-scale given by the distribution of oscillation frequencies. The observed value for the dephasing time-constant translates into a magnetic field gradient distribution on the order of $\pm 100\,\mathrm{mG/cm}$ over the cloud size, which is in good agreement with a-priori calculations of the magnetic field based on the location of the bias field coils. The field curvature is a contributing limitation for the observed RF spectroscopy linewidths of a few kHz between different magnetic sublevels of the $F = 9/2$ hyperfine manifold at offset fields around 200 G.

The distribution of different field gradients causes a residual background singlet-triplet oscillation even in the absence of a STO field gradient from the right Ioffe coil (this is also the case if the gradients are evenly distributed around zero, as the STO signal does not depend on the sign of the energy offset Δ). Figure 6.8b shows an exemplary measurement, which was obtained by preparing singlets in a deep cubic lattice, allowing for a variable holding at constant offset field without additional gradients and subsequent merging. A clear singlet-triplet oscillation is observed with an oscillation time of about $T = 0.3\,\mathrm{s}$ and a decay time on the same order, which are both comparable to the background time-constant of $\tau_{\mathrm{bkg}} = 0.3\,\mathrm{s}$ in this measurement. This confirms a symmetric distribution of field gradients around zero over the cloud size along the spatial x-axis.

From the simple dephasing picture of many isolated double-wells a similar decay time-constant for the measurement without STO gradient is expected as for the long-time singlet-triplet oscillations. Furthermore, when investigating the singlet-triplet oscillation amplitude a_{STO} after a variable waiting time in the deep cubic lattice before inducing the oscillations, a decay on a similar time-scale is observed with $\tau_{\mathrm{deph}} = 0.5\,\mathrm{s}$ [6]. A further increase of the singlet lifetime in the experiment is only possible by removing the residual field curvature,

[6] The overall STO signal strengths for (a) and (b) are lower than the other STO measurements presented, as a slightly different preparation sequence was used starting from a dimerized instead of a diagonal lattice.

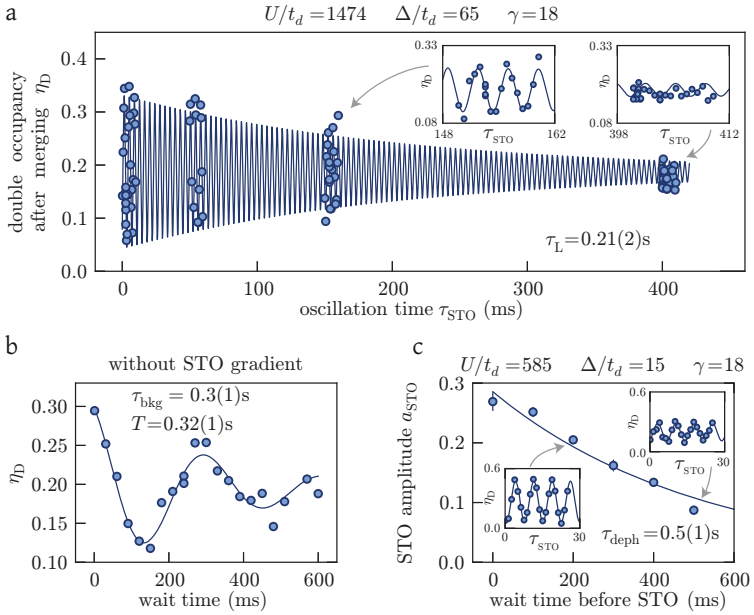

FIGURE 6.8.: **Lifetime of singlets.** (a) Singlet-triplet oscillation for very long oscillation times in a deep cubic lattice with $V_{\overline{X},Y,Z} = [30, 30, 50]E_R$ and an STO gradient of 17.4 G/cm. The solid line is an exponentially damped sinusoidal fit with a time constant τ_L. For clarity, two insets are shown with a zoom around selected times. (b) Background STO for the same parameters as in Fig. 6.7, but without any additionally applied magnetic field gradient. The oscillation is caused by the residual magnetic field curvature of the offset field at 221.4 G. This leads to a distribution of STO frequencies over the cloud, which causes a dephasing of the total signal observed as a finite lifetime of the singlets. The solid line shows an exponentially damped oscillation with matching decay time-constant τ_{bkg} and oscillation period T. (c) Singlet-triplet oscillation amplitude after a variable wait time in the lattice before starting the oscillations. The exponential decay time-constant is roughly comparable to the other decay times τ_L and τ_{bkg} as expected from the double-well dephasing picture.

either by adding additional coils or by placing the atomic cloud in the center of the Helmholtz configuration of the bias field coils.

The optical trapping potential creates an additional spatially varying energy offset between neighbouring sites, which – in contrast to the case of a magnetic field gradient – is not spin-dependent. In the regime of small applied energy offsets Δ, see Eq. 6.4, this potential offset does not play a role for the singlet-triplet oscillations, as it merely leads to an energy shift of the states $|\uparrow,\downarrow\rangle$ and $|\downarrow,\uparrow\rangle$ by the same amount. Furthermore, the spatially varying ratio U/t_d over the cloud size due to the finite beam waists of the lattice beams does not affect the visibility of the singlet triplet oscillations in this regime.

6.1.5. Additional experimental contributions

Single particle oscillations

All particles located on doubly occupied sites after loading into the diagonal lattice contribute to the singlet-triplet oscillations. Due to the underlying harmonic confinement in the system,

a certain fraction of atoms is located on singly occupied sites [164]. Similar to the case of two atoms with opposite spins on neighbouring sites, a single particle can also coherently oscillate between the two even and odd eigenstates $|+\rangle = (|\sigma,0\rangle + |0,\sigma\rangle)/\sqrt{2}$ and $(|-\rangle = |\sigma,0\rangle + |0,\sigma\rangle)/\sqrt{2}$ of a double-well when a magnetic field gradient is applied, see Tab. 3.3. Here $\sigma \in \{\uparrow,\downarrow\}$ denotes a single particle of any spin either located on the left or right site of a double-well. The time evolution of the two possible initial states $|\Psi_+(t)\rangle$ and $|\Psi_-(t)\rangle$ in the presence of a (spin-dependent) energy offset Δ_σ between adjacent sites is then

$$\begin{aligned} |\Psi_+(t)\rangle &= \frac{|\sigma,0\rangle + |0,\sigma\rangle\, e^{-2\pi i \frac{\Delta_\sigma}{h}\tau}}{\sqrt{2}} \\ |\Psi_-(t)\rangle &= \frac{|\sigma,0\rangle - |0,\sigma\rangle\, e^{-2\pi i \frac{\Delta_\sigma}{h}\tau}}{\sqrt{2}}. \end{aligned}$$

As is the case for the singlets and triplets, the detection of the even and odd single-particle states is possible by merging neighbouring sites together. While the $|+\rangle$ state remains in the lowest band, the $|-\rangle$ state is transferred into the first excited band. The even-odd oscillation frequencies $\nu_{+-}^{\uparrow}$ and $\nu_{+-}^{\downarrow}$ are found to be different from the STO frequency $\nu_{\mathrm{STO}} = 2\Delta/h$

$$\nu_{+-}^{\uparrow} = (\gamma+1)\Delta/h \tag{6.9}$$

$$\nu_{+-}^{\downarrow} = (\gamma-1)\Delta/h. \tag{6.10}$$

The single-particle oscillations should therefore be visible in the excited band fraction η_{HB} as a higher frequency component, whereas no change is expected for η_{D}. The major difference of these oscillations as compared to regular singlet-triplet oscillations is the sensitivity to the spin-independent potential energy offset between neighbouring sites, which essentially prevents a clear observation in the experiment. The potential offset is created by the harmonic trapping potential and can reach values up to $\Delta E_{\mathrm{pot}}/h = 10\,\mathrm{kHz}$ at the relevant lattice depths and densities. This causes a rapid dephasing of the even-odd oscillations on a timescale of less than $100\,\mu\mathrm{s}$, thus requiring a sufficiently strong magnetic field gradient for a clear observation of the oscillation. Additionally, the transient effects from the sudden turn-on of the current through the right Ioffe should be well below all these timescales, which is experimentally challenging and currently not feasible in the setup.

An additional requirement for the observation of an oscillation is the initial preparation of an imbalance between the odd and even single particle populations. This again turns out to be hindered by the potential offset from the harmonic trap: an even single-particle state can be created by splitting a singly occupied site in the diagonal lattice. This requires the potential energy offset between neighbouring sites to be much smaller than the even-odd energy splitting of $2t_d$ – otherwise the single particles are localized on either the left or right well after fully splitting the sites. For the relevant lattice depths the even-odd energy splitting is $2t_d/h = 5\,\mathrm{Hz}$, which is much smaller than the typical potential offset of $\Delta E_{\mathrm{pot}}/h = 10\,\mathrm{kHz}$. Therefore, only a few sites in the center of the harmonic trap contribute to the oscillation signal. An alternative route is the preparation of a thermalized gas in a dimerized lattice, which contains in thermal equilibrium a large imbalance between the even and odd states for temperatures below the even-odd energy splitting. The lattice can then be rapidly increased to a deep lattice configuration for detecting the single-particle oscillations, if the ramp time is well below the dephasing time from the potential energy offset. This approach might be experimentally possible.

Higher band tunnelling

After merging adjacent sites together a large fraction of atoms can be in the first excited band depending on the initial state. While the lattice can be considered deep for the lowest band, i.e. the nearest-neighbour tunnelling time-scale is very slow compared to the total detection time, this is no longer the case for the first excited band, as the tunnelling time is significantly faster. The delocalization of the atoms leads to two possible decay mechanism:

- elastic decay: at finite interactions two atoms in the first excited band can scatter into a state, where one atom is in the lowest band and one is the second excited band. This process is observed as a reduction in the first excited band fraction, while the total atom number remains constant. Due to energy conservation this process is only resonant for lattice depths of about $20E_{\mathrm{R}}$.

- inelastic decay: owing to the rapid higher-band tunnelling, configurations with three particles per site can be created. At large interactions and on-site densities inelastic three-body recombination [165, 166] leads to the production of high-energy molecules and single particles, which can leave the entire trapped lattice system. This process causes a reduction of the total atom number and higher-band fraction.

Both processes are found to be present in the experiment. A clear identification is possible by loading a repulsive two-component mixture into a cubic lattice and merging adjacent sites together. The system then contains a large fraction of atoms in the first excited band, which are found to decay exponentially in time. The dependence of the decay time on the lattice depth and interaction strength is shown in Fig. 6.9, where the elastic and inelastic decay processes are identified by a loss in the higher band fraction and/or the total atom number.

For a clean detection of the singlet-triplet oscillations in the experiment a suppression of these losses is desirable, as the merging of adjacent sites is followed by the double occupancy detection protocol with a duration of about 50 ms. As the detection of double occupancies requires ramps of the bias field, a reduction of the higher band decay rate can only be achieved by increasing the overall lattice depth. In the experiment a lattice depth of $V_Z = 40E_{\mathrm{R}}$ is used, where the higher band decay time is about 100 ms. Hence, the detected STO amplitude from the higher band fraction is slightly reduced as compared to the value without loss processes.

6.2. Spin correlations in thermalized systems

6.2.1. Measuring spin correlations from singlet-triplet oscillations

The singlet-triplet oscillation technique discussed in the previous chapter allows a reliable determination of spin correlations on neighbouring sites in the system. The spin correlations accessible with this method are the cloud averaged fraction of atoms forming singlets and triplets on neighbouring sites, which are present in the system before starting the oscillation. In brief, if the system contains more singlets than triplets, the maximum of the resulting STO signal corresponds to the singlet fraction p_s and the minimum to the triplet fraction p_{t_0}, where both states consist of two atoms with opposite spin. The observation of a finite STO amplitude hence directly implies an imbalance in the singlet-triplet population. The fractions p_s and p_{t_0} can be formally written as an integration over the left merging sites,

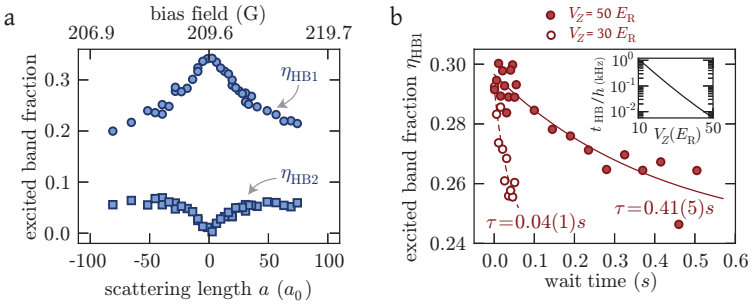

FIGURE 6.9.: **Decay of higher-band atoms.** (a) Remaining atomic fractions in the first and second excited band η_{HB1} and η_{HB2} after holding for 150 ms in a diagonal lattice with $V_{X,Y,Z} = [10, 16, 16]E_{\mathrm{R}}$ at variable s-wave scattering lengths a. In the initial state a large first excited band fraction was prepared by loading a repulsive two-component mixture into a cubic lattice and merging adjacent sites. As η_{HB1} decreases for larger interactions, η_{HB2} and the lowest band fraction (1-η_{HB1}-η_{HB2}) increase correspondingly by half the amount, whereas the total atom number remains constant. This confirms an underlying elastic decay process. For this plot the current to magnetic field calibration was shifted by $0.22A$ for the maximum/minimum to coincide with the independently measured zero-crossing of the scattering length located at 209.6 G [102]. (b) Decay of the first excited band fraction η_{HB1} at $a = -770(50)a_0$ in a deep diagonal lattice with either $V_Z = 30E_{\mathrm{R}}$ or $V_Z = 50E_{\mathrm{R}}$ (the other lattice depths are set to $30E_{\mathrm{R}}$). The preparation sequence is the same as in (a). For these parameters the elastic decay is energetically not accessible, such that the inelastic decay process remains. The total atom number (not shown) exhibits a corresponding decrease with time. The inset denotes the tunnelling matrix element in the first excited band versus the lattice depth V_Z.

which are denoted by $\mathcal{A}$, see Fig. 6.10

$$p_{\mathrm{s}} = 2\sum_{i\in\mathcal{A}} \left\langle \hat{P}_i^{\mathrm{s}} \right\rangle / N, \qquad \hat{P}_i^{\mathrm{s}} = |\Psi_i^{\mathrm{s}}\rangle \langle \Psi_i^{\mathrm{s}}| \tag{6.11}$$

$$p_{\mathrm{t_0}} = 2\sum_{i\in\mathcal{A}} \left\langle \hat{P}_i^{\mathrm{t_0}} \right\rangle / N, \qquad \hat{P}_i^{\mathrm{t_0}} = \left|\Psi_i^{\mathrm{t_0}}\right\rangle \left\langle \Psi_i^{\mathrm{t_0}}\right|. \tag{6.12}$$

The factors of two in both formulae arise because p_{s} and $p_{\mathrm{t_0}}$ measure atomic fractions. Here $\hat{P}_i^{\mathrm{s}}$ and $\hat{P}_i^{\mathrm{t_0}}$ are the projection operators on the singlet and triplet states $|\Psi_i^{\mathrm{s}}\rangle$ and $\left|\Psi_i^{\mathrm{t_0}}\right\rangle$ on neighbouring sites i and $i+1$, $\langle ...\rangle$ denotes the thermal average and N the total atom number.

Owing to the detection technique via merging of adjacent sites, the measured spin correlations do not correspond to an average over all possible neighbouring sites along all directions in the system. Instead, the experimental signal is obtained from adjacent sites along the spatial x-axis, where the entire measurement pattern of neighbouring sites is on a chequerboard. While the arrangement of the chequerboard pattern plays no role for the measurement of spin correlations in simple-cubic lattices, this is no longer the case for dimerized systems, see Fig. 6.10. In that case, the spin correlations can either be measured along the strong or weak links, which is controlled via the interference phase ϕ of the tunable-geometry optical lattice, see Eq. 2.3. For all measurements presented so far in the previous chapter 6.1, the spin correlations were determined in a deep lattice, where a large imbalance between the singlet and triplet populations was artificially prepared by first loading doubly occupied sites into a diagonal lattice and subsequently splitting the sites into two. In this case the system

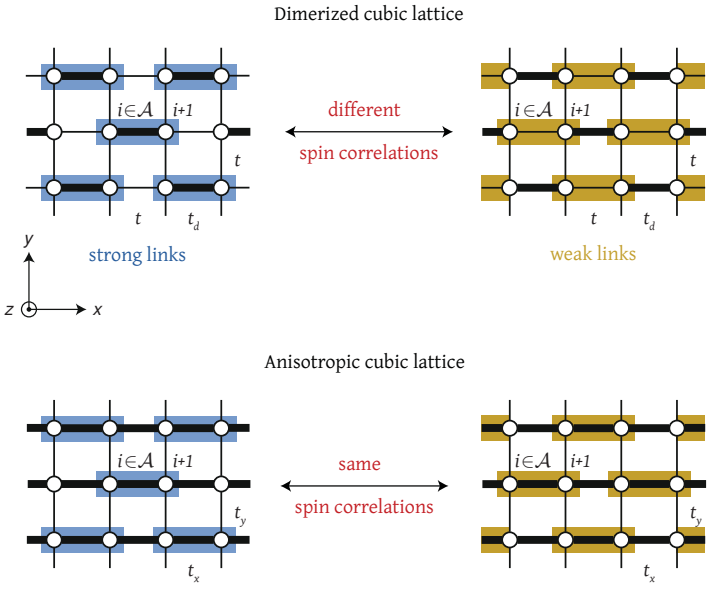

FIGURE 6.10.: **Spin correlations on neighbouring sites.** The spin correlations are detected on adjacent sites along the spatial x-direction, where the measurement links are arranged on a chequerboard pattern in the x-y plane, which reproduces along the z-direction. Different spin correlations are expected for the two possible arrangements of the measurement pattern shown in blue and yellow for the dimerized lattice. The measurement pattern configuration can be controlled via the interference phase ϕ. For the case of an anisotropic cubic lattice, both patterns are expected to give the same contributions (up to finite size effects). The left merging sites are indicated as $i \in$ A.

is far from equilibrium.

The measurement technique can also be applied to gases prepared in shallow lattices, where all relevant time-scales can be sufficiently fast such that the total system is in thermal equilibrium. For a clean detection of the spin correlations in this system, a more involved detection scheme is necessary. An overview of all steps is shown in Fig. 6.11. In short, the first step is a rapid increase of the lattice depth to a deep simple cubic detection lattice, which essentially "freezes" out the atomic motion and prevents further tunnelling of atoms to neighbouring sites. As explained in the next section, this step additionally leads to a projection of the singlet wavefunction defined on neighbouring sites, where the exact overlap between the initial and final state depends on the time-scale of the rapid lattice ramp. This is followed by a cleaning step, which removes all atoms on doubly occupied sites in order to omit additional contributions to the singlet-triplet oscillation signal. All sites then contain at most one atom and the STO measurement protocol can be applied in a last step. As neither single particles nor two particles with the same spin on adjacent sites contribute to the oscillation, the STO signal can be used to obtain the atomic fraction of singlets and triplets p_s and p_{t_0} in the initial thermalized shallow lattice system.

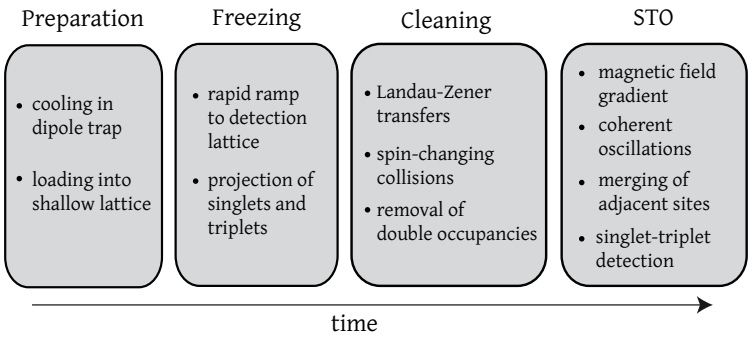

FIGURE 6.11.: **Spin correlation measurement scheme.** All relevant steps for the detection of spin correlations on neighbouring sites for a thermalized two-component spin mixture of fermionic ^{40}K loaded either into a dimerized or simple cubic lattice are shown. Details on the the freezing and cleaning can be found in the following sections, whereas the singlet-triplet oscillation (STO) technique is explained in the previous chapter 6.1.4.

6.2.2. Detection lattice ramp and projection

After loading the atoms into the optical lattice, the lattice depths are rapidly ramped within 500 μs to values of $V_{\overline{X},Y,Z} = [25, 30, 40]E_{\mathrm{R}}$, which corresponds to a deep simple cubic lattice and is denoted in the following with detection lattice (for details see chapter 7). This allows a clean detection of spin correlations, as the tunnelling time-scale between neighbouring sites is then much slower than the remaining total detection time. Depending on the parameters and time-scales, the ramp is either adiabatic, i.e. the initial singlet state follows adiabatically the two-site eigenstate, or the ramp is non-adiabatic and the singlet state is directly projected onto the singlet in the detection lattice $(|\uparrow,\downarrow\rangle - |\downarrow,\uparrow\rangle)/\sqrt{2}$.

While a full time-evolution of the many-body wavefunction is hopelessly complicated, insight into the influence of the detection lattice ramp on the state of the system can be gained by reducing the problem to a two-site basis with time-dependent tunnelling and interaction $t_d(\tau)$ and $U(\tau)$. This is a particularly good approximation for initially dimerized lattices, where the tunnelling between different double-wells is negligible such that only the dynamics within a single double-well are relevant. The time-dependence is studied by performing an exact time-evolution of the initial state and assuming a linear change of all quantities in a ramp-time τ_{ramp}. As all lattice depths are increased during the detection lattice ramp, t_d decreases and U increases in time. Within the double-well picture, an initial triplet state $|t_0\rangle$ or doublon state $|d\rangle$ remains unchanged, as their representations are independent of U/t_d, see Tab. 3.3. This is different for an initial singlet state $|s\rangle$, which couples to the mixed doublon state $|d_{\mathrm{mix}}\rangle$ as U/t_d is increased during the ramp. Figure 6.12 shows an overview for different ramp-times τ_{ramp} and initial ratios U/t_d. The adiabaticity of the ramp can be quantified by evaluating the overlaps O_s and O_d of the time-evolved final state $|\Psi_{\mathrm{final}}\rangle$ with the singlet or mixed doublon state s_{final} or d_{final} in the final U/t_d configuration according to

$$O_s = |\langle s_{\mathrm{final}}|\Psi_{\mathrm{final}}\rangle|^2 \qquad \text{and} \qquad O_d = |\langle d_{\mathrm{final}}|\Psi_{\mathrm{final}}\rangle|^2. \tag{6.13}$$

In total three different regimes can be identified. For large initial values of U/t_d the adiabaticity is independent of the total ramp-time, as the initial singlet state is already very close to the $U/t_d \gg 1$ singlet $(|\uparrow,\downarrow\rangle - |\downarrow,\uparrow\rangle)/\sqrt{2}$. In this regime there is hence no difference

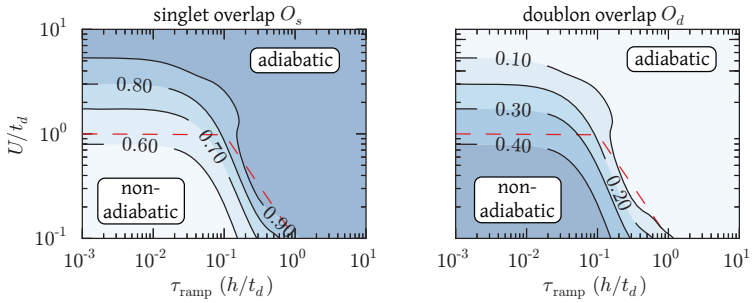

FIGURE 6.12.: **Detection lattice ramp on a double-well.** Exact time evolution of an initial singlet state on a double-well with two particles of opposite spin. The overlaps O_s and O_d (see main text) are shown for different lattice ramp-times τ_{ramp} and initial ratios U/t_d. The tunnelling t_d/h is linearly ramped from 1000 Hz to 10 Hz, whereas the interaction is increased by a factor of ten with varying start values. The ramp-time is normalized to the initial tunnelling time-scale. The red dashed line shows the qualitative expectation for the separation line between the adiabatic and non-adiabatic region (see main text).

between adiabatic and non-adiabatic ramping of the lattice. For small initial values of U/t_d the lattice ramp is only adiabatic for sufficiently long ramp-times and the singlet overlap drops significantly for very short ramp-times. In this case, the singlet representation changes significantly as U/t_d is ramped from very small to large values. The adiabaticity criterion for the ramp-time is determined by the value of the inverse tunnelling time h/t_d when the double occupancy admixture of the singlet state changes most during the ramp, i.e. at $U/t_d = 1$ (dashed red line in Fig. 6.12). Together with the border $U/t_d = 1$ this gives a good qualitative understanding of the exact results.

The detection lattice ramps used in the spin correlation experiments in the dimerized and anisotropic lattice are slightly more complicated, as both tunnelling and interaction strengths change exponentially. For most measurements in the dimerized lattice the ramp can be considered adiabatic, while being non-adiabatic for the anisotropic cubic lattice. The exact numerical values for the corresponding time evolutions on a double-well are given in chapter 7.

6.2.3. Cleaning of double occupancies

After freezing and projection the gas is located in a deep cubic lattice with lattice depths $V_{\overline{X},Y,Z} = [25, 30, 40]E_{\mathrm{R}}$. In principle, a singlet-triplet oscillation can be measured in this configuration analogously to the procedure explained in the previous section 6.1.4. As compared to the case of artificially preparing the initial state, the thermalized system contains a finite number of doubly occupied sites. As these contribute to the measured double occupancy after merging η_{D} – and thus the STO signal – a cleaning procedure was developed to remove all atoms on doubly occupied sites in the deep cubic lattice. After the cleaning procedure all sites contain at most one atom, such that a clean detection of singlet-triplet oscillations is then possible.

Atoms on doubly occupied sites are removed by spin-changing collisions, which have already been studied previously in bosonic ^{87}Rb and recently in fermionic ^{40}K to create transitions between different m_{F} states within a hyperfine manifold [167, 168, 169, 170, 171, 172]. Owing

spin mixture $\lvert m_\mathrm{F}, m'_\mathrm{F}\rangle$	spin mixture $\lvert m_\mathrm{F}, m'_\mathrm{F}\rangle$
-9/2, -7/2	-1/2, +3/2
-9/2, -5/2	+1/2, +3/2
-7/2, -5/2	+1/2, +5/2
-7/2, -3/2	+3/2, +5/2
-5/2, -3/2	+3/2, +7/2
-5/2, -1/2	+5/2, +7/2
-3/2, -1/2	+5/2, +9/2
-3/2, +1/2	+7/2, +9/2
-1/2, +1/2	

TABLE 6.2.: **Stable spin mixtures.** Summary of all two-component spin mixtures for ^{40}K in the $4S_{1/2}$ ground state and $F = 9/2$ hyperfine manifold, which are stable against spin-changing collisions at an offset field of 203.5 G (i.e. all possible inelastic collisions within the hyperfine manifold are endothermic). Spin mixtures with the same spin projection were omitted, as their s-wave scattering length is zero due to Pauli's principle.

to angular momentum conservation, two colliding particles can change their respective spin projections from $m_{\mathrm{F},1}$ and $m_{\mathrm{F},2}$ to $m'_{\mathrm{F},1}$ and $m'_{\mathrm{F},2}$ while keeping the total spin projection constant $m_{\mathrm{F},1} + m_{\mathrm{F},2} = m'_{\mathrm{F},1} + m'_{\mathrm{F},2}$. In general the collision can be either elastic or inelastic, where the collision time is determined by the overlap between the initial and final states under consideration of energy and momentum conservation. A complete list of spin mixtures, which are stable against spin-changing collisions within the $F = 9/2$ hyperfine manifold of ^{40}K in the $4S_{1/2}$ ground state is shown in Tab 6.2. The collision process used in the experiment for removing double occupancies is

$$|m_\mathrm{F} = -9/2, -3/2\rangle \longrightarrow |m_\mathrm{F} = -7/2, -5/2\rangle\,. \tag{6.14}$$

Due to the Zeeman level structure of ^{40}K, this particular collision is inelastic with a positive energy release of about $1230E_\mathrm{R}$ (in units of the optical lattice) at a magnetic bias field of 203.5 G. Since this is much larger than the lattice and dipole trap depth, two atoms with $m_\mathrm{F} = -9/2$ and $m_\mathrm{F} = -3/2$ initially located on a single lattice site undergo an inelastic spin-changing collision to the continuum and leave the entire lattice and trap system.

This scattering process is experimentally accessed by inducing adiabatic Landau-Zener transfers [173, 149] between different m_F states, starting from the initial $|m_\mathrm{F} = -9/2, -7/2\rangle$ mixture and ending via $|m_\mathrm{F} = -9/2, -5/2\rangle$ in the final $|m_\mathrm{F} = -9/2, -3/2\rangle$ configuration. For the case of ^{40}K in the $4S_{1/2}$ ground-state, clean and separate transfers between different m_F are possible, because the energy level structure is between the Zeeman and Paschen-Back regime [174] at bias fields around 200 G. The experimentally determined Landau-Zener parameters are given in Fig. 6.13 along with absorption images of the different transfer states for an initially spin-polarized cloud. Interaction shifts originating from a difference in scattering length between the different spin mixtures are at most 10 kHz and thus negligible compared to the frequency sweep range. The total Landau-Zener transfer efficiency is found to be essentially unity within the experimental reproducibility of a few percent. After the transfer all atoms on doubly occupied sites are lost on a rapid timescale below 10 ms. The initial $|m_\mathrm{F} = -9/2, -7/2\rangle$ spin-mixture is then retrieved by reversing the Landau-Zener transfers.

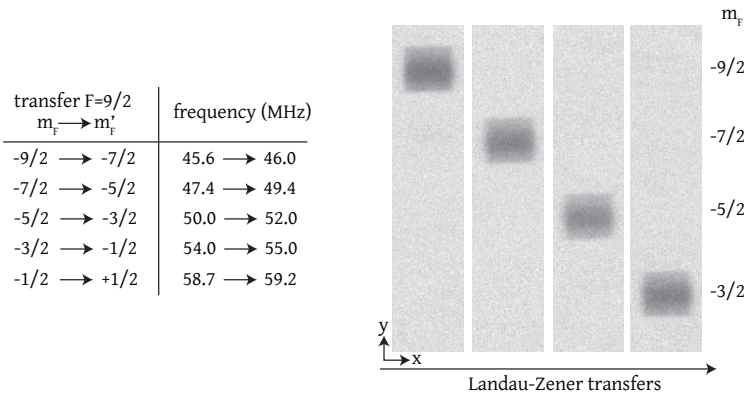

FIGURE 6.13.: **Landau-Zener transfers.** The experimentally optimized parameters for the Landau-Zener transfers between adjacent m_F states are shown for a bias field of 203.5 G and a linear frequency sweep in 8ms. The radio-frequency power is about 5W, which is radiated by a 10 windings coil close to the glass cell. Selection rules only allow transfers with a change in spin projection of $\Delta m_\mathrm{F} = \pm 1, 0$. The transfer efficiencies are found to be unity within the preparation reproducibility. On the right absorption images are shown after Stern-Gerlach separation and time-of-flight for an initially $m_\mathrm{F} = -9/2$ spin-polarized cloud at different stages of the transfer.

In the experiment, the residual double occupancy after the cleaning procedure was found to be below the experimental resolution of $\sim 1\%$ for a broad range of initial double occupancies of up to 60%. In principle, additional atom loss could occur if inelastically scattered atoms leaving the lattice collide additionally with single particles located on lattice sites. This effect was found to be well below 10% of the total atom number for typical parameters.

After the cleaning of double occupancies a singlet-triplet oscillation is measured in the same way as previously described in section 6.1.4. Since the cleaning procedure takes in total about 100 ms, during which the oscillations have already dephased due to the residual magnetic field gradients, the measured STO amplitude is rescaled by a factor of 1.16. Additionally, the cleaning is found to shift the phase of the STO oscillations by approximately 0.9π (modulo 2π).

7 Quantum Magnetism

7.1. Introduction

Magnetism in solids describes the ordering of magnetic moments and originates from an exchange coupling between the electron spins. While the direct dipole interaction between the intrinsic magnetic moment of the electrons is usually negligibly small, the interplay between quantum statistics, delocalization and interaction gives rise to an exchange coupling between electrons, which is responsible for the magnetic ordering [6]. The coupling can be either ferromagnetic, in which case the spins align along the same direction, or antiferromagnetic, where the spins align in alternating order. Although the origin of the exchange coupling is of quantum mechanical nature, a classical treatment of the magnetic state is often sufficient for an accurate analysis of many materials.

Quantum magnetism comes into play when the description of the magnetic state in a material – e.g. its ground-state or excitations – requires a quantum description. This is often the case for systems at low temperatures close to the ground state, where quantum fluctuations play an important role [175]. A simple example is a two-well system in the Heisenberg regime, where each site contains a spin-1/2 particle and both particles are coupled by an antiferromagnetic exchange interaction $J > 0$, see Fig. 7.1. In a quantum mechanical treatment the system contains four possible states, where three are in a spin triplet state and have an energy of $J/4$: $|\uparrow,\uparrow\rangle$, $|\downarrow,\downarrow\rangle$ and $(|\uparrow,\downarrow\rangle + |\downarrow,\uparrow\rangle)/\sqrt{2}$. The fourth state, the singlet configuration $(|\uparrow,\downarrow\rangle - |\downarrow,\uparrow\rangle)/\sqrt{2}$, has an energy of $-3J/4$. In contrast, for a classical treatment all energies between $-J/4$ and $J/4$ are possible. The reason for this difference is the quantum superposition of the singlet state, which changes the state to be entangled and, as a direct consequence, shifts its energy.

The regime of quantum magnetism in complex many-body systems contains many open questions and is a central topic of current research [7]. Already for the case of very simple model systems a correct treatment of the magnetic state can become exceedingly complex due to the exponentially growing number of quantum states. A paradigmatic example is the Fermi-Hubbard model, which contains an antiferromagnetically ordered ground-state at low temperatures in three dimensions [136]. This state is connected to the normal paramagnetic state via a phase transition with a critical temperature below $0.4t$, where t denotes the tunnelling between neighbouring sites. Even in the Heisenberg regime of very large interactions, where the half-filled system becomes an insulator with one particle fixed on each site, the ground-state wavefunction is not the classical Néel state: although the ground state is still characterized by a long-range order parameter with alternating spin order, it contains additionally a large number of quantum fluctuations, which makes an analytic expression of the wavefunction a very difficult task. Already for the calculation of the transition tempera-

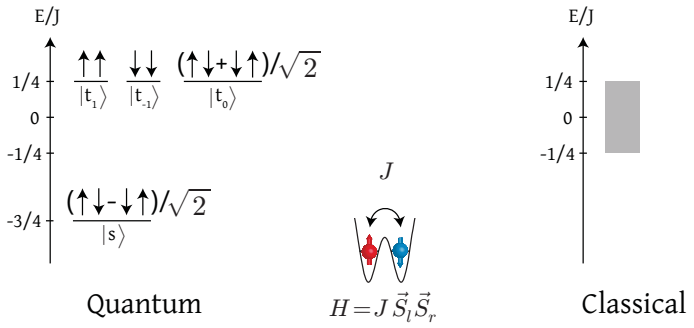

FIGURE 7.1.: **Energies on a spin-1/2 double-well system.** The energy states of a double-well with two spin-1/2 particles located on each site. Both particles are coupled by a Heisenberg exchange interaction $J > 0$, where $\vec{S}_l$ and $\vec{S}_r$ denote the left and right spin-1/2 operator. In a quantum mechanical treatment, three spin triplet states exist with an energy of $J/4$, whereas the spin singlet can lower its energy to $-3J/4$ due to quantum superposition. In a classical picture the spin $\vec{S}$ can take any value, such that all energies between $-J/4$ and $J/4$ are possible.

ture very sophisticated numerical techniques are necessary. These include various quantum Monte-Carlo methods [136, 176, 177, 178], dynamical mean-field theory [179, 180, 181, 182] and dynamical cluster approximations [183, 184, 138].

The system can completely change its physical state if the long-range magnetic order is frustrated. There are numerous ways of doing this, for example by reducing the dimensionality of the system, including next-nearest neighbour spin interactions, considering more complex lattice geometries or simply by doping the system [185, 162, 1, 8, 175, 11, 4, 5]. As a consequence, the long-range ordered state is no longer the lowest energy state of the system at $T = 0$. Instead, the true ground state is characterized by the interplay of local magnetic spin correlations and quantum fluctuations in absence of long-range spin order. These systems are considered to give rise to exotic quantum states with very interesting physical properties, such as spin-liquids, resonating valence-bond states or pseudo-gap physics, where a theoretical treatment quickly becomes extremely challenging [6, 10, 7, 9]. A prominent example is the doped two-dimensional Fermi-Hubbard model, which is expected to be closely connected to high-temperature superconductivity at low temperatures, see Fig. 7.2. Contrary to the half-filled system with long-range order, a detailed theoretical treatment and understanding of this strongly correlated phase is currently beyond hope.

Another possibility of frustrating long-range order, which has received great interest recently, is geometric frustration. This can be realized by introducing a dimerization into the lattice structure, see Fig. 7.2. For a spin-1/2 Heisenberg model on a square lattice this gives rise to an (explicit) valence-bond crystal (VBC) [1, 7, 9], which is connected to the Néel state via a quantum phase transition at a critical value of the lattice dimerization. The VBC state is characterized by a spin gap and contains a characteristic SU(2) symmetry preserving excitation called triplon. It has a vanishing excitation energy at the phase transition and becomes the triplet state on an isolated double-well for very large dimerizations. Recently, the phase transition and the accompanied mode-softening of the triplon excitations could be observed in Cu compound systems in the Heisenberg regime [186, 187, 188].

For the case of one-dimensional spin systems [8], no long-range ordered state is possible

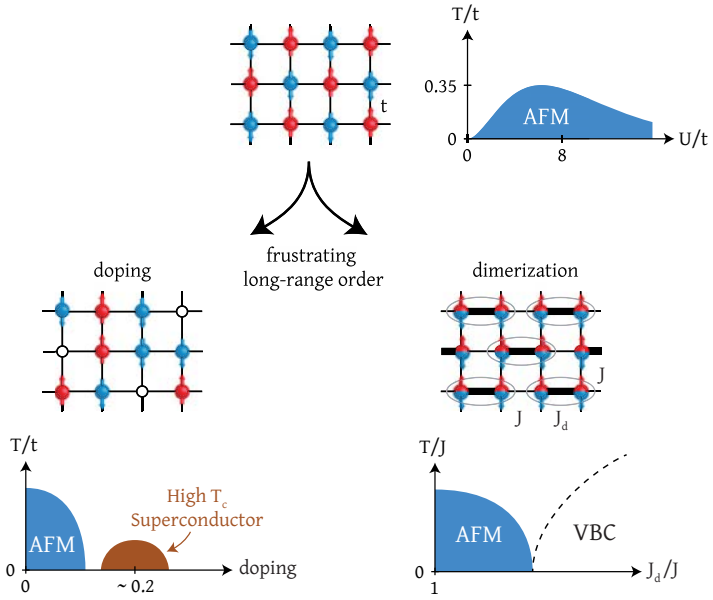

FIGURE 7.2.: **Frustrating long-range magnetic order.** The top shows a sketch of the long-range ordered antiferromagnetic Néel state (AFM) for a Fermi-Hubbard model on a cubic lattice, along with the schematic phase-diagram versus interaction and temperature [136]. Below, two possible scenarios for frustrating the long-range order in a two-dimensional square lattice are shown. Doping of a two dimensional Fermi-Hubbard system on a square lattice reduces the critical temperature of the AFM phase. For larger dopings a high-temperature superconducting phase is expected [10]. The introduction of a dimerization on a square lattice Heisenberg model gives rise to a zero-temperature quantum phase transition from the AFM state to an explicit valence-bond crystal (VBC) at a critical value of the exchange energy ratio J_d/J [7].

owing to the Mermin-Wagner theorem [189]. In a simple picture, long-range magnetic order is prevented by the dominant role of quantum fluctuations. One-dimensional spin chains have been thoroughly investigated in the past using specifically designed numerical tools such as density matrix renormalization group techniques [190]. Particularly well studied systems are the XXZ-model and the isotropic Heisenberg model, where at low temperatures quasi long-range order is expected with a power-law decay of the spin correlation function $\langle S_i^z S_{i+r}^z \rangle$, where S_i^z is the usual spin operator on site i defined via Pauli matrices and r is the distance between sites. Spin frustration can be introduced by including next-nearest neighbour spin interactions or changing the geometry to spin-ladders with different exchange energies along the rung and the ladder. In these cases the competition between the two exchange energy scales is expected to give rise to additional phase transitions.

7.2. Entropy redistribution and low temperatures

Ultracold atoms in optical lattices are an alternative approach to studying quantum magnetism in solids and may lead to a deeper understanding of the underlying physics [27, 29, 30]. Apart from the unique control and tunability, the cold atoms approach can provide observ-

ables that are complementary to the commonly used momentum-space techniques in solid-state research. These include for example single-site resolved images of a many-body state [40, 41] or measurements of local correlation functions [77]. Owing to the low energy scales, the lattice structure itself can be tuned dynamically on time-scales comparable to the intrinsic time-scales of the system, a scenario impossible to realize with real solids. The realization of ultracold fermions in one- and three-dimensional optical lattices has opened the possibility of a very clean and controlled experimental study of the phase diagram of the Fermi-Hubbard model [43, 42]. While the ordering of density degrees of freedom in the metal-Mott insulator transition has been realized experimentally [55, 56], the regime of quantum magnetism and spin ordering could so far not be accessed. The main reason for this are the very low temperatures required. The relevant energy scale is given by the exchange energy, which is usually much lower than the already very small tunnelling and interaction energy in cold atom systems. This leads to ultra-low temperature requirements in the lattice on the order of 1 nK. Achieving these temperatures in cold atom laboratories is far from easy.

A possible route to circumvent the temperature limitation is to map the spin to other degrees of freedom. Using that technique, one-dimensional decoupled Ising spin chains and classical magnetism on a triangular lattice could be simulated with bosonic atoms [58, 59]. Furthermore, exchange interactions were observed in artificially prepared arrays of isolated double-wells, plaquettes and one-dimensional chains [60, 61, 62].

So far, exchange driven spin ordering in a thermalized many-body state of fermionic atoms in an optical lattice has not been reported. The main limitation in achieving the necessary low temperatures originates from the preparation scheme of the system, where the gas is first evaporatively cooled down to low temperatures in the harmonic trap and then loaded into the lattice by smoothly turning on all laser beams forming the optical lattice. During this process two factors play an important role:

- The lowest temperatures after evaporative cooling of the Fermi gas are found to be between $0.05-0.1T_{\mathrm{F}}$ of the Fermi temperature T_{F}, as reported from several experiments with different atomic elements. The limitation in temperature is probably caused by the reduction of the scattering cross-section as the Fermi gas becomes more and more degenerate and the number of accessible scattering states is reduced due to Pauli's principle. Additionally, background heating mechanisms play a larger role due to deep Fermi sea heating [28]. Even for a perfectly adiabatic lattice loading, this sets a lower boundary for the temperature in the lattice, which is typically larger than the tunnelling [95].

- In experiments the loading of the lattice turns out to be not perfectly adiabatic. The entropy as compared to the initial value in the harmonic trap increases by $0.1 - 1.0k_{\mathrm{B}}$ depending on the scattering length [95, 57]. The basic limitation is connected to the thermalization time-scale, which becomes increasingly slower in deeper lattices. Additionally, the decay time of high-energy excitations has been reported to grow exponentially with the interaction energy and can become up to a few seconds for realistic experimental parameters [97, 98]. In fact, a detailed understanding of the dynamics during the lattice loading procedure is still missing and the exact time-scale for global thermalization is unknown.

Several schemes have been proposed to further reduce the temperature in the experiments.

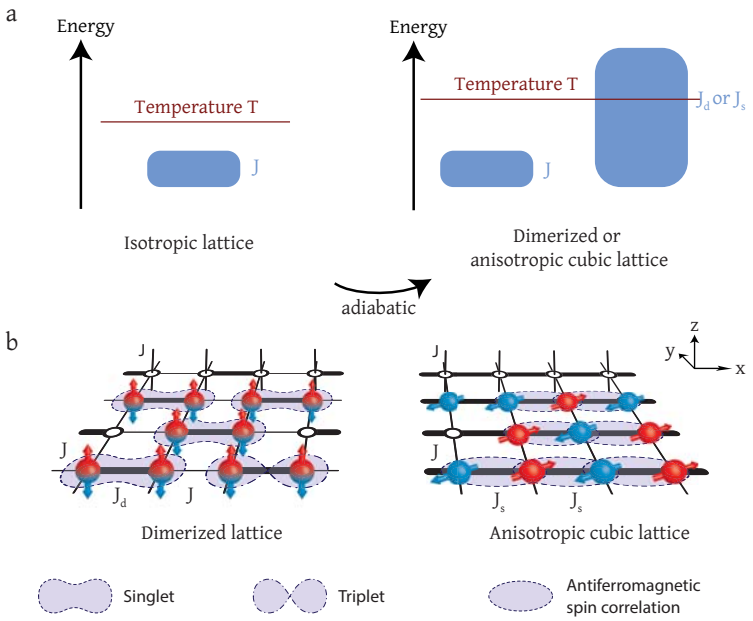

FIGURE 7.3.: **Local entropy redistribution scheme.** (a) At fixed entropy per particle the temperature in the experiment is above the exchange energy J for isotropic lattices and no magnetic spin correlations can be observed. In contrast, when introducing a second large exchange energy J_d or J_s on a subset of links – either via a dimerization or spatial lattice anisotropy – the temperature in the experiment is below the large exchange energy. Magnetic spin correlations then emerge along the strong links. (b) Schematic view of the nearest-neighbour spin correlations observed in the experiment. A two-component mixture of repulsively interacting fermionic atoms (red and blue) is prepared close to half-filling in a cubic lattice with two different coupling configurations. The dimerized lattice contains strong and weak dimer links with exchange energies J_d and J. Low temperatures lead to an excess number of singlets over triplets. The anisotropic lattice has strong and weak exchanges energies J_s and J along different spatial axes. Antiferromagnetic spin correlations in the transverse direction are formed along the strong link direction. In both figures exemplary thermal excitations in the form of spin excitations or holes are shown.

They mostly rely on redistribution of entropy between different regions of the trap, where a low entropy region is created by either loading a band insulating state into the lattice or adding a dimple potential to a low-temperature reservoir in the harmonic trap [73, 74]. The low-entropy region can then be separated by a repulsive potential, which after thermalization gives access to a low-temperature state. Other ideas include the artificial preparation of an initial state as close as possible to the Néel state using a superlattice potential [75] or the use of a second element for sympathetic cooling in the lattice. Until now, none of the theoretical proposals have been tested successfully in experiments.

In this chapter, we instead propose and implement a local entropy redistribution scheme within the lattice structure to reach the regime of quantum magnetism. We observe magnetic spin correlations on neighbouring sites when preparing the atoms either in a dimerized or an anisotropic lattice, see Fig. 7.3. In both geometries, a subset of links of the underlying simple cubic lattice is set to a larger exchange energy as compared to the other links. As a result, the entropy is predominantly stored in configurations involving the weak links. For fixed total

entropy in the trapped system, this essentially allows reaching temperatures between the two exchange energy scales, which is not possible for an isotropic lattice. In the dimerized lattice the resulting correlations on the strong links correspond to an excess population of the low energy singlet as compared to the triplet state. In the anisotropic lattice the low temperatures lead to antiferromagnetic spin correlations along one spatial axis, the transverse component of which is also detected via a singlet-triplet imbalance. For both systems we study the dependence of the spin correlations on temperature and tunnelling balance and find good agreement with theory[1].

7.3. Spin correlations in dimerized lattices

In this section the observation of magnetic spin correlations on neighbouring sites in a dimerized lattice geometry is presented and discussed. After loading a low-temperature two-component spin mixture of fermionic atoms with repulsive interactions into the optical lattice, the spin correlations emerge as an excess number of singlets as compared to triplets, which consist of two atoms with opposite spins. The dimerized lattice geometry is a simple cubic lattice, where the tunnelling bonds are strengthened on a chequerboard pattern in the $x-y$ plane. Changing the tunnelling strengths allows controlling the dimerization J_d/J, where the strong and weak exchange energies J_d and J denote the singlet-triplet energy splitting on adjacent sites. The singlet-triplet imbalance is obtained from coherent singlet-triplet oscillations. The dependence of the singlet-triplet imbalance is studied over a broad range of entropies, dimerization strengths and interactions. The largest imbalances are observed for the lowest entropies and strongest dimerizations.

7.3.1. Preparation and detection

The experiments are performed with a harmonically confined, balanced two-component mixture of a quantum degenerate Fermi gas of ^{40}K. The atoms are prepared in two magnetic sublevels, either in $m_F = -9/2, -7/2$ or $m_F = -9/2, -5/2$ of the $F = 9/2$ hyperfine manifold. The two spin components are denoted by $\uparrow$ and $\downarrow$. The atomic gas is evaporatively cooled in the optical dipole trap to temperatures below 10% of the Fermi temperature at atom numbers between $50,000$ and $100,000$. After setting the magnetic offset field to 221.4 G, where the repulsive s-wave scattering length is $106(1)\,a_0$ for the $-9/2, -7/2$ mixture and $640(10)a_0$ for the $-9/2, -5/2$ mixture, the atoms are loaded into the three-dimensional dimerized lattice using a spline-shaped ramp of all lattice depths in 200 ms. As explained in chapter 2, we independently control the tunnelling strengths along all three spatial axes and additionally introduce a chequerboard dimerization in the $x-y$ plane by strengthening every second tunnelling link along the x axis, see Fig. 7.3. The chequerboard pattern replicates along the z axis. The system is well described by a three-dimensional single-band Hubbard model with repulsive on-site interaction energy U and nearest-neighbour tunnelling t_d and t along the strong and weak links respectively. For comparison with theory the results of the high-temperature series expansion of coupled dimers developed in chapter 3.4 are used. The tunnelling along the

[1] Parts of this chapter have been published in [71].

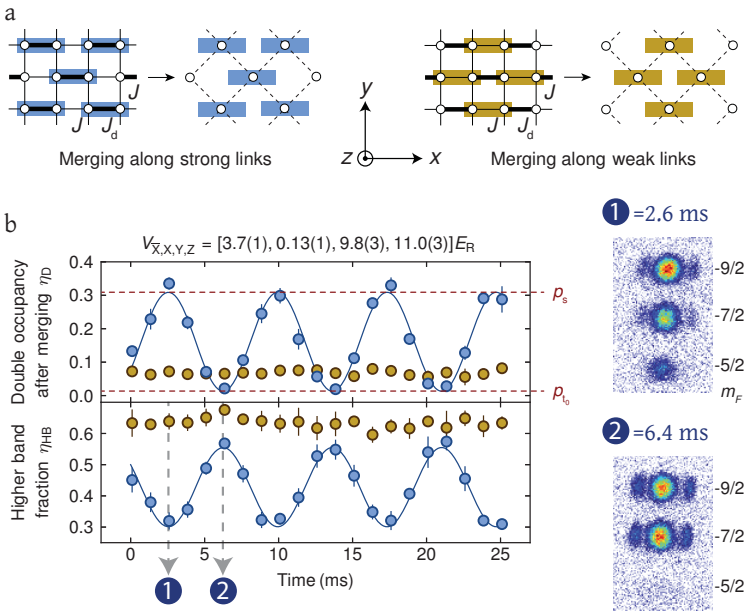

FIGURE 7.4.: **Spin correlations in dimerized lattices.** Exemplary measurement of the atomic singlet and triplet fractions p_s and p_{t_0} in a dimerized lattice. (a) The two possible merging configurations, where singlets and triplets are detected on a set of adjacent sites arranged on a chequerboard pattern in the plane. The detection is either along the strong or weak links. (b) Exemplary singlet-triplet oscillation in a strongly dimerized lattice at $U/t = 10.9(8)$ and $J_\mathrm{d}/J = 100(9)$ with $J/h = 24(2)$ Hz ($t_\mathrm{d}/t = 20(2)$). We observe an oscillation in the double occupancy after merging η_D and in the higher band fraction η_HB when merging along the strong links (blue data), whereas no oscillations are visible for the weak links (ochre data). The phase of the oscillation is shifted owing to the double occupancy removal procedure, see section 6.2.3. The red dashed lines denote the extracted singlet and triplet fraction p_s and p_{t_0}. Error bars show the standard deviation of at least five measurements. Depending on the oscillation time, the absorption images on the right show either a large double occupancy in the lowest band corresponding to singlets (large $-5/2$ fraction), or an increased higher band fraction indicating triplet states (large population at higher momenta).

weak links is set to a constant value of $t/h = 67(6)$ Hz for all measurements presented in the following in the dimerized lattice, whereas U and t_d are varied.

As shown in Fig. 7.4a, the fraction of atoms forming singlets and triplets on neighbouring lattice sites (p_s and p_{t_0}) is detected by transforming the lattice to a chequerboard geometry. In the following we briefly summarize the detection technique for measuring the atomic singlet and triplet fractions p_s and p_{t_0} defined in Eq. 6.11 – the full details can be found in chapter 6. In the first detection step, the atomic motion in the initial lattice is frozen by rapid conversion to a simple cubic structure with negligible tunnelling. This is done in a two-step process, where first all beam intensities are linearly increased over the course of 0.5 ms up to the point where $V_\mathrm{Y} = 30(1)\,E_\mathrm{R}$, $V_\mathrm{Z} = 40(1)\,E_\mathrm{R}$ and all other intensities in the $x-y$ plane are ramped such that the potential is not deformed. In a second linear ramp lasting 10 ms, the lattice is changed to a simple cubic geometry where $V_{\overline{X},X,Y,Z} = [25(1), 0, 30(1), 40(1)]\,E_\mathrm{R}$. The ramp to the detection lattice can be considered sudden for the inter-dimer links but

adiabatic for the intra-dimer links. Our singlet-triplet measurement procedure hence locally projects onto the two-site eigenstates of individual dimers, which includes an admixture of double occupancies. Using the exact time-evolution of the two-site Hubbard model presented in section 6.2.2, the adiabaticity of the detection lattice ramp can be estimated. For the given ramp-times and including site-offsets due to the harmonic trapping potential, the probability of populating excited states on a dimer during such a ramp remains below 0.1% for all values of U and t_d explored in the measurements in dimerized systems.

After the rapid ramp to the detection lattice a cleaning procedure is applied, which removes all atoms on doubly occupied sites, see section 6.2.3. In a next step a magnetic field gradient is applied, which creates a differential bias energy Δ for atoms of opposite spins on adjacent sites and causes coherent oscillations between the singlet $|\mathrm{s}\rangle = (|\uparrow,\downarrow\rangle - |\downarrow,\uparrow\rangle)/\sqrt{2}$ and the triplet $|\mathrm{t}_0\rangle = (|\uparrow,\downarrow\rangle + |\downarrow,\uparrow\rangle)/\sqrt{2}$ state at a singlet-triplet oscillation frequency $\nu = 2\Delta/h$. If the initial amount of singlets and triplets is equal, no overall oscillation will be visible, as $|\mathrm{s}\rangle$ and $|\mathrm{t}_0\rangle$ oscillate in antiphase.

After a certain oscillation time, we remove the gradient and merge two adjacent sites. Owing to the symmetry of the two-particle wavefunction, the singlet state on neighbouring sites evolves to a doubly occupied site with both atoms in the lowest band, while the triplet state transforms into a state with one atom in the lowest and one atom in the first excited band. The fraction of atoms forming double occupancies in the lowest band of the merged lattice η_D is detected by a radiofrequency transfer to the previously unpopulated $m_F = -5/2$ spin state [55], section 4.2.1. The fraction of atoms in the higher band η_HB is obtained from a band mapping technique [30], see section 4.2.2. For the final readout we take absorption images after Stern-Gerlach separation of the spin states during ballistic expansion. For an imbalance between the initial singlet and triplet populations, η_D and η_HB will show oscillations with opposite amplitudes. As the double occupancy in the lowest band contains only contributions from two particles with opposite spins, we can infer the fraction of atoms forming singlets and triplets from the maxima and minima of a sinusoidal fit to η_D. The higher band fraction has an additional offset caused by dimers containing two atoms with the same spin or one atom with an antisymmetric spatial wavefunction. Additionally, the higher band oscillation amplitude is lower due to higher-band tunnelling and subsequent loss processes, see section 6.1.5.

7.3.2. Results

When loading repulsively interacting atoms into a strongly dimerized lattice and merging along the strong links, we observe oscillations in η_D and η_HB, see Fig. 7.4b. This reveals an excess number of singlets, corresponding to magnetic order on neighbouring sites. We quantify this order by the normalized imbalance

$$\mathcal{I} = \frac{p_\mathrm{s} - p_{\mathrm{t}_0}}{p_\mathrm{s} + p_{\mathrm{t}_0}}. \tag{7.1}$$

The order in the strongly dimerized lattice originates from temperatures below the intra-dimer exchange energy $J_\mathrm{d} = -U/2 + \sqrt{16t_\mathrm{d}^2 + U^2}/2$, which denotes the singlet-triplet splitting on a single dimer. While such temperatures require very low entropies for isotropic lattices [138], in our system the access to the regime of magnetic ordering is facilitated by the presence of the weaker inter-dimer exchange energy $J \ll J_\mathrm{d}$. This leads to an entropy redistribution

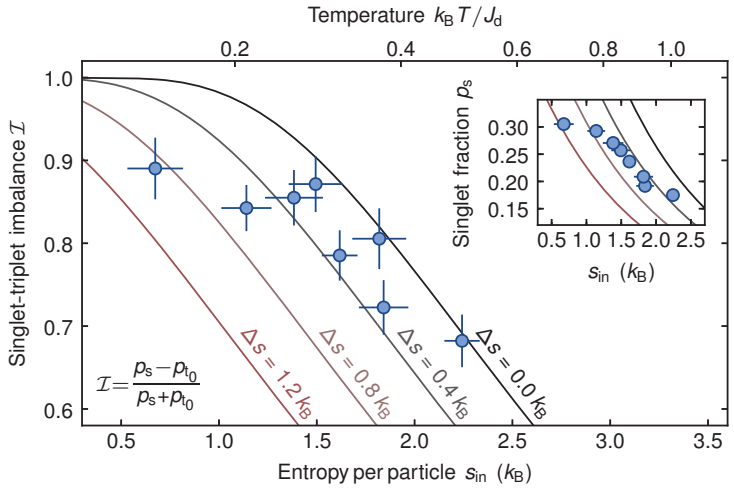

FIGURE 7.5.: **Dimerized simple cubic lattice.** Singlet-triplet imbalance on the strong dimer links vs. initial entropy before loading into the lattice s_{in} and temperature $k_{\mathrm{B}}T/J_{\mathrm{d}}$ in a dimerized lattice at $U/t = 10.9(8)$ and $J_{\mathrm{d}}/J = 100(9)$ with $J/h = 24(2)$ Hz ($t_{\mathrm{d}}/t = 20(2)$). The imbalance and the absolute singlet fraction (inset) decrease with increasing entropy. Solid lines are the prediction of a high-temperature series expansion taking into account different amounts of added entropy Δs during the lattice loading. These measurements were done at a scattering length of $106a_0$.

from states on the strong to the weak links and gives access to the temperature regime $J < k_{\mathrm{B}}T < J_{\mathrm{d}}$ for experimentally attainable entropies. As expected for strong dimerization, we find no visible oscillations when merging along the weak links, which indicates the absence of magnetic correlations on these links, see Fig. 7.4b. The observed constant values of $\eta_{\mathrm{D}} = 0.07(1)$ and $\eta_{\mathrm{HB}} = 0.63(3)$ are consistent with a state where nearly all singlets are located on neighbouring dimer links, with vanishing correlations between them.

To analyse the effect of temperature on the magnetic correlations, we measure the dependence of the singlet-triplet imbalance on the initial entropy s_{in} before loading the atoms into the lattice[2], see Fig. 7.5. The imbalance $\mathcal{I}$ and the absolute singlet fraction p_{s} reduce for larger entropies, as triplet states become thermally populated. The singlet fraction is additionally diminished by a shrinking half-filled region in the trapped system [77]. We find good agreement with a second order high-temperature series expansion of coupled dimers when including an entropy increase of $\Delta s = 0.4\,k_{\mathrm{B}}$ with respect to the initial entropy in the harmonic trap s_{in}. This heating is associated to the lattice loading [95] and is larger for the lowest entropies, consistent with previous results [77]. From the measured imbalances we infer temperatures below $0.4J_{\mathrm{d}}$.

For reduced dimerizations the coupling between dimers leads to increased inter-dimer correlations. The excitation energy of triplets is then lowered as they delocalize over the lattice, thus changing the nature of magnetic ordering. In Fig. 7.6 we use the tunable lattice to investigate the dependence of the imbalance $\mathcal{I}$ on the exchange energy ratio J_{d}/J, which is done by adjusting the dimer tunnelling t_d while keeping t constant. As the dimerization is

[2] After evaporative cooling, the initial entropy can be controlled by sweeping the magnetic offset field close to the Feshbach resonance located at 202.1 G, where losses and heating occur.

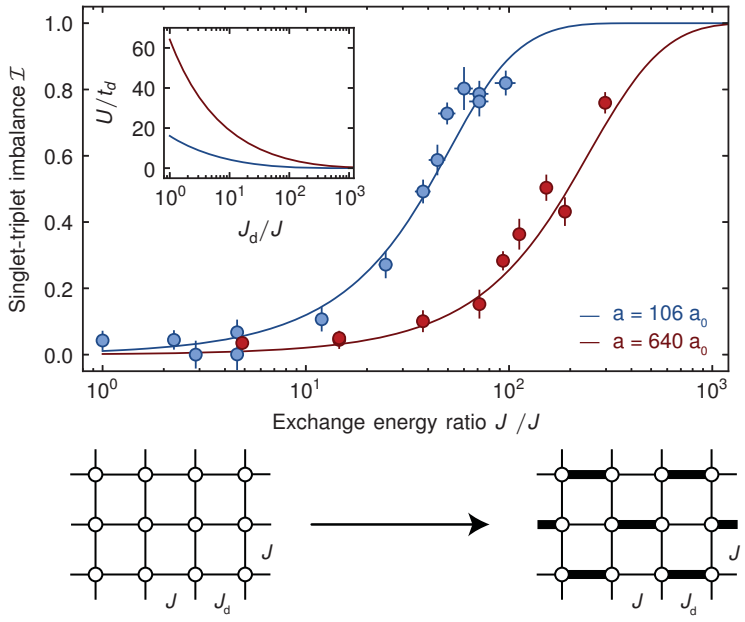

FIGURE 7.6.: **Tuning the lattice dimerization.** Imbalance versus dimerization J_d/J, showing an increase for strongly dimerized simple cubic lattices. Two data sets at different scattering lengths are shown, either with the atoms in a $m_F = -9/2, -7/2$ (blue) or $m_F = -9/2, -5/2$ mixture (red). The exchange energy ratio J_d/J is changed by tuning the dimer tunnelling t_d while keeping t constant. Solid lines are the high-temperature series predictions for an entropy per particle of $1.7\,k_\mathrm{B}$ and $2.3\,k_\mathrm{B}$ in the lattice (atomic limit). This includes the heating during loading. Measurements of the entropy per particles in the dipole trap after reversing the lattice loading again confirmed a larger heating of the $-9/2, -5/2$ mixture. Vertical error bars denote the fit error from singlet-triplet oscillations consisting of 63 measurements, the errors in J_d/J stem from lattice calibration uncertainties and the errors in s_in are the standard deviation of five measurements. The inset shows the dependence of the interaction energy U/t_d on J_d/J for the shown measurements.

progressively removed the imbalance decreases in good agreement with theory and eventually falls below our experimental resolution. This decrease can be attributed to the inter-dimer exchange energy J_d becoming smaller than the temperature T. For larger interactions (higher s-wave scattering length) the imbalance is found to already decrease at higher ratios of the exchange energies. This is in agreement with the expected behaviour, as in this case the absolute exchange energy scales are very small, such that the imbalance is strongly reduced at comparable temperatures. For vanishing temperatures the system is expected to undergo a quantum phase transition from a gapped spin-liquid state to a long-range ordered antiferromagnet as J_d/J is reduced below a critical value, where the spin gap becomes zero [7, 191]. For very large dimerizations the system in the center of the harmonic trap corresponds to an explicit valence-bond crystal [9].

Fig. 7.7 shows the distribution of the entropy per site and density in the trap for a dimerized and simple cubic lattice. Owing to the entropy redistribution explained in the introduction of this chapter, the local entropy per site s in the half filled region ($n = 1$) reduces to values below $0.6k_\mathrm{B}$ for the dimerized lattice. In contrast, the entropy per site does not fall below

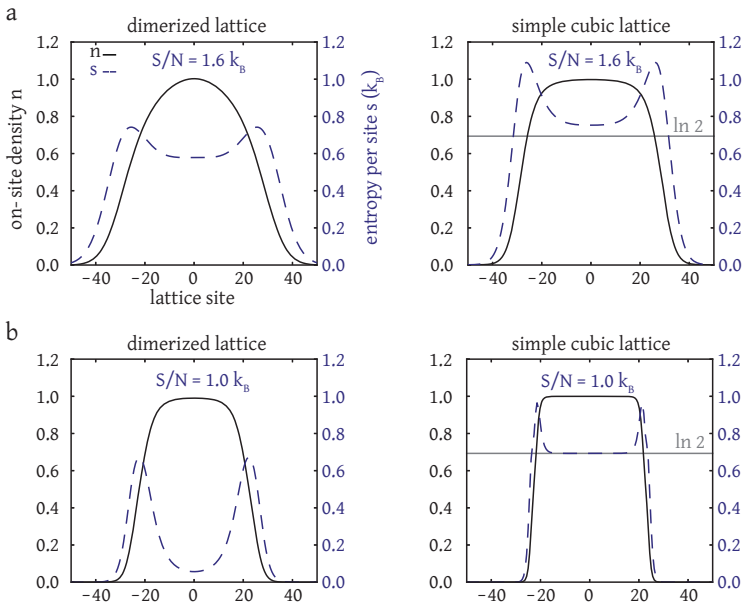

FIGURE 7.7.: **Entropy distribution.** Comparison of the density and entropy distribution in the harmonic trap for a simple cubic and dimerized lattice obtained from the second-order high-temperature series, see chapter 3.4. (a) Comparison for parameters realized in the experiment, where both systems have the same trap-averaged entropy per particle of $1.6k_\mathrm{B}$. This corresponds to the estimated lowest entropy in the lattice from the highest measured value of the singlet-triplet imbalance $\mathcal{I}$, see Fig. 7.5 in the main text. In both plots the total particle number is set to $100,000$ (as in the experiment) with a geometric mean trap frequency of $\overline{\omega} = 2\pi \times 79\,\mathrm{Hz}$, which gives one particle per site in the trap center. The density and entropy distribution are calculated from the second order high-temperature series expansion. The lattice parameters for the dimerized lattice correspond to the datapoint with the largest dimerization of Fig. 7.6: $U/6t = 1.6$ and $t_d/t = 34$, where $t/h = 67$ Hz. For comparison, the interaction is set to $U/6t = 12.7$ and $t/h = 67$ Hz in the simple cubic lattice. (b) Comparison of the local entropy reduction for a lower trap-averaged entropy of $1.0k_\mathrm{B}$ and $50,000$ particles. The entropy at half-filling in the dimerized lattice falls below $0.1k_\mathrm{B}$.

$k_\mathrm{B}\ln 2$ in the half-filled region in the simple cubic case, which originates from the spin degree of freedom of the two-component mixture. For lower values of the trap-averaged entropy, the entropy at half-filling can even fall below $0.1k_\mathrm{B}$ in the dimerized lattice.

7.4. Antiferromagnetic spin correlations in anisotropic lattices

7.4.1. Preparation and detection

The key to the observation of quantum magnetism in our system is the presence of two different exchange energy scales. While this can be achieved using a dimerized lattice structure, other scenarios are possible, where the strong and weak links are arranged on a different pattern. In this section we present measurements of spin correlations on neighbouring sites after loading a repulsive two component Fermi gas into a three-dimensional anisotropic cubic

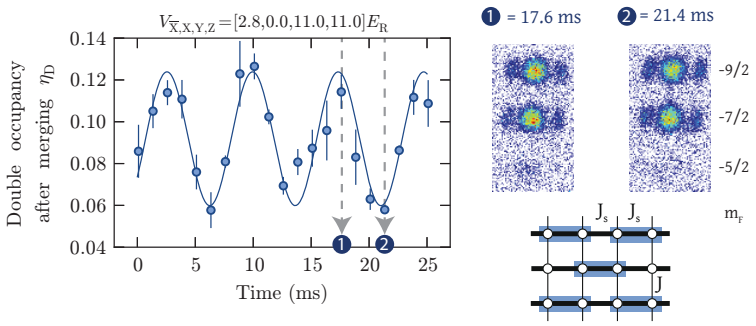

FIGURE 7.8.: **Spin correlations in anisotropic lattice.** An exemplary singlet-triplet oscillation is shown after loading a repulsive gas at $a = 106a_0$ into an anisotropic cubic lattice of $V_{\overline{X},Y,Z} = [2.8, 11.0, 11.0]E_R$ with a tunnelling ratio of $t_s/t = 7.3$. The double occupancy after merging η_D shows an oscillatory behaviour, from which the atomic singlet and triplet fractions are extracted. Two absorption images at different oscillation times are shown on the right, which were obtained after time-of-flight expansion of the gas from the confining trap and lattice. For measurements in the anisotropic cubic lattice the singlet and triplet numbers are the same on the two possible merging patterns.

lattice. In this configuration the tunnelling t_s along the spatial x-axis is stronger than the tunnelling t on the other two axes. This again leads to a separation of exchange energy scales, which facilitates the emergence of magnetic spin correlations along the strong tunnelling direction. We detect anti-ferromagnetic spin correlations on neighbouring sites, which are observed from a difference in the singlet and triplet populations in the system.

The preparation and detection scheme is analogous to the case of the measurements in the dimerized lattice. We load a $m_F = -9/2, -7/2$ mixture of fermionic ^{40}K at a repulsive s-wave scattering length of $106a_0$ into an anisotropic lattice, which is formed by setting $V_{Y,Z} = 11E_R$ while $V_{\overline{X}}$ is set to a smaller value. After the initial loading we directly ramp to the detection lattice with $V_{\overline{X},Y,Z} = [25(1), 30(1), 40(1)]\, E_R$ in 0.5 ms ($V_X = 0\, E_R$ throughout). In contrast to the detection lattice ramp for the dimer lattice, the ramp for the anisotropic lattice can be considered sudden for all links, as the duration of the ramp is always well below the tunnelling time in the initial lattice. Our detection method then corresponds to locally projecting the wavefunction of the system onto $(|\uparrow,\downarrow\rangle - |\downarrow,\uparrow\rangle)/\sqrt{2}$ on pairs of sites when measuring p_s, hence excluding any contributions from double occupancies. The probability of this projection, as calculated from the two-site Hubbard model, lies above 80% for all shown data and is higher for deeper lattices, see section 6.2.2. For both lattice geometries, the triplet state remains unaffected by changes in U and t.

Fig. 7.8 shows an exemplary measurement of the atomic singlet and triplet fractions p_s and p_{t_0} after loading a repulsively interacting gas at an s-wave scattering length of $106a_0$ and initial entropy below $1.0\, k_B$ into an anisotropic cubic lattice with $t_s/t = 7.3$. The observed singlet-triplet oscillation is much smaller than for the measurements in the dimerized lattice with an amplitude of a few percent, but still clearly visible in the double occupancy after merging η_D. We extract the oscillation amplitude from a sinusoidal fit with fixed frequency and phase.

In the anisotropic lattice the symmetry between neighbouring links is restored as compared to the dimerized lattice. The detected singlet and triplet fractions are then the same for

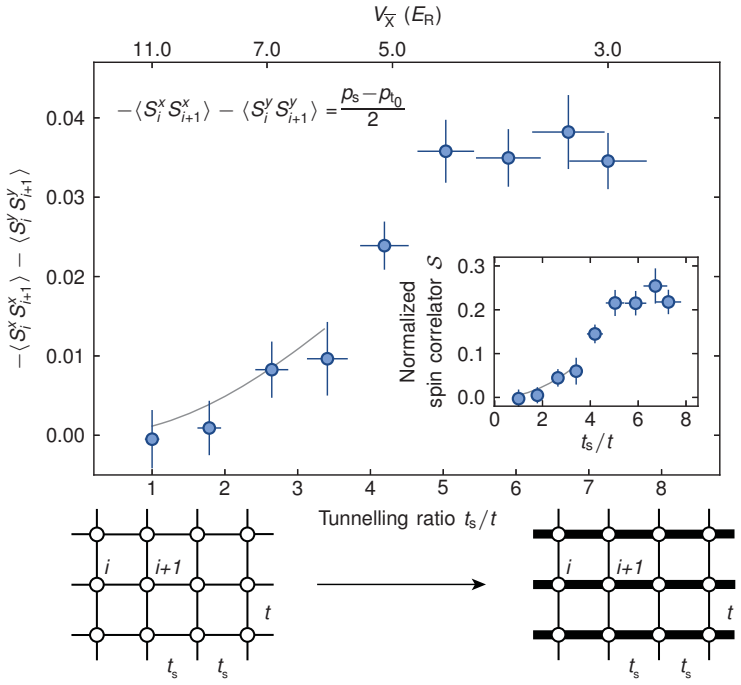

FIGURE 7.9.: **Nearest-neighbour antiferromagnetic order.** Transverse spin correlator versus tunnelling ratio t_s/t and lattice depth $V_{\bar{X}}$ in a three-dimensional anisotropic simple cubic lattice with $V_{Y,Z} = 11.0(3)\,E_R$. Positive values correspond to antiferromagnetic ordering. The inset shows the normalized spin correlator $\mathcal{S}$, denoting the fraction of antiferromagnetic ordering at half-filling density. In this measurement U/t decreases from 16(1) to 10.5(8). Solid lines are the prediction of a high-temperature series expansion for an entropy per particle of $1.8\,k_B$, as used in Fig. 7.5, and are shown up to $t_s/k_BT = 1/2$. Error bars as in Fig. 7.5.

both merging configurations. Additionally, the projection operators used in Eq. 6.11 to define the singlet and triplet fractions p_s and p_{t_0} are in this case related to the spin operators $\vec{S}_i = 1/2 \sum_{s,s'} \hat{c}^\dagger_{i,s} \vec{\sigma} \hat{c}_{i,s'}$, where $\vec{\sigma} = (\sigma_x, \sigma_y, \sigma_z)$ are the Pauli matrices

$$\hat{P}_i^{\mathrm{s}} = \frac{\hat{n}_i \hat{n}_{i+1}}{4} - \vec{S}_i \vec{S}_{i+1} \qquad \hat{P}_i^{\mathrm{t}_0} = \vec{S}_i \vec{S}_{i+1} - 2 S_i^z S_{i+1}^z + \frac{\hat{n}_i \hat{n}_{i+1}}{4}. \tag{7.2}$$

From this it is immediately clear that the population difference $(p_s - p_{t_0})/2$ is equal to the transverse spin correlator between neighbouring sites i and $i+1$ along the strong tunnelling direction

$$-\langle S_i^x S_{i+1}^x \rangle - \langle S_i^y S_{i+1}^y \rangle = (p_s - p_{t_0})/2. \tag{7.3}$$

This quantity characterizes the fraction of atoms with antiferromagnetic ordering on neighbouring sites in the entire atomic cloud. Note that the expectation in the above formula are integrated over the entire trapped system.

7.4.2. Results

The dependence of the transverse spin correlator on lattice anisotropy t_s/t is shown in Fig. 7.9. The trap averaged spin correlations are found to increase up to 4% for large anisotropies, whereas for the isotropic lattice $t_s/t = 1$ no spin correlations are found within the experimental resolution. The reason for the comparatively low values is that large parts of the cloud, in particular the outer wings of the atomic density distribution, are not at half-filling and thus cannot contribute to the spin correlation signal. This leads to a very small ratio when normalizing to the total atom number. A density-normalized fraction of antiferromagnetic ordering can be obtained by dividing with the fraction of atoms with two particles of arbitrary spins on adjacent sites. Under the assumption that all spin correlators $\langle S_i^{x,y,z} S_{i+1}^{x,y,z} \rangle$ are equal – which applies if all symmetry breaking fields are much smaller than all other energy scales – the normalized spin correlator $\mathcal{S}$ can be directly obtained from the measurement of singlets and triplets (here n_i^s is one for a single particle of any spin on site i and zero otherwise)

$$\mathcal{S} = \frac{-4\langle S_i^z S_{i+1}^z \rangle}{\langle n_i^s n_{i+1}^s \rangle} = \frac{p_s - p_{t_0}}{p_s + 3p_{t_0}}. \tag{7.4}$$

The normalized antiferromagnetic correlations along the strong tunnelling direction reach 25%, see inset Fig. 7.9. This corresponds to approximately $5,000$ ordered atoms. Our observations of anti-ferromagnetic spin correlations also extend to the regime of weak lattices, where correction terms to the single-band Hubbard model become relevant [137]. In this regime a variety of magnetic phases have been predicted [192, 193].

The results can be compared to the second order high-temperature series predictions for the spin correlator, see chapter 3.3. We find good agreement in the regime of small anisotropies. For larger anisotropies the expansion breaks down, as the strong tunnelling and the temperature become comparable. In this regime we expect the temperature to lie between the large and small exchange scales $J < k_B T < J_s$. The system then behaves as an array of one-dimensional spin-ordered chains without correlations between them [8], where the majority of the entropy is stored in configurations involving the weak links. Low-dimensional systems have been predicted to show enhanced nearest-neighbour correlations [194].

For temperatures much larger than the strong exchange energy the magnetic correlations should disappear. In Fig. 7.10 we study the dependence on the initial entropy s_{in} and find the correlations to vanish above $2.5\,k_B$, where $k_B T \gg J_s$ is expected.

7.5. Conclusion

In this work, we have demonstrated the observation of short-range quantum magnetism of repulsively interacting ultracold fermions in cubic lattices and investigated the dependence on temperature, interaction, lattice dimerization and anisotropy. Our approach is based on a local entropy redistribution scheme within the lattice structure and can be generalized to access the low temperature regime in different geometries, for example two-dimensional systems. The tunable geometry optical lattice allows the extension of our studies to spin-ladder systems, dimerized one-dimensional chains and zig-zag chains, where the interplay between quantum fluctuations and magnetic ordering plays a particularly important role [8, 195]. At even lower temperatures, the existence of spin-liquids in honeycomb or triangular lattices could be investigated [4].

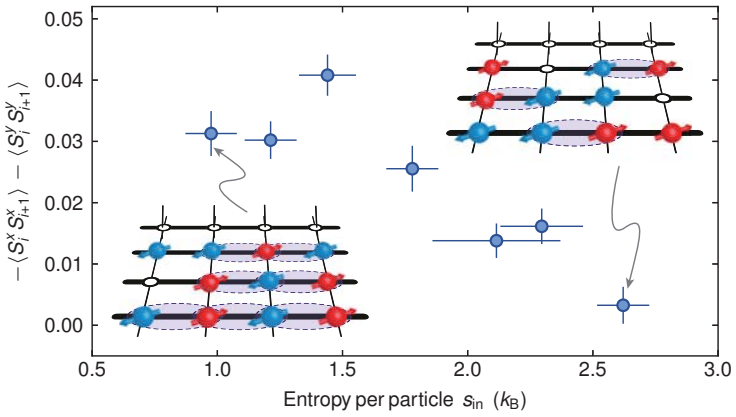

FIGURE 7.10.: **Nearest-neighbour antiferromagnetic order.** Transverse spin correlator versus entropy before loading into the lattice at $U/t = 10.5(8)$ and $t_s/t = 7.3(6)$, together with a schematic view of the spin ordering. Error bars as in Fig. 7.9.

8 Engineering Dirac points

8.1. Introduction

Ultracold gases in optical lattices have emerged as a versatile tool to simulate a wide range of condensed matter phenomena [27, 29]. For example, the control of interactions in fermionic quantum gases has lead to the observation of Mott insulating phases [33, 55, 56], thus providing new access to the physics of strongly correlated materials. However, the topology of the band structure is of equal importance to the properties of a solid. A prime example is the honeycomb lattice of graphene, where the presence of topological defects in momentum space – the Dirac points – leads to surprising properties of the material. These range from extraordinary transport properties and ultra-high mobilities to effectively massless electrons and conducting edge states in topological insulators [196, 197]. At a Dirac point, two energy bands intersect linearly and the particles behave as relativistic Dirac fermions. In quantum gases, a honeycomb lattice has recently been realised and investigated with a Bose-Einstein condensate [198, 199], but no signatures of Dirac points were observed.

In this chapter the creation and observation of Dirac points with adjustable properties is reported for an ultracold quantum gas in an optical lattice. The honeycomb lattice structure is created by the tunable-geometry optical lattice, which was introduced in chapter 2.1.2. The presence of Dirac points in the band structure is identified by a minimum band gap inside the Brillouin zone, which is detected from momentum-resolved interband transitions of a non-interacting gas of ^{40}K. The detection method is closely related to a technique recently used with bosonic atoms to characterize the linear crossing of two high-energy bands in a one-dimensional bichromatic lattice [69] – with the extension of providing additional momentum resolution. Exploiting the unique tunability of the lattice potential allows adjusting the effective mass of the Dirac fermions by breaking the inversion symmetry. Additionally, a change in the lattice anisotropy leads to a shift of the position of the Dirac points inside the Brillouin zone. When increasing the anisotropy beyond a critical limit, the two Dirac points merge and annihilate each other – a situation that has recently attracted considerable theoretical interest [87, 88, 89, 90, 91], but seems extremely challenging to observe in solids [92]. This topological transition in lattice parameter space is mapped out and is found to be in excellent agreement with *ab initio* calculations [1]. In following work [86, 93, 94] very good agreement of the experimentally determined transfer fractions after one full Bloch cycle was found with a simple Landau-Zener model for the two lowest bands.

[1] Parts of this chapter have been published in [85, 86].

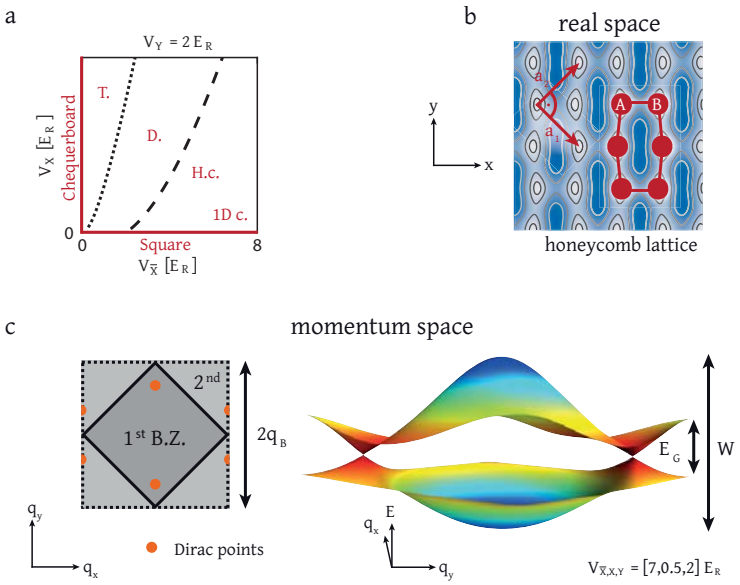

FIGURE 8.1.: **The honeycomb lattice.** (a) Different lattice potentials can be realised depending on the intensities of the lattice beams. The diagram shows the accessible lattice geometries as a function of the lattice depths $V_{\overline{X}}$ and V_X. The transition between triangular (T.) and dimer (D.) lattices is indicated by a dotted line. When crossing the dashed line into the honeycomb (H.c.) regime, Dirac points appear. The limit $V_{\overline{X}} \gg V_{X,Y}$ corresponds to weakly coupled one-dimensional chains (1D c.). (b) The real space potential of the honeycomb lattice has a 2-site unit cell (A,B sites) and the primitive lattice vectors are perpendicular. (c) Scetch of the first and second Brillouin zones (B.Z.) of the honeycomb lattice, indicating the position of the Dirac points. On the right, a three dimensional view of the energy spectrum shows the linear intersection of the bands at the two Dirac points. We denote the full bandwidth W, and the minimum energy gap at the edges of the Brillouin zone E_G.

8.2. The honeycomb lattice

The two-dimensional lattice potential is formed by the beams $V_{\overline{X}}$, V_X and V_Y of the tunable-geometry optical lattice, whereas we set $V_Z = 0$. For the measurements presented in this chapter there is along the z-axis no lattice potential and only a harmonic confinement present. The total expression for the lattice potential reads

$$V(x,y) = -V_{\overline{X}}\cos^2(kx+\theta/2) - V_X\cos^2(kx) \\ -V_Y\cos^2(ky) - 2\alpha\sqrt{V_X V_Y}\cos(kx)\cos(ky)\cos\phi. \tag{8.1}$$

Here $\alpha = 0.9$ is the visibility of the interference pattern and the interference phase is set to $\phi = 0$ and the symmetry phase to $\theta = \pi$, unless stated otherwise. As shown in Fig. 8.1a and explained in chapter 2.1.2, the exact lattice structure depends on the values of the lattice beam intensities. In the following we focus on the honeycomb lattice, which contains two Dirac points inside the first Brillouin zone. The corresponding real space potential for an exemplary set of lattice depths is shown in Fig. 8.1b.

The honeycomb lattice consists of two sublattices A and B. Therefore, the wavefunctions are two-component spinors. Tunnelling between the sublattices leads to the formation of two

energy bands, which are well separated from the higher bands and have a conical intersection at two quasi-momentum points in the Brillouin zone – the Dirac points. These points are topological defects in the band structure, with an associated Berry phase of $\pm\pi$. This warrants their stability with respect to lattice perturbations, so that a large range of lattice anisotropies only changes their position inside the Brillouin zone. In contrast, breaking the inversion symmetry of the potential by introducing an energy offset Δ between sublattices (or equivalently neighbouring sites) opens an energy gap at the Dirac points, which is proportional to the offset. In our implementation, the sublattice offset Δ depends only on the value of the symmetry phase θ and can be precisely adjusted. For $\theta = \pi$ a vanishing site offset is expected, corresponding to gapless Dirac points. The primitive lattice vectors are perpendicular, which leads to a square Brillouin zone with two Dirac points inside, see Fig. 8.1c. Their position is symmetric around the center and fixed to $q_x = 0$, owing to the time-reversal and reflection symmetries of the system [200]. The band structure for our lattice implementation is in the two lowest bands topologically equivalent to that of a hexagonal lattice with six-fold symmetry. For deep lattices both configurations then also map to the same tight-binding Hamiltonian.

8.3. Preparation and detection

The detection and characterization of the Dirac points in the honeycomb lattice is done by probing the energy splitting between the two lowest energy bands through interband transitions of a non-interacting Fermi gas. In the following the experimental preparation sequence is briefly outlined. After sympathetic cooling with ^{87}Rb in a magnetic trap, 2×10^6 fermionic ^{40}K atoms are transferred into the crossed beam dipole trap. A balanced spin mixture of the $|F, m_F\rangle = |9/2, -9/2\rangle$ and $|9/2, -7/2\rangle$ states is then evaporatively cooled at a magnetic field of 197.6(1) G down to typical temperatures of $0.2\,T_\mathrm{F}$, where T_F is the Fermi temperature. The magnetic bias field is subsequently reduced and a magnetic field gradient is used to selectively remove the $|9/2, -7/2\rangle$ component, while levitating the $|9/2, -9/2\rangle$ atoms against gravity. The resulting polarised Fermi gas contains about $50,000$ particles in the $|F, m_F\rangle = |9/2, -9/2\rangle$ state, which are then loaded into the lowest energy band of a honeycomb lattice with $V_{\overline{X},X,Y}/E_R = [4.0(2), 0.28(1), 1.8(1)]$ using a spline shaped ramp of all lattice depths within 200 ms. After turning off the crossed beam dipole trap in this configuration, the residual weak harmonic confinement from the lattice beams is $\omega_{x,y,z}/2\pi = [17.6(1), 31.8(5), 32.7(5)]$ Hz.

The interband transition is induced by applying a weak magnetic field gradient along the x direction, which subjects the atomic cloud to a constant force F – equivalent to an electric field in solid-state systems (for more details see chapter 4.1). The atoms are hence accelerated such that their quasi-momentum q_x increases linearly up to the edge of the Brillouin zone, where a Bragg reflection occurs. The cloud then eventually returns to the center of the band, performing one full Bloch oscillation [201]. The quasi-momentum distribution of the atoms in the different bands is then measured using a band-mapping technique [42], see chapter 4.2.2.

Owing to the finite momentum width of the cloud, trajectories with different quasi-momenta q_y are simultaneously explored during the Bloch cycle, as illustrated in Fig. 8.2. For a trajectory far from the Dirac points, the atoms remain in the lowest energy band (trajectory

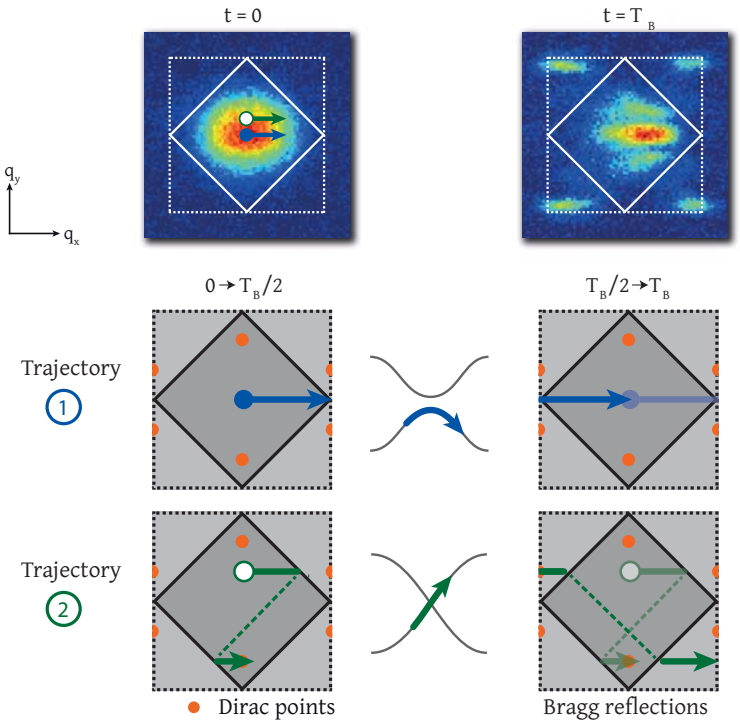

FIGURE 8.2.: **Probing the Dirac points.** Quasi-momentum distribution of the atoms before and after one Bloch oscillation of period T_B. The cloud explores several trajectories in quasi-momentum space simultaneously. For trajectory 1 (blue solid circle) the atoms remain in the first energy band. In contrast, trajectory 2 (green open circle) passes through a Dirac point at $t = T_B/2$. There, the energy splitting between the bands vanishes and the atoms are transferred to the second band. When measuring the quasi-momentum distribution at $t = T_B$, these atoms are missing in the first Brillouin zone and appear in the second one.

1). In contrast, when passing through a Dirac point (trajectory 2), the atoms are transferred from the first to the second band because of the vanishing energy splitting at the linear band crossing. When measuring the quasi-momentum distribution, these atoms are missing in the first Brillouin zone and appear in the second band, as can be seen in Fig. 8.2. We identify the points of maximum transfer with the Dirac points. The energy resolution of the method is set by the characteristic energy of the applied force [201] $E_B/h = F\lambda/2h = 88.6(7)$ Hz, which is small compared to the full bandwidth $W/h = 4.6$ kHz and the minimum band gap at the edges of the Brillouin zone $E_G/h = 475$ Hz.

To investigate how breaking the inversion symmetry of the lattice affects the Dirac points, we vary the sublattice offset Δ, which is controlled by the frequency detuning δ between the lattice beams, and measure the total fraction of atoms transferred to the second band ξ. The results obtained for a honeycomb lattice with $V_{\overline{X},X,Y}/E_R = [3.6(2), 0.28(1), 1.8(1)]$ are displayed in Fig. 8.3, and show a sharp maximum in the transferred fraction. We identify this situation as the point of inversion symmetry $\Delta = 0$ ($\theta = \pi$), where the band gap at the Dirac point vanishes. From the peak position we obtain a value of $\theta/\delta = [\pi/384.7(6)]$ MHz^{-1}, which is close to the value from the independent calibration using Raman-Nath diffraction $\theta/\delta = [\pi/390.0(4)]$ MHz^{-1}, see section 2.2.4. The population in the second band decreases

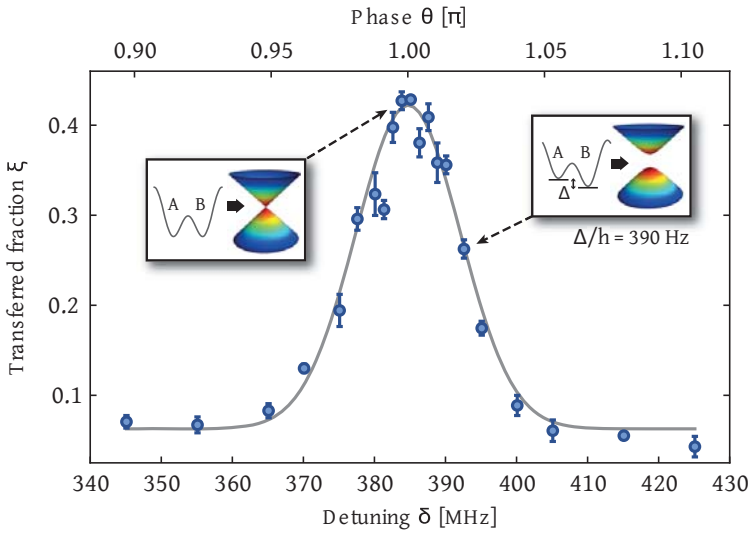

FIGURE 8.3.: **Probing the Dirac points.** Dependence of the total fraction of atoms transferred to the second band ξ on the detuning of the lattice beams δ, which controls the sublattice energy offset Δ. The maximum indicates the point of inversion symmetry, where $\Delta = 0$ ($\theta = \pi$ in equation 8.1) and the gap at the Dirac point vanishes. Away from the peak, the atoms behave as Dirac fermions with a tunable mass (see insets). Values and error bars denote the mean and standard deviation of five consecutive measurements, whereas the solid line is a Gaussian fit to the data.

symmetrically on both sides of the peak as the gap opens up, indicating the transition from massless to massive Dirac fermions.

8.4. Moving and merging Dirac points

The relative strength of the tunnel couplings between the different sites of the lattice fixes the position of the Dirac points inside the Brillouin zone, as well as the slope of the associated linear dispersion relation [87, 88, 89, 90, 91]. As explained in chapter 2.3, the tunability of our optical lattice structure allows an independent adjustment of the tunnelling parameters along the x and y directions simply by controlling the intensity of the laser beams. For isotropic tunnellings the slope of the Dirac cones is the same in all directions, while being anisotropic otherwise. The distance of the Dirac points to the corners of the Brillouin zone along q_y can be varied between 0 and $k/2$, whilst $q_x = 0$ due to reflection symmetry [200]. Here $k = 2\pi/\lambda$ denotes the Bloch wave vector.

We exploit the momentum resolution of the interband transitions to directly observe the movement of the Dirac points. Starting from a honeycomb lattice with $V_{\overline{X},X,Y}/E_R = [5.4(3), 0.28(1), 1.8(1)]$, we gradually increase the tunnelling along the x direction by decreasing the intensity of the $\overline{X}$ beam. As displayed in Fig. 8.4, the position of the Dirac points continuously approaches the corners of the Brillouin zone, as expected from the *ab initio* two-dimensional band structure calculation done in chapter 2.3. The deviations close to the merging point are possibly caused by the flattening of the dispersion relation between the two Dirac points as they approach each other [90].

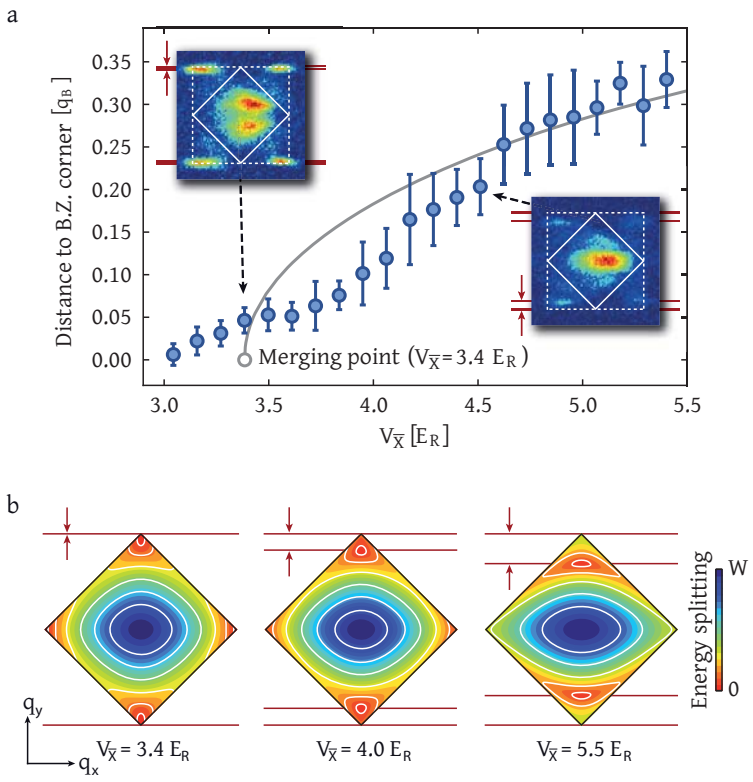

FIGURE 8.4.: **Movement of the Dirac points.** (a) Distance of the Dirac points to the corners of the Brillouin zone, as measured through momentum-resolved interband transitions. The tunnelling along the x direction increases when decreasing the lattice depth $V_{\overline{X}}$. The distance is extracted from the second band quasi-momentum distribution after one Bloch cycle (see insets). The merging of the two Dirac points at the corners of the Brillouin zone is signalled by a single line of missing atoms in the first band. Values and error bars are the mean and standard deviation of three to nine measurements. The solid line is the prediction of a two-dimensional band structure calculation without any fitting parameters. (b) Energy splitting between the two lowest bands, showing the displacement of the Dirac cones inside the Brillouin zone, as well as their deformation depending on the lattice depth $V_{\overline{X}}$.

When reaching the corners, the two Dirac points merge and annihilate each other. There, the dispersion relation becomes quadratic along the q_y axis and remains linear along q_x. Beyond this critical point, a finite band gap appears for all quasi-momenta of the Brillouin zone. This situation signals the transition between band structures of two different topologies, one containing two Dirac points and the other none. For two-dimensional honeycomb lattices at half filling, this corresponds to a Lifshitz phase transition from a semi-metallic to a band-insulating phase [88, 89].

We experimentally map out the topological transition line by recording the fraction of atoms transferred to the second band ξ as a function of the lattice depths $V_{\overline{X}}$ and V_X, while keeping $V_Y/E_R = 1.8(1)$. The results are displayed in Fig. 8.5a. There, the onset of population transfer to the second band signals the appearance of Dirac points in the band structure of the lattice. The transferred fraction ξ decreases for large values of $V_{\overline{X}}$, as the Dirac point positions exceed the momentum width of the cloud.

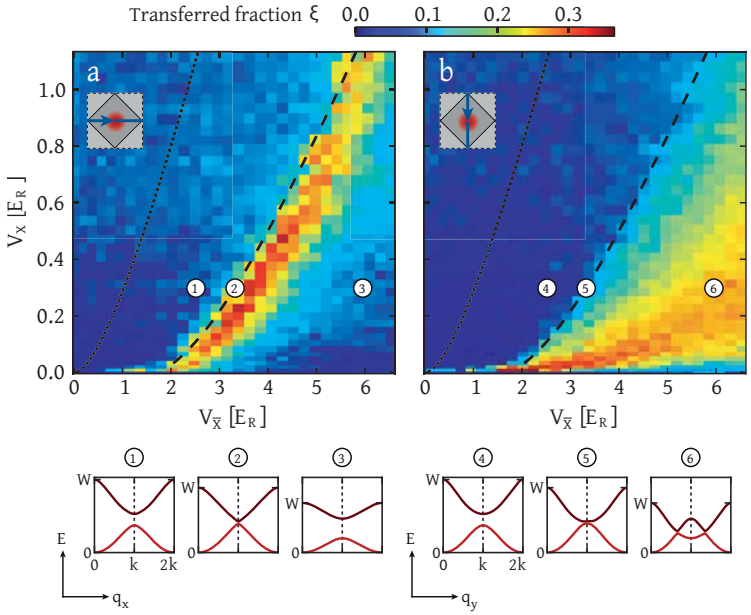

FIGURE 8.5.: **Topological transition.** Fraction of atoms transferred to the second band ξ as a function of lattice depths $V_{\overline{X}}$ and V_X, with $V_Y/E_R = 1.8(1)$. Different lattice geometries (square, diagonal, triangular, dimer and honeycomb) are realised, see Fig. 8.1a. We consider trajectories in quasi-momentum space along the q_x and q_y directions (**a** and **b** resp.). Each data point is a single measurement, resulting in at least 1200 points per diagram. To maximise the transfer for the q_y trajectories, where the cloud successively passes the two Dirac points, we set $\theta = 1.013(1)\pi$. In both cases, the onset of population transfer to the second band signals the topological transition, where the Dirac points appear. The dashed line is the theoretical prediction for the transition line without any fitting parameters, while the dotted line indicates the transition from the triangular to the dimer lattice. The insets show cuts of the band structure for increasing $V_{\overline{X}}$ along the q_x axis ($q_y = 0$) and q_y axis ($q_x = 0$) respectively.

To extend the range of our measurements and probe the Dirac points even in this regime, we apply a force along the y direction. We hence explore a new class of trajectories in quasi-momentum space. This allows for the investigation of very anisotropic Dirac cones, which become almost flat along the q_x direction as we approach the crossover to a one-dimensional lattice structure ($V_{\overline{X}} \gg V_X$). Along the q_y trajectories the center of the cloud successively passes the two Dirac points during the Bloch cycle, effectively realising a Stückelberg interferometer [202, 203] in a two-dimensional band structure. As displayed in Fig. 8.5b, we again identify the topological transition through the onset of population transfer to the second band. The results for the transition line obtained for both measurement series are in excellent agreement with *ab initio* band structure calculations. At the transition, the transfer is expected to be lower by a factor of two along the central q_y trajectory, as compared to the central q_x trajectory. This is caused by the dispersion relation at the corners of the Brillouin zone being quadratic along the q_y axis and linear along q_x. For the data points on the (dashed) transition line in Fig. 8.5 we find an average ratio for the transfer along q_y and q_x of 0.52(14), in good agreement with the simple model.

8.5. Conclusion

In this work we have realised Dirac points with highly tunable properties using ultracold fermionic atoms in a honeycomb optical lattice. A new class of physical phenomena is now within the domain of quantum gas experiments. Furthermore, the flexibility and novel observables of these systems will provide new insights. For example, the unique coherence of quantum gases offers the possibility of directly measuring the Berry phase associated to the Dirac points by interferometric methods. Topological order could be achieved by introducing artificial gauge fields, either via Raman transitions [204] or time-dependent lattice modulation [205]. Moreover, the exceptionally tunable lattice potential we have developed opens up a wealth of new avenues for optical lattice experiments. For spin mixtures with repulsive interactions, the dynamic transition between dimer and square lattices should facilitate the adiabatic preparation of an anti-ferromagnetic phase [75] and enable the study of quantum criticality [7]. Additionally, the triangular and honeycomb lattices provide the possibility to explore magnetic frustration and spin liquid phases [11, 4].

9 Outlook

The experiments presented in this thesis are only the first step in a series of experiments making use of the tunable-geometry optical lattice. In the following a few ideas for future experiments are presented, which in fact have already been implemented in parts.

Next generation entropy redistribution

The key to reaching the regime of quantum magnetism in the measurements presented in chapter 7 is a combination of entropy redistribution between different degrees of freedom and spatial regions of the trapped system. As shown in Fig. 9.1a, for an average entropy per particle of $S/N = 1.0k_\mathrm{B}$ the local entropy per particle at half-filling drops below $0.1k_\mathrm{B}$ in the dimerized lattice configuration. This low value can be exploited to create ultra-low entropy states after isolation of the high-entropy region via, for example, a repulsive ring potential created by a Laguerre-Gaussian beam [206]. After the isolation of the low entropy region, the lattice potential can then be changed adiabatically to a simple cubic configuration for the creation of a long-range ordered antiferromagnet, or to weakly coupled two-dimensional planes for investigating the possible presence of a d-wave superfluid state. Initial measurements have already been performed in the absence of a repulsive ring potential, where after loading a repulsive two-component Fermi gas into a strongly dimerized structure the lattice was quickly changed to a cubic configuration while observing the damping of the singlet-triplet imbalance. The decay time constant was found to be comparable to the tunnelling time between neighbouring sites in the final lattice configuration, which possibly suggests local thermalization of the state on this time scale.

An alternative route to isolating low-entropy regions is tailoring the trapping potential in a suitable way. The basic idea is to reduce the temperature of the gas in the lattice by choosing a very small harmonic confinement. While this of course leads to very low densities, the relevant density of half-filling in the lattice for creating the magnetic quantum state of interest is ensured by an additional dimple potential in the center of the trap, see Fig. 9.1b. Assuming global thermal equilibrium, the large harmonic trap then serves as an entropy reservoir and sets the temperature of the entire system, whereas the dimple potential is responsible for the filling in the center. In that way for example the Neel state can already be reached for an average entropy per particle in the entire system of $1.0k_\mathrm{B}$. This was determined from the equation of state obtained from dynamical-cluster approximation calculations, kindly provided to our group by Lode Pollet [138]. Following these ideas, an independent confinement control was installed into the experiment, which consists of two blue detuned beams co-aligned with the other optical beams along the spatial x- and z-axes and gives control over the trap frequencies along these directions, see right panel of Fig. 9.1b. Additionally a focussed red-detuned dimple beam was installed with a $1/e^2$ radius of about

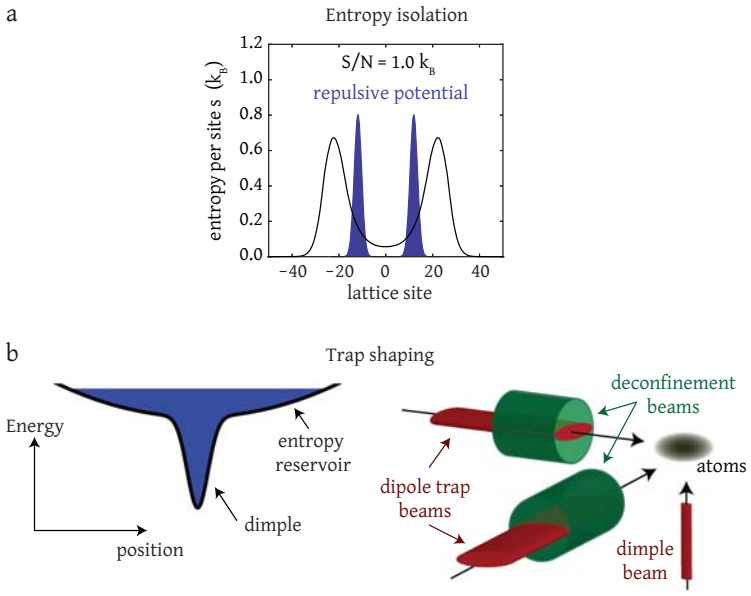

FIGURE 9.1.: **Entropy redistribution schemes.** (a) Entropy distribution via lattice dimerization and subsequent isolation of the low-entropy region. The entropy distribution in a harmonic trap for a dimerized lattice with $U/6t = 1.6$ and $t_d/t = 34$ ($t/h = 67$ Hz) calculated from the second order high-temperature series expansion is shown. The total entropy per particle in the entire trapped system is set to $S/N = 1.0k_B$ with a total atom number of $50'000$ and a geometric mean trap frequency of $\overline{\omega} = 2\pi \times 79$ Hz. A subsequently turned on repulsive potential originating for example form a blue-detuned Laguerre-Gaussian beam is indicated in blue. The central trap region then contains a very low entropy. (b) Entropy distribution by trap shaping. A schematic view of the low-density entropy reservoir and the dimple region ensuring half-filling is shown. On the right the installed experimental implementation is summarized, including two blue detuned deconfinement beams for reducing the trap frequencies and a tightly focussed red-detuned dimple beam.

12 μm. Whether or not this entropy distribution scheme works can be probed by measuring the normalized transverse spin correlator $\mathcal{S}$ as done in the measurements in the anisotropic cubic lattice of chapter 7.

Spin ladders and zig-zag chains

As shown in the measurements of chapter 7, the tunable-geometry optical lattice allows studying the quantum magnetism of one-dimensional spin systems. The experimental setup additionally gives access to more complex situations, where the lattice structure is *in between* one and two dimensions. A prominent yet not fully understood system are spin ladders, which have been a subject of intense research over the least decades [207]. One of the most remarkable properties is that these systems have a spin gap for an even number legs, whereas no gap is present for an odd number. In the presence of a magnetic field, a transition from a Luttinger-liquid of fermions to a Bose-Einstein condensate of hard-core bosons formed by triplons has been predicted [208]. In addition, doped spin-ladders have been proposed to show superconducting behaviour at very low temperatures [209] – however the exact phase-

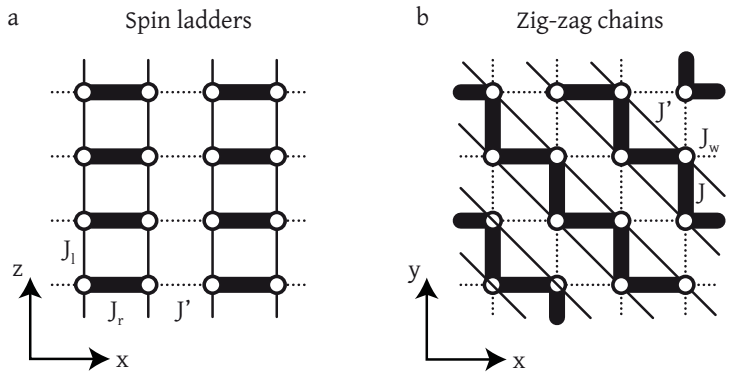

FIGURE 9.2.: **Accessible lattice topologies.** Two alternative lattice geometries are shown, which can be realized with the tunable-geometry optical lattice. (a) Spin ladders with a rung and ladder exchange energy J_r and J_l. Additionally the spin ladders can be coupled via inter-ladder exchange energy J'. All exchange energies can be controlled independently. The ladders are arranged on a chequerboard pattern in the $x-y$ plane. (b) By imbalancing the retro-reflected beams, zig-zag chains can be created in the $x-y$ plane with a nearest and next-nearest neighbour exchange energy J and J'. Additionally the zig-zag chains are coupled via an inter-chain exchange energy J_w.

diagram in the spin 1/2 Fermi-Hubbard regime is not well understood. Spin ladders can be realized and studied with the tunable-geometry optical lattice, where the rung and ladder exchange energies J_r and J_l as well as the inter-ladder exchange J' can be fully controlled, see Fig. 9.2.

An alternative is the investigation of zig-zag chains, which are one-dimensional spin chains with nearest-neighbour exchange energy J and frustrated next-nearest neighbour exchange energy J'. This system appears for example in $SrCuO_2$ [210] and has been predicted to contain a phase-transition from a spin fluid to a spontaneously dimerized state depending on the ratio of J/J' [211]. This structure can be obtained with the tunable-geometry optical lattice by breaking the reflection symmetry of the unit cell via imbalancing the power of the retro-reflected laser beams.

Strongly interacting graphene and ionic Hubbard models

For the measurements presented in chapter 8 a non-interacting fermionic gas was loaded into a honeycomb lattice to study the underlying band structure and investigate the Dirac points. The presence of the ^{40}K Feshbach resonance additionally gives access to strongly interacting two-component mixtures in a honeycomb lattice, which is well described by the Fermi-Hubbard model. While ordinary Graphene is in the weakly interacting regime with an interaction to kinetic energy ratio $U/t \sim 1$, the cold atoms approach allows free adjustment of all relevant parameters and gives access to a strongly interacting analogue of Graphene and a Mott-insulating state in the honeycomb lattice. Here, the expected experimental observation would be a suppression of doubly occupied sites for strong repulsive interactions, similar to the observation of a Mott-insulating state in a simple cubic lattice [55]. Additionally, the critical interaction for the metal to Mott-insulator transition in the two dimensional honeycomb lattice can be investigated, which was predicted to be non-zero, in contrast to the case

for a two-dimensional square lattice. Despite the comparatively high temperatures in the experiment, a shift in the interaction energy dependence of the double occupancy between the two lattices configurations might still be observable. When combining the honeycomb lattice with entropy redistribution schemes, cold atoms may be able to contribute to the debate of the disputed existence of a gapless spin-liquid state at low temperatures and intermediate interactions in a half-filled honeycomb lattice [4, 5]. The inter-band transfer technique presented in chapter 8, which was used for probing the Dirac points, can also be applied to the case of a weakly interacting gas in order to investigate for example the interaction-dressed band structure in the vicinity of the Dirac points.

The tunable-geometry optical lattice also allows the realization of ionic Hubbard models, where neighbouring sites on a bipartite lattice have alternating energy offsets Δ. For the half-filled spin-1/2 system a band-insulating state is expected in the limiting case $\Delta \gg U$, which is connected to a Mott-insulator in the opposite regime $\Delta \ll U$ [212]. The exact phase in the intermediate regime for dimensions higher than one remains disputed until today and the possible existence of an intermediate bond-ordered or metallic state is still questioned. In the experiment a two- or three-dimensional cubic lattice can be created, where the neighbouring site offset is controlled via the symmetry phase θ, see Eq. 2.3. The transition from a band- to a Mott-insulator can then be detected by a suppression of the double occupancy.

Topologically protected states

A very new direction of cold atoms in optical lattices is the creation of topologically protected states and the realization of artificial magnetic fields for neutral atoms. The essential idea is to start from a tight-binding lattice model and introduce complex instead of real tunnellings for some of the lattice bonds by explicit breaking of time-reversal symmetry. This can either lead to a flux lattice, which requires the phase-pickup around the lattice unit cell modulo 2π to be non-zero, or can give rise to a staggered flux lattice. The topological properties of the underlying lattice can then be characterized by the Chern number (the Brillouin zone integral over the Berry-curvature), which remains unchanged in the presence of disorder or interaction effects. For a detailed study of how to realize lattices with non-trivial topologies, see for example [213]. Already a few years ago an artificial magnetic field for cold atoms in a harmonic trap could be realized [204]. This was followed by the realization of complex tunnellings via lattice shaking [59, 214] and Raman beams [215] and the measurement of the Zak phase in a one-dimensional dimerized lattice [216].

Starting from a honeycomb lattice, topologically protected states can be created in our experimental either by circular shaking of the lattice or circular modulation of the tunnel couplings, similar to the initial proposals [217, 218], see Fig. 9.3. Both approaches lead to complex tunnel couplings between nearest and/or next-nearest neighbours on the honeycomb lattice – in close analogy to the Haldane model [219] – and require only minimal extension of the current optical lattice setup. The circular lattice shaking can either be realized by modulating the position of the retro-reflecting mirror via a piezo, or by applying a periodic force on the atoms via a modulating magnetic field gradient. The tunnel couplings can be changed by imbalancing the retro-reflected power periodically in time, which can be achieved by including and electro-optical modulator into the setup. Further details can be found in [220]. Following either scheme, a topologically protected state with a Chern number of $\nu = \pm 1$ can be created.

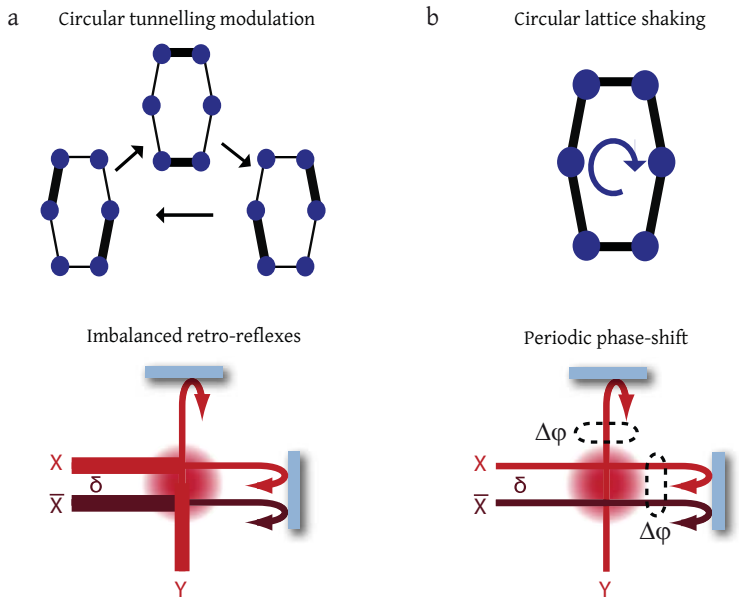

FIGURE 9.3.: **Topologically protected states.** Two approaches towards the creation of topologically protected states in a honeycomb lattice are shown. Both methods rely on explicit breaking of time-reversal symmetry and effectively realize a Haldane-type model with complex tunnelling matrix elements. The topologically protected state is then characterized by a Chern number of $\nu = \pm 1$. (a) Circular modulation of the tunnel couplings on the honeycomb unit cell. This can be achieved via a periodic imbalance of the retro-reflected laser beam power of the optical lattice beams. (b) Circular shaking of the entire lattice structure, achieved via a periodic phase-shift of the retro-reflected beams.

A Cubic lattice: high-temperature series

In the following we give the full expression for some observables up to second order in a high-temperature series. All other observables used in the main text can be derived from derivatives of the grand canonical potential. We use the same abbreviations as in the main text with $\beta = 1/k_{\mathrm{B}}T$, $\zeta = \exp(\beta\mu)$ and $w = \exp(-\beta \mathrm{U})$. For the on-site densities and nearest-neighbor correlators we furthermore give all graphs, relevant states and their contributions to the graph weight. The expression for the density can also be independently obtained from a derivative of the grand potential.

$$
\begin{aligned}
z_0 &= 1 + 2\zeta + \zeta^2 w && \text{(A.1)}\\
-\beta\Omega^s(\zeta, w, \beta t) &= \log(z_0) + && \text{(A.2)}\\
&\quad (\beta t)^2 \frac{c}{z_0^2}\left(2\zeta(1+\zeta^2 w) + \frac{4\zeta^2}{\beta U}(1-w)\right)\\
s(\zeta, w, \beta t) &= -\frac{\partial \Omega^s}{\partial T} && \text{(A.3)}\\
n(\zeta, w, \beta t) &= \frac{2\zeta + 2\zeta^2 w}{z_0} - \frac{12\zeta(1+\zeta w)X_2}{z_0^3}(\beta t)^2 + && \text{(A.4)}\\
&\quad \frac{6(\zeta + 4\zeta^2(1-w)/(\beta U) + 3\zeta^3 w)}{z_0^2}(\beta t)^2\\
d(\zeta, w, \beta t) &= \frac{\partial \Omega^s}{\partial U} && \text{(A.5)}\\
C_{dd}(\zeta, w, \beta t) &= \frac{4\zeta^2}{z_0^2} + \frac{4\zeta^2(\frac{1}{\beta U} + \frac{w-1}{(\beta U)^2})}{z_0^2}(\beta t)^2 - \frac{44\zeta^2 X_2}{z_0^4}(\beta t)^2 && \text{(A.6)}\\
&\quad + \frac{20\zeta^2(1+\zeta^2 w + 4\zeta(\frac{1}{\beta U} + \frac{w-1}{(\beta U)^2}))}{z_0^3}(\beta t)^2\\
C_{ss}(\zeta, w, \beta t) &= -\frac{\zeta^2(\frac{1}{\beta U} + \frac{w-1}{(\beta U)^2})}{z_0^2}(\beta t)^2. && \text{(A.7)}
\end{aligned}
$$

graph	state $\|\Psi_i\rangle$	$\frac{1}{\beta^2}\int\int\langle\Psi_i\|...\|\Psi_i\rangle$
○—●	$\|\uparrow,0\rangle, \|\downarrow,0\rangle$	$2\times 1\times\frac{1}{3}\zeta$
○—●	$\|0,\downarrow\rangle, \|0,\uparrow\rangle$	$2\times 1\times\frac{1}{6}\zeta$
○—●	$\|\uparrow,\downarrow\rangle, \|\downarrow,\uparrow\rangle$	$2\times 2\times\frac{\zeta^2}{\beta U}(1+\frac{w-1}{\beta U})$
○—●	$\|\downarrow\uparrow,0\rangle$	$1\times 2\times\frac{2\zeta^2 w}{\beta U}(-1+\frac{1/w-1}{\beta U})$
○—●	$\|\downarrow\uparrow,\downarrow\rangle, \|\downarrow\uparrow,\uparrow\rangle$	$2\times 1\times\frac{5}{6}\zeta^2 w$
○—●	$\|\downarrow,\downarrow\uparrow\rangle, \|\uparrow,\downarrow\uparrow\rangle$	$2\times 1\times\frac{4}{6}\zeta^2 w$

TABLE A.1.: **On-site density** Second order graph contributions to the on-site density n in the Fermi-Hubbard model. Only one graph contributes and a two site basis is chosen for evaluation ($l=2$). The left and right entry of the state $|\Psi_i\rangle$ corresponds to the left and right site of the graph. The matrix element is multiplied by the number of states (first number) and the amount of tunneling processes (second number), whereas the last number is the weight contribution according to Eq. 3.44. States that do not contribute are omitted. The total graph contribution for the enumerator correction is obtained by the sum of all contributions, see Eq. 3.39. The 0th order enumerator term for the density is $(2\zeta+2\zeta^2 w)z_0$.

graph	state $\|\Psi_i\rangle$	$\frac{1}{\beta^2}\int\int\langle\Psi_i\|...\|\Psi_i\rangle$
○—○	$\|\uparrow,\downarrow\rangle, \|\downarrow,\uparrow\rangle$	$2\times 2\times\frac{\zeta^2}{\beta U}(1+\frac{w-1}{\beta U})$
•—○ ○	$\|\downarrow,0,\uparrow\rangle, \|\uparrow,0,\uparrow\rangle$	$2\times 1\times\frac{\zeta^2}{6}$
•—○ ○	$\|\uparrow,0,\downarrow\rangle, \|\downarrow,0,\downarrow\rangle$	$2\times 1\times\frac{\zeta^2}{6}$
•—○ ○	$\|0,\downarrow,\uparrow\rangle, \|0,\uparrow,\uparrow\rangle$	$2\times 1\times\frac{\zeta^2}{3}$
•—○ ○	$\|0,\uparrow,\downarrow\rangle, \|0,\downarrow,\downarrow\rangle$	$2\times 1\times\frac{\zeta^2}{3}$
•—○ ○	$\|\uparrow,\downarrow,\uparrow\rangle, \|\uparrow,\downarrow,\downarrow\rangle$	$2\times 2\times\frac{\zeta^3}{\beta U}(1+\frac{w-1}{\beta U})$
•—○ ○	$\|\downarrow,\uparrow,\uparrow\rangle, \|\downarrow,\uparrow,\downarrow\rangle$	$2\times 2\times\frac{\zeta^3}{\beta U}(1+\frac{w-1}{\beta U})$
•—○ ○	$\|\uparrow\downarrow,\downarrow,\downarrow\rangle, \|\uparrow\downarrow,\downarrow,\uparrow\rangle$	$2\times 1\times\frac{\zeta^4 w}{3}$
•—○ ○	$\|\uparrow\downarrow,\uparrow,\downarrow\rangle, \|\uparrow\downarrow,\uparrow,\uparrow\rangle$	$2\times 1\times\frac{\zeta^4 w}{3}$
•—○ ○	$\|\downarrow,\uparrow\downarrow,\downarrow\rangle, \|\downarrow,\uparrow\downarrow,\uparrow\rangle$	$2\times 1\times\frac{\zeta^4 w}{6}$
•—○ ○	$\|\uparrow,\uparrow\downarrow,\downarrow\rangle, \|\uparrow,\uparrow\downarrow,\uparrow\rangle$	$2\times 1\times\frac{\zeta^4 w}{6}$

TABLE A.2.: **Density-density and spin correlator** Second order graph contributions to the density-density correlator C_{dd} in the Fermi-Hubbard model. The entries of the state $|\Psi_i\rangle$ correspond to the sites of the graph from left to right. Two graphs contribute, where one requires a three-site basis, such that the total evaluation is done in a three-site basis ($l = 3$). The 0th order enumerator term is $4\zeta^2 z_0$. For the spin correlator the 0th order enumerator term vanishes, whereas in second order only the two-site graph contributes with the same weight multiplied by $-1/4$.

B Dimerized lattice: high-temperature series

Since the second order expresssions are too complicated, we give here the full expression for the partition function and some observables (on-site density n, double occupancy probability per site d, singlet $|s\rangle$ and triplet $|t_0\rangle$ probability p_s and p_t) in lowest order (atomic limit). All other observables used in the main text can be derived from derivatives of the grand canonical potential. We use the same abbreviations as before and denote $\tau = \exp(\beta t_d)$. The single dimer partition function is denoted with z_0 and we abbreviate $\Delta E_\pm = 1 \pm \sqrt{(4t_d/U)^2 + 1}$.

$$
\begin{aligned}
z_0 &= 1 + 2\zeta^2 + (2\zeta + 2\zeta^3)(\frac{1}{\tau} + \tau) + \zeta^4 w^2 + \qquad \text{(B.1)}\\
&\quad \zeta^2(1 + w + \sqrt{w}^{\Delta E_-} + \sqrt{w}^{\Delta E_+}) \\
-\beta\Omega(\zeta, w, \tau) &= \log z_0 \qquad \text{(B.2)}\\
s(\zeta, w, \tau) &= -\frac{\partial \Omega}{\partial T} \qquad \text{(B.3)}\\
n(\zeta, w, \tau) &= \frac{4\zeta^2 + 4\zeta^4 w^2}{z_0} + \frac{2\zeta + 6\zeta^3 w}{z_0}(\frac{1}{\tau} + \tau) + \qquad \text{(B.4)}\\
&\quad \frac{2\zeta^2}{z_0}(1 + w + \sqrt{w}^{\Delta E_-} + \sqrt{w}^{\Delta E_+}) \\
d(\zeta, w, \tau) &= \frac{\frac{1}{2}\zeta^2 w + \zeta^3(\tau + \frac{1}{\tau}) + \zeta^4 w^2}{z_0} + \qquad \text{(B.5)}\\
&\quad \frac{\zeta^2 \sqrt{w}^{\Delta E_-}}{4 z_0 (1 + \frac{U^2}{16 t_d^2}\Delta E_+)} + \frac{\zeta^2 \sqrt{w}^{\Delta E_+}}{4 z_0 (1 + \frac{U^2}{16 t_d^2}\Delta E_-)} \\
p_s(\zeta, w, \tau) &= \frac{\zeta^2 \sqrt{w}^{\Delta E_-}}{z_0} \qquad \text{(B.6)}\\
p_t(\zeta, w, \tau) &= \frac{\zeta^2}{z_0} \qquad \text{(B.7)}
\end{aligned}
$$

C Physical constants and atomic properties

All physical constants used in this thesis have been taken from
http://physics.nist.gov/constants.
All atomic properties of ^{87}Rb and ^{40}K have been taken from [143, 144] and can be accessed via
http://steck.us/alkalidata/ and
http://staff.science.uva.nl/~tgtiecke/PotassiumProperties.pdf/.

Bibliography

[1] H. T. Diep, G. Misguich and C. Lhuillier. *Two-dimensional quantum antiferromagnets.* In *Frustrated Spin Systems*, (pp. 229–306) (World Scientific, 2005)

[2] J. G. Bednorz and K. A. Müller. *Possible highTc superconductivity in the* $\mathrm{Ba-La-Cu-O}$ *system.* Zeitschrift für Physik B Condensed Matter **64**(2), 189 (1986)

[3] A. K. Geim and K. S. Novoselov. *The rise of graphene.* Nature Materials **6**(3), 183 (2007)

[4] Z. Y. Meng, T. C. Lang, S. Wessel, F. F. Assaad and A. Muramatsu. *Quantum spin liquid emerging in two-dimensional correlated dirac fermions.* Nature **464**(7290), 847 (2010)

[5] S. Sorella, Y. Otsuka and S. Yunoki. *Absence of a spin liquid phase in the hubbard model on the honeycomb lattice.* Scientific Reports **2** (2012)

[6] A. Auerbach. *Interacting Electrons and Quantum Magnetism* (Springer, 1994)

[7] S. Sachdev. *Quantum magnetism and criticality.* Nature Physics **4**(3), 173 (2008)

[8] T. Giamarchi. *Quantum Physics in One Dimension* (Clarendon Press, 2003)

[9] C. Lacroix, P. Mendels and F. Mila. *Introduction to Frustrated Magnetism - Materials, Experiments, Theory* (Springer, 2011)

[10] P. W. Anderson, P. A. Lee, M. Randeria, T. M. Rice, N. Trivedi and F. C. Zhang. *The physics behind high-temperature superconducting cuprates: the plain vanilla version of RVB.* Journal of Physics: Condensed Matter **16**(24), R755 (2004)

[11] L. Balents. *Spin liquids in frustrated magnets.* Nature **464**(7286), 199 (2010)

[12] P.-G. de Gennes. *The Physics of Liquid Crystals* (Oxford University Press, 1995)

[13] J. Hubbard. *Electron correlations in narrow energy bands.* Proceedings of the Royal Society of London. Series A. Mathematical and Physical Sciences **276**(1365), 238 (1963)

[14] P. A. Lee, N. Nagaosa and X.-G. Wen. *Doping a mott insulator: Physics of high-temperature superconductivity.* Reviews of Modern Physics **78**(1), 17 (2006)

[15] B. Nachtergaele, J. P. Solovej and J. Yngvason. *Condensed Matter Physics and Exactly Soluble Models: Selecta of Elliott H. Lieb* (Springer, 2004)

[16] C. Cohen-Tannoudji, J. Dupont-Roc and G. Grynberg. *Atom - Photon Interactions: Basic Process and Appilcations* (2008). http://onlinelibrary.wiley.com/book/10.1002/9783527617197

[17] R. P. Feynman. *Simulating physics with computers*. International Journal of Theoretical Physics **21**(6-7), 467 (1982)

[18] H. J. Metcalf and P. V. d. Straten. *Laser cooling and trapping* (Springer, 1999)

[19] K. B. Davis, M. O. Mewes, M. R. Andrews, N. J. van Druten, D. S. Durfee, D. M. Kurn and W. Ketterle. *Bose-einstein condensation in a gas of sodium atoms*. Physical Review Letters **75**(22), 3969 (1995)

[20] M. H. Anderson, J. R. Ensher, M. R. Matthews, C. E. Wieman and E. A. Cornell. *Observation of bose-einstein condensation in a dilute atomic vapor*. Science **269**(5221), 198 (1995). PMID: 17789847

[21] B. DeMarco and D. S. Jin. *Onset of fermi degeneracy in a trapped atomic gas*. Science **285**(5434), 1703 (1999). PMID: 10481000

[22] S. Jochim, M. Bartenstein, A. Altmeyer, G. Hendl, S. Riedl, C. Chin, J. H. Denschlag and R. Grimm. *Bose-einstein condensation of molecules*. Science **302**(5653), 2101 (2003). PMID: 14615548

[23] M. Greiner, C. A. Regal and D. S. Jin. *Emergence of a molecular Bose–Einstein condensate from a fermi gas*. Nature **426**(6966), 537 (2003)

[24] M. W. Zwierlein, C. A. Stan, C. H. Schunck, S. M. F. Raupach, S. Gupta, Z. Hadzibabic and W. Ketterle. *Observation of bose-einstein condensation of molecules*. Physical Review Letters **91**(25), 250401 (2003)

[25] C. A. Regal, M. Greiner and D. S. Jin. *Observation of resonance condensation of fermionic atom pairs*. Physical Review Letters **92**(4), 040403 (2004)

[26] W. Ketterle, D. S. Durfee and D. M. Stamper-Kurn. *Making, probing and understanding bose-einstein condensates*. cond-mat/9904034 (1999)

[27] M. Lewenstein, A. Sanpera, V. Ahufinger, B. Damski, A. Sen(De) and U. Sen. *Ultracold atomic gases in optical lattices: mimicking condensed matter physics and beyond*. Advances in Physics **56**(2), 243 (2007)

[28] W. Ketterle and M. W. Zwierlein. *Making, probing and understanding ultracold fermi gases*. In M. Inguscio, W. Ketterle and C. Salomon, eds., *Ultracold Fermi Gases* (IOS Press, Amsterdam, 2007)

[29] I. Bloch, J. Dalibard and W. Zwerger. *Many-body physics with ultracold gases*. Reviews of Modern Physics **80**(3), 885 (2008)

[30] T. Esslinger. *Fermi-hubbard physics with atoms in an optical lattice*. Annual Review of Condensed Matter Physics **1**(1), 129 (2010)

[31] C. Chin, R. Grimm, P. Julienne and E. Tiesinga. *Feshbach resonances in ultracold gases*. Reviews of Modern Physics **82**(2), 1225 (2010)

[32] D. Jaksch, C. Bruder, J. I. Cirac, C. W. Gardiner and P. Zoller. *Cold bosonic atoms in optical lattices*. Physical Review Letters **81**(15), 3108 (1998)

[33] M. Greiner, O. Mandel, T. Esslinger, T. W. Hänsch and I. Bloch. *Quantum phase transition from a superfluid to a mott insulator in a gas of ultracold atoms*. Nature **415**(6867), 39 (2002)

[34] M. Greiner, O. Mandel, T. W. Hänsch and I. Bloch. *Collapse and revival of the matter wave field of a Bose–Einstein condensate*. Nature **419**(6902), 51 (2002)

[35] S. Trotzky, L. Pollet, F. Gerbier, U. Schnorrberger, I. Bloch, N. V. Prokof'ev, B. Svistunov and M. Troyer. *Suppression of the critical temperature for superfluidity near the mott transition*. Nature Physics **6**(12), 998 (2010)

[36] C.-L. Hung, X. Zhang, N. Gemelke and C. Chin. *Observation of scale invariance and universality in two-dimensional bose gases*. Nature **470**(7333), 236 (2011)

[37] M. J. Mark, E. Haller, K. Lauber, J. G. Danzl, A. J. Daley and H.-C. Nägerl. *Precision measurements on a tunable mott insulator of ultracold atoms*. Physical Review Letters **107**(17), 175301 (2011)

[38] X. Zhang, C.-L. Hung, S.-K. Tung and C. Chin. *Observation of quantum criticality with ultracold atoms in optical lattices*. Science **335**(6072), 1070 (2012). PMID: 22345397

[39] B. Gadway, D. Pertot, J. Reeves and D. Schneble. *Probing an ultracold-atom crystal with matter waves*. Nature Physics **8**(7), 544 (2012)

[40] W. S. Bakr, A. Peng, M. E. Tai, R. Ma, J. Simon, J. I. Gillen, S. Fölling, L. Pollet and M. Greiner. *Probing the superfluid–to–mott insulator transition at the single-atom level*. Science **329**(5991), 547 (2010)

[41] J. F. Sherson, C. Weitenberg, M. Endres, M. Cheneau, I. Bloch and S. Kuhr. *Single-atom resolved fluorescence imaging of an atomic mott insulator*. Nature **467**(7311), 68 (2010)

[42] M. Köhl, H. Moritz, T. Stöferle, K. Günter and T. Esslinger. *Fermionic atoms in a three dimensional optical lattice: Observing fermi surfaces, dynamics, and interactions*. Physical Review Letters **94**(8), 080403 (2005)

[43] G. Modugno, F. Ferlaino, R. Heidemann, G. Roati and M. Inguscio. *Production of a fermi gas of atoms in an optical lattice*. Physical Review A **68**(1), 011601 (2003)

[44] H. Moritz, T. Stöferle, K. Günter, M. Köhl and T. Esslinger. *Confinement induced molecules in a 1D fermi gas*. Physical Review Letters **94**(21), 210401 (2005)

[45] K. Günter, T. Stöferle, H. Moritz, M. Köhl and T. Esslinger. *p-wave interactions in low-dimensional fermionic gases*. Physical Review Letters **95**(23), 230401 (2005)

[46] M. Köhl, K. Günter, T. Stöferle, H. Moritz and T. Esslinger. *Strongly interacting atoms and molecules in a 3D optical lattice.* Journal of Physics B: Atomic, Molecular and Optical Physics **39**(10), S47 (2006)

[47] T. Stöferle, H. Moritz, K. Günter, M. Köhl and T. Esslinger. *Molecules of fermionic atoms in an optical lattice.* Physical Review Letters **96**(3), 030401 (2006)

[48] T. Rom, T. Best, D. van Oosten, U. Schneider, S. Fölling, B. Paredes and I. Bloch. *Free fermion antibunching in a degenerate atomic fermi gas released from an optical lattice.* Nature **444**(7120), 733 (2006)

[49] J. K. Chin, D. E. Miller, Y. Liu, C. Stan, W. Setiawan, C. Sanner, K. Xu and W. Ketterle. *Evidence for superfluidity of ultracold fermions in an optical lattice.* Nature **443**(7114), 961 (2006)

[50] K. Günter, T. Stöferle, H. Moritz, M. Köhl and T. Esslinger. *Bose-fermi mixtures in a three-dimensional optical lattice.* Physical Review Letters **96**(18), 180402 (2006)

[51] S. Ospelkaus, C. Ospelkaus, O. Wille, M. Succo, P. Ernst, K. Sengstock and K. Bongs. *Localization of bosonic atoms by fermionic impurities in a three-dimensional optical lattice.* Physical Review Letters **96**(18), 180403 (2006)

[52] T. Best, S. Will, U. Schneider, L. Hackermüller, D. van Oosten, I. Bloch and D.-S. Lühmann. *Role of interactions in* ^{87}Rb-^{40}K *bose-fermi mixtures in a 3D optical lattice.* Physical Review Letters **102**(3), 030408 (2009)

[53] S. Will, T. Best, U. Schneider, L. Hackermüller, D.-S. Lühmann and I. Bloch. *Time-resolved observation of coherent multi-body interactions in quantum phase revivals.* Nature **465**(7295), 197 (2010)

[54] N. Strohmaier, Y. Takasu, K. Günter, R. Jördens, M. Köhl, H. Moritz and T. Esslinger. *Interaction-controlled transport of an ultracold fermi gas.* Physical Review Letters **99**(22), 220601 (2007)

[55] R. Jördens, N. Strohmaier, K. Günter, H. Moritz and T. Esslinger. *A mott insulator of fermionic atoms in an optical lattice.* Nature **455**(7210), 204 (2008)

[56] U. Schneider, L. Hackermüller, S. Will, T. Best, I. Bloch, T. A. Costi, R. W. Helmes, D. Rasch and A. Rosch. *Metallic and insulating phases of repulsively interacting fermions in a 3D optical lattice.* Science **322**(5907), 1520 (2008)

[57] L. Hackermüller, U. Schneider, M. Moreno-Cardoner, T. Kitagawa, T. Best, S. Will, E. Demler, E. Altman, I. Bloch and B. Paredes. *Anomalous expansion of attractively interacting fermionic atoms in an optical lattice.* Science **327**(5973), 1621 (2010)

[58] J. Simon, W. S. Bakr, R. Ma, M. E. Tai, P. M. Preiss and M. Greiner. *Quantum simulation of antiferromagnetic spin chains in an optical lattice.* Nature **472**(7343), 307 (2011)

[59] J. Struck, C. Ölschläger, R. L. Targat, P. Soltan-Panahi, A. Eckardt, M. Lewenstein, P. Windpassinger and K. Sengstock. *Quantum simulation of frustrated classical magnetism in triangular optical lattices.* Science **333**(6045), 996 (2011)

[60] S. Trotzky, P. Cheinet, S. Fölling, M. Feld, U. Schnorrberger, A. M. Rey, A. Polkovnikov, E. A. Demler, M. D. Lukin and I. Bloch. *Time-resolved observation and control of superexchange interactions with ultracold atoms in optical lattices.* Science **319**(5861), 295 (2008)

[61] S. Nascimbène, Y.-A. Chen, M. Atala, M. Aidelsburger, S. Trotzky, B. Paredes and I. Bloch. *Experimental realization of plaquette resonating valence-bond states with ultracold atoms in optical superlattices.* Physical Review Letters **108**(20), 205301 (2012)

[62] T. Fukuhara, A. Kantian, M. Endres, M. Cheneau, P. Schauß, S. Hild, D. Bellem, U. Schollwöck, T. Giamarchi, C. Gross, I. Bloch and S. Kuhr. *Quantum dynamics of a mobile spin impurity.* Nature Physics **9**(4), 235 (2013)

[63] J. Sebby-Strabley, M. Anderlini, P. S. Jessen and J. V. Porto. *Lattice of double wells for manipulating pairs of cold atoms.* Physical Review A **73**(3), 033605 (2006)

[64] S. Fölling, S. Trotzky, P. Cheinet, M. Feld, R. Saers, A. Widera, T. Müller and I. Bloch. *Direct observation of second-order atom tunnelling.* Nature **448**(7157), 1029 (2007)

[65] C. Becker, P. Soltan-Panahi, J. Kronjäger, S. Dörscher, K. Bongs and K. Sengstock. *Ultracold quantum gases in triangular optical lattices.* New Journal of Physics **12**(6), 065025 (2010)

[66] P. Soltan-Panahi, J. Struck, P. Hauke, A. Bick, W. Plenkers, G. Meineke, C. Becker, P. Windpassinger, M. Lewenstein and K. Sengstock. *Multi-component quantum gases in spin-dependent hexagonal lattices.* Nature Physics **7**(5), 434 (2011)

[67] G. Wirth, M. Ölschläger and A. Hemmerich. *Evidence for orbital superfluidity in the p-band of a bipartite optical square lattice.* Nature Physics **7**(2), 147 (2011)

[68] G.-B. Jo, J. Guzman, C. K. Thomas, P. Hosur, A. Vishwanath and D. M. Stamper-Kurn. *Ultracold atoms in a tunable optical kagome lattice.* Physical Review Letters **108**(4), 045305 (2012)

[69] T. Salger, C. Geckeler, S. Kling and M. Weitz. *Atomic landau-zener tunneling in fourier-synthesized optical lattices.* Physical Review Letters **99**(19), 190405 (2007)

[70] T. Salger, C. Grossert, S. Kling and M. Weitz. *Klein tunneling of a quasirelativistic bose-einstein condensate in an optical lattice.* Physical Review Letters **107**(24), 240401 (2011)

[71] D. Greif, T. Uehlinger, G. Jotzu, L. Tarruell and T. Esslinger. *Short-range quantum magnetism of ultracold fermions in an optical lattice.* Science **340**(6138), 1307 (2013)

[72] S. M. Foreman, K. W. Holman, D. D. Hudson, D. J. Jones and J. Ye. *Remote transfer of ultrastable frequency references via fiber networks.* Review of Scientific Instruments **78**(2), 021101 (2007)

[73] T.-L. Ho and Q. Zhou. *Squeezing out the entropy of fermions in optical lattices.* Proceedings of the National Academy of Sciences **106**(17), 6916 (2009)

[74] J.-S. Bernier, C. Kollath, A. Georges, L. De Leo, F. Gerbier, C. Salomon and M. Köhl. *Cooling fermionic atoms in optical lattices by shaping the confinement.* Physical Review A **79**(6), 061601 (2009)

[75] M. Lubasch, V. Murg, U. Schneider, J. I. Cirac and M.-C. Bañuls. *Adiabatic preparation of a heisenberg antiferromagnet using an optical superlattice.* Physical Review Letters **107**(16), 165301 (2011)

[76] S. Trotzky, Y.-A. Chen, U. Schnorrberger, P. Cheinet and I. Bloch. *Controlling and detecting spin correlations of ultracold atoms in optical lattices.* Physical Review Letters **105**(26), 265303 (2010)

[77] D. Greif, L. Tarruell, T. Uehlinger, R. Jördens and T. Esslinger. *Probing nearest-neighbor correlations of ultracold fermions in an optical lattice.* Physical Review Letters **106**(14), 145302 (2011)

[78] T. Stöferle, H. Moritz, C. Schori, M. Köhl and T. Esslinger. *Transition from a strongly interacting 1D superfluid to a mott insulator.* Physical Review Letters **92**(13), 130403 (2004)

[79] C. Kollath, A. Iucci, I. P. McCulloch and T. Giamarchi. *Modulation spectroscopy with ultracold fermions in an optical lattice.* Physical Review A **74**(4), 041604 (2006)

[80] S. D. Huber and A. Rüegg. *Dynamically generated double occupancy as a probe of cold atom systems.* Physical Review Letters **102**(6), 065301 (2009)

[81] R. Sensarma, D. Pekker, M. D. Lukin and E. Demler. *Modulation spectroscopy and dynamics of double occupancies in a fermionic mott insulator.* Physical Review Letters **103**(3), 035303 (2009)

[82] F. Hassler and S. D. Huber. *Coherent pumping of a mott insulator: Fermi golden rule versus rabi oscillations.* Physical Review A **79**(2), 021607 (2009)

[83] S. Taie, R. Yamazaki, S. Sugawa and Y. Takahashi. *An SU(6) mott insulator of an atomic fermi gas realized by large-spin pomeranchuk cooling.* Nature Physics **8**(11), 825 (2012)

[84] J. Heinze, S. Götze, J. S. Krauser, B. Hundt, N. Fläschner, D.-S. Lühmann, C. Becker and K. Sengstock. *Multiband spectroscopy of ultracold fermions: Observation of reduced tunneling in attractive bose-fermi mixtures.* Physical Review Letters **107**(13), 135303 (2011)

[85] L. Tarruell, D. Greif, T. Uehlinger, G. Jotzu and T. Esslinger. *Creating, moving and merging dirac points with a fermi gas in a tunable honeycomb lattice.* Nature **483**(7389), 302 (2012)

[86] T. Uehlinger, D. Greif, G. Jotzu, L. Tarruell, T. Esslinger, L. Wang and M. Troyer. *Double transfer through dirac points in a tunable honeycomb optical lattice.* The European Physical Journal Special Topics **217**(1), 121 (2013)

[87] Y. Hasegawa, R. Konno, H. Nakano and M. Kohmoto. *Zero modes of tight-binding electrons on the honeycomb lattice.* Physical Review B **74**(3), 033413 (2006)

[88] S.-L. Zhu, B. Wang and L.-M. Duan. *Simulation and detection of dirac fermions with cold atoms in an optical lattice.* Physical Review Letters **98**(26), 260402 (2007)

[89] B. Wunsch, F. Guinea and F. Sols. *Dirac-point engineering and topological phase transitions in honeycomb optical lattices.* New Journal of Physics **10**(10), 103027 (2008)

[90] G. Montambaux, F. Piéchon, J.-N. Fuchs and M. O. Goerbig. *Merging of dirac points in a two-dimensional crystal.* Physical Review B **80**(15), 153412 (2009)

[91] K. L. Lee, B. Grémaud, R. Han, B.-G. Englert and C. Miniatura. *Ultracold fermions in a graphene-type optical lattice.* Physical Review A **80**(4), 043411 (2009)

[92] V. M. Pereira, A. H. Castro Neto and N. M. R. Peres. *Tight-binding approach to uniaxial strain in graphene.* Physical Review B **80**(4), 045401 (2009)

[93] L.-K. Lim, J.-N. Fuchs and G. Montambaux. *Bloch-zener oscillations across a merging transition of dirac points.* Physical Review Letters **108**(17), 175303 (2012)

[94] J.-N. Fuchs, L.-K. Lim and G. Montambaux. *Interband tunneling near the merging transition of dirac cones.* Physical Review A **86**(6), 063613 (2012)

[95] R. Jördens, L. Tarruell, D. Greif, T. Uehlinger, N. Strohmaier, H. Moritz, T. Esslinger, L. De Leo, C. Kollath, A. Georges, V. Scarola, L. Pollet, E. Burovski, E. Kozik and M. Troyer. *Quantitative determination of temperature in the approach to magnetic order of ultracold fermions in an optical lattice.* Physical Review Letters **104**(18), 180401 (2010)

[96] S. Sugawa, K. Inaba, S. Taie, R. Yamazaki, M. Yamashita and Y. Takahashi. *Interaction and filling-induced quantum phases of dual mott insulators of bosons and fermions.* Nat Phys **7**(8), 642 (2011)

[97] N. Strohmaier, D. Greif, R. Jördens, L. Tarruell, H. Moritz, T. Esslinger, R. Sensarma, D. Pekker, E. Altman and E. Demler. *Observation of elastic doublon decay in the fermi-hubbard model.* Physical Review Letters **104**(8), 080401 (2010)

[98] R. Sensarma, D. Pekker, E. Altman, E. Demler, N. Strohmaier, D. Greif, R. Jördens, L. Tarruell, H. Moritz and T. Esslinger. *Lifetime of double occupancies in the fermi-hubbard model.* Physical Review B **82**(22), 224302 (2010)

[99] U. Schneider, L. Hackermüller, J. P. Ronzheimer, S. Will, S. Braun, T. Best, I. Bloch, E. Demler, S. Mandt, D. Rasch and A. Rosch. *Fermionic transport and out-of-equilibrium dynamics in a homogeneous hubbard model with ultracold atoms.* Nature Physics **8**(3), 213 (2012)

[100] J. Heinze, J. Krauser, N. Fläschner, B. Hundt, S. Götze, A. P. Itin, L. Mathey, K. Sengstock and C. Becker. *Intrinsic photoconductivity of ultracold fermions in optical lattices.* Physical Review Letters **110**(8), 085302 (2013)

[101] N. Strohmaier. *Exploring the Hubbard model with ultracold fermionic atoms in an optical lattice.* Ph.D. thesis, ETH Zurich (2010)

[102] R. Jördens. *Metallic and Mott-insulating phases in fermionic quantum gases.* Ph.D. thesis, ETH Zurich (2010)

[103] T. Stöferle. *Exploring Atomic Quantum Gases in Optical Lattices.* Ph.D. thesis, ETH Zurich (2005)

[104] H. Moritz. *One-dimensional Atomic Gases.* Ph.D. thesis, ETH Zurich (2006)

[105] M. Greiner. *Ultracold quantum gases in three-dimensional optical lattice potentials.* Ph.D. thesis, LMU München (2003)

[106] M. Greiner, I. Bloch, O. Mandel, T. W. Hänsch and T. Esslinger. *Exploring phase coherence in a 2D lattice of bose-einstein condensates.* Physical Review Letters **87**(16), 160405 (2001)

[107] K. I. Petsas, A. B. Coates and G. Grynberg. *Crystallography of optical lattices.* Physical Review A **50**(6), 5173 (1994)

[108] A. Hemmerich and T. W. Hänsch. *Two-dimesional atomic crystal bound by light.* Physical Review Letters **70**(4), 410 (1993)

[109] G. Grynberg, B. Lounis, P. Verkerk, J.-Y. Courtois and C. Salomon. *Quantized motion of cold cesium atoms in two- and three-dimensional optical potentials.* Physical Review Letters **70**(15), 2249 (1993)

[110] A. Hemmerich, C. Zimmermann and T. W. Hänsch. *Sub-kHz rayleigh resonance in a cubic atomic crystal.* Europhysics Letters (EPL) **22**(2), 89 (1993)

[111] R. Mottl. *Towards a square - superlattice transition.* Semester thesis, ETH Zürich (2009)

[112] B. Edlén. *The refractive index of air.* Metrologia **2**(2), 71 (1966)

[113] P. E. Ciddor. *Refractive index of air: new equations for the visible and near infrared.* Applied Optics **35**(9), 1566 (1996)

[114] J. C. Owens. *Optical refractive index of air: Dependence on pressure, temperature and composition.* Applied Optics **6**(1), 51 (1967)

[115] L.-S. Ma, P. Jungner, J. Ye and J. L. Hall. *Delivering the same optical frequency at two places: accurate cancellation of phase noise introduced by an optical fiber or other time-varying path.* Optics Letters **19**(21), 1777 (1994)

[116] P. Horowitz and H. Winfield. *The Art of Electronics* (Cambridge University Press, 1989)

[117] C. Becker. *Multi component Bose-Einstein condensates.* Ph.D. thesis, Universität Hamburg (2008)

[118] R. Jördens. *A Radio Frequency Source for the Preparation of Quantum States.* Master thesis, ETH Zürich (2006)

[119] P. L. Kapitza and P. a. M. Dirac. *The reflection of electrons from standing light waves.* Mathematical Proceedings of the Cambridge Philosophical Society **29**(02), 297 (1933)

[120] D. L. Freimund and H. Batelaan. *Bragg scattering of free electrons using the kapitza-dirac effect.* Physical review letters **89**(28 Pt 1), 283602 (2002). PMID: 12513146

[121] P. L. Gould, G. A. Ruff and D. E. Pritchard. *Diffraction of atoms by light: The near-resonant kapitza-dirac effect.* Physical Review Letters **56**(8), 827 (1986)

[122] S. B. Cahn, A. Kumarakrishnan, U. Shim, T. Sleator, P. R. Berman and B. Dubetsky. *Time-domain de broglie wave interferometry.* Physical Review Letters **79**(5), 784 (1997)

[123] U. Bissbort. *Dynamical Effects and Disorder in Ultracold Bosonic Matter.* Ph.D. thesis, JWG Universität Frankfurt am Main (2010)

[124] F. Schwabl. *Quantenmechanik (QM I)* (Springer DE, 2002)

[125] B. Gao. *Quantum-defect theory of atomic collisions and molecular vibration spectra.* Physical Review A **58**(5), 4222 (1998)

[126] R. B. Diener and T.-L. Ho. *The condition for universality at resonance and direct measurement of pair wavefunctions using rf spectroscopy.* arXiv:cond-mat/0405174 (2004)

[127] Y. Castin. *Basic theory tools for degenerate fermi gases.* arXiv:cond-mat/0612613 (2006). Ultra-cold Fermi Gases, M. Inguscio, W. Ketterle, C. Salomon (Ed.) (2007) 289-349

[128] A. J. Moerdijk, B. J. Verhaar and A. Axelsson. *Resonances in ultracold collisions of* ^{6}Li, ^{7}Li, *and* ^{23}Na. Physical Review A **51**(6), 4852 (1995)

[129] M. H. Szymańska, K. Góral, T. Köhler and K. Burnett. *Conventional character of the BCS-BEC crossover in ultracold gases of* ^{40}K. Physical Review A **72**(1), 013610 (2005)

[130] E. L. Bolda, E. Tiesinga and P. S. Julienne. *Effective-scattering-length model of ultracold atomic collisions and feshbach resonances in tight harmonic traps.* Physical Review A **66**(1), 013403 (2002)

[131] T. Busch, B.-G. Englert, K. Rzażewski and M. Wilkens. *Two cold atoms in a harmonic trap.* Foundations of Physics **28**(4), 549 (1998)

[132] J. Oitmaa, C. Hamer and W. Zheng. *Series Expansion Methods for Strongly Interacting Lattice Models* (Cambridge University Press, Cambridge, 2006)

[133] D. F. B. ten Haaf and J. M. J. van Leeuwen. *High-temperature series expansions for the hubbard model.* Physical Review B **46**(10), 6313 (1992)

[134] J. A. Henderson, J. Oitmaa and M. C. B. Ashley. *High-temperature expansion for the single-band hubbard model.* Physical Review B **46**(10), 6328 (1992)

[135] M. Körner. *High-temperature series expansions for lattice systems.* Ph.D. thesis, ETH Zurich (2005)

[136] R. Staudt, M. Dzierzawa and A. Muramatsu. *Phase diagram of the three-dimensional hubbard model at half filling.* The European Physical Journal B - Condensed Matter and Complex Systems **17**, 411 (2000)

[137] F. Werner, O. Parcollet, A. Georges and S. R. Hassan. *Interaction-induced adiabatic cooling and antiferromagnetism of cold fermions in optical lattices.* Physical Review Letters **95**(5), 056401 (2005)

[138] S. Fuchs, E. Gull, L. Pollet, E. Burovski, E. Kozik, T. Pruschke and M. Troyer. *Thermodynamics of the 3D hubbard model on approaching the néel transition.* Physical Review Letters **106**(3), 030401 (2011)

[139] K. Günter. *Interacting Fermi gases and Bose-Fermi mixtures in optical lattices.* Ph.D. thesis, ETH Zurich (2007)

[140] L. Ricci, M. Weidemüller, T. Esslinger, A. Hemmerich, C. Zimmermann, V. Vuletic, W. König and T. Hänsch. *A compact grating-stabilized diode laser system for atomic physics.* Optics Communications **117**(5–6), 541 (1995)

[141] G. C. Bjorklund, M. D. Levenson, W. Lenth and C. Ortiz. *Frequency modulation (FM) spectroscopy.* Applied Physics B **32**(3), 145 (1983)

[142] U. Schünemann, H. Engler, R. Grimm, M. Weidemüller and M. Zielonkowski. *Simple scheme for tunable frequency offset locking of two lasers.* Review of Scientific Instruments **70**(1), 242 (1999)

[143] D. Steck. *Rubidium 87 D Line Data* (2013). `http://steck.us/alkalidata/`

[144] T. Tiecke. *Properties of Potassium* (2013). `http://staff.science.uva.nl/~tgtiecke/PotassiumProperties.pdf/`

[145] P. D. Lett, R. N. Watts, C. I. Westbrook, W. D. Phillips, P. L. Gould and H. J. Metcalf. *Observation of atoms laser cooled below the doppler limit.* Physical Review Letters **61**(2), 169 (1988)

[146] T. Esslinger, I. Bloch and T. W. Hänsch. *Bose-einstein condensation in a quadrupole-ioffe-configuration trap.* Physical Review A **58**(4), R2664 (1998)

[147] K. B. Davis, M.-O. Mewes, M. A. Joffe, M. R. Andrews and W. Ketterle. *Evaporative cooling of sodium atoms.* Physical Review Letters **74**(26), 5202 (1995)

[148] W. Petrich, M. H. Anderson, J. R. Ensher and E. A. Cornell. *Stable, tightly confining magnetic trap for evaporative cooling of neutral atoms.* Physical Review Letters **74**(17), 3352 (1995)

[149] C. Zener. *Non-adiabatic crossing of energy levels.* Proceedings of the Royal Society of London. Series A **137**(833), 696 (1932)

[150] C. A. Regal and D. S. Jin. *Measurement of positive and negative scattering lengths in a fermi gas of atoms.* Physical Review Letters **90**(23), 230404 (2003)

[151] A. Tokuno. *Private Communication*

[152] M. Eckstein and P. Werner. *Nonequilibrium dynamical mean-field calculations based on the non-crossing approximation and its generalizations.* 1005.1872 (2010)

[153] A. Iucci, M. A. Cazalilla, A. F. Ho and T. Giamarchi. *Energy absorption of a bose gas in a periodically modulated optical lattice.* Physical Review A **73**(4), 041608 (2006)

[154] A. Reischl, K. P. Schmidt and G. S. Uhrig. *Temperature in one-dimensional bosonic mott insulators.* Physical Review A **72**(6), 063609 (2005)

[155] F. Massel, M. J. Leskinen and P. Törmä. *Hopping modulation in a one-dimensional fermi-hubbard hamiltonian.* Physical Review Letters **103**(6), 066404 (2009)

[156] F. Hassler, A. Rüegg, M. Sigrist and G. Blatter. *Dynamical unbinding transition in a periodically driven mott insulator.* Physical Review Letters **104**(22), 220402 (2010)

[157] A. Korolyuk, F. Massel and P. Törmä. *Probing the fulde-ferrell-larkin-ovchinnikov phase by double occupancy modulation spectroscopy.* Physical Review Letters **104**(23), 236402 (2010)

[158] Z. Xu, S. Chiesa, S. Yang, S.-Q. Su, D. E. Sheehy, J. Moreno, R. T. Scalettar and M. Jarrell. *Response to dynamical modulation of the optical lattice for fermions in the hubbard model.* Physical Review A **84**(2), 021607 (2011)

[159] A. Tokuno, E. Demler and T. Giamarchi. *Doublon production rate in modulated optical lattices.* Physical Review A **85**(5), 053601 (2012)

[160] A. Tokuno and T. Giamarchi. *Spin correlations and doublon production rate for fermionic atoms in modulated optical lattices.* Physical Review A **85**(6), 061603 (2012)

[161] V. W. Scarola, L. Pollet, J. Oitmaa and M. Troyer. *Discerning incompressible and compressible phases of cold atoms in optical lattices.* Physical Review Letters **102**(13), 135302 (2009)

[162] P. W. Anderson. *The resonating valence bond state in La2CuO4 and superconductivity.* Science **235**(4793), 1196 (1987)

[163] T. Müller, S. Fölling, A. Widera and I. Bloch. *State preparation and dynamics of ultracold atoms in higher lattice orbitals.* Physical Review Letters **99**(20), 200405 (2007)

[164] M. Köhl. *Thermometry of fermionic atoms in an optical lattice.* Physical Review A **73**(3), 031601 (2006)

[165] C. A. Regal, M. Greiner and D. S. Jin. *Lifetime of molecule-atom mixtures near a feshbach resonance in ˆ{40}k.* Physical Review Letters **92**(8), 083201 (2004)

[166] D. S. Petrov, C. Salomon and G. V. Shlyapnikov. *Weakly bound dimers of fermionic atoms*. Physical Review Letters **93**(9), 090404 (2004)

[167] T.-L. Ho. *Spinor bose condensates in optical traps*. Physical Review Letters **81**(4), 742 (1998)

[168] C. K. Law, H. Pu and N. P. Bigelow. *Quantum spins mixing in spinor bose-einstein condensates*. Physical Review Letters **81**(24), 5257 (1998)

[169] T. Ohmi and K. Machida. *Bose-einstein condensation with internal degrees of freedom in alkali atom gases*. Journal of the Physical Society of Japan **67**(6), 1822 (1998)

[170] H. Pu, C. K. Law, S. Raghavan, J. H. Eberly and N. P. Bigelow. *Spin-mixing dynamics of a spinor bose-einstein condensate*. Physical Review A **60**(2), 1463 (1999)

[171] A. Widera, F. Gerbier, S. Fölling, T. Gericke, O. Mandel and I. Bloch. *Coherent collisional spin dynamics in optical lattices*. Physical Review Letters **95**(19), 190405 (2005)

[172] J. S. Krauser, J. Heinze, N. Fläschner, S. Götze, O. Jürgensen, D.-S. Lühmann, C. Becker and K. Sengstock. *Coherent multi-flavour spin dynamics in a fermionic quantum gas*. Nature Physics **8**(11), 813 (2012)

[173] L. D. Landau. Phys. Soc. Union **2**(46) (1932)

[174] H. Haken and H. C. Wolf. *Atom- und Quantenphysik* (Springer DE, 2003)

[175] U. Schollwöck, J. Richter, D. J. J. Farnell and R. F. Bishop. *Quantum Magnetism* (Springer, 2004), 2004 edition

[176] E. Kozik, K. V. Houcke, E. Gull, L. Pollet, N. Prokof'ev, B. Svistunov and M. Troyer. *Diagrammatic monte carlo for correlated fermions*. EPL (Europhysics Letters) **90**(1), 10004 (2010)

[177] K. Van Houcke, E. Kozik, N. Prokof'ev and B. Svistunov. *Diagrammatic monte carlo*. Physics Procedia **6**, 95 (2010)

[178] L. Pollet. *Recent developments in quantum monte carlo simulations with applications for cold gases*. Reports on Progress in Physics **75**(9), 094501 (2012)

[179] W. Metzner and D. Vollhardt. *Correlated lattice fermions in infinite dimensions*. Physical Review Letters **62**(3), 324 (1989)

[180] M. Jarrell. *Hubbard model in infinite dimensions: A quantum monte carlo study*. Physical Review Letters **69**(1), 168 (1992)

[181] A. Georges and W. Krauth. *Physical properties of the half-filled hubbard model in infinite dimensions*. Physical Review B **48**(10), 7167 (1993)

[182] M. Ulmke, V. Janiš and D. Vollhardt. *Anderson-hubbard model in infinite dimensions*. Physical Review B **51**(16), 10411 (1995)

[183] M. H. Hettler, A. N. Tahvildar-Zadeh, M. Jarrell, T. Pruschke and H. R. Krishnamurthy. *Nonlocal dynamical correlations of strongly interacting electron systems*. Physical Review B **58**(12), R7475 (1998)

[184] T. Maier, M. Jarrell, T. Pruschke and M. H. Hettler. *Quantum cluster theories*. Reviews of Modern Physics **77**(3), 1027 (2005)

[185] P. Anderson. *Resonating valence bonds: A new kind of insulator?* Materials Research Bulletin **8**(2), 153 (1973)

[186] A. Oosawa, M. Fujisawa, T. Osakabe, K. Kakurai and H. Tanaka. *Neutron diffraction study of the pressure-induced magnetic ordering in the spin gap system TlCuCl3*. Journal of the Physical Society of Japan **72**(5), 1026 (2003)

[187] C. Rüegg, N. Cavadini, A. Furrer, H.-U. Güdel, K. Krämer, H. Mutka, A. Wildes, K. Habicht and P. Vorderwisch. *Bose–Einstein condensation of the triplet states in the magnetic insulator TlCuCl3*. Nature **423**(6935), 62 (2003)

[188] M. Jaime, V. F. Correa, N. Harrison, C. D. Batista, N. Kawashima, Y. Kazuma, G. A. Jorge, R. Stern, I. Heinmaa, S. A. Zvyagin, Y. Sasago and K. Uchinokura. *Magnetic-field-induced condensation of triplons in han purple pigment BaCuSi_{2}O_{6}*. Physical Review Letters **93**(8), 087203 (2004)

[189] A. V. Chubukov, T. Senthil and S. Sachdev. *Universal magnetic properties of frustrated quantum antiferromagnets in two dimensions*. Physical Review Letters **72**(13), 2089 (1994)

[190] S. R. White. *Density-matrix algorithms for quantum renormalization groups*. Physical Review B **48**(14), 10345 (1993)

[191] C. Rüegg, A. Furrer, D. Sheptyakov, T. Strässle, K. W. Krämer, H.-U. Güdel and L. Mélési. *Pressure-induced quantum phase transition in the spin-liquid TlCuCl3*. Physical Review Letters **93**(25), 257201 (2004)

[192] C. J. M. Mathy and D. A. Huse. *Accessing the néel phase of ultracold fermionic atoms in a simple-cubic optical lattice*. Physical Review A **79**(6), 063412 (2009)

[193] P. N. Ma, S. Pilati, M. Troyer and X. Dai. *Density functional theory for atomic fermi gases*. Nature Physics **8**(8), 601 (2012)

[194] E. V. Gorelik, D. Rost, T. Paiva, R. Scalettar, A. Klümper and N. Blümer. *Universal probes for antiferromagnetic correlations and entropy in cold fermions on optical lattices*. Physical Review A **85**(6), 061602 (2012)

[195] P.-B. He, Q. Sun, P. Li, S.-Q. Shen and W. M. Liu. *Magnetic quantum phase transition of cold atoms in an optical lattice*. Physical Review A **76**(4), 043618 (2007)

[196] A. H. Castro Neto, F. Guinea, N. M. R. Peres, K. S. Novoselov and A. K. Geim. *The electronic properties of graphene*. Reviews of Modern Physics **81**(1), 109 (2009)

[197] M. Z. Hasan and C. L. Kane. *Colloquium: Topological insulators.* Reviews of Modern Physics **82**(4), 3045 (2010)

[198] P. Soltan-Panahi, J. Struck, P. Hauke, A. Bick, W. Plenkers, G. Meineke, C. Becker, P. Windpassinger, M. Lewenstein and K. Sengstock. *Multi-component quantum gases in spin-dependent hexagonal lattices.* Nature Physics **7**(5), 434 (2011)

[199] P. Soltan-Panahi, D.-S. Lühmann, J. Struck, P. Windpassinger and K. Sengstock. *Quantum phase transition to unconventional multi-orbital superfluidity in optical lattices.* Nature Physics **8**(1), 71 (2012)

[200] K. Asano and C. Hotta. *Designing dirac points in two-dimensional lattices.* Physical Review B **83**(24), 245125 (2011)

[201] M. Ben Dahan, E. Peik, J. Reichel, Y. Castin and C. Salomon. *Bloch oscillations of atoms in an optical potential.* Physical Review Letters **76**(24), 4508 (1996)

[202] S. Kling, T. Salger, C. Grossert and M. Weitz. *Atomic bloch-zener oscillations and stückelberg interferometry in optical lattices.* Physical Review Letters **105**(21), 215301 (2010)

[203] A. Zenesini, D. Ciampini, O. Morsch and E. Arimondo. *Observation of stückelberg oscillations in accelerated optical lattices.* Physical Review A **82**(6), 065601 (2010)

[204] Y.-J. Lin, R. L. Compton, K. Jiménez-García, J. V. Porto and I. B. Spielman. *Synthetic magnetic fields for ultracold neutral atoms.* Nature **462**(7273), 628 (2009)

[205] T. Kitagawa, E. Berg, M. Rudner and E. Demler. *Topological characterization of periodically driven quantum systems.* Physical Review B **82**(23), 235114 (2010)

[206] A. Ramanathan, K. C. Wright, S. R. Muniz, M. Zelan, W. T. Hill, C. J. Lobb, K. Helmerson, W. D. Phillips and G. K. Campbell. *Superflow in a toroidal bose-einstein condensate: An atom circuit with a tunable weak link.* Physical Review Letters **106**(13), 130401 (2011)

[207] E. Dagotto and T. M. Rice. *Surprises on the way from one- to two-dimensional quantum magnets: The ladder materials.* Science **271**(5249), 618 (1996). `http://www.sciencemag.org/content/271/5249/618.full.pdf`

[208] E. Orignac, R. Citro and T. Giamarchi. *Critical properties and bose-einstein condensation in dimer spin systems.* Physical Review B **75**(14), 140403 (2007)

[209] E. Dagotto, J. Riera and D. Scalapino. *Superconductivity in ladders and coupled planes.* Physical Review B **45**(10), 5744 (1992)

[210] M. Matsuda, K. Katsumata, K. M. Kojima, M. Larkin, G. M. Luke, J. Merrin, B. Nachumi, Y. J. Uemura, H. Eisaki, N. Motoyama, S. Uchida and G. Shirane. *Magnetic phase transition in the s= zigzag-chain compound SrCuO_{2}.* Physical Review B **55**(18), R11953 (1997)

[211] F. D. M. Haldane. *Spontaneous dimerization in the s=1/2 heisenberg antiferromagnetic chain with competing interactions.* Physical Review B **25**(7), 4925 (1982)

[212] S. S. Kancharla and E. Dagotto. *Correlated insulated phase suggests bond order between band and mott insulators in two dimensions.* Physical Review Letters **98**(1), 016402 (2007)

[213] P. Hauke, O. Tieleman, A. Celi, C. Ölschläger, J. Simonet, J. Struck, M. Weinberg, P. Windpassinger, K. Sengstock, M. Lewenstein and A. Eckardt. *Non-abelian gauge fields and topological insulators in shaken optical lattices.* Physical Review Letters **109**(14), 145301 (2012)

[214] J. Struck, C. Ölschläger, M. Weinberg, P. Hauke, J. Simonet, A. Eckardt, M. Lewenstein, K. Sengstock and P. Windpassinger. *Tunable gauge potential for neutral and spinless particles in driven optical lattices.* Physical Review Letters **108**(22), 225304 (2012)

[215] M. Aidelsburger, M. Atala, S. Nascimbène, S. Trotzky, Y.-A. Chen and I. Bloch. *Experimental realization of strong effective magnetic fields in an optical lattice.* Physical Review Letters **107**(25), 255301 (2011)

[216] M. Atala, M. Aidelsburger, J. T. Barreiro, D. Abanin, T. Kitagawa, E. Demler and I. Bloch. *Direct measurement of the zak phase in topological bloch bands.* arXiv:1212.0572 (2012)

[217] T. Oka and H. Aoki. *Photovoltaic hall effect in graphene.* Physical Review B **79**(8), 081406 (2009)

[218] T. Kitagawa, T. Oka, A. Brataas, L. Fu and E. Demler. *Transport properties of nonequilibrium systems under the application of light: Photoinduced quantum hall insulators without landau levels.* Physical Review B **84**(23), 235108 (2011)

[219] F. D. M. Haldane. *Model for a quantum hall effect without landau levels: Condensed-matter realization of the "Parity anomaly".* Physical Review Letters **61**(18), 2015 (1988)

[220] M. Lebrat. *Engineering artificial gauge fields in time-modulated optical lattices.* Master thesis, ETH Zürich (2013)

List of publications

1. **Observation of elastic doublon decay in the Fermi-Hubbard model.**
   N. Strohmaier, D. Greif, R. Jördens, L. Tarruell, H. Moritz, T. Esslinger, R. Sensarma, D. Pekker, E. Altman and E. Demler.
   Physical Review Letters 104(8), 080401 (2010)

2. **Lifetime of double occupancies in the fermi-hubbard model.**
   R. Sensarma, D. Pekker, E. Altman, E. Demler, N. Strohmaier, D. Greif, R. Jördens, L. Tarruell, H. Moritz and T. Esslinger.
   Physical Review B 82(22), 224302 (2010)

3. **Quantitative determination of temperature in the approach to magnetic order of ultracold fermions in an optical lattice.**
   R. Jördens, L. Tarruell, D. Greif, T. Uehlinger, N. Strohmaier, H. Moritz, T. Esslinger, L. De Leo, C. Kollath, A. Georges, V. Scarola, L. Pollet, E. Burovski, E. Kozik and M. Toyer.
   Physical Review Letters 104(18), 180401 (2010)

4. **Probing nearest-neighbor correlations of ultracold fermions in an optical lattice.**
   D. Greif, L. Tarruell, T. Uehlinger, R. Jördens and T. Esslinger.
   Physical Review Letters 106(14), 145302 (2011)

5. **Creating, moving and merging dirac points with a fermi gas in a tunable honeycomb lattice.**
   L. Tarruell, D. Greif, T. Uehlinger, G. Jotzu and T. Esslinger.
   Nature 483 (7389), 302 (2012)

6. **Short-range quantum magnetism of ultracold fermions in an optical lattice.**
   D. Greif, T. Uehlinger, G. Jotzu, L. Tarruell and T. Esslinger.
   Science 340 (6138), 1307 (2013)

7. **Double transfer through dirac points in a tunable honeycomb optical lattice.**
   T. Uehlinger, D. Greif, G. Jotzu, L. Tarruell, T. Esslinger, L. Wang and M. Troyer.
   The European Physical Journal Special Topics 217(1), 121 (2013)

Invited Talks

1. **Condensed Matter Physics Seminar, Harvard / USA 2009**
   "Equilibrium and non equilibrium physics with ultracold fermions in optical lattices"

2. **Cecam Ab Initio Workshop, ETH Zurich / Switzerland 2010**
   "Fermi-Hubbard physics with ultracold fermions in an optical lattice"

3. **AMO Seminar Stony Brook University, New York / USA 2011**
   "Condensed matter physics with ultracold fermions in optical lattices"

4. **Gruppenseminar LMU München, München / Germany 2011**
   "Probing nearest-neighbor correlations of ultracold fermions in optical lattices"

5. **Laser Seminar Institut für Laserphysik, Hamburg / Germany 2012**
   "Engineering Dirac points with ultracold fermions in a tunable optical lattice"

6. **AAAS Meeting, Boston / USA 2013**
   "Exploring Dirac points with ultracold fermions in a tunable honeycomb optical lattice"

Danksagung

Die letzten fünf Jahre hier in Zürich waren eine aussergewöhnlich schöne Zeit für mich mit unzähligen interessanten und neuen Erlebnissen. Besonders genossen habe ich die wunderbare Arbeitsatmosphäre in der Gruppe und die vielen gemeinsamen Unternehmungen ausserhalb der Arbeit. Sowohl das konstante gegenseitige Aushelfen als ich die motivierende Hingabe für die Wissenschaft aller Mitarbeiter machte die intensive Zeit während meiner Doktorarbeit zu einem besonders schönen Erlebnis.

Zuallererst möchte ich mich bei Tilman Esslinger bedanken, der mir die Gelegenheit gab in seiner Gruppe zu forschen. Schon sehr früh merkte ich dass er die treibende Kraft des stets aussergewöhnlichen Arbeitsklimas ist. Ganz im Speziellen erwähnen möchte ich seine motivierende Art über neue Ideen zu diskutieren und seine Fähigkeit Zusammenhänge aus einem anderen Blickwinkel zu betrachten. Er war eine stetige Quelle der Inspiration und Motivation für mich.

Ein grosser Dank geht an die vielen Leute vom Gitter-Team. Besonders bedanken möchte ich mich bei Niels Strohmaier, der mich zu Beginn in alle experimentellen Finessen der Gitter Apparatur einführte und von dem ich vieles lernen durfte. Bedanken möchte ich mich auch bei Robert Jördens, der mich in die Welt von Python einführte und stets versucht war mir einen anständigen Programmierstil beizubringen. Ein grosser Dank geht an Henning Moritz für seine eifrig-freudige Art, die vielen gemeinsamen Schwimmgänge und die zahlreichen spannenden Diskussionen mit ihm. Ein grosser Dank geht auch an Leticia Tarruell, mit der ich das grosse Glück hatte fast die gesamte Zeit während meiner Doktorarbeit verbringen zu dürfen. Besonders in Erinnerung werden mir die unzähligen intensiven Stunden im Labor bleiben, die wir gemeinsam verbringen durften. Ihr wissenschaftlicher Scharfsinn und Fähigkeit die richtigen physikalischen Fragen zu stellen haben mich immer wieder aufs Neue beeindruckt. Besonders bedanken möchte ich mich auch bei Thomas Uehlinger. Seine ruhige, professionelle und genaue Art zu arbeiten machte die Zusammenarbeit mit ihm zu einem aussergewöhnlich angenehmen Erlebnis. Von seiner Arbeitsweise konnte ich vieles lernen und ich wünsche ihm für den anstehenden Endspurt seiner Doktorarbeit alles erdenklich Gute. Ein grosser Dank geht auch an Gregor Jotzu, mit dem ich viele tiefgreifende Diskussionen führen durfte. Seine sachlich fokussierte und objektive Art zu diskutieren war für mich immer wieder inspirierend. Ganz besonders erfreut haben mich die vielen gemeinsamen Aktivitäten ausserhalb der Arbeit, sei es bei einer wunderschönen Reise durch Spanien mit Leticia, den zahlreichen Bergtouren und Iglu Wochenenden mit Thomas oder das Feiern auf den angesagtesten Partys in Zürich mit Gregor. Auf die Zusammenarbeit mit unserem neuesten Teammitglied Michael Messer freue ich mich schon jetzt ganz besonders.

Die intensive Zusammenarbeit der verschiedenen Experimente in der Arbeitsgruppe war stets Basis für zahlreiche neue Ideen und erhellende Diskussionen. Ein ganz besonderer Dank

geht an alle für den Verleih einer absurd hohen Zahl von Frequenzgeneratoren, ohne die der Aufbau des neuen optischen Gitters nicht möglich gewesen wäre. Für die wunderschöne Zeit während und ausserhalb der Arbeit, den vielen sportlichen Aktivitäten und die zahlreichen Abenden bei einem Bier bin ich vielen Personen sehr dankbar: Bruno Zimmermann, Torben Müller, Jakob Meineke, David Stadler, Jean-Philippe Brantut, Sebastian Krinner, Stephan Ritter, Christine Guerlin, Silvan Leinss, Kristian Baumann, Rafael Mottl, Renate Landig, Ferdinand Brennecke, Tobias Donner, Monjoo Lee und Julian Leonard. Besonders erwähnen möchte ich Bruno und Torben, mit denen ich ausserhalb der Arbeit gemeinsam in der Harmonie Birmsndorf musizieren durfte. Bei meinen beiden Mitstreitern Jakob Meineke und Kristian Baumann, die fast zeitgleich ihre Dokorarbeit begannen, möchte ich mich für die gemeinsame Zeit des Lernens, die vielen lehrreichen Diskussionen und die unzähligen gemeinsamen Partys bedanken. Ein grosser Dank geht auch an die zahlreichen Semester- und Masterstudenten, die neben ihren ausgezeichneten fussballerischen Qualitäten auch im Labor viel Freude und Heiterkeit brachten.

Ein ganz herzlicher Dank geht an Alexander Frank und Veronica Bürgisser. Alex danke ich für die unverzichtbar wertvolle Elektronik Beratung – ohne seine profunden Kenntnisse würde ich hoffnungslos im RF Dschungel umherirren. Bei Veronica möchte ich mich ganz speziell für die stets herzliche Art bedanken. Sie ist Dreh- und Angelpunkt aller verwaltungstechnischen und kaufmännischen Angelegenheiten und unverzichtbar zentraler Bestandteil der Gruppe. Für Ihren wohlverdienten Ruhestand wünsche ich ihr von Herzen alles Gute.

Zuletzt möchte ich mich bei meinen Eltern Jakob und Anna und meinem Bruder Thomas bedanken. Sie haben mich während meines gesamten Lebens immerzu unterstützt und aufgebaut, wofür ich unendlich dankbar bin. Ganz besoners erwähnen möchte ich Renate, die mir während der intensiven Zeit des Zusammenschreibens stets zur Seite stand. Die Beziehung mit ihr ist ein unerwartetes Glück und eine ganz besondere Kraftquelle.